

# UNCLASSIFIED

AD NUMBER
ADB183806
NEW LIMITATION CHANGE
TO Approved for public release, distribution unlimited
FROM Distribution authorized to U.S. Gov't. agencies and their contractors; Administrative/Operational Use; OCT 1991. Other requests shall be referred to National Aeronautics and Space Administration, Washington, DC.
AUTHORITY
NASA TR Website

THIS PAGE IS UNCLASSIFIED

N92-10184  
①

AD-B183 806



# Final Report

for the NASA/MIT

## Explosive Transient Camera

### (ETC)

### Program

DTIC  
ELECTE  
MAY 10 1994  
S G D

Principal Investigator: Dr. George Ricker

NASA Contract Number NSG-7339

Submitted: October, 1991

Center for Space Research  
Massachusetts Institute of Technology

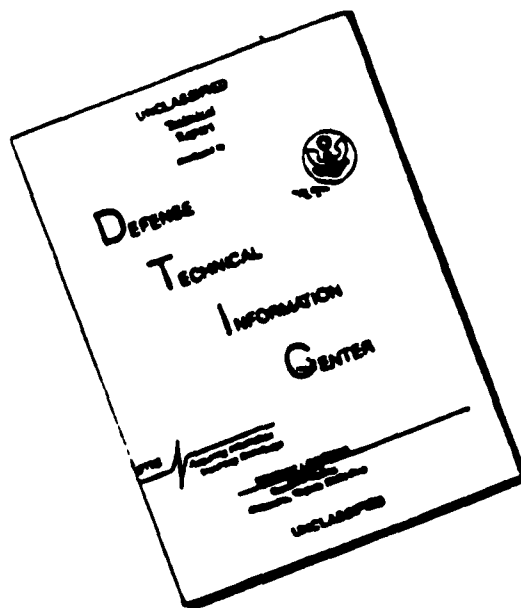
5426 94-13917



94 5 03  
DTIC QUALITY INSPECTED 1

009

# DISCLAIMER NOTICE



**THIS DOCUMENT IS BEST  
QUALITY AVAILABLE. THE COPY  
FURNISHED TO DTIC CONTAINED  
A SIGNIFICANT NUMBER OF  
PAGES WHICH DO NOT  
REPRODUCE LEGIBLY.**

# Final Report

for the NASA/MIT

## Explosive Transient Camera (ETC) Program

Principal Investigator: Dr. George Ricker

NASA Contract Number NSG-7339

Submitted: October, 1991

Center for Space Research  
Massachusetts Institute of Technology

Accession For	
NTIS CRA&I	<input checked="" type="checkbox"/>
DTIC TAB	
Unannounced	
Justification .....	
By .....	
Distribution /	
Availability Codes	
Dist	Avail and/or Special
12	



## **Final Report for the NASA/MIT ETC Program**

Since the inception of the ETC program in 1981, the MIT research team has developed a wide range of new technologies to support this novel astronomical instrument. The prototype unit was installed at ETC Site 1 on the summit of Kitt Peak in October, 1984. The first partially-automated observations were made in Spring, 1985. During CY1986, major renovations were made to the ETC hardware.

During 1986-1989, the ETC was outfitted with new, thermoelectrically-cooled CCD cameras and a sophisticated vacuum manifold, which, together, made the ETC a much more reliable unit than the prototype. The ETC instrumentation and building were placed under full computer control, allowing the ETC to operate as an automated, autonomous instrument with virtually no human intervention necessary. The first fully-automated operation of the ETC occurred in the spring and summer of 1987, during which time the ETC monitored the error region of the repeating soft gamma-ray burster SGR1806-21. In addition, the original Trigger Processors of the prototype were replaced with faster and more efficient single-board computers, with which the ETC improved its time resolution by 100%.

During the same period, construction of new camera systems for the ETC proceeded at MIT. By March, 1990, sixteen (16) of these "second generation" cameras were ready for installation at ETC Site 1. At the same time, new, more efficient observing software was prepared for installation and use at ETC Site 1. A list of the accomplishments of the ETC program is given below.

### **Summary of Accomplishments of the ETC Program**

1. Construction and installation at ETC Site 1 of a  $1/2$  steradian test unit. This unit was capable of monitoring the night sky under computer control, with only minimal human interaction.
2. Establishment of a new upper limit on the rate of celestial optical flashes of magnitude  $V < 10$  during observations with the  $1/2$  steradian test unit. The new upper limit is a full order of magnitude lower than the one determined using standard astronomical methods.
3. Observations of the mysterious "Perseus Flasher" were made during tests of automatic observations. The ETC monitored the error box of the Perseus Flasher for ~70 hours and saw no flash events. (The original source of the optical flashes was later determined to have been sunlight reflected from a Soviet Cosmos-series satellite).

4. Refurbishment of the original 1/2 steradian test unit with new, thermoelectrically-cooled CCD cameras and a new vacuum manifold. The cameras, developed at MIT, are significantly more efficient and reliable than the cameras used in the test unit; the vacuum manifold allows up to eight cameras to be mounted on a single telescope drive, and improves the integrity of the vacuum system as a whole.
5. Complete automation of the ETC hardware and environment. The ETC is equipped with weather sensors and the ability to determine observing conditions: its rule-based, AI-style software uses these capabilities to make decisions about observing in the same manner as would a human observer.
6. Observations spanning ~150 hours of the error region of the soft gamma-ray repeater SGR1806-21. Preliminary analysis has revealed no optical transients. (The southern declination of this object, combined with its "observing season" occurring during the summer Arizona monsoon, has severely limited the number of useful ETC observing hours on SGR1806-21.)
7. Detailed modelling of the contamination of ETC observations by artificial Earth satellites. This modelling has led to the development of a successful scheme, based upon observing into the earth's shadow, to dramatically reduce the rate of false events due to reflections of sunlight from artificial Earth satellites.
8. Upgrading of the original Trigger Processors to more sophisticated and flexible single-board computers. The new Trigger Processors allow the full dynamic range of the CCD electronics to be utilized.
9. Restructuring of the original ETC computer system architecture, introducing an Intermediate-Level Processor (ILP) between the Overseer Computer and the Trigger Processors. The use of the ILP, along with improvements in the real-time data analysis code, allowed the time resolution of ETC observations to be improved by 100%.
10. Construction of sixteen (16) "second generation" CCD cameras for use at Site 1.
11. Selection of 16 CCDs (TI 4849) for use at Site 1. The installation of the last of the CCDs in cameras occurred in Fall 1990.
12. Replacement of the dome on the ETC building at Site 1 by AutoScope, Inc. A computer-controllable replacement roof was installed in Spring, 1990.
13. Development of automated data post-processing software at MIT. The post-processing supplemented the real-time analysis code by examining flash data for subtle indications of a non-celestial origin, significantly improving the background rejection capability of the ETC system. This work was complete in Summer, 1990.

An important long-term, unexpected spin-off of the ETC Grant program was the necessary technology development for reliable, compact, low noise, thermoelectrically-cooled CCD cameras. This technology development was an **essential** precursor for the MIT-developed X-ray CCD camera to be flown as a US contribution to the Japanese Astro-D mission in 1993, and for the UV CCD camera to be flown on the USA/France/Japan High Energy Transient (HETE) mission in 1994.

In 1989, one major stumbling block in the way of a completed ETC Site 1 was removed: after over two years of searching, we found a competent vendor willing to replace the dome on the ETC Site 1 building with a reliable, automated roll-off roof. The original dome roof on the ETC building had a useful field-of-view of only  $\sim .5$  steradians, and thus prevented the ETC from performing true wide-field observations. AutoScope, Inc, of Mesa, AZ, was selected to install a computer controllable roll-off roof at Site 1; the work was completed in 1990. ETC Site 1 was ready for integration and testing in the Summer of 1990, and was fully operational in time to carry out a 6 month "minisurvey" prior to beginning simultaneous observations with the Gamma-Ray Observatory (GRO) in May 1991.

The efforts of the ETC team in CY 1990 were concentrated on the completion and full operation of ETC Site 1. By Winter 1990, ETC Site 1 was equipped with sixteen (16) wide-field CCD cameras with a full complement of data generation and reduction hardware and software, and that the site was operating in an automatic fashion. In addition, a SUN 4/60 workstation was installed at ETC Site 1 to act as a server for Internet communications to MIT and to GSFC (joint support for the Rapidly-Moving Telescope (RMT)), as well as to support the post-processing of ETC data.

A timetable of events for CY1990 is given below.

### **Schedule of events for 1990**

<b>March:</b>	Continued construction of CCD cameras. Construction of replacement roof for ETC Site 1.
<b>April:</b>	Final construction and checkout at MIT of the last of sixteen CCD cameras intended for use at ETC Site 1. Completed development of new real-time data analysis software at MIT using these cameras. Partially dismantled ETC Site 1 in anticipation of the replacement of the roof structure. Returned ETC cameras from Site 1 to MIT for cleaning and checking.
<b>May:</b>	Constructed computer hardware for control of the new roof structure.
<b>May/June:</b>	Installation of roll-off roof at Kitt Peak completed. Installation and integration of roof-control hardware and software completed. Began installation and on-site checkout of CCD cameras.
<b>June/July</b>	Installation of new Trigger Processors and full checkout of the complete ETC software system. Establishment of a data interface to the Rapidly Moving Telescope (RMT). Full checkout of the ETC weather system, including lightning detection during the Arizona monsoon season, completed.

- July/August: Completion of data post-processing software.
- December: Full wide-field, routine automatic ETC observations began; establishment of an Internet node at ETC Site 1.

As appendices to this final report, we include a set of technical and scientific papers completed under the sponsorship of this grant. These appendices are as follows:

- Appendix A *A Dual Charge-Coupled Device (CCD), Astronomical Spectrometer and Direct Imaging Camera I. Optical and Detector Systems*, Meyer, S.S., and Ricker, G.R., 1980, *SPIE*, 264, 38.
- Appendix B *A Dual Charge-Coupled Device (CCD), Astronomical Spectrometer and Direct Imaging Camera II. Data Handling and Control Systems*, Dewey, D., and Ricker, G.R., 1980, *SPIE*, 264, 42.
- Appendix C *Optical Studies of X-Ray Sources with the MASCOT - A Charge-Coupled Device (CCD)-Based Astronomical Instrument*, Ricker, G.R., Bautz, M.W., Dewey, D., Meyer, S.S., 1981, *SPIE*, 290, 190.
- Appendix D *The Explosive Transient Camera (ETC): An Instrument for the Detection of Gamma-Ray Burst Optical Counterparts*, Ricker, G.R., Doty, J. P., Vallerger, J.V., and Vanderspek, R. K. 1983, in *Instrumentation for Astronomy V*, eds. A. Boksenberg and D. Crawford (SPIE: Bellingham, Washington), 445, 370.
- Appendix E *Size of a Gamma Ray Burster Optical Emitting Region*, Schaefer, B.E., Ricker, G.R., 1983, *Nature*, 302, No. 5903, 43.
- Appendix F *A Search for High Proper Motion Objects in Two Gamma-Ray Burst Error Regions*, Ricker, G. R., Vanderspek, R. K., and Ajhar, E. A. 1986, *Adv. Space Res.*, 6, 75.
- Appendix G *A Search for Optical Flashes from the 'Perseus Flasher'*, 1986, Vanderspek, R.K., Ricker, G.R., and Zachary, D.S., *Adv. Space Res.*, 6, No.4, 69.
- Appendix H *Deep CCD Imaging of the Optical Flash Error Region Near GBS 1810+31* Ricker, G.R., Ajhar, E., A., Luu, J. P., and Vanderspek, R. K., 1986 *Ap. J. (Letters)*.
- Appendix I *The Effect of Artificial Earth Satellites on ETC Observations*, 1988, Vanderspek, R.K.
- Appendix J *Deep Optical and Radio Searches for a Quiescent Counterpart to the Optical Transient Source OTS 1809+31*. 1989, Ricker, G.R., Mock, P.C. , Ajhar, E.A., and Vanderspek, R.K. *Astrophys. J.*, 388, No. 2, 983.
- Appendix K *Three Faint Objects in the Optical Error Region of GBS2251-02*, 1989, Vanderspek, R.K., Ricker, G.R.
- Appendix L Vanderspek, Roland K. Ph.D. Thesis, Department of Physics, Massachusetts Institute of Technology, 1986. *The Explosive Transient Camera: A Wide Field Sky Monitor of Celestial Optical Flashes*.

## Bibliography of the Principal Investigator

## CURRICULUM VITA

**Name:** George Rollins Ricker

**Address of Institution:** Massachusetts Institute of Technology  
Center for Space Research, 37-535  
77 Massachusetts Avenue  
Cambridge, MA 02139

**Telephone:** (617) 253-7532

**Home:** 4 Coolidge Hill Road  
Cambridge, MA 02138

**Telephone:** (617) 354-1697

**Date of Birth:** 2 July 1944

**Place of Birth:** Tampa, Florida

**Education:** B.S. in Physics  
Massachusetts Institute of Technology  
(June 1966)

M.S. in Astronomy  
Yale University  
(September 1967)

Ph.D. in Physics  
Massachusetts Institute of Technology  
(September 1971)

**Professional Positions:**

1985 to present: Senior Research Scientist  
MIT Center for Space Research

1978 to 1985 Principal Research Scientist  
MIT Department of Physics

1971-1978 Staff Member  
MIT Center for Space Research

**Professional Societies:** International Astronomical Union  
American Physical Society  
American Astronomical Society

## CAREER HIGHLIGHTS

In collaboration with other members of the MIT X-ray Astronomy Group, Dr. Ricker has had a leading role in the:

- Discovery of the first of the slow X-ray pulsars, GX 1+4 (1970).
- Discovery of the size and shape of the hard X-ray emitting region of the Crab Nebula (1974).
- Establishment of the pulsed character of the hard X-ray emission from the transient source A0535+26 (1975).
- Establishment of a new class of X-ray galaxies typified by NGC5506 (1977)
- Discovery of the first "X-ray QSO," MR2251-178 (1977).
- Development of a highly efficient ground-based, solid state imager/ spectrometer constructed using silicon charge-coupled devices (the MIT Astronomical Spectrometer/Camera for Optical Telescopes, [MASCOT], first deployed at the McGraw-Hill Telescope on Kitt Peak, 1980).
- Development of the first practical wide bandgap semiconductor detectors for use in X-ray Astronomy (mercuric iodide detectors, flown by the MIT Balloon Group, 1980).
- Conducting the first astronomical observations with adequate sensitivity to directly image objects near the Galactic Center using the MASCOT CCD system (1981).
- Development of an advanced X-ray imager/spectrometer using silicon charge-coupled devices (CCDs) which were successfully tested at MIT in 1978 and accepted for flight on the NASA Advanced X-Ray Astrophysics Facility [AXAF] (1984).
- Development of a novel, wide field instrument, the Explosive Transient Camera (ETC), for surveying the entire sky for suspected flashes of light associated with gamma ray bursts (deployed in its initial configuration at an AURA-approved new observatory on Kitt Peak, 1984). The completed ETC became operational in 1990.
- Conception of the first practical multiwavelength observatory for the dedicated study of gamma-ray bursts – the High Energy Transient Experiment (HETE) - in 1987.
- Proposal and acceptance in 1987 of the first practical X-ray CCD imaging spectrometer which will fly on a satellite (Astro-D, February 1993 launch).

Beginning in 1972, Dr. Ricker served as Project Scientist for the MIT Balloon Group. In that role he was responsible for the development of four generations of balloon gondolas and participated in twelve flight expeditions. At the present, Dr. Ricker directs the efforts of the CCD Laboratory in the MIT Center for Space Research.

From 1987–1989, Dr. Ricker chaired the international Small Attached Payloads Working Group for Space Station *Freedom*. From 1987–1990, Dr. Ricker served as a member of NASA's High Energy Management Working Group. In 1990, he chaired a NASA Panel Workshop on Space Borne Data Processing for the 21st Century. He has served on numerous NASA advisory and mission review panels, including the adhoc U.S.–U.S.S.R. High Energy Astrophysics Cooperative Programs Panel.

Since 1980, Dr. Ricker has served as Undergraduate Research Opportunities Program (UROP) Coordinator for the Center for Space Research. The CCD Laboratory has provided research projects for more than 200 undergraduate students over the past decade. Dr. Ricker has supervised more than 50 senior thesis students during his tenure at MIT. Four graduate students have earned their Ph.D.'s in Physics in his group over the past decade.

Currently, Dr. Ricker is P.I. for the Explosive Transient Camera (ETC), a NASA-funded program, and is Deputy -P.I. for the AXAF CCD instrument, a core instrument for the NASA orbiting observatory (launch 1998). Dr. Ricker is Director of the National Transient Observatory (NTO), jointly operated by MIT and Goddard Space Flight Center at Kitt Peak National Observatory. He is the lead U.S. Co-Investigator for the detector effort on the Reflection Grating Spectrometer (RGS) on the European X-Ray Multi-Mirror Mission (XMM; launch 1999), and an RGS Science Working Group member. He also is the P.I. for the CCD Solid State Imaging Spectrometer on the Japan/USA ASTRO-D mission (launch February 1993), as well as the P.I. for the International High Energy Transient Experiment (HETE) – a dedicated small satellite incorporating instruments from France, Japan, and the USA – scheduled for launch in July 1994. During 1991, he heads (as P.I.) an international team utilizing the ROSAT orbiting observatory to study gamma-ray burst positions. In addition to gamma-ray burst sources, his current astronomical interests also include studies of active galactic nuclei.



## PUBLICATIONS LIST

### 1969

1. *Pulse Risetimes in Proportional Counters*, 1969, G.R. Ricker and J.J. Gomes, *Rev. Sci. Instrum.*, 40, 227.

### 1971

2. *Rapid Fluctuations in the High Energy X-ray Flux from a Source in Crux*, 1971, J.E. McClintock, G.R. Ricker and W.H.G. Lewin, *Ap.J. (Letters)*, 166, L73.
3. *X-rays from a New Variable Source GX 1+4*, 1971, W.H.G. Lewin, G.R. Ricker and J.E. McClintock, *Ap.J. (Letters)*, 169, L17.

### 1972

4. *High Energy X-ray Sources Near the Galactic Equator Between Galactic Latitude 335° and 350°*, 1972, J.E. McClintock, G.R. Ricker, S.G. Ryckman, and W.H.G. Lewin, *Ap.J.(Letters)*, 173, L57.

### 1973

5. *High Energy X-ray Spectra of Five Sources*, 1973, G.R. Ricker, J.E. McClintock, M. Gerassimenko, and W.H.G. Lewin, *Ap.J.*, 184, 227.
6. *Upper Limits to the High-Energy X-ray Flux from 16 X-ray Sources and 10 Pulsars*, 1973, G.R. Ricker, M. Gerassimenko, J.E. McClintock, and W.H.G. Lewin, *Ap.J. (Letters)*, 186, L111.

### 1974

7. *An Orientable, Stabilized Balloon-Borne Gondola for Around-the-World Flights*, 1974, G.R. Ricker, and W.H.G. Lewin, *Telescope Systems for Balloon-Borne Research*, ed. C. Swift, F. Witteborn, and A. Shipley, (NASA, Washington, D.C.), 71.

### 1975

8. *High Energy X-ray Observations of a Lunar Occultation of the Crab Nebula*, 1975, G.R. Ricker, A. Scheepmaker, S.G. Ryckman, J.E. Ballintine, J.P. Doty, P.M. Downey, and W.H.G. Lewin, *Ap.J. (Letters)*, 197, L83.

9. *High Energy X-ray Observations*, 1975, W.H.G. Lewin, G.R. Ricker, A. Scheepmaker, J.E. Ballintine, G.A. Kriss, J.P. Doty, P.M. Downey, and S.G. Ryckman, *Proceedings of the 14th International Cosmic Ray Conference*, 1, 200,
10. *The Perseus and Coma Clusters of Galaxies at Energies Above 20 keV*, 1975, A. Scheepmaker, G.R. Ricker, K. Brecher, S.G. Ryckman, J.E. Ballintine, J.P. Doty, P.M. Downey, and W.H.G. Lewin, *ApJ. (Letters)*, 205, L65.

#### 1976

11. *High Energy X-ray Observations of the Transient Source A0535+26 from a Balloon-Borne Telescope*, 1976, G.R. Ricker, A. Scheepmaker, J.E. Ballintine, J.P. Doty, G.A. Kriss, S.G. Ryckman, and W.H.G. Lewin, *ApJ. (Letters)*, 204, L73.
12. *Observations of Cygnus X-3 from a Balloon-Borne X-ray Telescope*, 1976, G.R. Ricker, A. Scheepmaker, J.E. Ballintine, J.P. Doty, G.A. Kriss, S.G. Ryckman, and W.H.G. Lewin, *X-ray Binaries*, ed. E. Boldt and Y. Kondo, NASA (Washington, D.C.), 299.

#### 1977

13. *Transient Structure in the High Energy X-ray Light Curve of NP0532*, 1977, S.G. Ryckman, G.R. Ricker, A. Scheepmaker, J.E. Ballintine, J.P. Doty, P.M. Downey, and W.H.G. Lewin, *Nature*, 266, 431.

#### 1978

14. *Fairall 9: An X-ray Seyfert Galaxy?*, 1978, G.R. Ricker, *Nature*, 271, 334.
15. *Discovery of an X-ray QSO*, 1978, G.R. Ricker, G.W. Clark, R.E. Doxsey, R.G. Dower, J.G. Jernigan, C.R. Canizares, J.P. Delvaille, G.M. MacAlpine, R.M. Hjellming, *Nature*, 271, 35.
16. *Spectrophotometry of the X-ray QSO MR2251-178*, 1978, C.R. Canizares, J.E. McClintock, and G.R. Ricker, *ApJ. (Letters)*, 226, L1.

#### 1979

17. *Observations of an X-ray QSO*, 1979, G.R. Ricker, G.W. Clark, R.E. Doxsey, R.G. Dower, J.G. Jernigan, C.R. Canizares, J.P. Delvaille,

G.M. MacAlpine, R.M. Hjellming, in *Advances in Space Exploration*, 3, (ed. L. Peterson and W. Baity).

#### 1980

18. *A Dual Charge-Coupled Device (CCD) Astronomical Spectrometer and Direct Imaging Camera I. Optical and Detector Systems*, 1980, S.S. Meyer and G.R. Ricker, in *Applications of Digital Image Processing to Astronomy*, ed. Elliott, D. (NASA/JPL Proceedings S.P.I.E. 264, Billingham, Washington), 38.
19. *A Dual Charge-Coupled Device (CCD) Astronomical Spectrometer and Direct Imaging Camera II. Data Handling and Control Systems*, 1980, D. Dewey and G.R. Ricker, in *Applications of Digital Image Processing to Astronomy*, ed. Elliott, D. (NASA/JPL Proceedings S.P.I.E. 264 Billingham, Washington), 42.
20. *X-Ray Observations of Seyfert Galaxies with the Einstein Observatory*, 1980, G.A. Kriss, C.R. Canizares and G.R. Ricker, *Ap. J.*, 242, 492.

#### 1981

21. *Optical Studies of X-Ray Sources with the MASCOT, a Charge-Coupled Device (CCD)-based Astronomical Instrument*, 1981, G.R. Ricker, M.W. Bautz, D. Dewey, and S.S. Meyer, in *Solid State Imagers for Astronomy* eds. J. Geary and D. Latham (S.P.I.E., Billingham, Washington), 290, 190.
22. *High Energy X-Ray Spectrum of Her X-1*, 1981, A. Scheepmaker, F.A. Jansen, A.J.M. Deerenberg, G.R. Ricker, J.E. Ballintine, J.V. Vallergera, and W.H.G. Lewin, *X-Ray Astronomy*, ed. R.D. Anderson (D. Riedel: Dordrecht, Holland), 325.

#### 1982

23. *Discovery of Three Far Red Objects in CCD Images of the Galactic Center*, 1982, G.R. Ricker, M.W. Bautz, D.L. DePoy, and S.S. Meyer, *Ap. J. (Letters)*, 266, L59.
24. *Studies of Near Infrared Objects in CCD Images of the Galactic Center*, G.R. Ricker, M.W. Bautz, D.L. DePoy, and S.S. Meyer, in *The Galactic Center*, ed. G. Riegler (American Institute of Physics, 1982), 97.

25. *A New Measurement of the Fano Factor in Mercuric Iodide*, 1982, G.R. Ricker, J. Vallerger, A. Dabrowski, and J. Entine, *Review of Scientific Instruments*, 53, 700.
26. *X-Ray Observations of the 1980 Cygnus X-1 "High State"*, 1982, Y. Ogawara, K. Mitsuda, J.V. Vallerger, L. R. Cominsky and G.R. Ricker, *Nature*, 295, 675.
27. *A Bismuth Germanate Shielded Mercuric Iodide Detector for Space Applications*, 1982, J.V. Vallerger, G.R. Ricker, W. Schnepfle, and C. Ortale, *IEEE Trans. on Nuclear Science*, NS-29, 151.
28. *Performance of Room-Temperature X-Ray Detectors Made from Mercuric Iodide (HgI<sub>2</sub>) Platelets*, 1982, J.B. Barton, A.J. Dabrowski, J.S. Iwanczyk, J.H. Kusmiss, G.R. Ricker, J.V. Vallerger, A. Warren, M.R. Squillante, S. Lis, G. Entine, in Volume 25 of *Advances in X-Ray Analysis*, ed. J.C. Russ (Plenum: New York), 31.

#### 1983

29. *HO323+022: A Puzzling High-Latitude X-ray/Optical/Radio Source*, 1983, R. Doxsey, H. Bradt, J. McClintock, L. Petro, R. Remillard, G.R. Ricker, D. Schwartz, and K. Wood, *Ap. J.(Letters)*, 264, L43.
30. *Periodic Variability of the X-Ray Nova A0620-00 in Quiescence*, 1983, J.E. McClintock, L.D. Petro, R.A. Remillard and G.R. Ricker, *Ap.J. (Letters)*, 266, L27.
31. *The Size of a Gamma-Ray Burst Optical Emitting Region*, 1983, B.E. Schaefer and G.R. Ricker, *Nature*, 302, 43.
32. *A Faint Star Astrometric Grid for the Galactic Center*, 1983, R.K. Vanderspek and G.R. Ricker, *Astron. J.*, 88, 1264.
33. *A Mercuric Iodide Detector System for X-Ray Astronomy I. Design Considerations and Predictions of Background and Sensitivity*, 1983, G.R. Ricker, J.V. Vallerger and D.R. Wood, *Nucl. Instr. and Meth.*, 213, 133.
34. *A Mercuric Iodide Detector System for X-Ray Astronomy II. Results from Flight Tests of a Balloon-Borne Instrument*, 1983, J.V. Vallerger, R.K. Vanderspek and G.R. Ricker, *Nucl. Instr. and Meth.*, 213, 133.

#### 1984

35. *The Explosive Transient Camera (ETC): An Instrument for the Identification of Gamma Ray Burst Optical Counterparts*, 1984, G.R. Ricker, J.P. Doty, J.V. Vallergera, and R.K. Vanderspek, in *High Energy Transients in Astrophysics*, ed. S.E. Woosley, (New York: American Inst. of Physics), 669.
36. *Optical Observations of the Millisecond Pulsars PSR 1937+214 and PSR 1953+29*, 1984, T. Laredo, G.R. Ricker, S. Rappaport, and J. Middleditch, in *Millisecond Pulsars* (ed. S.P. Reynolds and D.R. Stinebring, NRAO), 48.
37. *An Intercontinental Baseline Coincidence Search for Optical Flashes with Two Schmidt Telescopes*, 1984, B.E. Schaefer, R.K. Vanderspek, G.R. Ricker, and H.V. Bradt, *Ap. J.*, 283, 887, 96.
38. *Methods for Realtime Optical Transient Searches*, 1984, G.R. Ricker, J.P. Doty, J.V. Vallergera, and R.K. Vanderspek, in *High Energy Transients in Astrophysics*, ed. S.E. Woosley (AIP, New York), 669.
39. *The High Energy Transient Explorer (HETE)*, 1984, E.L. Chupp, T.L. Cline, W.D. Evans, E. Fenimore, P. Gorenstein, J. Grindlay, D.Q. Lamb, W.H.G. Lewin, R.E. Lingenfelter, J.L. Matteson, R. Ramaty, G.R. Ricker, G. Share, B. Teegarden, S.E. Woosley. AIP Conf. Proc., No. 115, (AIP, New York) 709.

#### 1985

40. *A High Speed, Dual-CCD Imaging Photometer*, 1985, E.W. Dunham, R.L. Baron, J.L. Elliot, J.V. Vallergera, J.P. Doty, and G.R. Ricker, *Publ. Astron. Soc. Pac.*, 97, No. 598, 1196.

#### 1986

41. *The AXAF CCD Imaging Spectrometer*. 1986, G.P. Garmire, D. Burrows, C. Canizares, G. Clark, S.A. Collins, E. Feigelson, J. Morrison, J. Nousek, S.H. Pravdo, S.A. Rappaport, G.R. Ricker, G.R. Riegler, and D. Weedman. *Proc. SPIE Int. Soc. Opt. Eng.*, 597, 261.
42. *A Search for Optical Flashes from the 'Perseus Flasher'*, 1986, R.K. Vanderspek, G.R. Ricker and D.S. Zachary, *Adv. Space Res.*, 6, No.4, 69.

43. *A Search for High Proper Motion Objects in Two  $\gamma$ -Ray Burst Error Regions*, 1986, G. R. Ricker, R. K. Vanderspek and E. A. Ajhar, *Adv. Space Res.*, 6, No. 4, 75.
44. *Early Photometry of Comet P/Halley: Development of the Coma*, 1986, K. J. Meech, D. Jewitt, G. R. Ricker, *Icarus*, 66, No. 3, 561.
45. *Future Gamma Ray Burst Observations and Missions*, K. Hurley, R. Kaipa, T.M.K. Marar, C. Meegan, J. Nishimura, H. Pedersen, G. Pizzichini, G. Ricker, and B. Teegarden, 1986, *AIP Conf. Proc.*, No. 141, 1.
46. *Near-infrared [S III] and H-alpha Imaging of Nearby Starburst Galaxies*. 1986, W.H. Waller, S.G. Kleinmann, G.R. Ricker. *Publ. Astron. Soc. Pac.*, 98, No. 609, 1108.

#### 1987

47. *Design of Low Noise, High Performance X-ray Charge-Coupled-Device Cameras*, 1987, J.P. Doty, G. A. Luppino, G.R.Ricker, *Optical Engineering*, 26, 1055.
48. *Imaging and Nondispersive Spectroscopy of Soft X-Rays Using a Laboratory X-Ray Charge-Coupled-Device system*, 1987, G.A. Luppino, N.M.Ceglio, J.P.Doty, G.R.Ricker, J.V.Vallerga, *Optical Engineering*, 26, 1048.
49. *Matching a Curved Focal Plane with CCD's: Wide Field Imaging of Glancing Incidence X-Ray Telescopes*, 1987, J.A.Nousek, G.P.Garmire, G.R.Ricker, M.W.Bautz, A.M.Levine, S.A.Collins, *Proc. SPIE Int. Soc. Opt. Eng.*, 818, 296.
50. *The MIT Spectroscopy Investigation on AXAF and the Study of Supernova Remnants*, 1987, C.R.Canizares, H.V.D.Bradt, B.W.Clark, A.C.Fabian, P.C.Joss, A.M.Levine, T.H.Markert, W.Mayer, G.R.Ricker, M.L.Schattenburg, H.I.Smith, B.E.Woodgate, *Astro. Lett. and Communications*, 26, Nos. 1-2, 87.
51. *The AXAF CCD Imaging Spectrometer Experiment (ACIS)*, 1987, J.A.Nousek, G.P. Garmire, G.R.Ricker, S.A.Collins, G.R.Reigler, *Astro. Lett. and Communications*, 26, Nos. 1-2, 35.
52. *A CCD X-Ray Detector Performance Model*, 1987, M.W.Bautz, G.E.Berman, J.P.Doty, G.R.Ricker, *Optical Engineering*, 26, No. 8, 757.

53. *Prediction Methods for CCD X-Ray Detector Performance*, 1987, M.W. Bautz, G.E. Berman, J.P. Doty, G.R. Ricker, *SPIE*, 688, 202.
54. *X-ray CCD Cameras: I. Design of Low Noise, High Performance Systems*, 1987, J.P. Doty, G.A. Luppino, G.R. Ricker, *SPIE*, 570, 82.
55. *X-Ray CCD Cameras: A Versatile Laboratory System*, 1987, G.A. Luppino, N.M. Ceglio, J.P. Doty, G.R. Ricker, J.V. Vallergera, *SPIE*, 688, 222.
56. *The "Jet" of M89; CCD Surface Photometry*. 1987, G. Clark, P. Plucinsky, G. Ricker, in *Structure and Dynamics of Elliptical Galaxies*, ed. T. De Zeeuw (Princeton, Institute for Advanced Study), 453.

#### 1988

57. *Obscuration and Star Formation in NCG 253: H $\alpha$  and Near-Infrared [SIII] Imagery*. 1988, W.H. Waller, S.G. Kleinmann, G.R. Ricker. *Astron. J.*, 95, No. 4, 1057.
58. *The Explosive Transient Camera: An Automatic, Wide-field Monitor of Short-timescale Celestial Optical Flashes*. 1988, R.K. Vanderspek, D.S. Zachary, G.R. Ricker. *Bull Am. Astron. Soc.*, 20, No. 4, 953.
59. *Performance Characteristics of CCDs for the ACIS Experiment*. 1988, G.P. Garmire, J. Nousek, D. Burrows, G. Ricker, M. Bautz, J. Doty, S. Collins, J. Janesick, R. W. Mountain, B. E. Burke, in *X-Ray Instrumentation in Astronomy II.*, ed. L. Golub (*SPIE*, Bellingham, WA), 982, 432.
60. *CCD X-Ray Detectors: A Review*, 1988, G.R. Ricker, in *X-Ray Instrumentation in Astronomy II*, ed. L. Golub, (*SPIE*, Bellingham, WA), 982, 420.
61. *The High Energy Transient Experiment - HETE - A Multi-Wavelength Survey Mission for the 1990's*. 1988, G.R. Ricker, J. Doty, S. Rappaport, K. Hurley, E. Fenimore, D. Roussel-Dupre, M. Niel, G. Vedrenne, D. Lamb, S. Woosley, in *Nuclear Spectroscopy of Astrophysical Sources*, eds. N. Gehrels, and G.H. Share (New York: American Institute of Physics), 407.

### 1989

62. *Deep Optical and Radio Searches for a Quiescent Counterpart to the Optical Transient Source OTS 1809+31*. 1989, G.R. Ricker, P.C. Mock, E.A. Ajhar, R.K. Vanderspek. *Astrophys. J.*, 388, No. 2, 983.

### 1990

63. *Advanced CCD Imager Technology for use from 1 to 10 000 Å*. 1990, J.C. Twichell, B.E. Burke, R.K. Reich, W.H. McGonagle, C.M. Huang, M.W. Bautz, J.P. Doty, G.R. Ricker, R.W. Mountain, and V.S. Dolat. *Rev. Sci. Instrum.*, 61, 10, 2744.
64. *An Abutable CCD Imager For Visible and X-ray Focal Plane Arrays*, B. E. Burke, R. W. Mountain, D. C. Harrison, G. R. Ricker, M. W. Bautz, J. P. Doty, J. Reynold, and C. Doherty, *ISSCC Digest of Technical Papers* (IEEE, New York, 1989), 94.
65. *The Energy Transient Array - ETA - A Network of 'Space Buoys' in Solar Orbit for Observations of Gamma-Ray Bursts*, 1990, G.R. Ricker, in High Energy Astrophysics in the 21st Century (ed. P. Joss) Am. Inst. of Physics., 375.

### 1991

66. *An Abutable CCD Imager for Visible and X-Ray Focal Plane Arrays*, 1991, B. Burke, R. Mountain, D. Harrison, G. Ricker, M. Bautz and J. Doty. *IEEE Transactions on Electron Devices*, 38, No. 5., 1069.

### IAU Telegrams

67. *Lunar Occultations of the Crab Nebula in High Energy X-Rays*, 1975, G.R. Ricker, A. Scheepmaker, J.E. Ballintine, J.P. Doty, P.M. Downey, S.G. Ryckman, and W.H.G. Lewin, Circular No. 2704.
68. *Crab Pulsar*, 1975, S.G. Ryckman, G.R. Ricker, A. Scheepmaker, J.E. Ballintine, J.P. Doty, P.M. Downey, and W.H.G. Lewin, Circular No. 2760.
69. *Transient X-ray Source A0535+26 Recurrence*, 1976, G.R. Ricker and F.A. Primini, Circular No. 3078.
70. *MXB1730-335*, 1977, P.C. Joss, G.R. Ricker, W.F. Mayer, and J.A. Hoffman, Circular No. 3108.
71. *Periodic Comet Halley (1982i)*, 1985, D. Jewitt, K. Meech, G. Ricker, Circular 4148.



**AAS Papers (in Bulletin of the American Astronomical Society)**

72. "Hard X-rays from the Southern Sky," 1971, W.H.G. Lewin, G.R. Ricker, J.E. McClintock, S.G. Ryckman, and M. Gerassimenko, 3, 456.
73. "Balloon Observations of High Energy X-ray Sources from the Southern Sky," 1973, W.H.G. Lewin, G.R. Ricker, J.E. McClintock, M. Gerassimenko, and S.G. Ryckman, 5, 57.
74. "Far IR Photometry from a Balloon-Borne Telescope," 1973, G.R. Ricker, J.P. Doty, M. Shao, S.G. Ryckman, W.H.G. Lewin, W.M. Poteet, and F.J. Low), 5, 437,
75. "A Hard X-ray Observation of the Perseus and Coma Clusters," 1974, G.R. Ricker, A. Scheepmaker, J.E. Ballintine, J.P. Doty, P.M. Downey, S.G. Ryckman, and W.H.G. Lewin, 6, 437,
76. "High Energy X-ray Observations of a Lunar Occultation of the Crab Nebula from a Balloon-Borne Telescope," 1974, G.R. Ricker, A. Scheepmaker, S.G. Ryckman, P.M. Downey, J.P. Doty, J.E. Ballintine, and W.H.G. Lewin, 6, 437.
77. "A Study of the Hard X-ray Emission from the Crab Pulsar (NP0532) Using a Balloon-Borne Telescope," 1974, G.R. Ricker, A. Scheepmaker, S.G. Ryckman, P.M. Downey, J.P. Doty, J.E. Ballintine, and W.H.G. Lewin, 6, 454.
78. "High Energy X-ray Observations of the Transient Source A0535+26 from a Balloon-Borne Telescope," 1974, G.R. Ricker, A. Scheepmaker, J.E. Ballintine, J.P. Doty, G.A. Kriss, S.G. Ryckman, and W.H.G. Lewin, 7, 431.
79. "High Energy X-ray Balloon Observations of NP0532, Cyg X-1, Cyg X-3, and A0535+26," 1975, G.R. Ricker, A. Scheepmaker, J.E. Ballintine, J.P. Doty, G.A. Kriss, S.G. Ryckman, and W.H.G. Lewin, 7, 524.
80. "Discovery of an X-ray QSO," 1977, G.R. Ricker, G.W. Clark, R.E. Doxsey, R.G. Dower, J.G. Jernigan, J.P. Delvaille, G.M. MacAlpine, and R.M. Hjellming, 9, 578.
81. "NGC5506 and NGC7582: Counterparts to X-ray Sources," 1978, G.R. Ricker, R.G. Dower, J.G. Jernigan, R.E. Doxsey, H.V. Bradt, and H.W. Schnopper, 10, 403.

82. "High Energy X-ray Observations of Compact Extragalactic Sources," 1979, G.R. Ricker, J.E. Ballintine, S. Haid, J.V. Vallerger, W.H.G. Lewin, A. Scheepmaker, A.J.M. Deerenberg, and A.G. Visser, *11*, 693,
83. "Temporal Structure in the Hard X-ray Emission of Cyg X-1," 1979, G.R. Ricker, J.E. Ballintine, J.V. Vallerger, S. Haid, W.H.G. Lewin, A.J.M. Deerenberg, A. Scheepmaker, and A.G. Visser, *11*, 702.
84. "High Energy X-ray Spectra of Cyg X-1 and Cyg X-3," 1979, G.R. Ricker, A. Scheepmaker, A.J.M. Deerenberg, A.G. Visser, J.E. Ballintine, S. Haid, J.V. Vallerger, and W.H.G. Lewin, *11*, 795,
85. "High Energy X-Ray Observations of QSOs and Active Galaxies," 1980, G.R. Ricker, J.E. Ballintine, J.V. Vallerger, J.S. Kruper, E. Basinska, and W.H.G. Lewin, *12*, 795.
86. "High Energy X-Ray Spectra of Cyg X-1 and the Crab," 1980, G.R. Ricker, A. Scheepmaker, A.J.M. Deerenberg, F.A. Jansen, J.E. Ballintine, J.V. Vallerger, J.S. Kruper, E. Basinska, and W.H.G. Lewin, *12*, 856.
87. "High Energy X-Ray Spectrum of Her X-1," 1981, G.R. Ricker, F.A. Jansen, A. Scheepmaker, A.J.M. Deerenberg, A.G. Visser, J.E. Ballintine, J.V. Vallerger, J.S. Kruper, E. Basinska, and W.H.G. Lewin, *12*, 857.
88. "High Energy X-Ray Observations of the COS-B Gamma Ray Source CG135+1," 1981, G.R. Ricker, A. Scheepmaker, F.A. Jansen, A.J.M. Deerenberg, J.E. Ballintine, J.V. Vallerger, J.S. Kruper, and W.H.G. Lewin, *13*, 557.
89. "Optical Studies of Empty Field X-Ray Sources with a Charge-Coupled Device (CCD) Detector," 1981, G.R. Ricker, M. Bautz, D. Dewey, and S.S. Meyer, *13*, 529.
90. "Observations of the Galactic Center near 1 micron with a Charge Coupled Device (CCD)," 1981, G.R. Ricker, M. Bautz, D.L. DePoy, and S.S. Meyer, *13*, 786.
91. "An Intercontinental Baseline Coincidence Search for Optical Flashes Using Two Schmidt Telescopes: Preliminary Results," 1982, G.R. Ricker, H.V. Bradt, B.E. Schaefer, and R.K. Vanderspek, *14*, 867.
92. "Mercuric Iodide X-Ray Detectors for Space Astronomy: Sensitivity and Background Rate Measurements at Balloon Altitudes," 1982, G.R. Ricker, J.V. Vallerger, *14*, 883.

93. "An Explosive Transient Camera (ETC) for the Identification of Gamma Ray Burst Counterparts and Other Fast Optical Transients," 1982, G.R. Ricker, J.P. Doty, W.H.G. Lewin, J.V. Vallergera, and R.K. Vanderspek *14*, 885.
94. "A Faint Star Astrometric Grid for the Galactic Center," 1982, R.K. Vanderspek and G.R. Ricker, *14* , 951.
95. "The AXAF CCD Imaging Spectrometer Experiment (ACIS)", 1985, J. Nousek, G. Garmire, G.R. Ricker, S.A. Collins, *17*, 864.

## Thesis Listing for the CCD Group

## ***BS Thesis Students 1975-1991***

<b>Finley, David</b>	'75	BS	Physics	Lunar Occultation of the Crab Pulsar at 20-150 keV
<b>Preyer, Norris W.</b>	'75	BS	Physics	A Lunar Occultation of the Crab Nebula at 20-150 keV
<b>Roby, Scott W.</b>	'76	BS	Physics	Data Analysis from the 1 June 1975 Flight of the MIT X-ray Balloon Gondala
<b>Kriss, Gerard A.</b>	'78	BS	Physics	Improving the Accuracy of a Solar Sensor for a Balloon-Borne X-ray Telescope
<b>Dewey, Daniel</b>	'79	BS	Physics	Prospects for Single Photon X-ray Imaging with a CCD
<b>Walling, Juaquin L.</b>	'79	BS	EECS	Toward a Navigation Computer for Balloon-Borne Astronomy
<b>Allen, Karl K.</b>	'80	BS	Physics	Auto Correlation and Fourier Transform Analysis of X-ray Emission from Cygnus X-1
<b>Armstrong, Brian S.</b>	'80	BS	ME	Analysis of Balloon-Borne Telescope Data to Determine Extragalactic Source Spectra
<b>Grunsfeld, John M.</b>	'80	BS	Physics	Characterization Study of Energy Resolution in Mercuric Iodide X-ray Spectrometers
<b>Haid, Steven</b>	'80	BS	Physics	A Simulation Study of Hard X-ray Diffraction Telescopes
<b>Robinson, David M.</b>	'80	BS	Physics	A Scan Converter for the MIT Astronomical Spectrometer/Camera for Optical Telescopes
<b>Bono, John T.</b>	'81	BS	Physics	Electron Radiation Damage Effects in Mercuric Iodide X-ray Dectectors
<b>Biagioni, Eduodo S.</b>	'82	BS	Physics	TRUEFIND: A Computer Analysis of CCD Images
<b>DePoy, Darren</b>	'82	BS	Physics	A Far Red Map of the Galactic Center
<b>Inglese, Ralph J.</b>	'82	BS	EECS	Development of a High Speed, Low Cost Microprocessor Communications Network
<b>Kruper, John S.</b>	'82	BS	Physics	CCD Spectroscopy of Radio-Selected Active Galactic Nuclei
<b>Ravel, Mihir K.</b>	'82	BS	EECS	Analog Processing for Single Photon X-ray Detection with a Virtual Phase CCD
<b>Weatherby, Gerard C.</b>	'82	BS	Physics	Relative Spectral Efficiency and Temperature Dependence of the MASCOT

**Wood, Darien R.** '82 BS Physics  
 Effects of Atmospheric Gamma-Rays on the Background of a Bismuth Germanate-Shielded Mercuric Iodide X-ray Detector: A Monte Carlo Analysis

**White, Catherine** '83 BA Wellesley  
 Planetary Nebulae Candidates Near the Galactic Center

**Aguero, Victor** '84 BS Physics  
 The Spectrum of the Planetary Nebula NGC7027 in the Far Red

**Ellingson, Erica** '84 BS Physics  
 The Efficiency of the Explosive Transient Camera as a Detector of Optical Counterparts of Gamma-Ray Transients

**Kimball, Charles H.** '84 BS EECS  
 Inter-Processor Communications Control of an Explosive Transient Camera

**Rosenthal, Steven M.** '84 BS EECS  
 Event Discrimination in the Explosive Transient Camera

**Soch, Kevin** '84 BS Physics  
 A Study of X-Ray Interactions Near Pixel Boundaries in Virtual Phase CCDs

**Schaffer, Richard L.** '85 BS Physics  
 A Search for Rapid Optical Variations in the BL Lac Object PKS 2155-304

**Ajhar, Edward A.** '86 BS Physics  
 A Search for High Proper Motion Optical Counterparts to Gamma Ray Bursters

**Doyle, John** '86 BS Physics  
 Investigation of Rapid Optical Variability in Seyfert Galaxies

**Eisgruber, Michelle** '86 BS Physics  
 A Feasibility Study of the Identification of High Redshift QSOs Using Narrow Band CCD Photometry

**Horowitz, Irwin** '86 BS Physics  
 Search for Optical Time Variability in the Active Nucleus of the Galaxy NGC 5506

**Kuntz, Kip** '86 BS Physics  
 CCD Spectroscopy of Two Objects Specifically Selected for Spectral Reduction Properties: Their Reduction and Preliminary Analysis to Which is Appended the User's Manual for the KKSPECT CCD Spectral Analysis Program

**Mitsuoka, George** '86 BS EECS  
 MIDAS: The MASCOT Interactive Data Acquisition System

**Berman, Gregg E.** '87 BS Physics  
 A CCD X-Ray Detector Performance Model

**Shing, Laurence** '88 BS Physics  
 High Resolution Ultraviolet Reference Detector

**Zolty, Nerissa S.** '88 BS Physics  
 Photometry of the Narrow Emission Line Galaxy NGC5506

**Carreiro, Richard L.** '89 BS Physics  
Charge Transport in High-Resistivity CCDs

**Davis, Paul M.** '89 BS EECS  
Design and Construction of Digital Command and Housekeeping Modules for the ASTRO-D Project

**Hadjimichael, Thespina** '89 BS Physics  
Photometric Study of the OTS 1938+38 Error Box

**Lund, Eric** '89 BS Physics  
An Optical Search for Quiescent Emission from the Gamma-Ray Burst Source GB781006B

**Setty, Madhav K.** '89 BS EECS  
A Digital Signal Processing Approach to Interfacing CCD Cameras

**Fishman, George P.** '90 BS Physics  
The Detection Rate of the High Energy Transient Experiment for Ultraviolet Transient Sources

**Morgenthaler, Jeffrey P.** '90 BS Physics  
The Study of Charge Coupled Device Soft X-Ray Quantum Efficiency

**Rafizadeh, Deana** '91 BS EECS  
Data Acquisition Interface for Charge-Coupled Device Camera Assembly

**Shauger, Todd C.** '91 BS EECS  
An Interface for the Motorola 56001 Digital Signal Processor

**Thresher, Duane E.** '91 BS EECS  
A High-Speed Serial Link

### ***MS Thesis Students***

**Strauss, David W.** '77 MS EECS  
A CCD-Based Star Detection and Identification System

**Zachary, Daniel S.** '86 MS Physics  
A Search for Optical Flashes with an Automated Wide Field Camera

**Chang, Daniel H.** '91 MS Aero/Astro  
Attitude Control System for the High Energy Transient Experiment Small Satellite

### ***Ph.D. Thesis Students***

**Ballentine, James** '81 PhD Physics  
High Energy Observations of Four Cosmic X-Ray Sources: Cygnus X-1, Cygnus X-3, 3C273, and 3C382

**Vallerga, John** '82 PhD Physics  
Studies of New Hard X-Ray Detection Methods and Observations of Cosmic X-Ray Sources

**Vanderspek, Roland K.** '86 Ph.D. Physics  
The Explosive Transient Camera: A Wide Field Sky Monitor of Celestial Optical Flashes

**Luppino, Gerard A.** '89 Ph.D. Physics  
Design and Use of a Large-Format CCD Instrument for the Identification and Study of Distant Galaxy Clusters

### ***Current Graduate Students***

**Doeleman, Shepard** Physics

**Gendreau, Keith C.** Physics

**Mock, Patrick C.** Physics



## Appendix A

*A Dual Charge-Coupled Device (CCD), Astronomical Spectrometer and Direct Imaging Camera I. Optical and Detector Systems*, Meyer, S.S., and Ricker, G.R., 1980, *SPIE*, **264**, 38.

## A dual charge-coupled device (CCD), astronomical spectrometer and direct imaging camera

### I. Optical and detector systems

S. S. Meyer, G. R. Ricker

Massachusetts Institute of Technology

Department of Physics and Center for Space Research

Room 37-527, 77 Massachusetts Avenue, Cambridge, Massachusetts 02139

#### Abstract

The MASCOT (MIT Astronomical Spectrometer/Camera for Optical Telescopes) is an instrument capable of simultaneously performing both direct imaging and spectrometry of faint objects. The optical design is dictated by the characteristics of the charge coupled device (CCD) detectors and the observational requirements for the instrument. The mechanical configuration of the instrument allows maximum flexibility in the choice of angular scales for the imager and resolution for the spectrometer. The sensitivity of the device is limited by the sky brightness, the overall quantum efficiency, the resolution, and the readout noise of the CCD. This is the first of two papers describing the MASCOT.

#### Introduction

The high quantum efficiency, linearity, and stability of charge coupled devices (CCDs) allow an accurate measurement of the light of the night sky and its subsequent subtraction. This light often limits the precision of photometry and spectrophotometry of faint, low-surface brightness astronomical objects.

Two CCDs are used in the instrument. Both are Texas Instruments 245x328 virtual phase CCDs with square pixels 25 microns on a side. The detectors are mounted on a common liquid nitrogen cooled block. The detector's operating temperature is at about 130 K. One CCD is the spectrometer detector which receives light that passes through a slit and is dispersed by a diffraction grating. The optics are arranged so that the monochromatic slit image is exactly 25 microns wide at the CCD. The second CCD images the light reflected from the jaws of the spectrometer entrance slit. It can function as an area photometer through the use of a filter set and is also helpful in positioning faint objects onto the slit. Figure 1 is a photograph of the MASCOT in the laboratory.

All the optics are mounted on optical benches so that different lenses can easily be introduced into the system. This makes the instrument very flexible and capable of being adapted to many different problems in astronomy.

#### Optics

Figure 2 is a schematic of the optical layout for the MASCOT. The light enters from the upper left. The entrance slit, where the imager and spectrometer beams split, is at the focal plane of the telescope. The instrument is designed to accept the beam from an f/7.5 or slower telescope (specifically the 1.3m f/7.6 McGraw-Hill telescope at Kitt Peak, Arizona).

The light which passes through the slit is collimated by an f/3.2 300 mm lens. This lens can accept the beam from a 2 inch long slit. The parallel beam is then dispersed by the grating and imaged by an f/0.95 50 mm camera lens onto the CCD. Since the camera lens is the limiting optic in the spectrometer beam, the collimator is placed so that it images the telescope entrance aperture onto the camera lens.

The slit jaws are mounted at a 45° angle to the incident beam so that the light is reflected from the jaws at a right angle. This beam passes through a 317 mm f/4.8 field lens, and is reflected by a folding mirror. It then passes through a filter to the 55 mm f/1.2 transfer lens. The transfer lens reimages the telescope focal plane onto the imager CCD. Transfer lenses of different focal lengths give different magnifications of the telescope image at the CCD.

The demagnification of the spectrometer beam is 1:6. The slit width is 150 microns, so that it exactly images onto one row of pixels (25 microns wide). This corresponds to 3-1/2 arc seconds on the sky at the McGraw-Hill telescope. Various other slit widths can be accommodated by the spectrometer. In the same way the pixel size of the imager is 3 arc sec with the 55 mm transfer lens or 0.7 arc sec with an f/2.0 90mm lens.

A DUAL CHARGE-COUPLED DEVICE (CCD), ASTRONOMICAL SPECTROMETER AND DIRECT IMAGING CAMERA  
I. OPTICAL AND DETECTOR SYSTEMS



FIGURE 1. The MASCOT in the laboratory. At the top are the slit holder and folding mirror mount, both at a  $45^\circ$  angle to the vertical. On the left side is the spectrometer collimator lens, with the grating mount at the bottom left. The spectrometer camera lens is at bottom center, next to the grating. The imager transfer lens is at right center. The pentagonal structure at lower right is the vacuum housing which contains the two CCD detectors.

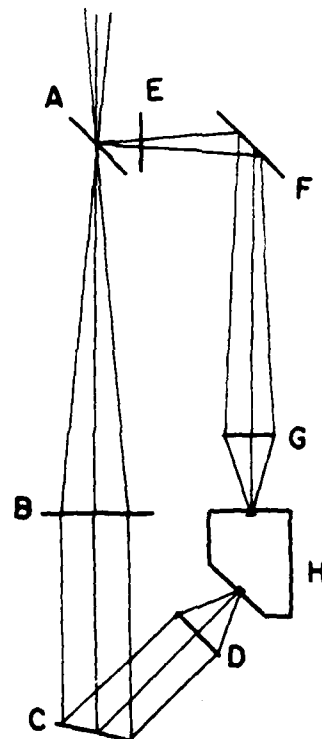


FIGURE 2. A line drawing of the MASCOT optics in the same orientation as Figure 1. The components are labeled as follows: A, entrance slit/beam splitter; B, 300mm  $f/3.2$  spectrometer collimator lens; C, diffraction grating; D, 50mm  $f/0.95$  spectrometer camera lens; E, 317mm  $f/4.8$  imager field lens; F, folding mirror; G, 55mm  $f/1.2$  imager transfer lens; H, 130 K temperature controlled CCD mount.

#### Detector Mount

Because of the way the beams are folded, both CCDs can be mounted on the same temperature regulated detector block. The block is cooled by a liquid nitrogen dewar which is outside the optical instrument itself. The nitrogen dewar and the detector block share a common vacuum system which is pumped by a molecular sieve pump. Both the dewar and the detector block are insulated with aluminized mylar to minimize the heat loss. The dewar accommodates 4.5 liters of liquid nitrogen, and has a hold time of about 20 hours.

The detector block is maintained at about 130 K by a temperature control circuit. It is connected to the nitrogen dewar through an adjustable heat resistor and a copper cold finger. The temperature control circuit dissipates less than 5 watts and maintains regulation to better than 0.1 K.

Signal to Noise

There are two sources of noise on the signal: 1) the CCD readout noise, which results in a constant uncertainty in the number of electrons collected from each pixel; and 2) the photon counting noise. The photon counting noise is the uncertainty in the estimate of a flux which is proportional to  $N^{1/2}$ , where  $N$  is the number of electrons arriving in the measurement interval.

Figure 3 shows the signal to noise ratio for typical observing conditions at 45Å resolution on a 20th magnitude object for several values of CCD readout noise. The top line applies to an ideal CCD with no readout noise. Note that the readout noise becomes less important at higher signal to noise ratios.

Figure 4 shows the signal to noise ratio as a function of object magnitude for a one hour integration for the spectrometer and for the imager. The two curves differ because the bandwidth and focal plane scale of the spectrometer and imager are different. In this example the bandwidth is assumed to be 1000Å for the imager. Under these conditions the readout noise is unimportant for the imager for integration times longer than 4 minutes and so the signal to noise ratio scales as the square root of the integration time. Reference 1 describes the signal to noise calculations in more detail.

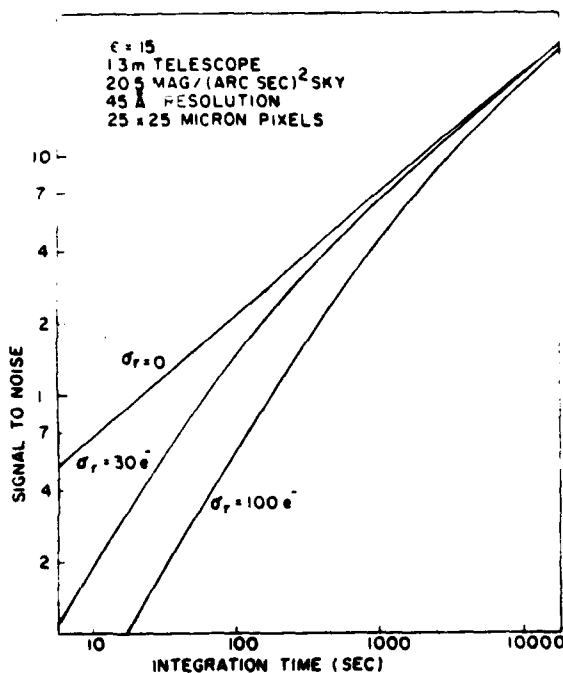


FIGURE 3. The signal to noise ratio as a function of integration time for a 20th magnitude object observed with the spectrometer at 45Å resolution.  $\epsilon$  is the system quantum efficiency. The top curve is for an ideal photon counting detector with no readout noise and the lower curves are for two values of readout noise. For observations at high signal to noise ratios the CCD photon counting noise dominates the CCD readout noise.

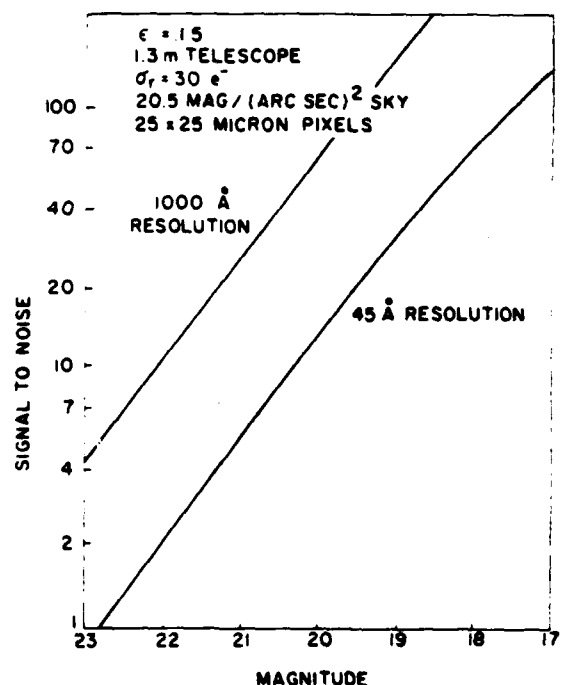


FIGURE 4. The signal to noise ratio as a function of object magnitude for a one hour integration near 7000Å. The bottom curve is for the spectrometer with 45Å resolution and the top curve is for the direct imager with a 1000Å bandpass filter.

A DUAL CHARGE COUPLED DEVICE (CCD) ASTRONOMICAL SPECTROMETER AND DIRECT IMAGING CAMERA  
I. OPTICAL AND DETECTOR SYSTEMS

Quantum Efficiency

The sensitivity of the instrument depends on the total quantum efficiency of the system. The total quantum efficiency in turn depends on several factors: the CCD quantum efficiency, the throughput of the optics, and the transparency of the atmosphere. The CCD quantum efficiency as a function of wavelength is shown in Figure 5. This graph is taken from data supplied by Texas Instruments. Losses in the telescope mirrors, the lenses, the grating, and the vacuum window reduce the optical throughput to about 30%. The imager has about the same throughput as the spectrometer, since the light loss of the filter is comparable to that of the grating, and the other optical elements are similar. Good atmospheric conditions result in about 45% transmission at 7000Å although this can vary greatly. Thus the total system efficiency is about 15%. Figures 3 and 4 were calculated for a total efficiency of 15%.

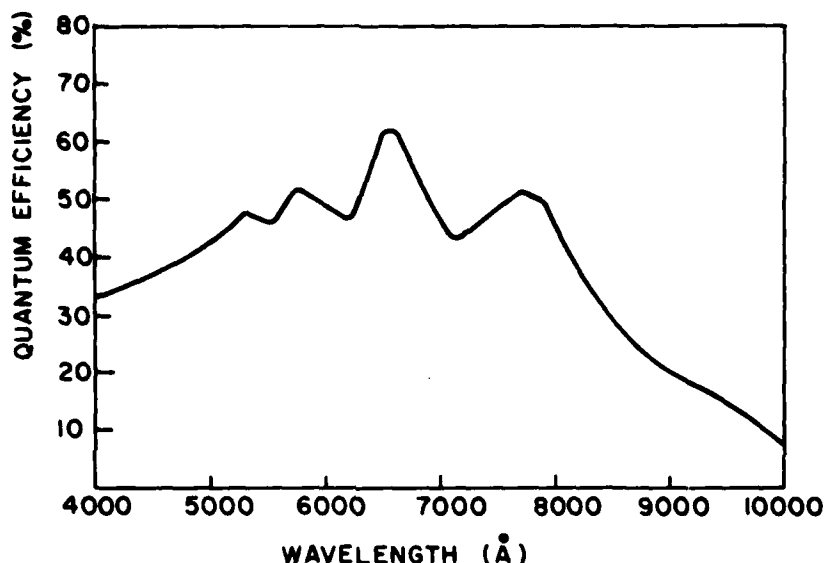


FIGURE 5. The Texas Instruments virtual phase CCD quantum efficiency as a function of wavelength. After including the losses from the atmosphere and the MASCOT optics, the overall system quantum efficiency is about 15% between 5000Å and 8500Å.

Summary

The MASCOT is designed to match the ability of CCD detectors to a wide variety of astronomical problems. In conjunction with the MASCOT data handling system, the instrument will make maximum use of telescope time through its high quantum efficiency, area detection, and ease of use.

Acknowledgements

We are grateful to Paul Greiff, Harold Hosack, Jeff McClintock, Leo Rogers, and Peter Tappan for their contributions to this project. We thank Brenda Parsons for the preparation of the manuscript.

This work was supported by NASA under Grant NSG 7643.

References

1. Meyer, S.S., Rev.Sci.Instrum., 51, 5 (1980).

## Appendix B

*A Dual Charge-Coupled Device (CCD), Astronomical Spectrometer and Direct Imaging Camera II. Data Handling and Control Systems*, Dewey, D., and Ricker, G.R., 1980, *SPIE*, 264, 42.

## Dual charge-coupled device (CCD), astronomical spectrometer and direct imaging camera II. Data handling and control systems

D. Dewey, G. R. Ricker

Massachusetts Institute of Technology, Department of Physics and Center for Space Research  
Room 37-527, 77 Massachusetts Avenue, Cambridge, Massachusetts 02139

### Abstract

The data collection system for the MASCOT (MIT Astronomical Spectrometer/ Camera for Optical Telescopes) is described. The system relies on an RCA 1802 microprocessor-based controller, which serves to collect and format data, to present data to a scan converter, and to operate a device communication bus. A NOVA minicomputer is used to record and recall frame images and to perform refined image processing. The RCA 1802 also provides instrument mode control for the MASCOT. Commands are issued using STOIC, a FORTH-like language. Sufficient flexibility has been provided so that a variety of CCDs can be accommodated. At present, Texas Instruments virtual phase CCDs are utilized. This is the second of two papers describing the MASCOT.

### Introduction

Various requirements and constraints have led to the adoption of the specific control and data handling system for the MASCOT (MIT Astronomical Spectrometer/Camera for Optical Telescopes). The following is a list of those that most influenced the present design:

1. The system must be able to handle the large volume of high speed data present when a CCD is readout.
2. The many frames from an observing run must be stored in a convenient, retrievable form.
3. Each frame should be labelled with time of day, CCD exposure time, CCD temperature and other instrument status information, as well as operator comments (such as the name of the source, right ascension, declination, etc.).
4. A hard copy log of the evening's observations should be produced.
5. Capability for real time picture processing should exist to aid in focusing and alignment and assessing the quality of data taken.
6. CCD dependent hardware and software should be kept to a minimum to allow for the use of different CCDs as the technology improves.
7. The system should be easy to work with and transport.

With these ideas in mind the system of Figure 1 was chosen. The system is physically separated into three assemblies: The "upstairs" electronics, attached to the instrument, consisting of the necessary clock generators and analog processing circuitry to run the CCD and produce digital data; the "downstairs" rack of electronics consisting of an RCA 1802 microprocessor with associated peripherals and a scan converter capable of storing 128K, 16 bit words of data; and finally a NOVA minicomputer system. In practice only the first two assemblies are transported when an on-site NOVA system is available.

The single most important feature of the system is the division of tasks between the two computers. When observing, all commands to the instrument originate at the 1802 teletype keyboard. These commands are sent serially along a single cable to the clocking unit of the "upstairs" electronics where they initiate readouts, change desired temperatures, control shutters, etc. Data and status information from the CCDs are also sent serially along a single cable and loaded into the scan converter under the 1802's oversight. Again under 1802 control the NOVA can be called on to transfer frames from the scan converter to magnetic tape. Thus the 1802 microcomputer handles the mechanics of data collection and the NOVA minicomputer provides real time picture processing capabilities and bulk storage.

DUAL CHARGE-COUPLED DEVICE (CCD), ASTRONOMICAL SPECTROMETER AND DIRECT IMAGING CAMERA  
II. DATA HANDLING AND CONTROL SYSTEMS

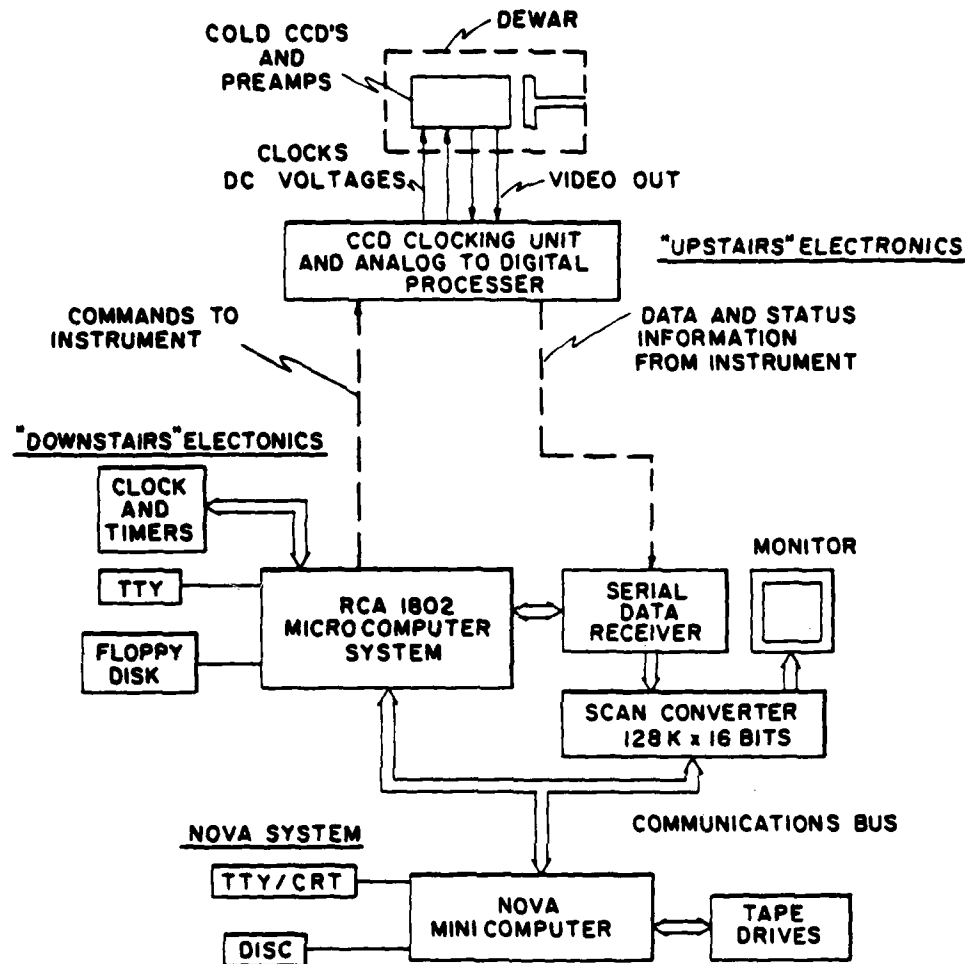


FIGURE 1. Overall block diagram of the MASCOT data handling and control system. An RCA 1802 microcomputer, using the STOIC language, controls the instrument and collects and formats the data. A NOVA minicomputer provides data storage and real time data analysis capabilities.

"Upstairs" Electronics

The "upstairs" electronics consist of a single card cage mounted on the MASCOT. Commands to and data from the unit are carried on two shielded two-conductor cables in order to minimize cable clutter at the telescope. The circuit cards in the cage each perform a specific function as shown in Figure 2. In particular, the clocking unit card, which produces the required TTL clocking signals, and the regulator/driver card, which converts the TTL signals to the proper CCD analog levels, are the only CCD dependent electronics in the whole system.



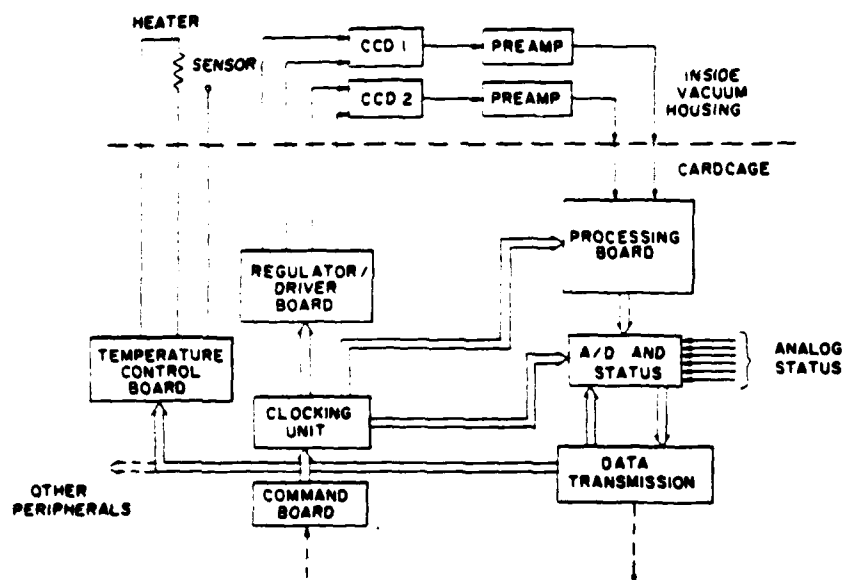


FIGURE 2. Block diagram of "upstairs" electronics. Mounted in a card cage on the MASCOT, this system clocks the CCDs and transmits digital video and status information to the "downstairs" system. The clocking unit and regulator/driver board are the only CCD dependent components in the system.

To accommodate the two CCDs used in the MASCOT and keep hardware to a minimum, a single CCD is readout at any one time. The CCDs are kept in an integrating mode until a readout command is received by the clocking unit. This unit then clocks the selected CCD at a 100 K pixel/second rate and sends control signals to the processing board. This board uses an FCDS (Filtered Correlated Double Sampler) circuit, shown in Figure 3, to achieve low noise readout. When the frame is finished an additional line of data consisting of status information is added. The data is transmitted with flags at the end of each line and at the end of the frame, thus allowing for various sizes of CCDs and CCD operating modes.

#### "Downstairs" Electronics

The function of the "downstairs" electronics is to convert an operator's requests into commands to the "upstairs" electronics and receive and channel the resulting data. At the center of this electronics is an RCA 1802 microcomputer. This computer uses the STOIC (Stack Oriented Interpretive Compiler) language which is much like FORTH in that previously defined commands are executed when entered and new commands can be easily defined in terms of old commands. The system has 24K bytes of memory, a floppy disc unit, a real-time clock and two programmable timers. These timers are used to keep track of each CCD's integration time and generate interrupts to the processor when a CCD should be readout.

A scan converter is the second piece of essential equipment in the "downstairs" system. Its 128K x 16 bit semiconductor memory, arranged into 341 lines of 384 pixels each, is able to quickly store one frame of CCD data. The contents of the scan converter are continuously displayed on a monitor allowing evaluation of the raw data.

DUAL CHARGE-COUPLED DEVICE (CCD), ASTRONOMICAL SPECTROMETER AND DIRECT IMAGING CAMERA  
II. DATA HANDLING AND CONTROL SYSTEMS

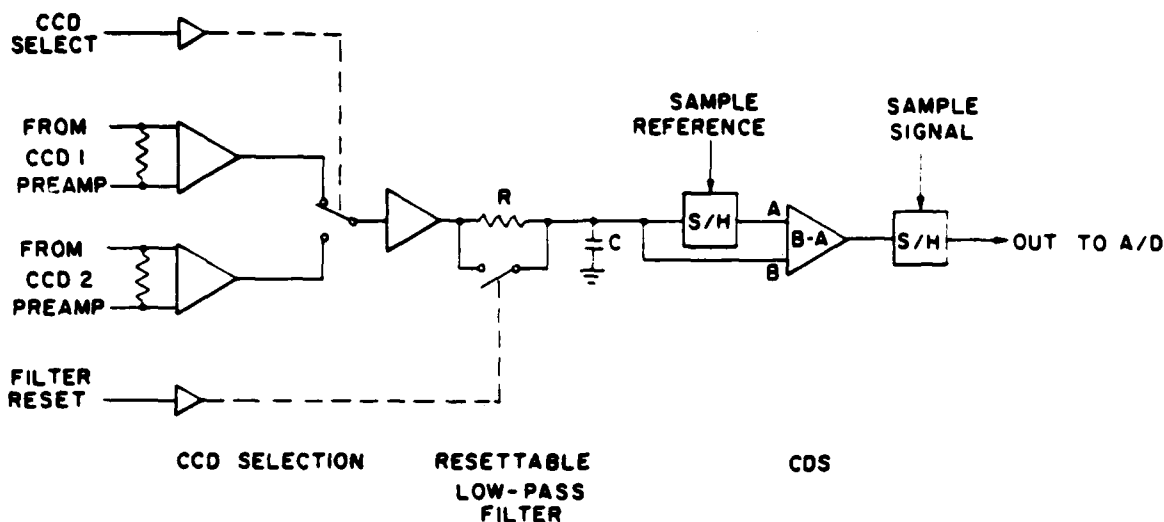


FIGURE 3. Filtered correlated double sampler (FCDS). Low readout noise is achieved by using a one microsecond RC filter, which provides high frequency noise rejection and a double sampling circuit, which attenuates low frequency noise. Pixel-to-pixel memory is eliminated by resetting the RC filter after each pixel.

Finally, a communications bus is provided to allow data to be read from and written to the scan converter. The 1802 computer, limited in storage capacity, can examine 32x32 subarrays of the frame and perform some data analysis. More importantly, after a frame has been loaded into the scan converter from the CCD, the 1802 can write on an unused line the time-of-day, the integration time, and user comments. This, together with the status information, provides efficient, permanent marking of the data. The communications bus is also critical in transferring the frames to the NOVA where they are stored on tape and processed. The bus is bidirectional so that processed pictures can be loaded into the scan converter for real time examination.

#### The NOVA System

The NOVA system provides data storage and reduction capabilities for both realtime and post-observation analyses. To analyze the data a large FCRTAN program has been developed. This program accepts user commands, which call subroutines to manipulate frames of data on disc and tape. Many internal variables specify parameters such as CCD size, electrons per A/D unit, windows of interest, etc. and allow the passing of results from one routine to another.

During observations a subset of this software is resident on the NOVA system and, except for occasional requests by the 1802 system to store new data on tape, on-line data analysis is continuous. A sample of the commands available is given below:

1. Input/Output: Transfer data between scan converter or magnetic tape and the program's work file.
2. Type: Type out the pixel values in a selected window of the array.
3. Picture Arithmetic: Pixel-by-pixel arithmetic operations used for dark frame subtraction, field flattening, etc.
4. Spectrum: Produce a background-subtracted spectrum from a spectrometer picture.
5. Plot: Plot on CRT: spectra, surface brightness distributions, etc.

#### Operating Modes

The system just discussed can be operated in various data-taking modes. The MASCOT uses two CCDs, a direct imager and a spectrometer, which are given equal treatment by the hardware. Thus the data taking sequence and the assignment of CCD priorities are left up to the 1802 software. This software is stored on the 1802's floppy disc drive and is readily available and easily changed.

```

9/23 17:43:12 0 100 DINT
9/23 17:43:21 0 DSINGLE
9/23 17:43:33 0
9/23 17:45:06 *** DIRECT LOADED ***
9/23 17:45:12 0 31 32 LINE 25 35 SERIAL TYPE
51. 25 1 187 173 183 186 1190 780 181 179 186 182
52. 25 1 185 177 179 187 1093 682 179 183 180 183
9/23 17:46:05 0 1 DINT
9/23 17:46:14 0 DLCONT
9/23 17:46:25 0

```

FIGURE 4. Example of controller printout during stand-alone operation. A 100 second integration time for the direct CCD is specified (100 DINT). An exposure is requested and the resulting frame loaded into the scan converter (DSINGLE). Some pixels are examined on the teletype. A one second integration time is chosen (1 DINT) and the direct CCD output will be continuously loaded into the scan converter after each integration (DLCONT).

For testing, aligning and debugging, the system can be operated without the NOVA computer. In this stand-alone mode the 1802 system can type out pixel values and perform frame subtractions and pulse height analyses on 32x32 subarrays of the data. In this way quantitative data on dark current, system noise and alignment can be obtained. Figure 4 shows an example of commands in this mode. The direct integration timer is set to 100 seconds, a single frame is readout and loaded into the scan converter and a group of pixels is examined. The CCD is then put into a 1 second integration mode and continuously readout and loaded into the scan converter. This now allows the operator to see the effects of adjusting lenses, moving the telescope, etc.

When the NOVA system is present and observations are being made, the 1802 system executes more complex commands designed to collect specific sets of data. Thus a preprogrammed observation or calibration sequence can be initiated and carried out efficiently. While other data is being taken, these frames can be examined by the NOVA system to provide quick feedback on instrument performance. In Figure 5 a sample 1802 output during an observation is shown. A 500 second spectrometer integration is initiated and

```

9/24 23:17:43 0 500 SPECTRUM
9/24 23:17:52 0 40 FLTRSET
9/24 23:18:01 EXPOSURE STARTED
9/24 23:18:41 EXPOSURE COMPLETE, COMMENTS: FILTER A, CALIB STAR 17
9/24 23:19:11 FRAME TRANSFERRED TO NOVA. TAPE RECORD: 19
9/24 23:19:22 NEXT FILTER
9/24 23:19 42 EXPOSURE STARTED
    .
    .
    .
9/24 23:24:07 FRAME TRANSFERRED TO NOVA. TAPE RECORD: 23
9/24 23:24:10 NEXT FILTER
9/24 23:24:31 0
9/24 23:26:12 *** SPECTROMETER EXPOSURE COMPLETE ***
    COMMENTS: SOURCE 12, SEEING POOR
9/24 23:26:44 FRAME TRANSFERRED TO NOVA. TAPE RECORD: 24
9/24 23:26:54 0

```

FIGURE 5. Example of controller printout during operation with NOVA present. A 500 second spectrometer integration is requested (500 SPECTRUM) and during this integration a series of 40 second exposures with the direct CCD is taken (40 FLTRSET). The frames of data, including user comments, are transferred to NOVA tape storage. The filter sequence is terminated by the operator and later the spectrometer CCD is automatically readout and stored by the NOVA on tape.

DUAL CHARGE-COUPLED DEVICE (CCD), ASTRONOMICAL SPECTROMETER AND DIRECT IMAGING CAMERA  
II. DATA HANDLING AND CONTROL SYSTEMS

then a series of 40 second exposures through a set of filters is taken with the direct system. Here 20 seconds has been allotted to manually change the filters. Each frame is subsequently transferred to the NOVA for storage. After 500 seconds the spectrometer is also readout and stored. Note the possibility of the 1802 system being busy with one CCD when the other should be readout. In this case the integration counter continues counting until the CCD is finally readout. The actual integration time is thus always recorded. By choosing appropriate interrupt software, no data need be lost.

Summary

The MASCOT control and data handling system combines the control capabilities of an 1802 microprocessor and the storage and processing capabilities of a NOVA minicomputer. The separation of tasks allows efficient data collection and simultaneous data analysis. The examples of the MASCOT software given above are meant to show the capabilities of the system. Modifications and evolution are expected to follow as operating experience with the MASCOT accumulates.

Acknowledgements

Many people have contributed to the MASCOT data collection system. In particular, Mark Bautz, Robert Goeke, John Kucera, Dave Robinson, and Roberto Sierra have each contributed much to the project and their help is gratefully acknowledged. Patient manuscript preparation was provided by Brenda Parsons.

This work was supported by the National Aeronautics and Space Administration under grant NSG 7643.

## Appendix C

*Optical Studies of X-Ray Sources with the MASCOT – A Charge-Coupled Device (CCD)–Based Astronomical Instrument*, Ricker, G.R., Bautz, M.W., Dewey, D., Meyer, S.S., 1981, *SPIE*, **290**, 190.

## Optical studies of x-ray sources with the MASCOT—a charge-coupled device (CCD)-based astronomical instrument

G. R. Ricker, M. W. Bautz, D. Dewey, S. S. Meyer

Massachusetts Institute of Technology, Department of Physics and Center for Space Research  
Room 37-527, 77 Massachusetts Avenue, Cambridge, Massachusetts 02139

### Abstract

The first observing run with the MASCOT (MIT Astronomical Spectrometer/Camera for Optical Telescopes) on the 1.3 m telescope at the McGraw-Hill Observatory in March 1981 demonstrated that the spectrophotometric sensitivity and stability of the instrument is consistent with the estimates made by Meyer and Ricker (1981) and Dewey and Ricker (1980), based on their calculations and laboratory calibrations. A pair of Texas Instruments virtual phase CCD's were used as the MASCOT optical detectors. In the  $J$  band (4000-7000 Å), the MASCOT achieved a sky-limited sensitivity of  $+24.4$  mag arc sec<sup>-2</sup> in an 1800s integration (1 arc sec pixel size; 5 $\sigma$  level of significance). The ability to "flatten" pictures to a level consistent with (sky + source) photon statistics and readout noise was demonstrated. As an example of the capabilities which the MASCOT has demonstrated, we discuss our preliminary results from optical observations of four high galactic latitude Einstein x-ray sources without optical counterparts (i.e. "empty field" sources). For the four sources we observed, we established an optical counterpart for one source (1412+12), based on positional coincidence (better than 1.8 arc sec); detected four possible candidates in the error box of another source (1009+35); and established sensitive upper limits ( $>20.2$  mag; 4000 Å - 7000 Å, 5 $\sigma$  upper limits) for optical counterparts in the error boxes for the other two sources (0920+39 and 0931-11).

### 1. Introduction

As astronomical detectors, charge-coupled devices (CCDs) hold forth the promise of high quantum efficiency and broad dynamic range, coupled with excellent linearity and stability. These properties should permit the accurate measurement of the light of the night sky and its subsequent subtraction from an astronomical "picture" (e.g. narrow or broad-band optical image, polarization map, spectrum, etc.). Ideally, the signal-to-noise in such pictures should not suffer in the subtraction process. The MASCOT (MIT Astronomical Spectrometer/Camera for Optical Telescopes) has been designed to facilitate the simultaneous acquisition of such "sky (photon noise)-limited" spectral and spatial images with CCD detectors.

The optical and mechanical details of the MASCOT have been described in some detail by Meyer and Ricker (1980), while Dewey and Ricker (1980) have described the manner in which the MASCOT provides for image data acquisition and processing, as well as instrument control. In this paper, we briefly review the instrument configuration, describe the actual performance levels achieved by the MASCOT in its first observing run on the 1.3m telescope at the McGraw-Hill Observatory, and present preliminary data obtained in searches for optical counterparts to four "empty-field" X-ray sources. Primary emphasis will be placed on discussions of the "area photometer" MASCOT channel; the "spectrometer" MASCOT channel will be discussed in a subsequent paper. A fairly detailed review of the performance of the two Texas Instruments (TI) 490x328 "virtual phase" CCDs used in the MASCOT will be given, as this application marks their first reported operational use in a ground-based observatory instrument.

### 2. MASCOT Operational Characteristics

The MASCOT is designed to be a "standalone" instrument, capable of performing both sky-limited area photometry and spectroscopy. It is optimized for use at the Cassegrain focus of telescopes having focal ratios of  $f/7.5$  or larger. Figure 1a shows the optical and detector assemblies of the MASCOT in the laboratory. (The top cover has been removed.) Figure 1b gives the MASCOT optical layout in schematic form. Light from the telescope secondary is shown entering from above, coming to a focus at A, the location of the entrance slit/beam splitter. Light which passes through the slit (i.e. the left-hand path) is fed to the spectrometer channel (CCD detector following element D), while the reflected light from the slit jaws is fed into the area photometer channel (CCD detector following element G). In order to provide for a broad range of focal plane scales, the various refractive elements are mounted on optical benches to facilitate rapid interchanges. Additional optical details are given in Meyer and Ricker (1980). A photograph of the MASCOT being prepared for use on the 1.3m telescope at McGraw Hill Observatory is shown in Figure 1c.

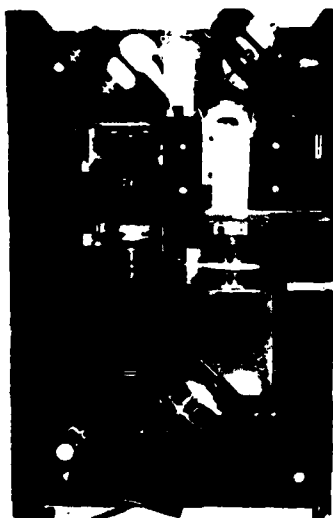


FIGURE 1a. The MASCOT in the laboratory. At the top are the slit holder and folding mirror mount, both at a  $45^\circ$  angle to the vertical. On the left side is the spectrometer collimator lens, with the grating mount at the bottom left. The spectrometer camera lens is at bottom center, next to the grating. The imager transfer lens is at right center. The pentagonal structure at lower right is the vacuum housing which contains the two CCD detectors.

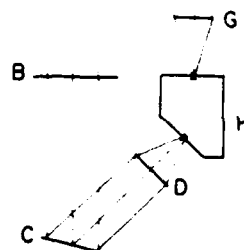


FIGURE 1b. A line drawing of the MASCOT optics in the same orientation as Figure 1a. The components are labelled as follows: A, entrance slit/beam splitter; B, 300mm  $f/5.2$  spectrometer collimator lens; C, diffraction grating; D, 50mm  $f/5.25$  spectrometer camera lens; E, 500mm  $f/5.2$  imager field lens; F, folding mirror; G, 55mm  $f/1.8$  imager transfer lens; H, 100 K temperature controlled CCD mount.

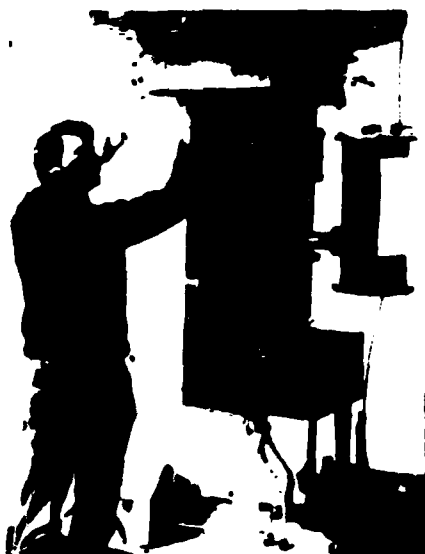


FIGURE 1c. The MASCOT mounted at the Nasmyth focus of the Hale Telescope at Kitt Peak. The upright cylinder opposite the observer is the liquid nitrogen dewar. A horizontal solid finger extends from the side of the dewar to the MASCOT video CCD housing. The protruding box affixed to the bottom of the MASCOT housing (beneath the dewar bottom plate) is the "on telescope" electronics package.

In Table 1, we present additional information concerning three VASCOOT subsystems: CCD's, area photometer, and spectrometer. In order to enhance the VASCOOT near IR response during the McGraw Hill observing run (March 1981), the CCD cold block operating temperature was deliberately chosen to be  $-100^{\circ}\text{C}$ . At this temperature, the virtual phase CCD's still have measurable dark current ( $10.25$  electrons  $\text{s}^{-1}$  pixel $^{-1}$ ). Furthermore, the readout noise for the two chips was quite high ( $100 - 150$  e $^{-}$  rms) during the observing run. After the completion of the run, laboratory studies revealed more optimum values for the clocking voltages (see discussion in section 3), resulting in lower noise levels ( $30 - 40$  e $^{-}$  rms; see Section 3).

We also present performance levels actually achieved for the area photometer and spectrometer in Table 1. Of particular note are the high system throughput (up to  $10^{11}$  for the area photometer in various standard pass bands from  $4000$  Å to  $10000$  Å). The limiting broad band sensitivity achieved ( $+24.4$  mag arc  $\text{sec}^{-2}$ ;  $5\sigma$  level of significance) was quite satisfying, being consistent with that expected from photon statistics and readout noise (added in quadrature). The performance of the spectrometer will be discussed further in a later paper.

### 3. Noise Characterization of the CCD's

The total CCD readout noise for a picture may be due to several contributions, including:

- On-chip FET noise
- Off-chip preamplifier noise
- Noise on clock signals and DC voltages
- Shot noise due to source and sky photons, and dark current
- Noise of poorly-understood origin ("excess noise", etc.)

To separate these contributions, the noise was measured in a variety of CCD configurations:

- 1) Quiescent Noise: With the reset clock on and all other clocks held at 0 levels; we expect the first 3 noise sources to dominate.
- 2) Clocking Noise: With the reset clock and the serial clock operating, but no parallel transfers taking place; we presume that the additional noise is due to the dynamics of clocking.
- 3) Overclocked Noise: With the CCD operating under normal conditions, the noise of the "overclocked pixels" (i.e. those corresponding to column numbers  $>335$ ) is measured.
- 4) Zero Signal Real Noise: With no light illuminating the CCD and frequent readouts, the noise of "real pixels" (i.e. those corresponding to column numbers  $0-335$ ) is measured.
- 5) Extrapolated Zero Real Noise: With light illuminating the CCD, the signal variance vs. signal level is measured and plotted. From the y-intercept of this plot, a zero signal variance is calculated. The square root of this quantity is the real readout noise expected while observing. The actual signal and variance values (in A/D converter units) obtained in our testing procedure in this configuration are shown in Figure 2.

Ideally, if the FET and preamplifier noise dominated, then all five of these configurations would give the same noise level. In reality, the readout noise was actually observed to increase as each of the above five configurations was considered successively. In Table 2, we summarize the result of five such noise measurements\* for each of two  $400 \times 328$  vertical phase CCD's (residing in the area photometer and the spectrometer,

\*These noise measurements were made after a source of "excess charge" noise associated with the serial clock amplitude and DC levels was eliminated. Janesick (private communication) has accounted for this noise as arising from leakage charge collecting in the CCD potential wells as a result of gate oxide breakdown when the negative level of a phase clock goes below a certain critical level. The phenomenon is not fully understood. Janesick, Hynecek, and Blouke (1981) also discuss this problem.



I. General Description

General Description: This instrument is designed for the observation of the solar corona and the solar wind. It consists of a series of coronagraphs and a solar wind monitor. The coronagraphs are used to observe the solar corona, while the solar wind monitor is used to measure the solar wind. The instrument is located at the Solar and Heliospheric Observatory (SOHO) in Earth orbit.

\* The instrument is designed to observe the solar corona and the solar wind. \*\* The instrument is designed to observe the solar corona and the solar wind.

II. Instrument Description

Instrument Description: The instrument consists of a series of coronagraphs and a solar wind monitor. The coronagraphs are used to observe the solar corona, while the solar wind monitor is used to measure the solar wind. The instrument is located at the Solar and Heliospheric Observatory (SOHO) in Earth orbit.

\* The instrument is designed to observe the solar corona and the solar wind. \*\* The instrument is designed to observe the solar corona and the solar wind.

III. Performance Characteristics

Active Wavelength Range: 4000-10000 Å  
 Minimum FWHM: 7.5  
 Dispersion: 1000/line mm gratings  
 Minimum slit width: 0.5 mm  
 Maximum slit width: 1.0 mm  
 The instrument is designed to observe the solar corona and the solar wind.

Table 2: Noise Characterization of Two Texas Instruments  
490x328 Virtual Phase CCDs

Measurement <sup>†</sup>	Area Photometer CCD		Spectrometer CCD	
	(ADU)	(e <sup>-</sup> rms) <sup>*</sup>	(ADU)	(e <sup>-</sup> rms) <sup>*</sup>
Quiescent Readout Noise	1.35	42	1.35	33
Clocking Readout Noise	1.57	52	1.50	37
Overclocked Readout Noise	1.80	56	1.60	39
Zero Signal Readout Noise	2.25	70	1.92	45
Extrapolated Zero Signal Readout Noise (see Fig. 2)	2.95	92	2.21	57

<sup>†</sup> See text for description of measurement technique. The extrapolated zero signal readout noise is the appropriate value to use in sensitivity calculations, since it represents the value one measures under normal imaging conditions (see Figure 2).

<sup>\*</sup> During the March 1981 observing run at the McGraw-Hill Observatory, the noise levels for both CCDs were in the range ~100-150 e<sup>-</sup>rms. The gain factors for both were ~50 e<sup>-</sup>/ADU. A reoptimization of the serial clocking levels in May 1981 resulted in the above improved values.

respectively). We do not fully understand the origin of the increases observed at each configuration change, and are continuing to investigate the problem.

#### 4. Photometric Calibrations

Calibration of the MASCOT area photometer channel was carried out using both individual standard stars previously adopted (Strom 1977; Landolt 1973), as well as globular cluster star fields recently suggested for this purpose (Christian 1981). Generally, "IDS" (Strom 1977) or "Landolt" standards were observed shortly after dusk, near midnite, and shortly before dawn during each night's observing. In addition, two selected fields near the globular cluster NGC2419 (Christian 1981) were observed extensively (through standard B, V, R, and I filters, as well as through special broad and narrow band filters) and reobserved each time the MASCOT optical configuration was changed in a major way (e.g. substitution of a different transfer lens). A preliminary analysis of data from the IDS standards (including observations of Hiltner 500, Feige 98, and Kopff 27) resulted in the following transformation relations for various apparent color magnitudes (Kron/Cousins system; Bessel 1979):

$$\begin{aligned}
 m_B &= -2.5 \log S \text{ (ADU/s)} + (17.98 \pm 0.03) \\
 m_V &= -2.5 \log S \text{ (ADU/s)} + (18.97 \pm 0.03) \\
 m_R &= -2.5 \log S \text{ (ADU/s)} + (19.04 \pm 0.05) \\
 m_I &= -2.5 \log S \text{ (ADU/s)} + (18.48 \pm 0.04)
 \end{aligned}$$

In these relations, S is the source counting rate (summed over the seeing disk) expressed in analog-to-digital converter units per second (1 ADU/s  $\approx$  50 e<sup>-</sup>/s during the March '81 McGraw Hill run). The errors given are 1 $\sigma$  values, calculated by repeated observations of the same set of standards. Systematic errors are currently estimated to be  $\sim \pm 0.1$  magnitude. Atmospheric absorption (air mass) corrections have not yet been made in the above relations. Currently, we are using the NGC2419 fields to extend the directly measured MASCOT photometric sequences to  $> +20$  magnitude.

### 5. Field Flattening

Field flattening with the TI 490x328 virtual phase CCD has proved to be rather straightforward, at least in our preliminary assessment. We suspect that this is primarily due to the extremely good overall uniformity of the MASOT devices. Figure 2, before

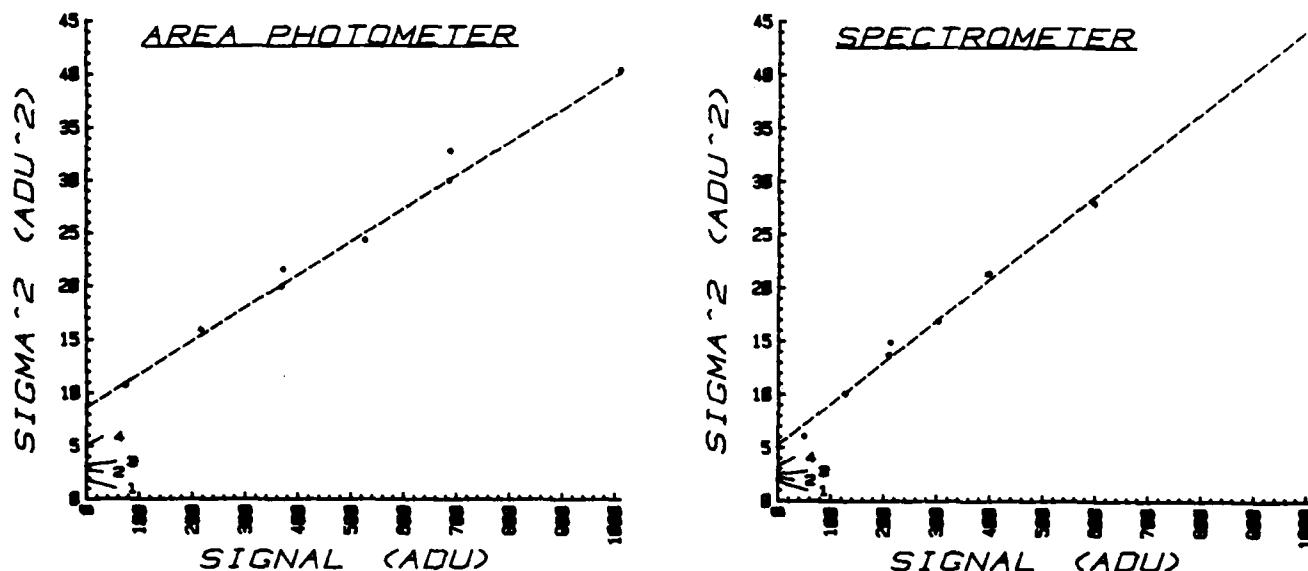


FIGURE 2: Variance versus signal level for the two MASOT CCDs. The measurements were made in May 1981 (following the McGraw-Hill observing run), after reoptimization of the CCD serial clock levels. The dashed line is a least squares fit to the data points (represented as dots). The 4 short lines (labelled 1, 2, 3, 4) refer to the readout noise, the clocking readout noise, the overclocked readout noise, and the zero signal readout noise, respectively (see text and Table 2 for details). From this graph, we conclude that:

- Area Photometer CCD:
  - Gain is  $31.3 \text{ e}^-/\text{ADU}$
  - A/D converter (12 bits) full scale value is  $1024 \text{ ke}^-$
  - Extrapolated zero signal readout noise is  $32.3 \text{ e}^- \text{ rms}$
- Spectrometer CCD:
  - Gain is  $25.2 \text{ e}^-/\text{ADU}$
  - A/D converter (12 bits) full scale value is  $100 \text{ ke}^-$
  - Extrapolated zero signal readout noise is  $57.6 \text{ e}^- \text{ rms}$

flattening). In an attempt to achieve an even higher degree of field flattening, we used the relation:

$$FF(1) = \frac{F(1) - OCL(1) - DF(1') - OCL(1')}{[T_1/T_2][F(2) - OCL(2)] - DF(1') - OCL(1')}$$

where:

- F(1) = Sky frame of interest (integration time  $T_1$ )
- F(2) = Another sky frame (integration time  $T_2 \sim T_1$ , taken within a few hours of sky frame (1))
- OCL(1) = Overclocked level (measured for each frame)
- DF(1') = Dark frame (integration time  $T_1' = T_1$ )
- FF(1) = Flattened sky frame

In the passband 4000Å-7000Å, this relation results in fields which are flat to 1.4%, consistent with (signal photon + sky) noise plus readout noise (added in quadrature) for the longest integration time we used (30 minutes). Thus, the degree of flattening achieved is consistent with theoretical (i.e. Poisson noise) limitations. Of course, for lower readout noise levels and longer integrations, this condition may no longer hold. Further study of this important problem is planned in future observing runs.

In Figure 3, we demonstrate the (somewhat) subtle effect of our field flattening procedure. We show a cross section along a single row of an image obtained of the optical counterpart to the X-ray source 1413+13. (Further details regarding this object are given in Section 5.) The left panel shows data from a raw (unflattened) image, while the right panel shows data from a processed (flattened) image. Further details are given in the caption.

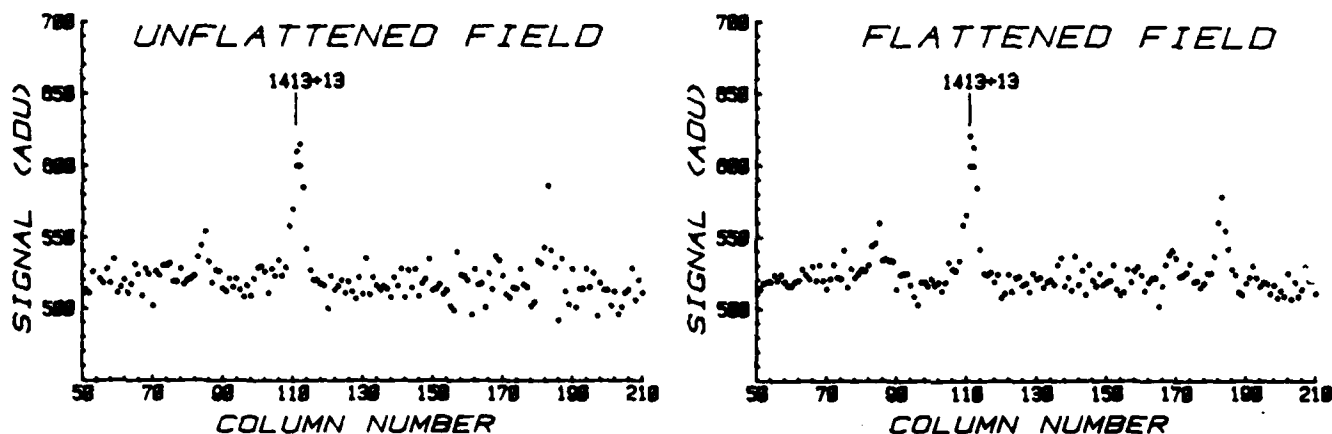


FIGURE 3: Cross-sections of the image of the optical counterpart for the X-ray source 1413+13. Each pixel value (in A/D converter units) along a row 165 of the CCD has been plotted. (N.B. Suppressed zero on both axes.) The optical counterpart for 1413+13 is centered at (row 165, column 110) and is indicated by a vertical line. (Field stars were also "sliced through" at columns 55 and 180.) The "Unflattened Field" cross section was taken from a raw CCD image (an 1800 s exposure taken through an HA-11 filter), from which the CCD oversampled level and an 1800 s dark frame were subtracted. The "Flattened Field" cross section was obtained by flattening the "Unflattened Field" by a second exposure to another portion of the sky taken 1.5 hours later on the same night. The degree of field flattening achieved is particularly evident to the right of 1413+13, and is consistent with that expected from (sky + source) photon statistics and detector readout noise. In this case, this limit was 1.4% of the sky, but further relaxations are anticipated for longer integrations and lower readout noise (see Table 2).

## 5. MASCOT Studies of Four Einstein "Empty Field" X-ray Sources

In studies of X-ray sources with the Einstein Observatory (Giacconi et al. 1979), there have been several instances of X-ray objects discovered which do not have optical counterparts down to the limit of the Palomar Observatory Sky Survey (POSS). Such objects are of great potential interest because of their large values of  $L_x/L_{opt}$  (X-ray to optical luminosity ratio), possibly implying that they may comprise (or include) new classes of astronomical objects.

In order to illustrate the capabilities of an instrument like the MASCOT mounted on a moderate-sized (1.3m) telescope, we will discuss our preliminary results on searches for optical counterparts of four such X-ray objects at higher sensitivities than the POSS plate limits. Figures 4, 5, 6, and 7 show the optical fields for the X-ray objects 0220+20, 0231-11, 1002+26 and 1412+12, respectively. In each of the 4 figures the left hand panel ("a" in each figure) is a reproduction of the POSS "E" print, while the right hand panel is a CCD picture taken with the MASCOT. Additional details are given in the figure captions.

0920+39

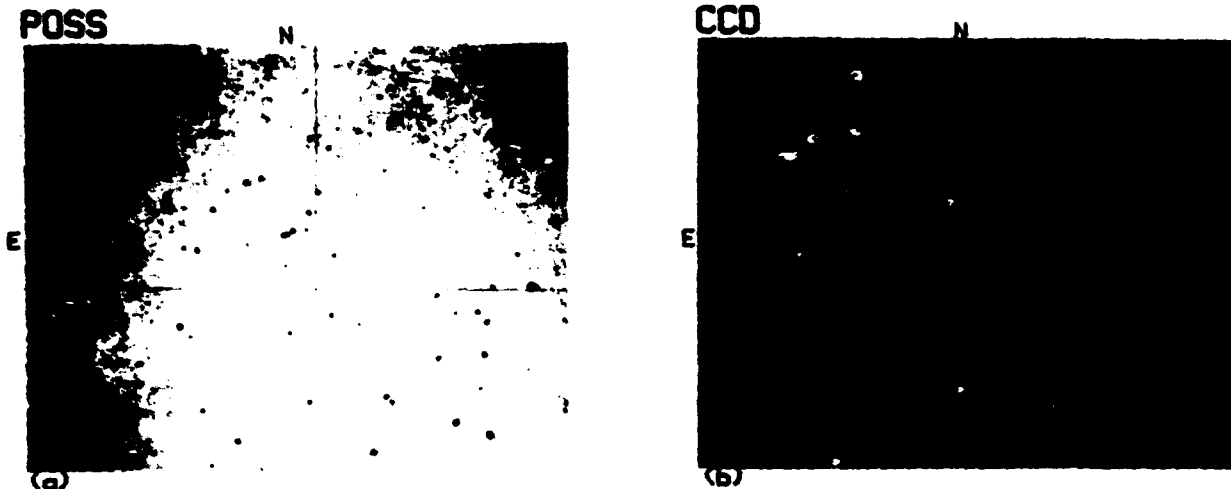


FIGURE 4: Optical images of the field near the object 0920+39 taken from: (a) A reproduction of the Palomar Observatory Sky Survey red print. The reproduction shown is 750 arc seconds N-S. The radio position is marked by the crosshairs. (b) A MASCOT CCD image taken through an HA-II filter (4100Å-7000Å bandpass). The integration time was 1500 s on the McIlraw-Hill 1.3m telescope. The reproduction shown is 250 arc seconds N-S. The radio position is centered between two short diagonal lines.

0931-11

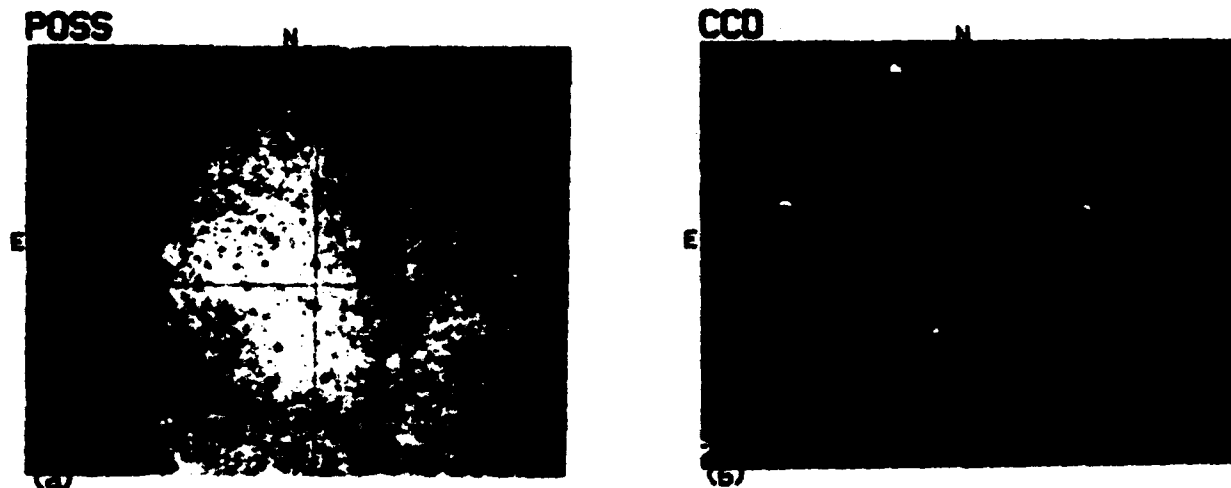


FIGURE 5: Optical images of the field near the object 0931-11 taken from: (a) A reproduction of the Palomar Observatory Sky Survey red print. The reproduction shown is 750 arc seconds N-S. The radio position is marked by the crosshairs. (b) A MASCOT CCD image taken through an HA-II filter (4100Å-7000Å bandpass). The integration time was 1200 seconds on the McIlraw-Hill 1.3m telescope. The reproduction shown is 250 arc seconds N-S. The radio position is centered between two short diagonal lines.

1009+35

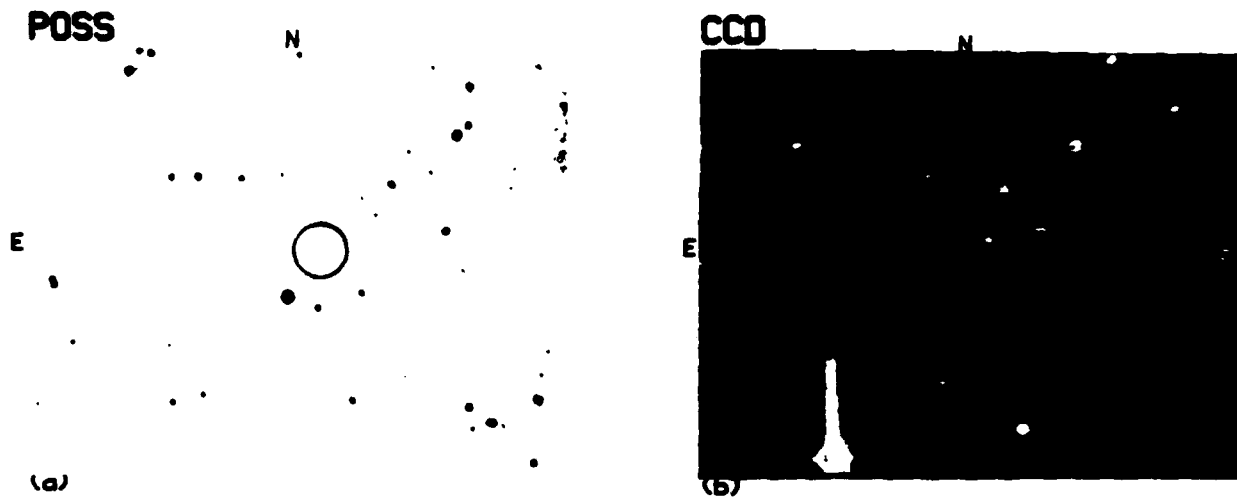


FIGURE 6: Optical images of the field near the object 1009+35 taken from: (a) A reproduction of the Palomar Sky Survey red print. The reproduction shown is 630 arc seconds N-S. The heavy source region is marked by a circle. (b) A NASCOT CCD image taken through an HA-11 Filter (4000Å-7000Å bandpass). The integration time was 1200 s on the McGraw-Hill 1.8m telescope. The reproduction shown is 361 arc seconds N-S. Four of the candidate objects are connected to the line of short diagonal lines. The heavy N-S black band in the left half of the picture is the entrance slit to the spectrometer.

1413+13

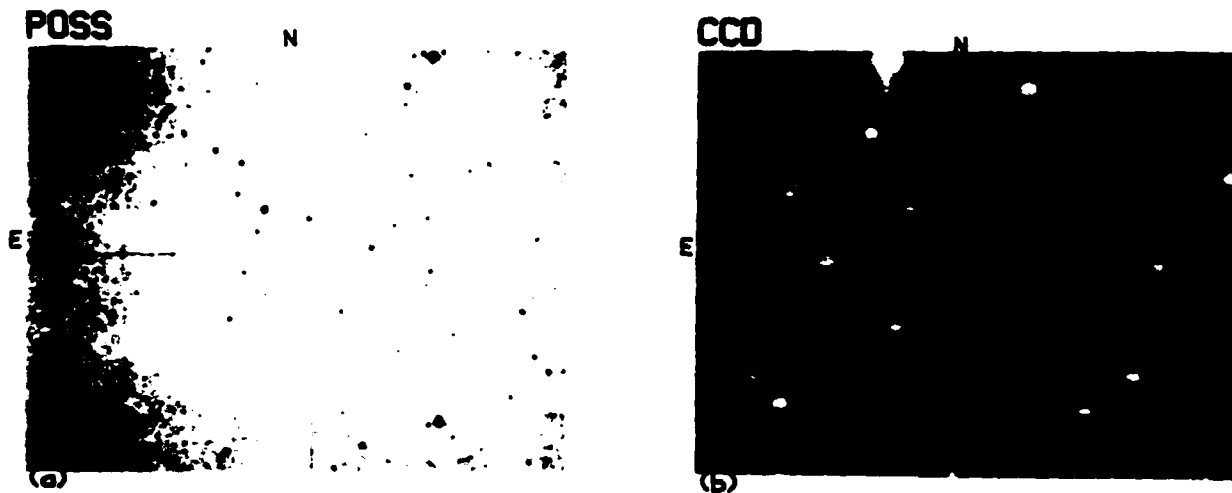


FIGURE 7: Optical images of the field near the object 1413+13 taken from: (a) A reproduction of the Palomar Sky Survey red print. The reproduction shown is 750 arc seconds N-S. The radio position is marked with a crosshair. (b) A NASCOT CCD image taken through an HA-11 Filter (4000Å-7000Å bandpass). The integration time was 1900 s on the McGraw-Hill 1.8m telescope. The reproduction shown is 361 arc seconds N-S. The optical counterpart to the radio and X-ray object is centered between two short diagonal dashes. The heavy N-S black band in the left half of the picture is the entrance slit to the spectrometer.

Table 3: Preliminary Results from Optical Observations of High Energy Radio Sources with the MASCOT on the Mount-Hill 1.3 Meter Telescope During March 1981

Source	R.A. (1950)	DEC (1950)	$m_{\text{open}}$	$m_{\text{H}}$	$m_{\text{H}}$
<b>0920+39</b>					
X-ray	9 <sup>h</sup> 20 <sup>m</sup> 07 <sup>s</sup> .36	+39°02'21.0"			
Radio <sup>a</sup>	9 <sup>h</sup> 20 <sup>m</sup> 06 <sup>s</sup> .29±0.03	+39°02'32.4±0.5			
Optical Candidate	[None Detected] <sup>*</sup>		>21.6 (300s) <sup>**</sup>	>22.4 (1500s) <sup>***</sup>	--
<b>0931-11</b>					
X-ray	9 <sup>h</sup> 31 <sup>m</sup> 08 <sup>s</sup> .81	-11°25'52"			
Radio <sup>a</sup>	9 <sup>h</sup> 31 <sup>m</sup> 08 <sup>s</sup> .38±0.08	-11°23'02.6±1.9			
Optical Candidate	[None Detected] <sup>*</sup>		>21.6 (300s) <sup>**</sup>	>22.3 (1500s) <sup>***</sup>	--
<b>1009+35</b>					
X-ray	10 <sup>h</sup> 09 <sup>m</sup> 46 <sup>s</sup> .4±0.56	+35°16'51"±40"			
Radio	[None Established]				
Optical Candidate 1	10 <sup>h</sup> 09 <sup>m</sup> 46 <sup>s</sup> .8±0.51	+35°16'14"±2"	20.50±0.04 (1200s) <sup>††</sup>	--	19.84±0.06 (2400s)
Optical Candidate 2	10 <sup>h</sup> 09 <sup>m</sup> 50 <sup>s</sup> .0±0.51	+35°16'13"±2"	21.71±0.15 (1200s) <sup>††</sup>	--	20.54±0.10 (1200s)
Optical Candidate 3	10 <sup>h</sup> 09 <sup>m</sup> 51 <sup>s</sup> .0±0.51	+35°16'31"±2"	21.75±0.20 (600s) <sup>††</sup>	--	21.14±0.20 (1200s) <sup>††</sup>
Optical Candidate 4	10 <sup>h</sup> 09 <sup>m</sup> 49 <sup>s</sup> .1±0.51	+35°16'47"±2"	21.61±0.17 (600s) <sup>††</sup>	--	21.02±0.17 (1200s) <sup>††</sup>
<b>1413+13</b>					
X-ray	[Precise position not yet available]				
Radio <sup>a</sup>	14 <sup>h</sup> 13 <sup>m</sup> 33 <sup>s</sup> .90±0.03	+13°34'17.08±0.5			
Optical Candidate	14 <sup>h</sup> 13 <sup>m</sup> 35 <sup>s</sup> .04±0.06	+13°34'16.76±1.0	---	20.71±0.04 (800s) <sup>††</sup>	19.77±0.05 (900s) <sup>††</sup>

#### NOTES

\*Passband of MASCOT area photometer with no filter.

\*\*Passband of MASCOT area photometer with 2mm HA-11 filter (4000 Å - 7000 Å).

\*\*\*Passband of MASCOT area photometer with KPHO filter (1173 Å from Cousins R band).

† In the case where no optical objects were detected within the radio error box, 5 sigma upper limits for a 3 pixel by 3 pixel aperture are given.

†† Integration times in seconds.

<sup>a</sup> Radio coordinates from Condon et al. (1979).

<sup>b</sup> Radio coordinates from Condon et al. (1977).

#### Supplementary Explanations

##### 1. Selection criteria for optical candidates:

###### a. 1009+35:

- Candidates lie within 40 arc seconds of the center of the X-ray error circle.
- Candidates were detected at a 2-sigma level of significance in at least 2 exposures.

###### b. 1413+13:

- Candidate lies within a 2-sigma error circle radius of the precise radio position. (Cohen et al. (1979) have reported an infrared object near the radio position, and Condon et al. (1977) reported a radio source lying near its true object in the POSS plate limit. There was no object visible on the set of 500s prints showing area of field CCD photometry of the radio position, and no object was detected.)
- Candidate was detected at a 2-sigma level of significance in at least 2 exposures. (In fact, this candidate object was detected at 2-sigma level of significance in both the X-ray and radio exposures.)

##### 2. Magnitude estimates:

- Listed magnitudes were determined from a 2-sigma pixel aperture (1200s) and are shown in parentheses on the position given.
- Magnitude errors listed are inferred from the signal-to-noise ratio of the object in the single pixel level. Error bars are not shown for the magnitude estimates for the objects which were detected at a 2-sigma level.

Three of the four X-ray objects are also flat spectrum radio sources (Condon et al. 1977, 1978), for which the radio error circles are very small (radius  $\leq 2''$ ), while the fourth object (1009+35) has only an approximate ( $\sim 40''$  error radius) X-ray position. We have searched these error circles for optical candidates down to the CCD "plate limit" (somewhat arbitrarily taken as corresponding to a 5 $\sigma$  level of confidence for source detection). In Table 3, we summarize the results of these searches. For 0320+39 and 2231-11, we find no candidates within the 2" error circles, down to limiting magnitudes (4000-7000Å) of +22.4 and +22.2, respectively. For 1009+35, there are 4 possible optical candidates within the X-ray error circle, with R magnitudes ranging from +19.8 to +21.1. In the case of 1413+13, we have found what we believe to be the optical counterpart at a location  $1''$  from the radio position, which is within the 2 $\sigma$  error circle radius given by Condon et al. 1977. It is likely that this is the same object reported by Condon et al. 1977 as a "faint red stellar object" near the POSS plate limit. (There was no object visible on the set of POSS prints we used, so that CCD photometry of the radio position seemed warranted.) Rieke et al. (1979) have also reported an IR object near the radio position.

### 7. Conclusions

In the first run of the MASCOT on the 1.3m McGraw Hill telescope, the following features of the instrument have been demonstrated.

- High throughput ( $\sim 15\%$  over 5000Å-7000Å).
- Good Photometric stability ( $\pm 0.04$  mag, even for  $>22$  mag objects, over periods of several days).
- Relatively "flat" unprocessed pictures ( $\sim 2\%$  uniformity).
- Additional field flattening is straightforward (A field uniformity of 1.4% of the sky brightness has been achieved. This degree of flattening is consistent with sky shot noise plus readout noise for integrations up to 30 minutes [i.e., the longest ones attempted so far]).
- Excellent sensitivity ( $\sim 24.4$  mag arc sec $^{-2}$  in an 1800 s integration, over a 4000Å-7000Å bandpass, at a 5 $\sigma$  level of significance).

The preliminary astronomical results attained with the MASCOT include the following information concerning four "empty field" X-ray sources:

- 1413+13: Identification of an optical counterpart ( $1''$  from the radio position).
- 1009+35: Isolation of 4 candidates for further study.
- 0320+39, 2231-11: Still empty to  $m_r > 22.3$  magnitude.

Among the areas of further study which we have identified within the MASCOT system are: operation at the telescope with newly-reduced CCD readout noise ( $\sim 3$  times lower than during March 1981 run); more sophisticated field flattening (if necessary); and a systematic evaluation of the spectrometer channel performance.

### Acknowledgments

We are grateful to the many people who have provided advice, assistance, and encouragement during the preliminary CCD studies leading to, as well as the actual, MASCOT project. Among the helpful friends and colleagues with whom we have consulted at the C.S. Draper Laboratory, at Texas Instruments, at the Jet Propulsion Laboratory, and at MIT are: P. Greiff, H. Huemmler, M. Blouke, J. Carlo, H. Vosack, D. McGrath, J. Janesick, F. Vescelus, R. Baron, D. Chan, D. DeVov, E. Dunham, J. Elliot, J. Kriss, J. Kucera, M. Manolitu, and R. Schaffer. During the actual observations at the McGraw-Hill Observatory, Matt Johns and Mike Dreslin were extremely helpful. We thank Brenda Parsons for the preparation of the manuscript.

This work was supported by the National Aeronautics and Space Administration under grants NGL22-009-015 and NGL22-009-638

### References

- Bessell, M.S. 1979, P.A.S.P., 91, 589.
- Christian, C.A. 1981, "Video Camera/CCD Standard Fields" (KPNO memorandum, unpublished).
- Condon, J.J., Ruckman, M.A., and Machalski, J. 1979, A. J., 94, 149.



- nden, J.C., Hixs, P.D., and Janney, D.L. 1977, A.J., 81, 400.
- ewey, D. and Packer, G.R. 1980, in Applications of Digital Image Processing to Astronomy, ed. Elliott, D. (NASA/JPL Proceedings S.P.I.E. 264 Bellingham, Washington), p. 40.
- Hiacconi, R. et al. 1979, Ap. J., 230, 540.
- Hall, J.E., Breitzmann, J.F., Blouke, M.M. and Carlo, J.T. 1979, Proc. IEDM (Washington, D.C.)
- Hynecek, J. 1981, IEEE Trans. on Electron Devices, ED-28, 499.
- Janesick, J., Hynecek, J., and Blouke, M. 1981, in Solid State Imagers for Astronomy (ed. J. Geary and D. Latham, SPIE, Bellingham, Washington).
- Landolt, A.U. 1973, Ap. J. 78, 959.
- Meyer, S.S. and Packer, G.R. 1980, in Applications of Digital Image Processing to Astronomy, ed. Elliott, D. (NASA/JPL Proceedings S.P.I.E. 264 Bellingham, Washington), p. 29.
- Rieke, G.H., Lebofsky, M.J., and Kinman, T.D. 1979, Ap. J. (Letters), 232, L151.
- Strom, K.M. 1977, "Standard Stars for Intensified Image Dissector Scanner Observations" (KPNQ memorandum, unpublished).

## Appendix D

*The Explosive Transient Camera (ETC): An Instrument for the Detection of Gamma-Ray Burst Optical Counterparts*, Ricker, G.R., Doty, J. P., Vallerger, J.V., and Vanderspek, R. K. 1983, in Instrumentation for Astronomy V, eds. A. Boksenberg and D. Crawford (SPIE: Bellingham, Washington), 445, 370.

THE EXPLOSIVE TRANSIENT CAMERA (ETC):  
An Instrument for Identification  
of  
Gamma Ray Burst Optical Counterparts

G.R. Ricker, J.P. Doty, J.V. Valleria, and R.K. Vanderspek

M.I.T. Department of Physics and Center for Space Research

ABSTRACT

The Explosive Transient Camera (ETC) is a wide field ( $\sim 3$  steradians) electronic camera array which can detect coincident optical flashes with durations of  $\sim 10^{-1}$  to  $10^{-2}$  seconds. It is anticipated (but not yet conclusively demonstrated) that simultaneous optical flashes will be associated with certain classes of gamma ray bursts (GRBs). For the ETC, each array element is a  $20^\circ \times 30^\circ$  FOV, cooled CCD detector, developed at MIT. An optical transient as faint as  $B = +11$  (1 second duration) can be detected with  $S/N > 20$ , and its position determined to an accuracy of  $\pm 10$  arc seconds. Thus, candidate events  $\sim 10^3$  times fainter than the archived event (plate taken in 1928) reported for the 19 November 1978 gamma ray burst (GRB) by Schaefer (1981) should be detectable in real time. In addition to detecting GRBs, the ETC is expected to catalog large numbers of flare stars, as well as potentially new classes of astronomical transients.

The coordinates established by the ETC will be immediately transmitted ( $\sim 1$  second delay) to the Rapidly Moving Telescope (RMT) under development at NASA/GSFC (Teegarden, Cline and von Rosenvinge 1982), which can further refine the position of a flash and follow its (presumed) subsequent decline. Communications to other rapid response radio or IR instruments will also be provided for, as well as time comparisons to gamma ray events detected by the International GRB Satellite Network (Hurley 1981).

A prototype camera element was first tested in April 1982 to establish sky background levels and spurious event rejection schemes. A  $1/2$  steradian test version of the ETC is planned for operation in early 1984. Expansion to the full 3 steradian complement of 16 detectors at each of two sites is planned during the 1984-1985 period.

1. Introduction

In the past two decades, our perception of the "violent universe" has resulted from the discovery of quasars (1962), pulsars (1968), gamma-ray bursters (1970), and X-ray bursters (1973). For each of these classes of objects, the initial discovery was made by non-optical means, and optical counterparts were subsequently established. Curiously, the prototypical example for each class of optical counterpart has turned out to be rather bright, at least at the peak of its time-variable emission (e.g. the quasar 3C273,  $m_v \approx +13$  [e.g., Hewitt and Burbidge 1980]; the pulsar NP0532+21,  $m_v \approx +15$  [e.g., Smith 1981]; the gamma ray burst source GRB 0116-289,  $m_v \approx +3$  [Schaefer 1981]; the X-ray burster MXB1636-53,  $m_v \approx +17$  [Pedersen et al. 1982]). Thus, one might reasonably ask the question: *"Are there in fact biases against the ab initio discovery of violent optical transients inherent to current optical instrumentation or observing methods used by astronomers?"* To such a question, the answer would appear to be: *"Yes: Current standard optical survey methods rely on either long integrations ( $\sim$  minutes to hours) and/or study rather limited areas of the sky ( $\sim 100$  deg<sup>2</sup> out of  $\sim 40,000$  deg<sup>2</sup> accessible)."*

Hence, it is not surprising that standard optical surveys fail to detect short duration phenomena occurring with low duty cycles. An instrument which circumvents those limitations is the Explosive Transient Camera (ETC), described below, which integrates for short times ( $\sim 1$  s) while imaging a very wide field-of-view ( $\sim 10^4$  deg<sup>2</sup>) with good source location accuracy ( $\pm 10$  arc seconds). The ETC is well-suited to discovering optical burst sources with time profiles and duty cycles of the type exhibited by gamma ray bursters (in gamma rays) as well as "ultra rapid" flare stars. As such, it will explore a new "window" into the parameter space of optical sources. Since, based on historical experience, the opening of such a new "window" in astronomy often reveals entirely unexpected new phenomena, the prospects for serendipitous discovery are very attractive.

In the following section, we discuss the sensitivity considerations relevant to the ETC, as well as the importance of anticoincidence techniques in its design. The specific design we have chosen for the ETC is described, along with the provisions for linking it to other rapid response detectors. Results from prototype tests are presented. We also compare the particular approach we have chosen for the ETC with other optical flash detection methods. Finally, we attempt to estimate the type and frequency of flashes which we might detect, and discuss areas of further development for ETC-like instruments.

## 2. Sensitivity Considerations in Wide Field Searches

In this section, we derive a set of general expressions for the sensitivity (i.e. minimum detectable flux for a given S/N ratio) of an instrument for detecting brief bursts of optical radiation. Since these expressions differ significantly from those traditionally used in evaluating sensitive "long integration" astronomical detectors, it follows that the optical transient system design is quite different from a standard telescope-detector arrangement.

The two principle assumptions which lead to the different design constraints are:

- The briefness ( $\sim 1$  s) and low duty cycle ( $\sim 10^{-4}$  to  $10^{-5}$ ) of burst events for typical survey program durations ( $\sim 10^5$  -  $10^6$  s)
- The low surface density of burst events on the sky (possibly  $\lesssim 10^2$  events  $\text{yr}^{-1}$  sterad $^{-1}$ ).

To assess the effect of various limiting values of these two assumptions, we will evaluate a very general form of the fundamental signal-to-noise relation for a "background limited" astronomical detector. The fundamental relation for the signal-to-noise ratio for an imaged event in the "background-limited" case is given by:

$$m = \frac{\Sigma}{B^{1/2}} \quad (1)$$

$$= \frac{\phi_{\min} \epsilon A t \Delta \lambda}{(\epsilon A t \Omega_p \Delta \lambda)^{1/2}} \quad (2)$$

Where:

- $m$  = significance level of a detection, or signal-to-noise ratio
- $\Sigma$  = number of source photons detected
- $B$  = number of background ("sky") photons detected
- $\phi_{\min}$  = source flux which will result in a detection at a signal-to-noise of  $m$ ; units of  $\text{ph cm}^{-2} \text{s}^{-1} \text{\AA}^{-1}$
- $\epsilon$  = system photon efficiency (or "throughput")
- $A$  = system geometric area; units of  $\text{cm}^2$
- $t$  = burst duration; units of seconds
- $\Delta \lambda$  = system passband; units of  $\text{\AA}$
- $\phi$  = sky brightness; units of  $\text{ph cm}^{-2} \text{s}^{-1} \text{\AA}^{-1} \text{sr}^{-1}$
- $\tau$  = system integration time; units of seconds
- $\Omega_p$  = solid angle subtended by a single pixel of a multielement system; units of sr.

Equation (2) can be solved for  $\phi_{\min}$ , the "minimum detectable flux", for a signal-to-noise ratio of  $m$  obtained for a burst of duration  $t$  during an integration time  $\tau$ :

$$\phi_{\min}(m, t, \tau) = m \frac{1}{t} \left( \frac{\phi \tau \Omega_p}{\epsilon A \Delta \lambda} \right)^{1/2} \quad (3)$$

In the "steady source" limit ( $t = \tau$ ), equation (3) reduces to the more familiar form:

$$\phi_{\min}(m, t = \tau) = m \left( \frac{\phi \Omega_p}{\epsilon A \tau \Delta \lambda} \right)^{1/2} \quad (4)$$

The total number of bursts,  $\xi$ , detectable at a level of significance of " $m$  sigma" expected for a total observing time  $T$  is given by:

$$\xi = N(>\phi_{\min}) \frac{\Omega_s}{4\pi} T \quad (5)$$

where:

- $N(>\phi_{\min})$  = occurrence rate for bursts brighter than  $\phi_{\min}$  over the entire sky; units of  $\text{s}^{-1}$
- $\Omega_s$  = system solid angle; units of steradians
- $T$  = observing time; units of seconds

Our present knowledge of  $N(>\phi_{\min})$  for gamma ray bursts is quite uncertain. However, we can bound the plausible range of  $N(>\phi_{\min})$  for anticipated optical bursts by using  $L_{\text{opt}}/L_y$  assumptions derived from the burst observation of Schaefer (1982) and the "LogN - LogS" calculations of Jennings (1982). There are three interesting special cases for Eq. (5). These are:

Case 1 "Distance Limited Population"

$$\xi_{DL} = \gamma \frac{\Omega_s}{4\pi} T \quad (6),$$

corresponding to the situation in which all sources in the Galaxy are detectable at  $S/N > m$ . For this case,  $\gamma$  is the total number of such sources in the Galaxy.

Case 2 "Infinite-Disk Population"

$$\xi_{ID} = \gamma \frac{t}{m} \left( \frac{\epsilon A \Delta \lambda}{\phi \tau \Omega_p} \right)^{1/2} \frac{\Omega_s}{4\pi} T \quad (7),$$

corresponding to  $N(>\phi_{min}) = \gamma \phi_{min}^{-1}$ .

Case 3 "Infinite-Halo Population"

$$\xi_{IH} = \gamma \left( \frac{t}{m} \right)^{3/2} \left( \frac{\epsilon A \Delta \lambda}{\phi \tau \Omega_p} \right)^{3/4} \frac{\Omega_s}{4\pi} T \quad (8),$$

corresponding to  $N(>\phi_{min}) = \gamma \phi_{min}^{-3/2}$ .

For each of these three limiting expressions for  $\xi$ , it is clear that both large solid angle coverage and a long observing time are extremely important for maximizing the number of detected bursts, since  $\xi$  is linear in both. On the other hand, large detecting area and small pixel solid angle are less important since  $\xi$  varies more slowly as they are changed. For burst gamma fluences  $S_{opt} < 10^{-5}$  ergs cm<sup>-2</sup>, the Log N - Log S relations considered by Jennings (1982) indicate that Case 1 ("Distance Limited Population") will result in the smallest number of total bursts. Therefore, we will be conservative and adopt Eq. 6 for the remaining discussion. Furthermore, recent measurements of faint gamma ray bursts by Fishman (private communication) indicate that the Galaxy population may very well be cutoff below  $S \sim 10^{-6}$  ergs cm<sup>-2</sup>, with  $\gamma \sim 10^3$ . Hence, if we adopt  $S_{opt}/S_\gamma \sim 10^{-3}$ , (Schaefer 1981), then Eq. (6) predicts:

$$\begin{aligned} \xi_{DL} &= (10^3 \frac{\text{events}}{\text{year}}) \left( \frac{2.7 \text{ sterad}}{4\pi \text{ sterad}} \right) (0.1 \text{ year}) \\ &\approx 20 \text{ events detected,} \end{aligned}$$

where we have assumed a 2.7 sterad instrument operating for a year with a duty cycle of 10% (i.e. observing only when it is dark [0.5x], clear [0.5x], and there is no moon [0.5x]). The optical fluence of  $10^{-9}$  ergs cm<sup>-2</sup> corresponds to a visual magnitude  $m_v = +9.5$ , for 1 second flash durations.

### 3. ETC Configuration and Characteristic

In Section 2 we estimated the level of sensitivity needed by the ETC to detect optical flashes from gamma ray burst counterparts. A number of questions then arise: namely, given such an instrumental sensitivity, how should the instrument be configured to provide the solid angle coverage and to reject non-astronomical light flashes? Also, is it possible to obtain sufficiently accurate ( $\sim 10$  arc sec) burst positions to permit detailed study of a quiescent object? In this section, we present a configuration which appears to satisfy these needs.

The ETC configuration we have chosen consists of two independent, "flys eye" arrays of short focal length CCD optical cameras, operated in coincidence. Figure 1 shows such a configuration as it will appear when deployed at Kitt Peak, Arizona. As shown, one array (and the control center) is located on the southwest ridge of the mountain, while the other is located near the summit. By requiring that a candidate flash be recorded simultaneously ( $\pm 0.5$  sec) at both sites and that its arrival direction appear the same ( $\pm 2$  arc minutes) at both sites, we can distinguish flashes of astronomical origin (type "A", see Figure 1) from those of local origin (type "B" or "C"; see Figure 1).

A detailed listing of instrument characteristics is shown in Table 1. The parameters given include both specifications, as well as previously measured values, indicated by an asterisk (see Section 6). All of the above-mentioned requirements for the ETC will be satisfied by such an instrument.

#### 4. Camera Module Design

As listed in Table 1, the ETC will eventually consist of an array of 16 CCD cameras at each of 2 sites. At each site, the 16 cameras will be organized into 4 modules, each bearing 4 CCD cameras. The 4 cameras on each module will be mounted on a sidereal drive and arranged to view adjacent  $20^\circ \times 30^\circ$  patches of sky, as shown in Figure 2. By adjusting a system of mounting brackets on each module mount, the cameras on neighboring modules will be directed to distinct  $2400 \text{ deg}^2$  areas of sky. (Because of the well-known difficulty of mapping rectangles onto the surface of a sphere, a small amount of overlapping and a few small gaps in coverage are unavoidable.) In all,  $\sim 9000 \text{ deg}^2$  will be viewed, with the sky coverage extending from the zenith down to an elevation angle of  $\sim 35^\circ$ .

Each CCD is mounted within a magnesium cryostat, and is cooled to  $-60^\circ\text{C}$ . A 25 mm f/0.85 lens is

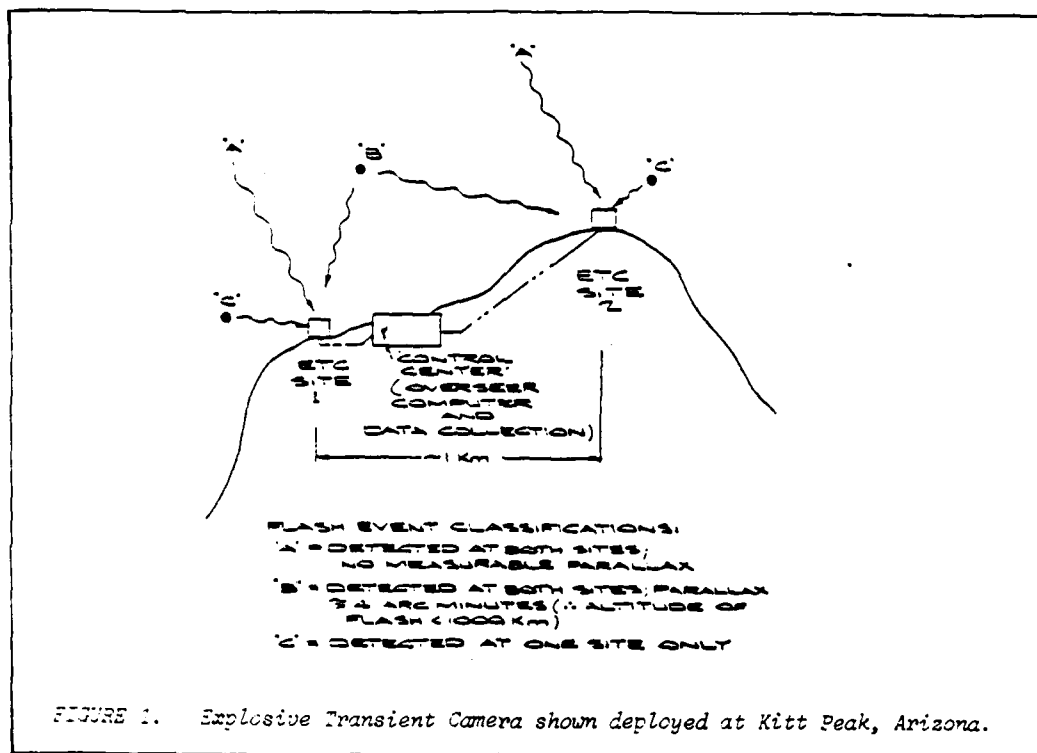
Table 1

Characteristics of An  
EXPLOSIVE TRANSIENT CAMERA (ETC)  
Array To Search For Gamma Ray  
Burst Counterparts And Other  
Astronomical Flash Sources

Parameter	Expected Value
Field of View:	2.7 Sterad (i.e. 43% of sky)
Sensitivity * :	$S/N=20^{**}$ for $B=+11$ magnitude event (1 s duration, 4000 Å BW)
Source Location Accuracy:	$\pm 10$ arc-seconds (for a $S/N=40$ burst)
Expected Optical/Gamma Burst Detection Rate:	$\sim 20$ per year
Pixel Size:	$3' \times 3'$
Number of Detectors:	4 per module
Number of Modules:	4 per site
Number of Sites:	2
Spacing Between Sites:	$\sim 1$ km
External Bit Rate:	$\sim 10$ bits/sec
Optical Throughput * :	50 per cent
Optical Elements:	25 mm f/0.85 CCTV lenses
Detector Elements:	TI 584x390 CCDs
Readout Noise (per pixel):	$\sim 20 \text{ e}^- \text{ rms}$
Sky Noise * (per pixel):	$\sim 20 \text{ e}^- \text{ rms}$
Operating Temperature:	$-60$ degrees Celsius
Weight (per module):	$\sim 70$ kg
Size (per module):	$\sim 60 \text{ cm} \times 60 \text{ cm} \times 60 \text{ cm}$

\* Estimated from actual values measured with an improvised prototype array element at Mauna Kea Observatory on April 2, 1982.

\*\* If indeed  $B_{\text{cutoff}} = +9.5 \text{ mag}$ , as would be implied from  $L_{\text{opt}}/L \sim 10^{-3}$  (Schaefer 1983) and a  $\text{Log } N(>S) - \text{Log } S$  rollover for the Galaxy near  $S \sim 10^{-6} \text{ ergs cm}^{-2}$  [Fishman 1982], then we expect  $S/N \sim 80$  for every detected  $\gamma$  flash.



threaded directly into the cryostat face. Filters are mounted directly over the first element of each 25 mm lens, while a rotary shutter (not shown) in front of each 25 mm lens determines integration times.

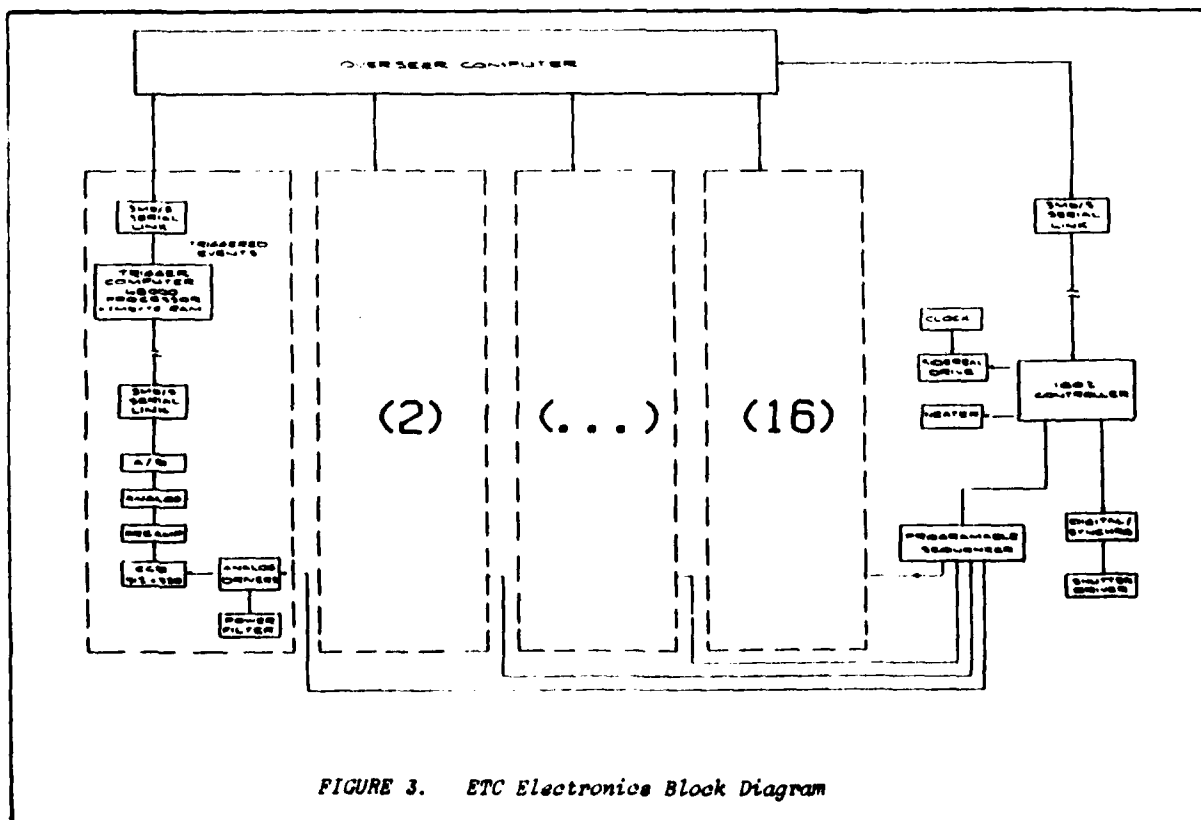
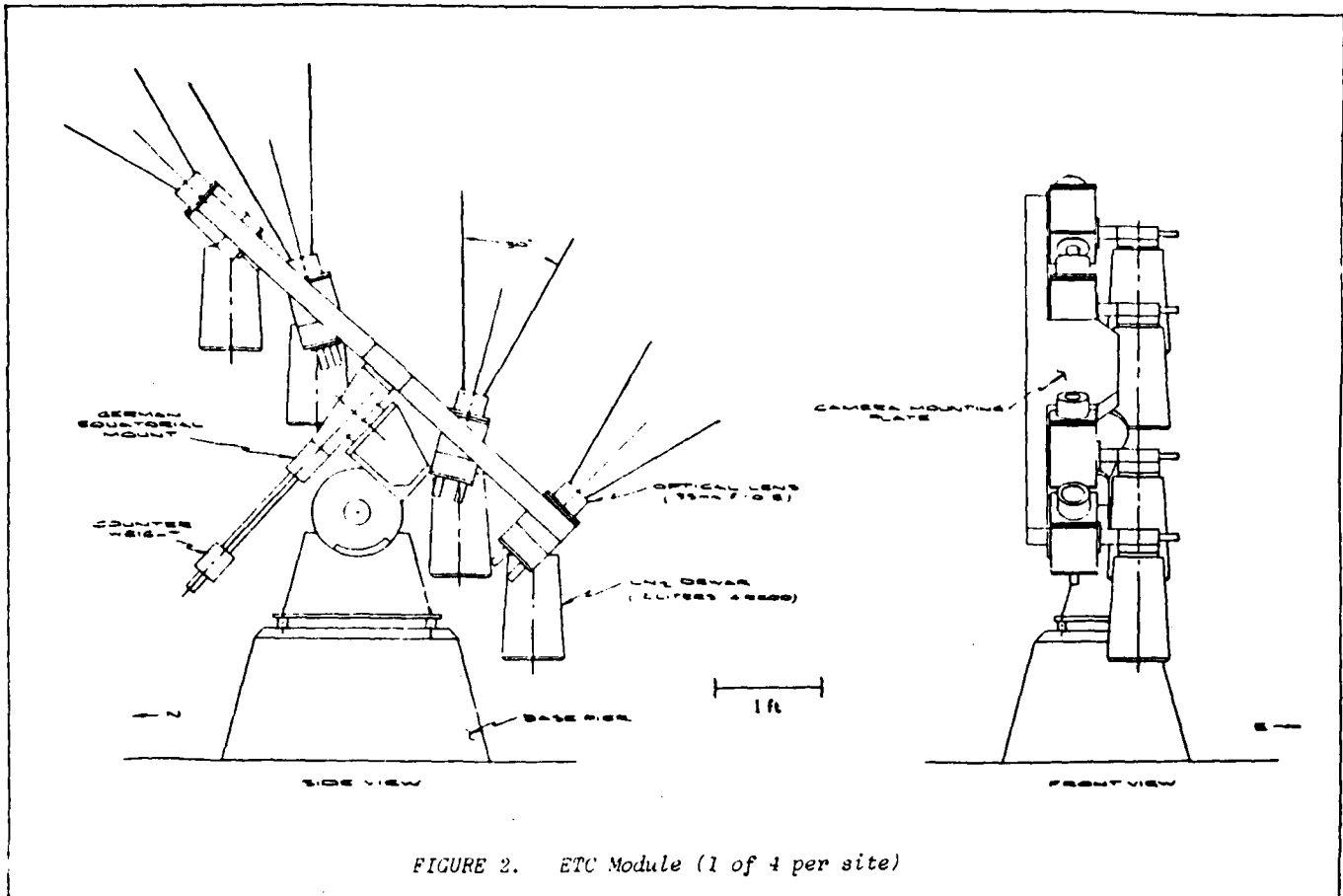
The German equatorial mount (with its 4 CCD cameras) will track at the sidereal rate from 7.5 degrees East of the meridian to 7.5 degrees West of the meridian, and then slew back under the control of an Overseer Computer (see below). The slewing motion requires about 30 seconds to complete.

The analog electronics for the ETC are derivatives of systems previously constructed for the MIT "MASCOT" observatory instrument (Ricker *et al.* 1981). In Fig. 3, we show an overall block diagram of the ETC control and data handling electronics. As indicated in the figure, each CCD camera will be connected to its own trigger processor through a 3 Mb/sec serial link. The trigger processor is based on a Motorola 68000 microprocessor and 1.0 Mbyte of random access memory. Its function is to detect changes in the optical images by subtracting two successive CCD frames. This operation will be performed continuously as the newest frames will overwrite the earliest in the memory until a difference greater than a preprogrammed value (an "event") occurs in any pixel location. (Further details on event processing are given in Section 5.)

Events detected by the trigger processors will be passed to the Overseer Computer (Figure 4). The Overseer Computer controls the sidereal drive, heaters, shutters, and all the CCD cameras (through the 1802 microprocessor), as well as servicing the trigger processors. This computer is also based on a Multibus compatible Motorola 68000 microprocessor board, and operates under UNIX. A similar design has been successfully used in the X-ray CCD development program at M.I.T. for image acquisition and processing. The Overseer Computer is extremely cost effective, as it achieves "VAX-level" speeds in integer operations on CCD image data, yet can be purchased and assembled for only 1/10 the cost of a VAX/780 minicomputer system.

## 5. Event Processing and Links to Other Rapid Response Detectors

The ETC will be sensitive to an optical flash with a fluence equal to or greater than that of an  $\sim 11$ th magnitude star. Because of the large number of anticipated spurious sources of optical flashes of at least this brightness, the ETC software has been designed to recognize most terrestrial sources and further analyze only those flashes which might possibly have cosmic origins. In Table 2, we categorize the successive event sifting which is to be carried out by the CCD Trigger Processors and the ETC Overseer Computer, working in tandem to reject terrestrial flashes while retaining cosmic flashes. After a CCD image is loaded into a Trigger Processor, the sifting proceeds by the asking of a series of questions concerning the magnitude and clustering of high amplitude pixels (First, Second, and Third level sifting; see table). Based on data obtained in an ETC prototype test carried out at Mauna Kea Observatory in April 1982 (see Section 6), we have established approximate "passthrough fractions" for the first two levels of sifting. To estimate the passthrough fraction for the third sieve, we have used CCD cosmetic characterization data obtained in the laboratory and in long term studies with the MASCOT system (Ricker *et al.* 1981). If a cluster of high pixels passes these sieves, the 32x32 subarray in which it is contained is sent from the Trigger Processor to the Overseer Computer. Two further, more elaborate sifting operations occur in the





Overseer Computer, based on profile fitting and statistical testing, respectively. We estimate that  $\sim 2$  "candidate triggers" per minute from a single 3 sterad ETC site will successfully pass these 5 tests. The vast majority of these successful candidate triggers will be cosmic rays or local optical events, and will be rejected as a result of the coincidence check with the second ETC site. Of those which pass the coincidence check and are cosmic in origin, we estimate that  $\sim 10^{-1}$  to  $10^{-2}$  will be due to flare stars, while only  $\sim 10^{-4}$  may correspond to gamma ray burst-related optical flashes (see Sections 7 and 8).

For each "single ETC site event," a location centroid can be calculated to an accuracy of  $\sim$  pixel angle  $\times [S/N]^{-1}$ , based on our experience with the MASCTT software autoguider (Ricker et al. 1981). Calibration difficulties limit the achievable accuracy to  $\sim 0.02$  pixels. Thus, for an  $m_b = +10$  flash, a realizable positioning accuracy of  $\pm 10$  arc seconds can be expected. The excellent centroiding capability of each ETC site on its own will also permit rejection of flashes due to near earth phenomena in all but the highest satellite orbits ( $> 10,000$  km).

Although the  $\pm 10$  arc second error boxes expected from the ETC will be sufficient for many types of follow-up observations, even smaller error boxes may prove necessary if the quiescent counterparts turn out to be extremely faint. Tyson and Jarvis (1979) find that the density of  $m_b \sim +23$  objects (galaxies plus stars) is  $\sim 7 \times 10^{-5}$  per square arc second near the North Galactic pole. For such faint objects,  $\sim 1''$  error boxes would be required for identification based strictly on positional grounds.

Such a factor of  $\sim 10^2$  reduction in error box area from the ETC results can in principal be achieved with an instrument called the Rapidly Moving Telescope (RMT), operating in tandem with the ETC. The RMT has been discussed by Teegarden, Cline, and von Rosenvinge (1982). It will consist of a single 17 cm aperture telescope with the capability of slewing to any region of the sky in 1 second or less and remaining stable thereafter to  $\pm 2$  arc seconds for a period of at least several minutes. A CCD focal plane detector (with  $\sim 1'' - 2''$  pixels) can read out selected subarrays of its  $\sim 0.2$  degree FOV every  $\sim 0.1$  second.

Table 2

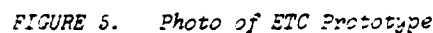
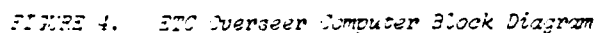
ETC EVENT SIFTING PROCESSES\* (PER SITE)

Sifting Process	Fraction Of Entering Events Exiting Process Per Second	Number Of Events Remaining Per Second
CCD readout into trigger memory	1.0	$4 \times 10^6$ pixels (584x390 CCDs; 16 required)
First level sifting: Pixel value above certain pre-set threshold?	.01 accepted <sup>+</sup>	$4 \times 10^4$ events**
Second level sifting: No corresponding event in previous frame?	.001 accepted <sup>+</sup>	40 events
Third level sifting: No known defects in CCD at event site? (Table look up)	.1 accepted	4 events
Fourth level sifting: Does image have a PSF-like profile?	.1 accepted	.4 events
Fifth level sifting: Statistical significance of image greater than some preset value? (variable threshold)	.1 accepted	.04 events

\* These processes are a sieve to determine the onset of an optical burst. Once a burst has been determined to be in progress, a separate list of selection criteria will be followed.

\*\* For this and the following levels, an "event" is a selected cluster of pixels.

<sup>+</sup> Criterion established in April 1982 ETC prototype test at MKO.



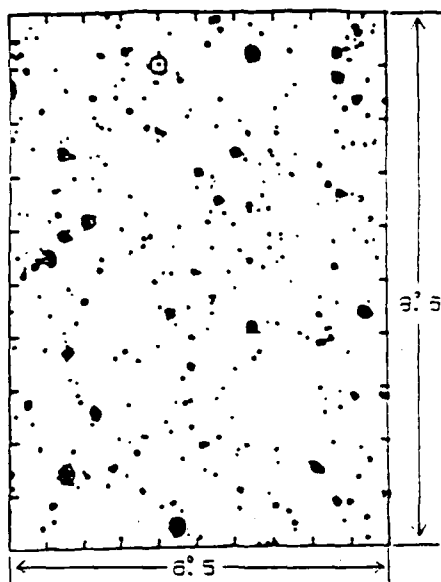


FIGURE 6. Image obtained in a 2 second exposure taken 1/2 April 1982 at Mauna Kea Observatory with an MIT wide-field CCD camera (ETC prototype). The  $f/0.95$  lens used had a 50 mm focal length, giving the  $6.5 \times 8.6$  FOV indicated. The optical detector was a Texas Instruments virtual phase CCD (see Ricker, et al., 1981, for additional details).

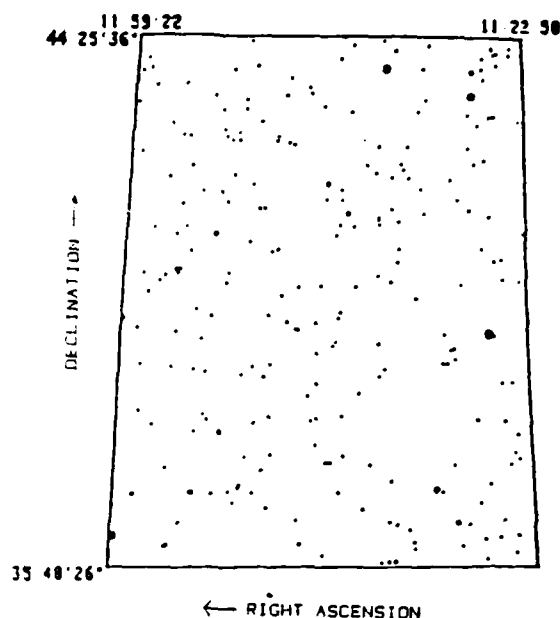


FIGURE 7. Plot of SAO catalog stars (epoch 1932.0) for the ground-based ETC prototype test conducted at Mauna Kea Observatory on 1/2 April 1982. Stars ranging in visual brightness from magnitude 5.5 to 3.5 are shown.

The time line for the interaction between the ETC and the RMT is shown in Table 3. As indicated, it will require that the ETC test an event for validity as quickly as possible, and transmit the sky coordinates of the event to the RMT (via a modem link). By utilizing parallelism as much as possible the notification delay can be reduced to a most probable value of 1.2 seconds, and can range from 0.2 seconds to 2.3 seconds, depending upon where in the ETC field of view the event occurs and when it occurs with respect to the ETC shuttering cycle.

In addition to facilitating a ready exchange between the ETC and the RMT, an attempt will be made to link the ETC (via modem) to other "rapid response" facilities capable of utilizing positions and times of occurrence of optical bursts detected by it. Such other facilities might include, among others, IR and radio instruments.

## 6. Prototype Tests

During the April 1982 observing run with the MASCOT CCD system (Ricker et al., 1981) at Mauna Kea Observatory (MKO), we carried out a trial experiment to measure the optical burst sensitivity of a Texas Instruments virtual phase CCD detector (Meyer and Ricker 1980). In this experiment, a 50 mm  $f/0.95$  TV camera lens was used to image a  $6.5 \times 8.6$  field onto one-half of the CCD. With this lens, a single pixel subtended a solid angle of  $1.7 \times 1.7$ . Figure 5 is a photo of the test apparatus, shown mounted on the back plate of the 61 cm Air Force telescope at MKO. (The telescope was used only as a sidereal drive for the test apparatus, with the TV lens actually viewing the sky at right angles to the telescope viewing direction). The TV lens and CCD mounting head are at the left edge of the photo, about one-third of the way up from the bottom edge. During the observing period, we obtained unfiltered exposures, each of 2 seconds duration, of two fields near the North Galactic Pole. The image from one of these 2 second exposures is shown in Figure 6. Figure 7 (adjoining) is a plot of the SAO catalog stars for the same field. There are 221 SAO stars plotted in Figure 7, while the number of stars detected in the 2 second CCD exposure is  $> 300$ .

The contour plot threshold in Figure 6 was set at a statistical S/N level of 10:1. This level corresponds to a brightness of  $\sim +12$  magnitude (B) per pixel. Because the lens was used without a filter,

chromatic aberration (and to a lesser extent, the lens/CCD point spread function) blurred all of the stellar images so that only  $\sim 25\%$  of their total energy was within a single pixel. Thus, if we add together the energy dispersed in neighboring pixels, the detection criterion can be re-expressed as  $S/N \sim 20$  for  $B = +11.5 \pm .7$  magnitude objects. For the lens which we plan to use with the operational ETC, the limiting magnitude will be reduced to  $B = +11$  for  $S/N = 20$ , given in Table 1. From the Mauna Kea tests, we also established values for sky noise contributions and optical throughput for CCTV lenses of the generic type we will use with the ETC. These values are also given in Table 1.

The issue of an optimum filter choice for the ETC optical system is a complex one. There are theoretical arguments for choosing a U or B band for the optical burst searches with the ETC, since the optical radiation is expected to lie on the Rayleigh-Jeans tail of reprocessed  $\gamma$ -, X-, or hard UV radiation (Schaefer and Ricker 1982). Of course, whether one should prejudice an initial survey by such a choice is a debatable point! Our inclination at this time would be to strive for optimum sensitivity, so that we plan to use as broad a passband as possible. Limitations on filter bandwidths will arise from chromatic aberration in the camera lens, from ozone absorption in the UV, and from excessive sky brightness principally due to OH band emission in the near IR.

## 7. Comparison with Other Optical Flash Detection Methods

In Section 2, we discussed the design considerations for an optimally sensitive flash detector for optical phenomena with characteristic durations of  $\sim 1$  second. An additional consideration is the rejection of non cosmic flash phenomena. (For the ETC, such non cosmic flashes are rejected by an anticoincidence method.) A third consideration relates to contributions expected from various non-GRB cosmic phenomena.

Schaefer (1983) has estimated the contributions of various cosmic optical flash phenomena to a number of different survey instruments, including the ETC. In Figure 8, we show these estimates in the form of expected flash rates,  $R$  [events  $hr^{-1} \text{sterad}^{-1}$ ], versus apparent magnitude,  $m$ , of the flash. Of the four

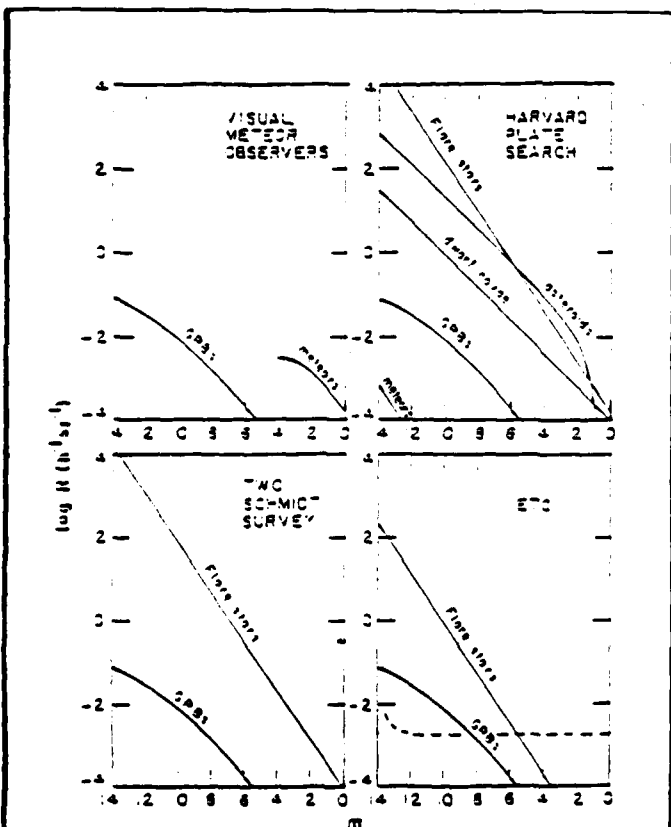


FIGURE 8. Expected background rate,  $R$ , as a function of apparent magnitude,  $m$ , for 4 different optical flash search techniques (Schaefer, 1983). For the panel labeled "ETC", a dashed line gives the upper limit on  $R$  ( $3\sigma$  level of confidence) which would be deduced from a one-year search that detected no flash events.

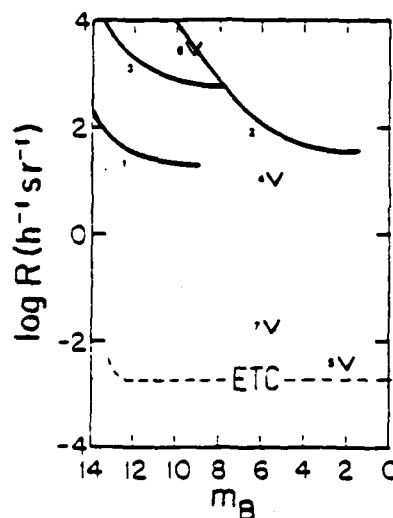


FIGURE 9. Upper limits ( $3\sigma$  level of confidence) on the optical background flash rate deduced from the null results reported from various searches (Schaefer, 1983). The rate,  $R$ , is plotted as a function of  $B$  magnitude for the results of: (1) a search using two Schmidt telescopes (Ricker, et al., 1982; Schaefer, et al., 1983); (2) Harvard archival plate searches (Schaefer, 1983); (3) Variable star searches (J. Graham, M. Liller (unpublished)); (4) "Problicom" searches (amateur groups); (5) Stationary meteor records (amateur groups); (6) Galactic Center flash search (Byrne and Wayman, 1975); (7) Silicon Intensified Target TV searches (Hurley, 1983). The dashed line marked "ETC" gives the upper limit on  $R$  ( $3\sigma$  level of confidence) which would be deduced from a one-year search that yielded a null result.

Table 4

CALCULATED NUMBER OF OPTICAL BURST EVENTS  
DETECTABLE WITH THE EXPLOSIVE TRANSIENT CAMERA (ETC)  
AND WITH A PAIR<sup>+</sup> OF 1 METER-CLASS SCHMIDT TELESCOPES (PST)  
FOR THREE SIMPLIFIED SOURCE DISTRIBUTION MODELS

Model for Source Distributions	Instrument	$T_{OBS}^{**}$ (sec)	$\xi^{**}$ (# of Detectable Events Expected)
Distance-Limited Population	ETC: 1 Year	$3 \times 10^6$	20
(e.g., cutoff $S^{-1}$ or cutoff $S^{-3/2}$ )	PST: 1 Year	$3 \times 10^6$	0.065
<hr/>			
Infinite Disk	ETC: 1 Year	$3 \times 10^6$	65.8
( $S^{-1}$ )	PST: 1 Year	$3 \times 10^6$	2.0
<hr/>			
Infinite Halo	ETC: 1 Year	$3 \times 10^6$	95.1
( $S^{-3/2}$ )	PST: 1 Year	$3 \times 10^6$	9.3

<sup>+</sup> NB: Two such 1 meter Schmidt Telescopes at two sites are required for an optical flash search, just as there are two sites for the ETC system.

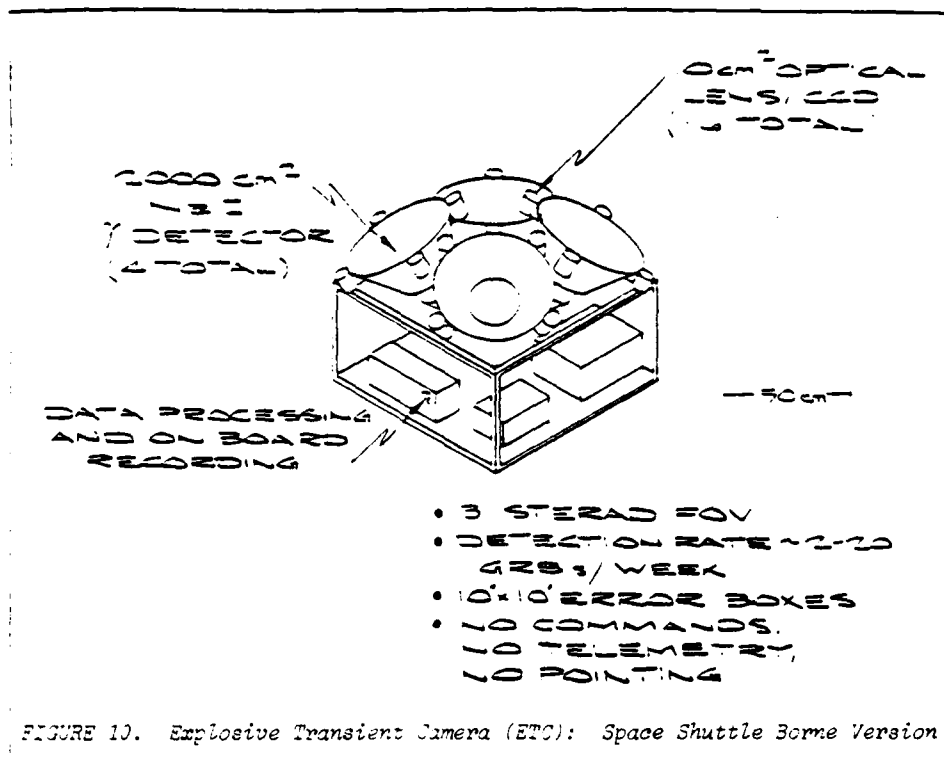
<sup>\*\*</sup> Detected at  $S/N > 20$ .

<sup>\*\*</sup> Assumes  $\sim 10\%$  duty cycle for observations (i.e., nighttime, clear, moon less than half full).

techniques considered (1 visual, 2 photographic, and 1 electronic), the ETC should be effected the least by known non-GRB phenomena. Nonetheless, it is apparent from Figure 8 that the ETC, with a coverage factor of  $\sim 30$  hr-sterad per night of observing, should discover  $\sim 10^2$  flare stars per night with peak brightnesses of  $\sim +11$  magnitude. An extensive catalog of new flare stars with  $\sim 10^3$  to  $10^4$  entries (depending on the recurrence rate; Gurzadyan 1980) will thus be a byproduct of a 1 year ETC survey. In addition, there is also the important promise of serendipitous discovery of new classes of astronomical phenomena.

From the point of view of comparison with alternative search methods, it is interesting to consider the relative advantages of the ETC and the "Two Schmidt" Search method. The later method relies upon a "matched pair" of widely-separated Schmidt telescopes simultaneously observing the same patch of sky. It was first attempted by our group at MIT in 1982 (Ricker et al. 1982; Schaefer et al. 1983), using the Burrell Schmidt at Kitt Peak, Arizona, and the Curtis Schmidt at Cerro Tololo, Chile. Although no bursts were detected in a short (9 night) observing period, interesting upper limits to burst rates were obtained, and it is interesting to consider how well a dedicated pair of such telescopes would perform over an extended period. In Table 4, we have compared the ETC and the Schmidt Pair, in terms of the number of expected GRB-related flashes which might be detectable in a year's observing. A comparison for each of the three different source distribution models discussed in Section 1 is given. For each source distribution, the ETC expected rate exceeds that of the Schmidt Pair by a wide margin, ranging from  $\sim 10:1$  to  $\sim 300:1$ . Thus, for the "distance-limited" population model which the current gamma ray evidence seems to favor (Fishman 1983), more than 100 years of Schmidt Pair operation might be required to detect the same number of bursts which the ETC might detect in a single year.

To further evaluate the potential of the ETC as a means of investigating unexplored regions of astronomical "parameter space," it is interesting to consider the sensitivities of previously reported searches for optical flashes. In Figure 9, we display a compilation of previous work from Schaefer (1983). Since none of the searches to date have reported positive detections, only "3 $\sigma$ " upper limits for detected rates,  $R$ , are shown from the seven surveys as a function of apparent blue magnitude,  $m_b$  (a code number for each of the seven is given in the caption to the figure; search 2 refers to the "non GRB error box" field areas which Schaefer examined). For comparison, the rate sensitivity of a "null result" ETC search (i.e.,



3 $\sigma$  upper limit) is also shown (dashed line). Compared to the previous most sensitive search at faint magnitudes (Ricker et al. 1982; Schaefer et al. 1983), a one year survey with the ETC should be  $\sim 10^4$  times more sensitive.

### 3. Future Developments

Given the necessary resources, it should be possible to deploy a "full up" version of the ETC in 1985. Thus, it should be possible to obtain 1-2 years of observations prior to the launch of the Gamma Ray Observatory (GRO; scheduled in 1988). Positive detections of gamma-ray burst related optical flashes could well bear upon the scheduling of pointings for GRO.

Recently, attention has been drawn to the possible detectability of extragalactic gamma ray bursts from M31 by Jennings (1983), based on the contention that the sources in our Galaxy might have a characteristic halo distribution with a radius of  $\sim 100$  kpc. If we assume that the M31 halo sources have comparable  $L_{\text{opt}}/L_{\gamma}$  ratios to those in the Milky Way, then they should appear to be  $\sim 4.2$  magnitudes dimmer. Since for the ETC, the burst detecting sensitivity scales as  $A^{1/2} Q^{-1/2}$  ( $A$  = collecting area,  $Q$  = pixel solid angle), we could achieve the increased sensitivity by equipping each of its CCD cameras with a 75 mm f/1 lens, rather than with the 25 mm f/0.85 lenses currently used. Of course, this would reduce its field-of-view by a factor of 9, which would be inappropriate for "all sky" studies. Nonetheless, for dedicated studies of M31, only 4 such CCD cameras would provide coverage of the entire galaxy. Using the scaling relations developed in Section 1, we estimate that  $\sim 10$  flashes might be detected in a 4 month observing period. The promise of this observation is such that we are contemplating a devoted ETC observation in late 1984 or 1985.

On a longer time scale, it is interesting to consider the prospect of operating an ETC optical array and a gamma-ray burst detector on the same space-borne platform. We first proposed such a combined instrument in 1982, with the form shown schematically in Figure 10. The major advantage of such a configuration is that a combined instrument would permit investigation of detailed relations in time between the rise and fall of the gamma-ray and optical light for the very same burst. The wealth of physical information which can be obtained by such means has been amply demonstrated in simultaneous optical/X-ray observations of X-ray bursters (see e.g., Pedersen et al. 1982). For example, should an optical flash arise from the fluorescing of a companion object by the gamma ray burst, then the separation (in light-seconds) of the two objects is directly measured by the time delay from the GRB to the optical flash. Furthermore, "cross triggering" of the two instruments can be used to study gamma bursts which emit no optical light, and vice versa, at much lower thresholds than are practical for disconnected instruments. Finally, the optical array can provide much more accurate ( $\pm 10$  arc second) positions than can a single gamma ray instrument. In the future, such an optical transient detector might be appropriate for inclusion in an Explorer-class mission dedicated to studies of gamma ray bursts (such as the High Energy Transient Explorer [HETE]).

## 9. Acknowledgements

The authors gratefully acknowledge helpful discussions with many of their colleagues at the MIT Center for Space Research, including H. Bradt, H. Bridge, J. Binsack, C. Canizares, G. Clark, W. Lewin, and J. McClintock. At Texas Instruments, J. Freeman, H. Hosack and R. Jascott have expressed continuing interest in this effort. B. Schaefer, whose fundamental work established the possibility of a class of optical flash sources related to gamma ray bursters, was helpful in many ways; we especially appreciate his providing the material for two of the figures in this paper. We also thank T. Cline, B. Teegarden, and T. von Rosenvinge of the Goddard Space Flight Center for information relating to the Rapidly Moving Telescope (RMT). G. R. Ricker and J. P. Doty were Guest Observers at Mauna Kea Observatory when the ETC prototype testing was carried out. This work was supported in part by the National Aeronautics and Space Administration under Grant NSG-7339.

## 10. References

- Byrne, P. B. and Wayman, P. A., 1975, M.N.R.A.S., 173, 537.
- Dewey, D. and Ricker, G. R., 1980, in Applications of Digital Image Processing to Astronomy, S.P.I.E., 264, 42.
- Fishman, G. J., 1983, presentation at the Santa Cruz Summer Workshop on High Energy Transients.
- Gurzadyan, G. A., 1980, in Flare Stars, New York: Pergamon Press.
- Hewitt, A. and Burbidge, G., 1980, Ap. J. (Suppl.), 43, 57.
- Hurley, K., 1981, in Gamma Ray Transients and Related Astrophysical Phenomenon, eds. R. E. Lingenfeiter, Worrall, D. M., Hudson, H. S., New York: Am. Inst. Phys., 85.
- Hurley, K., 1983, presentation at the Santa Cruz Summer Workshop on High Energy Transients.
- Jennings, M. C., 1982, Ap. J., 258, 110.
- Jennings, M. C., 1983, presentation at the Santa Cruz Summer Workshop on High Energy Transients.
- Meyer, S. S. and Ricker, G. R., 1980, in Applications of Digital Image Processing to Astronomy, S.P.I.E., 264, 38.
- Pedersen, H. et al. (28 co-authors), 1982, Ap. J., 263, 340.
- Ricker, G. R., Bautz, M. W., Dewey, D. and Meyer, S. S., 1981 in Solid State Imagers for Astronomy, S.P.I.E., 290, 190.
- Ricker, G. R., Bradt, H. V., Schaefer, B. E. and Vanderspek, R. K., 1982, B.A.A.S., 14, 867.
- Schaefer, B., 1981, Nature, 294, 722.
- Schaefer, B. E. and Ricker, G. R., 1983, Nature, 302, 43.
- Schaefer, B. E., 1983, Ph.D. Dissertation, Department of Physics (MASSACHUSETTS INSTITUTE OF TECHNOLOGY).
- Schaefer, B. E., Vanderspek, R. K., Bradt, H. V., and Ricker, G. R., 1983 (submitted to Ap. J.).
- Smith, F. G., 1981, in Pulsars: 13 Years of Research on Neutron Stars, eds. W. Sieber and R. Wielebinski (IAU Symposium No. 95, Riedel: DORDRECHT), 221.
- Teegarden, B. J., Cline, T. L., and T. T. von Rosenvinge 1983, B.A.A.S., 14, 885.
- Tyson, J. A. and Jarvis, J. F. 1979, Ap. J. Lett., 230, L153.

## Appendix E

*Size of a Gamma Ray Burster Optical Emitting Region*, Schaefer, B.E.,  
Ricker, G.R., 1983, *Nature*, **302**, No. 5903, 43.



Restriction enzyme reinjection experiments, which linearize fully formed minichromosomes, would suggest that a linear molecule cannot maintain the chromatin conformation necessary for its assembly into a transcription complex. Whereas our experiments do not define the level at which a circular DNA molecule is recognized as different from a linear, the surprisingly large difference in transcription we have ob-

served suggests that the topology of a DNA molecule has a fundamental role in the transcription process.

This work was supported by grants from the NIH and an SERC/NATO fellowship to R.M.H. We thank R. Kingsbury for technical assistance, J. Burch and M. Dunaway for carefully reading the manuscript, and J. Mertz for communicating results prior to publication.

Received 8 November; accepted 3 December 1982.

1. Lilley, D. M. *J. Proc. natn. Acad. Sci. U.S.A.* **77**, 6468-6472 (1980).
2. Panavatos, N. & Wells, R. D. *Nature* **289**, 466-470 (1981).
3. Peck, L. J., Nordheim, A., Rich, A. & Wang, J. C. *Proc. natn. Acad. Sci. U.S.A.* **79**, 4560-4564 (1982).
4. Singleton, C. K., Klysik, J., Sturdivant, S. M. & Wells, R. D. *Nature* **299**, 312-316 (1982).
5. Beard, P., Morrow, J. F. & Berg, P. *J. Virol.* **12**, 1303-1313 (1973).
6. Larsen, A. & Weintraub, H. *Cell* **29**, 609-622 (1982).
7. Katinka, M., Vasseur, M., Montreau, N., Yaniv, M. & Blangy, D. *Nature* **290**, 720-722 (1981).
8. Nordheim, A. *et al.* *Nature* **294**, 417-422 (1981).
9. Benyajati, C. & Worcel, A. *Cell* **9**, 393-407 (1976).
10. Cook, P. R., Brazell, I. A. & Jost, E. *J. Cell Sci.* **22**, 303-324 (1976).
11. Gellert, M. A. *Rev. Biochem.* **50**, 879-910 (1981).
12. Wang, J. C. *Cell* **29**, 724-726 (1982).
13. Sinden, R. R., Carlson, J. & Pettijohn, D. E. *Cell* **21**, 773-783 (1980).

14. Gurdon, J. B. & Melton, D. A. *Rev. Genet.* **15**, 189-218 (1981).
15. Probst, E., Kressmann, A. & Birnstiel, M. L. *J. molec. Biol.* **135**, 709-732 (1979).
16. Wylie, A. H., Laskey, R. A., Finch, J. & Gurdon, J. B. *Dev. Biol.* **64**, 178-188 (1978).
17. McKnight, S. L. & Kingsbury, R. *Science* **217**, 316-324 (1982).
18. Miller, T. J. & Mertz, J. E. *Molec. cell. Biol.* **2**, 1595-1607 (1982).
19. McKnight, S. L., Gavis, E. R., Kingsbury, R. & Axel, R. *Cell* **25**, 385-398 (1981).
20. Reeder, R. H., Higashinakagawa, T. & Miller, O. *Cell* **8**, 449-454 (1976).
21. Cremisi, C., Pignatti, R. F. & Yaniv, M. *Biochem. biophys. Res. Commun.* **73**, 548 (1976).
22. Lee, D. C. & Roeder, R. G. *Molec. cell. Biol.* **1**, 635-651 (1981).
23. Berk, A. J. & Sharp, P. A. *Cell* **12**, 721-732 (1977).
24. Baker, C. C. & Ziff, E. B. *J. molec. Biol.* **149**, 189-221 (1981).
25. Gurdon, J. B. & Brown, D. D. *Dev. Biol.* **67**, 346-356 (1978).
26. Kressmann, A., Clarkson, S. G., Telford, J. L. & Birnstiel, M. L. *Cold Spring Harb. Symp. quant. Biol.* **42**, 1077-1082 (1978).
27. Mertz, J. E. *Molec. cell. Biol.* **2**, 1608-1618 (1982).
28. Wahl, C. M., Stern, M. & Stark, G. R. *Proc. natn. Acad. Sci. U.S.A.* **76**, 3683-3687 (1979).
29. McKnight, S. L. *Nucleic Acids Res.* **8**, 5949-5964 (1980).
30. Gingeras, T. R. *et al.* *J. biol. Chem.* **257**, 13475-13491 (1982).

## LETTERS TO NATURE

### Size of a $\gamma$ -ray burster optical emitting region

Bradley E. Schaefer & George R. Ricker

Department of Physics and Center for Space Research,  
Massachusetts Institute of Technology, Cambridge,  
Massachusetts 02139, USA

Most models of  $\gamma$ -ray bursters require the formation of a thermal plasma, whose properties are relatively insensitive to its mode of formation. Radiation at lower photon energies or during quiescence may be more diagnostic of the underlying cause of the  $\gamma$ -ray bursters. Searches for quiescent  $\gamma$ -ray bursters at low photon energies require an accurate position. Recently, three such accurate positions have been published<sup>1-3</sup> which have allowed X-ray<sup>1-2</sup>, optical<sup>3</sup>, IR<sup>10</sup> and radio<sup>11</sup> searches for the GRB counterpart. We present here new limits on the quiescent optical and IR flux of the 19 November 1978 burster<sup>2</sup>. We shall use the measurement of the optical flux during outburst<sup>3</sup> to place a lower limit on the size of the optical emitting region.

This measurement of the optical flux during outburst was made from a blue emulsion archival photographic plate exposed in 1928<sup>4</sup>. On this plate was an image that was presumably formed by optical radiation during a burst by the 19 November 1978  $\gamma$ -ray burster. The small (8 by 18 arc s) error box for the 1928 image allows for very deep searches for the quiescent optical counterpart.

We observed the region around the 1928 optical error box with the MASCOT CCD camera<sup>12</sup> on the McGraw-Hill 1.3-m telescope on the first two nights of November 1981. The bandpass used was defined by the UV cutoff of the CCD ( $\sim 3,700$  Å) and by an HA-11 filter ( $\sim 6,250$  Å) which is similar to a  $B+V$  magnitude system. The pixel size was 1.2 arc s which was smaller than the seeing disk due to the relatively large zenith angle for the observations. We obtained a total of 305 min of exposure. The telescope was shifted slightly between each exposure, and each frame was independently dark field subtracted and flattened. When the 21 frames were co-added, no image was visible above the  $2\sigma$  confidence level in or near the 1928 optical error box. This limit corresponds to 6.7 mag fainter than star number 11 of Fishman *et al.*<sup>6</sup> ( $m_v = 17.13$  mag,  $m_B - m_v = 1.64$

mag) in the 3,700-6,250 Å bandpass. The exact magnitude limit is uncertain due to a lack of measured comparison stars in the passband. Our procedure flattened a starless area of the sky to 0.3% (r.m.s.) of the background. (A  $\sim 23$  mag object appears in a position which is consistent with the polarized radio source 'B' which was reported by Hjellming and Ewald<sup>11</sup>.) For a reasonable upper limit on the distance of 1 kpc (ref. 13) (the burster is at high galactic latitude), the absolute magnitude of the system is fainter than roughly +15 in the bandpass used. With this limit, it is hard to see how any non-degenerate star can be in the burster system<sup>14</sup>.

M. H. Liller obtained deep  $B$  and  $V$  plates on the CTIO 4-m telescope on 1 October 1981, both of which appear to show a faint object at the same location within the 1928 optical error box<sup>8</sup>. These images were measured with a PDS microdensitometer; detections were at confidence levels of  $3.2\sigma$  and  $4.9\sigma$  above the grain noise for the  $B$  and  $V$  plates respectively. We have re-examined both of these plates after it was learned that they were exposed with a Racine wedge, which creates a secondary image for each star which is 6.8 mag fainter than the primary image. No star is positioned such that its secondary image will appear near the 1928 optical error box. The secondary images allow the magnitude sequence of Fishman *et al.*<sup>6</sup> to be extended to the plate limiting magnitude. The image on the  $B$  plate has an apparent magnitude of  $22.9 \pm 0.3$  mag, while the apparent magnitude on the  $V$  plate is  $21.5 \pm 0.4$  mag, which would indicate a red object. If the object on Liller's plate is real, then it must be highly variable ( $\Delta m \geq 2$ ). This variability would be strong evidence that the object is the true counterpart and not just a background star. However, when viewed by eye, these images do not inspire confidence in their reality. Hence, despite the low probability of two significant grain enhancements occurring in the same place (within 1 arc s) in a small error box, we prefer to think of the images on Liller's plates as possible detections.

On the night of 1-2 December 1981, C. Telesco and one of us (G.R.R.) examined the 19 November 1978 error region in the IR at 2.2  $\mu$ m. The InSb photometer on the Infrared Telescope Facility (IRTF) 3.0-m telescope was used. They searched to a  $K$  magnitude of 18.8 mag and found no object in the 1928 optical error box to the  $3\sigma$  level of confidence. Once again, for a reasonable upper limit on the distance of 1 kpc, we find  $M_K \geq 8.8$  mag; a faintness achieved by few stars<sup>15</sup>.

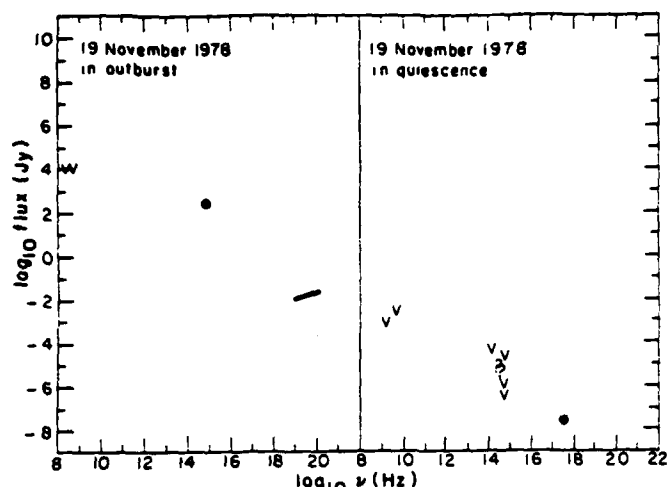


Fig. 1 Spectrum during outburst and quiescence of the 19 November 1978  $\gamma$ -ray burster. 'V' indicates an upper limit, while '?' indicates a possible detection. The outburst data have been collected from refs 8, 16, 17. The data for the quiescent  $\gamma$ -ray burster have been collected from refs 6, 8, 9, 11, 18 and this work.

From a variety of sources<sup>6,8,9,11,16-18</sup>, we have collected observations of the 19 November 1978 burster during both outburst and quiescence. For each observation, the measured flux has been plotted versus frequency in Fig. 1. Unfortunately, most of the observations are either upper limits or questionable detections.

If the  $\gamma$ -ray bursters have a high space density, then they would contribute significantly to the local invisible mass density. However, the  $\gamma$ -ray burster density cannot exceed Oort's upper limit on the local invisible mass density<sup>19</sup>. This fact can be used to limit the scale of distances to  $\gamma$ -ray bursters, or equivalently, to limit the average  $\gamma$ -ray burster luminosity:

$$\frac{Nm}{(4\pi D_0^3/3)} \leq 0.088 \frac{M_\odot}{\text{pc}^3} \quad (1)$$

The mass of an individual  $\gamma$ -ray burster is  $m$ .  $D_0$  is the average distance to a  $\gamma$ -ray burster which is observed with a fluence of  $S_0$ .  $N$  is the total number of  $\gamma$ -ray bursters inside a volume of radius  $D_0$ .  $N$  will be greater than the total number of observed  $\gamma$ -ray bursters with a fluence greater than  $S_0$  (this statement can be confirmed for any luminosity function and any reasonable distribution in space). With  $S_0$  equalling  $2 \times 10^{-4} \text{ erg cm}^{-2}$ , a literature search<sup>17,20-24</sup> reveals 17 bursts with a greater or equal  $\gamma$ -ray fluence. It is thought that the  $\gamma$ -ray burster phenomenon is related to neutron stars<sup>25,26</sup>, so that most probably  $m \geq 1.4 M_\odot$  (ref. 27). The mean  $\gamma$ -ray burster luminosity,  $L_0$ , is  $4\pi D_0^2 S_0$ . The distance  $D$  to a  $\gamma$ -ray burster with observed fluence  $S$  is given by

$$D = D_0 \left( \frac{S_0}{S} \right)^{1/2} \quad (2)$$

where  $L$  is the luminosity of that  $\gamma$ -ray burster in units of  $L_0$ . From equations (1) and (2) and the limits on  $N$  and  $m$ , the distance to the 19 November 1978  $\gamma$ -ray burster is constrained by

$$D \geq 3.2 \text{ pc}(L)^{1/2} \quad (3)$$

Similarly, the average  $\gamma$ -ray burster luminosity is constrained to be  $> 4 \times 10^{35} \text{ erg}$ .

With the assumption that the optical radiation from the 1928 flash is the result of a thermal process, we can derive a lower limit on the size of the optical emitting region. The observed optical fluence ( $f$ ) from the 1928 flash can be related to the

emittance ( $F$ ) on the surface of the optical emitting region by

$$\left( \frac{D}{R} \right)^2 \frac{f}{\Delta\lambda} = F \quad (4)$$

In equation (4),  $\Delta\lambda$  is the bandpass ( $9.8 \times 10^{-6} \text{ cm}$ ) and  $R$  is the radius of the optical emitting region. The optical flux  $f$  is observed<sup>8</sup> to be  $(4.2 \times 10^{-7} \text{ erg cm}^{-2})/t$ , where  $t$  is the duration of the optical flash. We do not know the value of  $F$ ; however, we know that it cannot exceed the Rayleigh-Jeans emittance provided that the optical light is being emitted by a thermal process:

$$F \leq \frac{c_1}{c_2} \frac{T}{\lambda^4} \quad (5)$$

$\lambda$  is  $4.4 \times 10^{-5} \text{ cm}$  and  $c_1/c_2$  equals  $2.60 \times 10^{-5} \text{ erg cm}^{-1} \text{ K}^{-1}$ .  $T$  is the temperature of the optical emitting region, which must be equal to or less than the temperature of the  $\gamma$ -ray emitting region. For the 1978 burst, Teegarden and Cline<sup>28</sup> found a  $\gamma$ -ray temperature of 500 keV ( $5.8 \times 10^9 \text{ K}$ ). The equality sign in equation (5) is valid when the optical light comes from a hot, optically thick region. With the limit on  $T$ , equation (5) becomes

$$F \leq 4.0 \times 10^{22} \text{ erg s}^{-1} \text{ cm}^{-2} \quad (6)$$

From equations (3), (4) and (6), we can place a lower limit on  $R$  of

$$R \geq 100 \text{ km}(L/t)^{1/2} \quad (7)$$

Equation (7) is based on the conservative distance limit from equation (3). If instead, a reasonable<sup>13</sup> distance of 100 pc is adopted, then the radius of the optical emitting region must be  $> 3,000 \text{ km } t^{-1/2}$ .

In a physical situation which may be similar to  $\gamma$ -ray bursters, the duration of optical flashes from X-ray bursters nearly equals the X-ray duration<sup>29</sup>. This leads us to believe that the  $\gamma$ -ray burster optical and  $\gamma$ -ray durations are similar<sup>30</sup> (the 1978 burst had a FWHM duration of 3 s in  $\gamma$ -ray energies). By further making the assumption that  $L \sim 1$ , we deduce that the size of the optical emitting region is more than an order of magnitude larger than that of a neutron star. This is a conservative lower limit, because for the equality in equation (7) to hold, the entire local invisible mass must be composed of  $\gamma$ -ray bursters and  $kT$  of the optical emitting region must be  $\sim 500 \text{ keV}$ . Another way of stating this result is that the  $\gamma$ -ray emitting region is evidently too small to emit the observed optical flux. This suggests that the optical flux comes from elsewhere in the system, perhaps from an accretion disk or a companion star. Any such system component must satisfy the severe optical and IR limits on the absolute magnitude which were reported above. The presence of an accretion disk or a companion star would suggest that the energy source for the 19 November 1978 burster is not inside the neutron star.

We thank Drs M. H. Liller and J. E. McClintock for relinquishing observing time at short notice and Drs H. V. Bradt and P. C. Joss for helpful discussions. This work was supported in part by NASA grant NSG-7643 and NSF grant AST-8214569. G.R.R. is a visiting astronomer to the Infrared Telescope Facility.

Received 2 August; accepted 17 December 1982.

1. Laros, J. G. *et al.* *Astrophys. J. Lett.* **248**, L63-66 (1981).
2. Evans, W. D. *et al.* *Astrophys. J. Lett.* **237**, L7-9 (1980).
3. Cline, T. L. *et al.* *Astrophys. J. Lett.* **246**, L133-136 (1981).
4. Pizzichini, G. *et al.* *Space Sci. Rev.* **30**, 467-470 (1981).
5. Helfand, D. J. & Long, K. S. *Nature* **282**, 589-591 (1979).
6. Fishman, G. J., Duthie, J. G. & Dufour, R. J. *Astrophys. Space Sci.* **78**, 135-143 (1981).
7. Chevalier, C. *et al.* *The Messenger* No. 24, 11-12 (1981).
8. Schaefer, B. E. *Nature* **294**, 722-724 (1981).
9. Peterson, H. *et al.* *IAU Circ.* No. 3711 (1982).
10. Apparo, K. M. V. & Allen, D. *Astr. Astrophys.* **107**, L5-6 (1982).
11. Hjellming, R. M. & Ewald, S. P. *Astrophys. J. Lett.* **246**, L137-140 (1981).
12. Ricker, G. R. *et al.* *Solid State Imagers for Astronomy* (eds Geary, J. & Latham, D.) 190 (SPIE 290, Bellingham, Washington, 1981).
13. Jennings, M. C. & White, R. S. *Astrophys. J.* **238**, 110-121 (1980).
14. Liebert, J., Lebofsky, M. J. & Rieke, G. H. *Astrophys. J. Lett.* **246**, L73-76 (1981).
15. Reid, I. N. & Gilmore, G. *Mon. Not. R. Astr. Soc.* **196**, 15-19P (1981).
16. Inzani, P. *et al.* *Gamma Ray Transients and Related Astrophysical Phenomena* (eds Lingenfelter, R. E., Hudson, H. S. & Worrall, D. M.) 79 (American Institute of Physics, New York, 1982).

17. Mazets, E. P. et al. *Astrophys. Space Sci.* **80**, 3-83 (1981).
18. Grindlay, J. et al. *Nature* **300**, 730-731 (1982).
19. Spitzer, L. *Physical Processes in the Interstellar Medium* (Wiley, New York, 1978).
20. Mazets, E. P. et al. *Astrophys. Space Sci.* **80**, 85-117 (1981).
21. Mazets, E. P. et al. *Astrophys. Space Sci.* **80**, 119-143 (1981).
22. Metzger, A. E. et al. *Astrophys. J. Lett.* **194**, L19-25 (1974).
23. Klebesadel, R. W. & Strong, I. B. *Astrophys. Space Sci.* **42**, 3-15 (1976).
24. Cline, T. L. & Desai, U. D. *Astrophys. Space Sci.* **42**, 17-27 (1976).
25. Mazets, E. P. & Golenetskii, S. V. *Astrophys. Space Sci.* **75**, 47-81 (1981).
26. Lamb, D. Q. *Gamma Ray Transients and Related Astrophysical Phenomena* (eds Lingener, R. E., Hudson, H. S. & Worrall, D. M.) 249 (American Institute of Physics, New York, 1982).
27. Arnett, W. D. & Bowers, R. L. *Astrophys. J. Suppl.* **33**, 415-436 (1977).
28. Teegarden, B. J. & Cline, T. L. *Astrophys. J. Lett.* **236**, L67-70 (1970).
29. Lewin, W. H. G. & Joss, P. C. *Space Sci. Rev.* **28**, 3-87 (1981).
30. London, R. A. & Cominsky, L. R. *Bull. Am. Astr. Soc.* **14**, 667 (1982).

## First detection of radio emission from a dwarf nova

A. O. Benz\*, E. Fürst† & A. L. Kiplinger‡

\* Institut of Astronomy, ETH, Zurich, Switzerland

† Max-Planck-Institut für Radioastronomie, Bonn, FRG

‡ Applied Research Corp., Landover, MD and NASA/Goddard Space Flight Center, Greenbelt, Maryland 20771, USA

The dwarf novae represent a class of cataclysmic variable stars that typically exhibit random optical outbursts of 2-6 mag with mean outburst periods of 10-150 days. Dwarf novae are close binary systems composed of a late-type star which fills its critical Roche lobe and a white dwarf companion. The white dwarf is surrounded by a luminous accretion disk sustained by mass transfer from the late-type star. The disk is the seat of the eruptions. Although radiation has been detected from dwarf novae from IR through X-ray energies, radio emission has never been reported from these objects. We describe here a search for radio emission at 4.75 GHz from dwarf novae that has been carried out with the 100-m telescope at Effelsberg, West Germany. We have searched for radio emission from six dwarf novae and a source was discovered at the position of SU UMa. The source could only be detected during optical outbursts and was below the threshold during quiescence. We suggest here that the radio emission arises from a non-thermal process.

SU UMa was observed with a double horn receiver system. System parameters and times of observation are listed in Table 1. The observations consist of scans in elevation, 15 arc min long, that are centred on the optical position of SU UMa, with the offset horn situated 8 arc min east. In fair weather conditions, effects of clouds are mostly cancelled out with the double horn system, but the scans suffer from source confusion by neighbouring sources. At the galactic latitude of SU UMa (+30°) most confusion sources can be expected to be of extragalactic origin. Source counts<sup>1</sup> near 5 GHz suggest a probability of  $16 \pm 9\%$  for finding a source stronger than 1 mJy in the Effelsberg beam. To smooth the effects of source confusion we scanned the optical position with different parallactic angles. Due to the sidereal time periods available for observation, the directions of the scans varied by  $\pm 35^\circ$  with respect to the celestial meridian. After rejecting poor scans obtained in unacceptable weather, 123 scans of SU UMa were found to be suitable for further analysis.

Each scan consists of thirty-one 3-s integrations separated by 30 arc s. A linear baseline was subtracted from all scans by using a mean of eleven data points at both ends of the scans. This subtraction would be expected to fail if strong confusion sources exist; however, inspections of the individual scans do not show such sources around SU UMa. The scans were then combined by averaging data points as a function of distance from the optical position, thus minimizing source confusion.

The average flux per beam position as a function of distance from SU UMa is shown in Fig. 1. For comparison the measured antenna response of a point source is also given. A source was detected at the optical position with a flux corresponding to

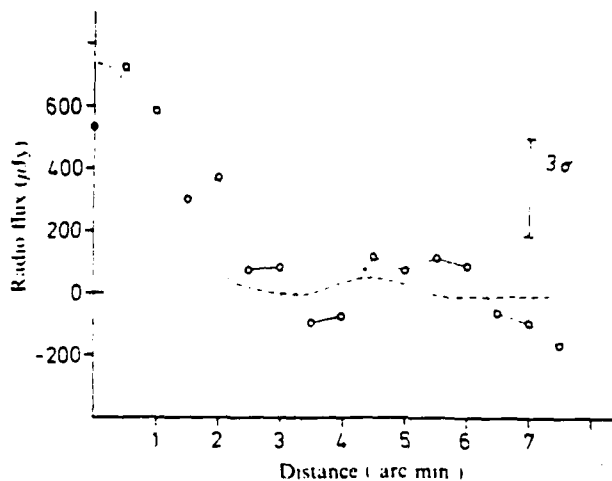


Fig. 1 Radio flux plotted against distance from optical source SU UMa. The antenna response of a point source (3C84) is shown for comparison.

Table 1 System parameters and observing periods

Frequency	4.75 GHz
System temperature	65 K
Bandwidth	600 MHz
Half power beam width	2.4 arc min
Observing periods (1982)	
22-23 April	Outburst (decline)
13 June	Outburst (decline)
25-27 June	Quiescence

about 6 s.d. of the background noise at distance 3 arc min from SU UMa. The noise is close to the expected level from the receiver. Background sources seem to be weak and effectively smoothed out. The field is apparently not rich in extragalactic sources. The half power width of the detected source is close to the actual beam size. No corresponding peak in the polarized intensity could be detected, suggesting that linear polarization is  $< 30\%$ .

In a second analysis we divided the observations according to the optical activity of SU UMa. The first two observing periods were obtained 1 or 2 days after the peak of optical brightness as determined from the visual light curve of SU UMa supplied by the American Association of Variable Star Observers (AAVSO). Similar to Fig. 1, Fig. 2 shows two radial intensity profiles of SU UMa corresponding to the outburst and quiescence observations. Although the noise properties at distances beyond 2 arc min are comparable during the two states, a peak flux of 1.3 mJy is found at the position of SU UMa only during outburst. The probability of a chance coincidence with a source of 1.3 mJy or more is about 10%. However, the radio flux dependence on optical activity suggested by Fig. 2 strongly supports the idea that the detected emission during peak optical brightness can be attributed to SU UMa.

X-ray observations of SU UMa in quiescence<sup>2</sup> yield an emission measure of  $7.6 \times 10^{54} \text{ cm}^{-3}$  in the 0.1-4.5 keV band assuming a temperature of  $10^8 \text{ K}$  and a distance of 220 pc (ref. 3). Independently of whether this hot plasma is optically thick or thin to radio waves, the estimated free-free emission turns out to be more than 3 orders of magnitude lower than the observed flux. Alternatively, the mass loss observed in UV lines of dwarf novae in outburst may be expected to emit free-free emission at a temperature of a few  $10^4 \text{ K}$ . The radio flux was calculated following the derivation of ref. 4. For an outflow velocity of  $3,000 \text{ km s}^{-1}$  and a mass loss rate of  $10^{-11} M_\odot \text{ yr}^{-1}$  observed in similar systems<sup>5</sup>, the calculated flux is 7 orders of magnitude below the observed value. It is therefore more reasonable to propose suprathermal electrons as the origin of the radio emission of SU UMa.

## Appendix F

*A Search for High Proper Motion Objects in Two Gamma-Ray Burst Error Regions*, Ricker, G. R., Vanderspek, R. K., and Ajhar, E. A. 1986, *Adv. Space Res.*, 6, 75.

# A SEARCH FOR HIGH PROPER MOTION OBJECTS IN TWO $\gamma$ -RAY BURST ERROR REGIONS

George R. Ricker,\*\* Roland K. Vanderspek\*\* and Edward A. Ajhar\*

\*Department of Physics and Center for Space Research, Massachusetts Institute of Technology, MA, U.S.A

\*\*Visiting Astronomer, Kitt Peak National Observatory, National Optical Astronomy Observatories, which is operated by the Association of Universities for Research in Astronomy, Incorporated under contract with the National Science Foundation

## ABSTRACT

Deep optical images of small  $\gamma$ -ray burst error regions have generally resulted in the detection of several faint ( $m_v \approx 22$ ) sources in each error region. It may be possible to identify the neutron star source of a GRB on the basis of a high transverse peculiar velocity if the source is at moderate distance ( $\sim 100$  pc). We report the results of searches for high proper motion objects in the error regions of GBS1412+78 (13 June 1979 /1,14/) and GBS2251-02 (5 November 1979 /2/).

## INTRODUCTION

The identification of a quiescent counterpart to most  $\gamma$ -ray bursts (GRBs) is difficult because of their large error regions (typically measured in square degrees). Deep optical surveys of  $\sim 10$  small GRB error regions have generally revealed several objects of  $m_v \approx 20 - 23$  in each error region /3,4,5,6,7,8/. Further measurements of the color and variability of the detected objects have failed to resolve the ambiguity in the identification of the quiescent GRB source.

In the work discussed here, we pursue an alternative method of identifying possible candidates for the optical counterpart of a quiescent GRB source. Because (1) GRBs are widely believed to originate at or near the surface of a neutron star /9/, and (2) neutron stars have been seen to have high peculiar velocities (100 - 300 km/s), it may be possible to locate a quiescent GRB source by detecting its proper motion if the source is nearby. A neutron star at a distance of 100 pc with a transverse velocity of 300 km/s will have a proper motion of  $\sim 0.6''/\text{year}$ . Such large proper motions should be measureable using images taken at epochs separated by just a few years.

The high proper motion  $\mu$  of an object suggests the following about the source's distance  $d$  and burst energy  $E$ :

$$d = 100 \text{ pc} \left( \frac{v}{100 \text{ km s}^{-1}} \right) \left( \frac{\mu}{0.2'' \text{ year}^{-1}} \right)^{-1} \quad (1)$$

$$E = 1.2 \times 10^{36} \text{ erg} \left( \frac{d}{100 \text{ pc}} \right)^2 \left( \frac{f}{10^{-6} \text{ erg cm}^{-2}} \right), \quad (2)$$

where  $v$  is the transverse velocity of the source and  $f$  is the fluence of the burst.

We report here the results of a search for objects with high proper motions in the error regions of two GRBs -- GBS1412+78 and GBS2251-02. The error region of GBS1412+78 was chosen because of its burst duration, which was one of the shortest ever detected ( $\sim 48$  ms /3/); its fast rise and fall times ( $\sim 2$  ms); and the small size of its error region ( $\sim 0.5 \text{ arcmin}^2$  -- the second smallest error box known). The error region of GBS2251-02 was selected because it is one of the three archival optical flash sources reported /13/ and because its error circle would only extend to about a  $90''$  radius with a proper motion of  $\sim 1''/\text{year}$ . Based on the work reported here, no objects in the error region of GBS1412+78 over a baseline of 2.4 years show a proper motion greater than  $0.6''/\text{year}$ . Similarly, our search of the error box associated with the optical transient detected in the error region of GBS2251-02 reveals no objects with a proper motion of greater than  $0.9''/\text{year}$ .

## OBSERVATIONS

Deep images of the error regions of GBS1412+78 and GBS2251-02 were made with MIT's MASCOT instrument /10,11,12/ in September 1983 on the 4m telescope at Kitt Peak and in October 1985 and February 1986 on the 1.3m telescope at the McGraw-Hill Observatory, located on Kitt Peak and operated jointly by the University of Michigan, Dartmouth College, and the Massachusetts Institute of Technology. Observations were made through Mould R filters at both epochs. The error regions of both GRBs are displayed in Figures 1 and 2.

The entire area shown in Figure 1 surrounding the error region of GBS1412+78 was searched for objects with high proper motion. In Figure 2, part of the GRB error region of GBS2251-02 is shown. Since the 99% level-of-confidence error region of GBS2251-02 was too large for a reasonable search, only the region surrounding the error box associated with the optical transient

discovered by Schaefer *et al.* /13/ was analyzed for high proper motion objects. As shown in Figure 2, the area searched includes the optical error box and most of a circular region  $84''$  in radius. This circular region delimits the area in which the source of the optical transient discovered by Schaefer would be found if it had a proper motion of  $1''/\text{year}$ .

#### PROCEDURE

Each CCD image was bias-subtracted and flattened in a standard fashion. The magnitude limit for the detection of an object at a  $3\sigma$  level-of-confidence was  $m_{\lambda} \approx 22.5$  in 1983 and  $m_{\lambda} \approx 22.5$  in 1985 and 1986.

The boundaries of the error regions of the two GRBs were determined from the coordinates cited in the discovery papers /1,2,14/. The astrometry of each CCD image was calibrated by calculating the coordinates of the 20 to 40 stars in the CCD image which are also visible on the Palomar Sky Survey plate of the region. A least-squares fit of a linear mapping of the coordinates of these stars to their positions on the CCD image allowed the calculation of the coordinates of any location on the CCD image to a precision of  $\sim 0.5''$  ( $1\sigma$ ). The position of the corners of the error region were calculated from this linear mapping on the CCD image.

The CCD images of each error region were scanned for objects above the detection threshold. Two CCD images of the same error region from two different epochs were then analyzed for proper motion by calculating the difference in relative positions of the detected objects between the two epochs. The positions  $(x_A, y_A)$  in epoch A of each detected object was mapped onto a quadratic function of the position  $(x_B, y_B)$  of the object in epoch B.

$$x_A = a_1 + b_1 x_B + c_1 y_B + d_1 x_B^2 + e_1 x_B y_B + f_1 y_B^2 \quad (3)$$

$$y_A = a_2 + b_2 x_B + c_2 y_B + d_2 x_B^2 + e_2 x_B y_B + f_2 y_B^2 \quad (4)$$

This mapping takes into account most standard sources of distortion (*e.g.*, field rotation, differential precession, optical distortion,

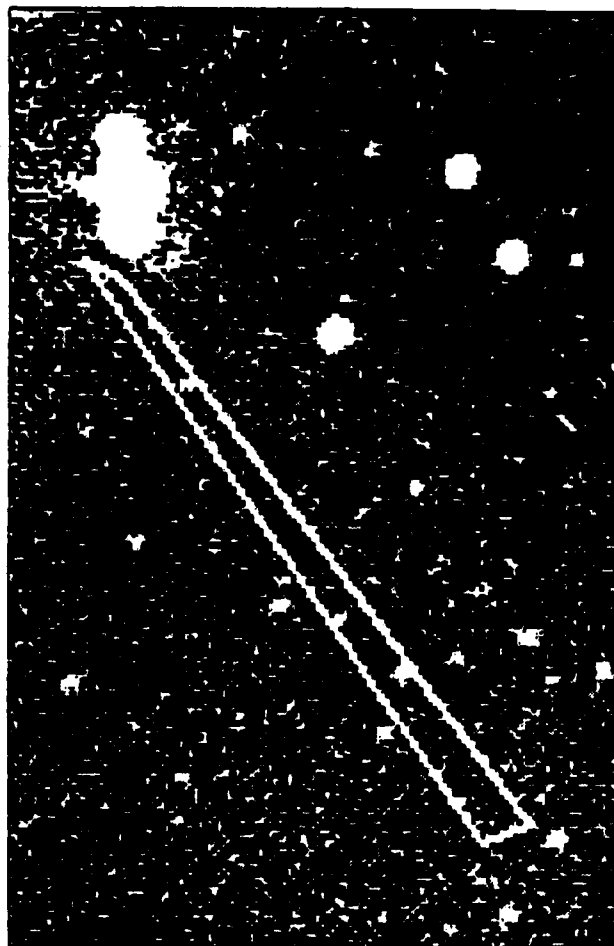


Fig. 1. The quadrilateral indicates the error box of GBS1412+78/U. The entire area shown was searched for high proper motion objects. This image was taken in February of 1986.

etc.). The parameters of the mapping were calculated from the positions of the detected objects using a least-squares fit. Any object showing a high residual to the fit was considered a candidate for having high proper motion. The candidate was then removed from the fit, and the fit and the rms error of the fit were recalculated. If the candidate's predicted position (based on the recalculated parameters) then differed from its measured position by more than three times the rms error of the fit and the image of the candidate object had a profile consistent with a single point source, it was considered to have high proper motion.

### DISCUSSION

The GRB error region of GBS1412+78 and the optical error region of GBS2251-02 were searched for objects with high proper motion using the procedure described above. A significant area surrounding each error region was also searched since an object with high proper motion may have moved out of the error region in the time since the GRB (or optical flash). The entire area surrounding the error region of GBS1412+78 shown in Figure 1 was searched, and the positions and R magnitudes of the objects found within the box are reported in Table 1. The area around the optical error box of GBS2251-02 which was searched is indicated by the large rectangle in Figure 2. The positions and R magnitudes of the objects checked for proper motion are given in Table 2.

No objects in either GRB field were detected to have a proper motion higher than the  $3\sigma$  limit described above. The lower limit on the proper motion of any detected object in the region surrounding GBS1412+78 is  $0.''6/\text{year}$ ; near the optical error box in GBS2251-02, the lower limit is  $0.''9/\text{year}$ .

The absence of a detection of an object with high proper motion does not introduce constraints on any models of GRB source localization or distribution since the source of the GRB is not required *a priori* to have any transverse velocity. However, if we assume that one of the detected sources in each error region is a neutron star with a transverse velocity of 300 km/s, minimum source distances of 105 pc and 70 pc can be calculated for GBS1412+78 and GBS2251-02, respectively.



Fig. 2. The small rectangle is the error region given by Schaefer /13/ for the archival optical transient of GBS2251-02. The large rectangle is the region searched for high proper motion objects. The circle delimits the area in which an object found in Schaefer's error region with a proper motion of  $1''/\text{year}$  would have moved since the archival plate was taken. The remaining lines, which extend below the figure shown, represent a portion of the 90% level-of-confidence error region. This image was taken in October of 1985.

TABLE 1 Objects in the GBS1412+78 Error Box

Object	R. A. (1950) ( $\pm 0.2s$ )	Dec. (1950) ( $\pm 0.5$ )	$m_R$ ( $\pm 0.4$ )
A	14h 12m 19.9s	78° 54' 27."1	19.9
B	16.9s	54' 31."0	21.7
C	17.9s	54' 44."7	19.5
D	24.6s	55' 01."0	20.6
E	30.0s	55' 13."1	20.7
F	30.0s	55' 34."2	21.5
G	40.3s	56' 11."4	19.9
H	44.1s	56' 22."4	22.0
I	37.1s	55' 53."1	22.4

TABLE 2 Objects Analyzed for High Proper Motion near the Archival Optical Transient Associated with GBS2251-02

Object	R. A. (1950) ( $\pm 0.04s$ )	Dec. (1950) ( $\pm 0.6$ )	$m_R$ ( $\pm 0.5$ )
A	22h 51m 44.91s	-2° 30' 57."3	—
B	36.80s	31' 01."2	21.1
C	43.53s	31' 20."7	20.6
D	40.62s	31' 22."0	17.4
E	36.31s	31' 25."1	20.7
F	38.70s	31' 56."8	16.1
G	39.45s	32' 06."5	19.4
H	44.58s	32' 29."4	19.7

## ACKNOWLEDGEMENT

This research was supported in part by the National Aeronautics and Space Administration under grant NSG-7339.

## REFERENCES

1. C. Barat, K. Hurley, M. Niel, G. Vedrenne, W.D. Evans, E.E. Fenimore, R.W. Klebesadel, J.G. Laros, T.L. Cline, I.V. Estulin, V.M. Zenchenko, and V.G. Kurt, "Time History, Energy Spectrum, and Localization of an Unusual Gamma-Ray Burst," *Ap. J.* 280, 150 (1984)
2. T.L. Cline, U.D. Desai, B.J. Teegarden, C. Barat, K. Hurley, M. Niel, G. Vedrenne, W.D. Evans, R.W. Klebesadel, J.G. Laros, I.V. Estulin, A.V. Kuznetsov, V.M. Zenchenko, V.G. Kurt, and B.E. Schaefer, "Three Precise Gamma-Ray Burst Source Locations," *Ap. J. (Letters)* 286, L15 (1984)
3. C. Barat, K. Hurley, M. Niel, G. Vedrenne, T. Cline, U. Desai, B. Schaefer, B. Teegarden, W.D. Evans, E.E. Fenimore, R. Klebesadel, J.G. Laros, I.V. Estulin, V.M. Zenchenko, A.V. Kuznetsov, V.G. Kurt, S. Ilovaisky, and C. Motch, "1979 January 13: An Intense Gamma-Ray Burst with a Possible Associated Optical Transient," *Ap. J. (Letters)* 286, L5 (1984)
4. C. Chevalier, S.A. Ilovaisky, C. Motch, C. Barat, K. Hurley, M. Niel, G. Vedrenne, J.G. Laros, W.D. Evans, E.E. Fenimore, R.W. Klebesadel, I.V. Estulin, and V.M. Zenchenko, "A Deep Optical Search of the 1979 April 6 Gamma-ray Burst Error Box," *Astron. Astrophys.* 100, L1 (1981)
5. G.J. Fishman, J.G. Duthie, and R.J. Dufour, "Optical Studies of the Regions of the Gamma-Ray Bursts of 19 November, 1978 and 5 March, 1979," *Astrophys. Sp. Sci.* 75, 135 (1981)
6. J.G. Laros, W.D. Evans, E.E. Fenimore, R.W. Klebesadel, C. Barat, K. Hurley, M. Niel, G. Vedrenne, I.V. Estulin, V.M. Zenchenko, and G.A. Mersov, "Location of the 1979 April 6 Gamma-Ray Burst," *Ap. J. (Letters)* 245, L63 (1981)
7. H. Pedersen, C. Motch, M. Tarengi, J. Danziger, G. Pizzichini, and W.H.G. Lewin, "Optical Candidates for the 1978 November 19 Gamma-Ray Burst Source," *Ap. J. (Letters)* 270, L43 (1983)
8. B.E. Schaefer, P. Seitzer, and H.V. Bradt, "Candidates for a Gamma-Ray Burst Optical Counterpart," *Ap. J. (Letters)* 270, L49 (1983)
9. D.Q. Lamb, "Surface and Magnetospheric Physics of Neutron Stars and Gamma-Ray Bursts," in: *Gamma Ray Transients and Related Astrophysical Phenomena*, Proc. AIP Conference No. 77, p. 249 (1981)
10. S.S. Meyer and G.R. Ricker, "A dual charge-coupled device (CCD), astronomical spectrometer and direct imaging camera: I. Optical and detector systems," in: *Applications of Digital Image Processing to Astronomy*, SPIE Vol. 264, p. 38 (1980)
11. D. Dewey and G.R. Ricker, "Dual charge-coupled device (CCD), astronomical spectrometer and direct imaging camera: II. Data handling and control systems," in: *Applications of Digital Image Processing to Astronomy*, SPIE Vol. 264, p. 42 (1980)
12. G.R. Ricker, M.W. Bautz, D. Dewey, and S.S. Meyer, "Optical Studies of X-ray Sources with the MASCOT -- a charge-coupled device (CCD)-based astronomical instrument," in: *Solid State Images in Astronomy*, SPIE Vol. 290, p. 190 (1981)
13. B.E. Schaefer, H.V. Bradt, C. Barat, K. Hurley, M. Niel, G. Vedrenne, T.L. Cline, U. Desai, B.J. Teegarden, W.D. Evans, E.E. Fenimore, R.W. Klebesadel, J.G. Laros, I.V. Estulin, and A.V. Kuznetsov, "Two Probable Optical Flashes from Gamma-Ray Bursters," *Ap. J. (Letters)* 286, L1 (1984)
14. Erratum to /1/, *Ap. J.* 299, 1079 (1985)



## Appendix G

*A Search for Optical Flashes from the 'Perseus Flasher' , 1986,  
Vanderspek, R.K., Ricker, G.R., and Zachary, D.S., Adv. Space Res., 6,  
No.4, 69.*

## A SEARCH FOR OPTICAL FLASHES FROM THE "PERSEUS FLASHER"

Roland K. Vanderspek, Daniel S. Zachary and  
George R. Ricker

*Department of Physics and Center for Space Research, Massachusetts  
Institute of Technology, MA, U.S.A.*

### ABSTRACT

We report the results of an extended search for short-timescale optical flashes from a four square-degree area centered on the coordinates of the Perseus Flasher, a phenomenon photographed by Katz, et al. /1/. The photographed optical flash was of brightness  $m_v = -1.7$  and had a duration of roughly 0.5 s. In 70 hours of observation with the Explosive Transient Camera /2,3,4/ no celestial optical flashes were detected in the region of the Perseus Flasher to a limiting magnitude of 7.1 for a one-second flash. On 5 February 1986, simultaneous observations with the ETC and the EXOSAT satellite /16/ were carried out. Neither X-ray nor optical flashes were seen. A survey of archived photographic images of the Perseus Flasher revealed no optical transients in over 700 hours of total exposure time to a limiting magnitude of  $m_v \approx 4.5$  for a one-second flash /15/. Based on the ETC data base, we discuss possible terrestrial sources of optical flashes which might account for the phenomenon reported by Katz et al.

### INTRODUCTION

In 1985, a group of Canadian amateur astronomers reported visual sightings of 13 short (duration  $\approx 1$  s) optical flashes from a small region of the sky near the Perseus-Aries border /5/. The subsequent publication of a photograph of an optical flash in the constellation of Perseus later that year generated considerable interest /6/. The photograph showed an optical transient of peak magnitude  $m_v = -1.7$  and a duration less than 13 seconds; visual detection of the flash by the photographer indicated a duration  $< 0.5$  seconds. *A posteriori* calculations show that the coordinates of the photographed flash lie within the error circles of 17 of 20 optical flashes detected by the Canadian group since October, 1984; 7 flashes have  $m_v \leq 2$ . The significance of these detections by experienced observers merits serious consideration of these events.

The discovery of Schaefer /7/ of transient optical radiation in a gamma-ray burst (GRB) error region has made clear that short (duration  $< 1$  s), bright ( $m_v < 10$ ) optical flashes could be associated with GRBs (see /8,9/). Pedersen, et al. /10/ have reported the detection of three optical transients of  $m_v = +6$  to  $+8$  and duration  $< 0.5$  seconds in 910 hours of photoelectric monitoring of a GRB error region. The coordinates of the photographed flash lie in the error region of three known gamma-ray bursts (GB781006b, GB721218, GB730721; /11,12/). However, as the error regions of these three GRBs are rather large (2400, 300 and 4400 square degrees, respectively), the overlap is probably coincidental. If the numerous recurrences of the Perseus Flasher were associated with GRBs and they were to satisfy the relation for the ratio of  $\gamma$ -ray to optical fluence of  $S_\gamma/S_{opt} \approx 10^3$  from Schaefer, et al. /20/, then the GRB associated with the photographed flash should have had  $S_\gamma \approx 10^2$  erg  $\text{cm}^{-2}$ . Such GRBs could have been detected by such network spacecraft as PVO and ISEE-3 /13/. As both of these spacecraft would have detected bursts of flux  $> 10^{-6}$  erg  $\text{cm}^{-2} \text{ s}^{-1}$ , the fact that no associated GRB was detected /14/ yields estimates of  $S_\gamma/S_{opt} \leq 10^1$ .

Since the publication of the photograph of the Perseus Flasher /6/, several investigations of the Perseus Flasher phenomenon have been made. A. Zytow /15/ has searched for optical flashes in archived photographic images of the Perseus Flasher error region. In the roughly 1700 hours of total exposure time in this survey, no optical transients were discovered. The complete survey was sensitive to a one-second flashes of  $m_v \leq -0.5$ ; a subset of the survey covering about 700 hours of total exposure time was sensitive to one-second flashes of  $m_v \leq 4.5$ . The error region of the Perseus Flasher has been examined in two  $10^4$  second exposures with EXOSAT /16/: no X-ray source of flux  $> 10^{-13}$  erg  $\text{cm}^{-2} \text{ s}^{-1}$  was detected. (The analysis of the EXOSAT data did not account for the effects of interstellar absorption, so the actual flux limit may be higher). Deep optical images of the Perseus Flasher taken at the McGraw-Hill Observatory, which is located on Kitt Peak and is operated jointly by the University of Michigan, Dartmouth College, and the Massachusetts Institute of Technology, reveal more than 30 optical images of  $m_v \geq 17$  in the error box of the photographed flash.

We report here the results of a real-time search for optical flashes from the Perseus Flasher with the Explosive Transient Camera /2,3,4/. No positive detections of optical flashes of  $m_v < 7.1$  (for one-second optical bursts) were made in 69.9 hours of observation of a four square degree area centered on the Perseus Flasher error region. The resulting  $3\sigma$  Poisson upper limit (estimated according to the method of Gehrels (1986) /17/) on the rate of flashes from the Perseus Flasher region of  $0.09 \text{ hr}^{-1}$  is barely consistent with the rate of flashes detected visually flashes by Katz, et al. ( $0.07 \text{ hr}^{-1}$ ). We discuss the possibility that the observed flashes in Perseus are due to a near-Earth phenomenon, such as a satellite (or other orbiting debris) or meteor.

### OBSERVATIONS

Observations of the Perseus Flasher error region were made with the Explosive Transient Camera (ETC) on Kitt Peak in October and November, 1985 and February, 1986. For the observations of the Perseus Flasher, the ETC's CCD cameras were outfitted with 75 mm lenses (in October) or 50 mm lenses (in November and February), giving each camera a field-of-view of  $5^\circ \times 7^\circ$  or  $7^\circ \times 10^\circ$ , respectively. Each lens was fitted with a standard Mould V filter. The exposure time was set at 5.0 seconds, resulting in a  $10\sigma$  sensitivity to image detection of  $m_v \approx 9.5$ . During observations, the fields-of-view of both cameras were roughly centered on the coordinates of the photographed flash in Perseus. In October, a  $2^\circ \times 2^\circ$  region centered on the photographed flash's

coordinates were monitored; in November and February, 35 square degrees were covered, including the four square degrees centered on the Perseus Flasher.

A total of 69.9 hours of observations of the Perseus Flasher were made, including 39.7 hours in October, 29.4 hours in November and 0.8 hours in February. (The 0.8 hours of observations in February were made during one of two  $10^4$  second exposures of the Perseus Flasher region by EXOSAT). The observations resulted in no positive detections of an optical flash from the location of the photographed flash. No visual detections of an optical flash from the Perseus Flasher region were reported during the ETC observations.

Because of a saturation-related effect in the CCD amplification and digitization electronics, it is possible that extremely bright flashes may not be detected by the ETC. The CCD signal processing electronics can return a value of zero, instead of the standard maximum value of 4095, if a pixel has been exposed to a very high light level. This effect is significant for 0.5 second flashes of  $m_v \approx 0-1$ . In such cases, the stellar image would have a valley where its peak should be, and the brightest part of the image would be the wings of the image. Although the center of the image would not trigger a flash, the wings would, and so the flash would still be detected as an event in a single camera. However, because of asymmetries in image profiles in the two cameras, it is possible that the brightest points in the two images could not be recognized as coming from the same celestial coordinates, and the event would not be recognized.

### DISCUSSION

The observations of the Perseus Flasher error region with the ETC do not confirm the existence of optical flashes from the Perseus Flasher. This null result implies a  $3\sigma$  Poisson upper limit on the rate of optical flashes from the Perseus Flasher error region of 0.09 per hour of observations at a sensitivity of  $m_v \approx 8$  for a one-second flash. This upper limit is included, along with flash rates taken from Katz, et al. /1/, in a plot of the rate of flashes of  $m \leq m_v$  versus  $m_v$  in Figure 1. The sensitivity of the ETC to one-second flashes is indicated by the cutoff in the upper limit curve at  $m_v \approx 8$ . The magnitude at which a one-second flash will saturate the CCD is indicated by the cutoff of the curve at  $m_v \approx 2$ .

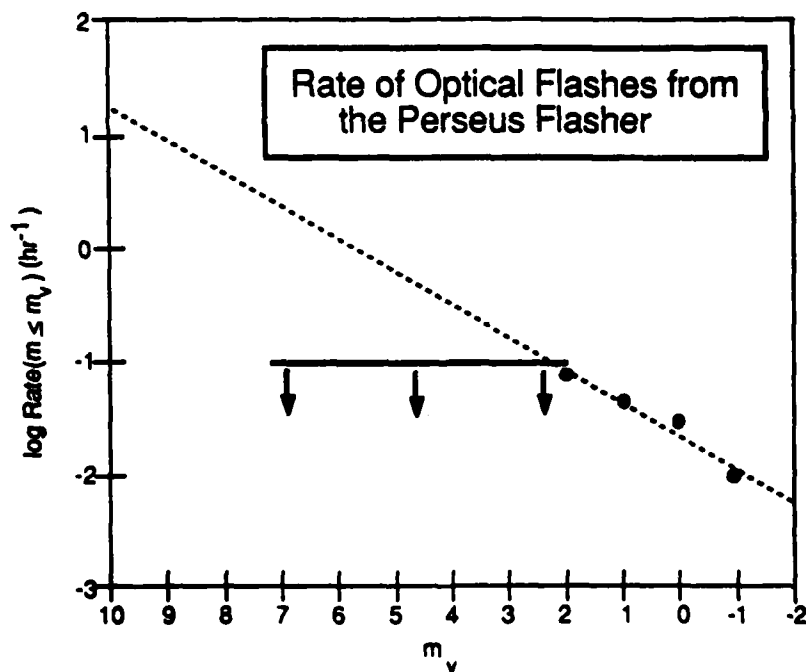


Figure 1: The rate of optical flashes from the Perseus Flasher, from Katz, et al. (1986) and this paper. Plotted are the rates of optical flashes of magnitude  $< m_v$  versus  $m_v$ . The points are the rates of flash detections taken from Katz, et al. The dashed line is an extrapolation of these data points to higher magnitudes. The solid horizontal line indicates the three-sigma Poisson upper limit on the rate of optical flashes reported here. The cutoff at faint magnitudes occurs at the detection limit of the ETC; the high-brightness cutoff indicates the magnitude at which a one-second flash would saturate the CCD.

The upper limit presented here is barely consistent with the rate of optical flashes reported by Katz, et al. (Katz, et al. have reported an average of optical flashes of  $0.07 \text{ hr}^{-1}$ , based on 7 detections in 95 hours of observations by two members of the group). However, as is shown in Figure 1, the rate of flashes of  $m \leq m_c$ , reported by Katz, et al. is an increasing function of  $m_c$ . The upper limit established here is below the rate of optical flashes implied by an extrapolation of the data points from Katz, et al. Our results are consistent with the results of Katz, et al. only if the  $\log R(m \leq m_c) - m_c$  relation for the Perseus Flasher flattens out near  $m_c \approx 2$ .

A flattening of the  $\log R(m \leq m_c) - m_c$  curve for a single source implies that there is a minimum brightness for all flashes coming from the source. Such a situation could arise if the mechanism for the flash requires that certain minimum conditions be met before a flash can occur (as in, e.g., the thermonuclear flash model for X-ray and  $\gamma$ -ray bursts of Wallace, Woosley and Weaver /18/ and Fryxell and Woosley /19/). A flattening of the  $\log R(m \leq m_c) - m_c$  curve for the Perseus Flasher at  $m \approx 2$  would mean that all flashes from the Perseus Flasher will have  $m < 2.3$ . The observations of the Perseus Flasher with the ETC do not allow us to reject this scenario, as the upper limit is still consistent with the rate of flashes at the magnitude of the putative turnover.

### THEORY

If the Perseus Flasher is a celestial phenomenon, observations made to date can be used to provide a partial description of the source of the flashes. The typical risetimes of about one second points to an emitting region with a typical size  $< 3 \times 10^{10} \text{ cm}$ . The fact that the error region is empty to  $m_c \approx 17$  on the Palomar Sky Survey /1/ indicates that the source brightness increases by 15-18 magnitudes during outburst. No celestial objects are presently known to exhibit such an enormous brightening on a one-second timescale. GRBs are thought to be potential sources of large-amplitude brightenings (see /7,8,9,20/). However, there is no clear evidence that the optical flashes associated with GRBs occur on a one-second timescale /21/. Flare stars have long been known to increase their brightness by one to six magnitudes on timescales of tens of seconds /22,23/.

On the other hand, the flashes from the Perseus-Aries border may not be celestial in nature, but rather due to some near-Earth source of optical flashes. A number of the optical flashes could be the result of meteor events with a small angular size. Katz, et al., report that the Perseus Flasher event of 23 October 1984 was sighted by two observers at two sites separated by 8 km. The difference in the coordinates reported by the two observers is consistent in magnitude and direction with the effect of parallax between the two sites, if the source of the flash were at an altitude of roughly 80 km. Since 80-100 km is the typical range of altitude for meteors, the Perseus Flasher event of 23 October 1984 could have been two sightings of a single meteor.

It is also possible that some of the optical flashes attributed to the Perseus Flasher could be due to the reflection of sunlight from a tumbling satellite. The reflected light would have a roughly solar spectrum, so the glints would tend to have the same color as the Sun (4 of the 7 flashes of  $m_c \leq 2$  were described as yellow or orange). A simple calculation, modelling a satellite as a plane mirror with an albedo of 1%, shows that sunlight reflected from a  $1 \text{ m}^2$  surface 1000 km from an observer would be perceived as light from a star of magnitude -1. The brief duration of the flash can be accounted for by the tumbling motion of the satellite. The absence of repetitions of the flash could be explained by the motion of the satellite across the sky or a chaotic tumbling motion.

If the single flash photographed by Katz, et al. was produced by a satellite glint, the coordinates and time of the flash can be used to constrain the location and orbit of the satellite. At the time of the photograph, the Sun was  $3^\circ$  west and  $30^\circ$  south of the apparent coordinates of the flash. The flash was seen  $21^\circ$  over the western horizon a few hours after sunset. The lower limit on the satellite altitude is given by the height of the Earth's shadow at the point where the line-of-sight to the Perseus Flasher intersects the edge of the shadow: a rough calculation puts this altitude at 600 km. The upper limit on the satellite altitude is determined by the satellite size and distance: a  $1 \text{ m}^2$  surface of 1% albedo would look like a star of  $m_c = -1.5$  at an altitude of 700 km; a  $10 \text{ m}^2$  surface would have  $m_c = -1.5$  at an altitude of 1200 km. The lower limit on the inclination of the orbit can be calculated from the upper limit on the satellite altitude and the apparent declination of the flash (see Figure 2). An upper limit of 3000 km yields a lower limit on the orbital inclination of  $40^\circ$ . According to the Satellite Situation Report of December 31, 1985 /24/, roughly half of the approximately 6000 objects in orbit at that time had an inclination  $> 40^\circ$  and a perigee  $> 700 \text{ km}$ . It is therefore possible that the photographed flash was caused by a glint from an orbiting satellite. More detailed calculations would require compilations of exact orbital elements for all satellites with inclinations  $> 40^\circ$  and perigees  $> 700 \text{ km}$ .

### CONCLUSION

We have detected no optical flashes from the Perseus Flasher error region in 70 hours of observations with the ETC. The sensitivity of this survey to one-second flashes extends over the brightness range  $m_c = +2$  to  $+7.1$ . The upper limit on the rate of flashes we have determined is marginally consistent with the rate of flashes reported by Katz, et al. Although we are unable to definitively prove or disprove the existence of the Perseus Flasher, we can state that the Perseus Flasher most likely does not produce optical flashes of  $m > 3$ , based on the extrapolation of the  $\log R(m \leq m_c) - m_c$  curve taken from Katz, et al.

The question of the nature of the Perseus Flasher remains open, as we were unable to confirm it to be a celestial object with a detection by the ETC at Kitt Peak. A confirming photographic or electronic detection of an optical flash from Perseus an important step toward resolving this question. A second flash at the same celestial coordinates would confirm the celestial nature of the Perseus Flasher, especially if detected at a site removed from the one at which the first photograph was taken. A second flash at a different celestial location would indicate that the source of the flashes in Perseus is near-Earth in origin (either a head-on meteor or satellite).

Finally, we urge that a thorough set of visual observations be conducted of some other part of the night sky. Such a control experiment would improve our knowledge of the rate of background flashes due to satellites and head-on meteors.

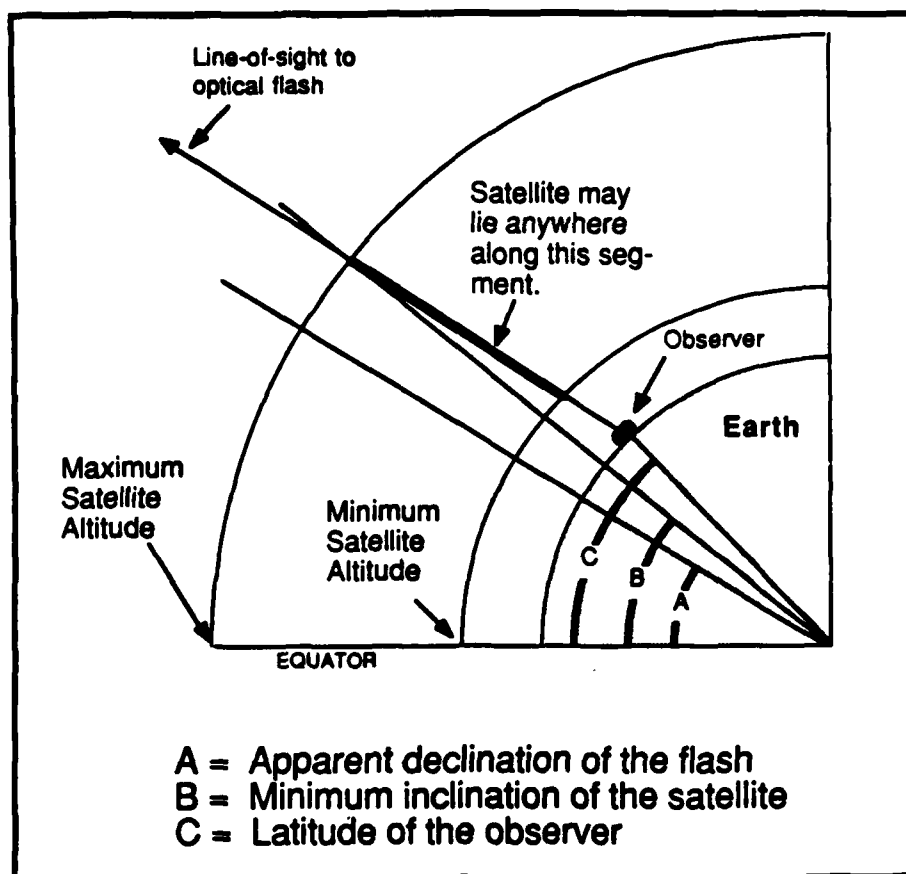


Figure 2: The geometry of a satellite glint. The lower limit on the latitude of a satellite creating a glint is the apparent declination of the flash. The upper limit is the latitude of the observer. More stringent constraints can be calculated from the minimum and maximum possible satellite altitude at the time of the flash.

#### ACKNOWLEDGEMENTS

The authors wish to thank John Doty, Walter Lewin, Saul Rappaport, and Anna Zytkow of MIT, Scott Tremaine and Marshall McCall of the University of Toronto, and Robert Scarlett of the Los Alamos National Laboratory for helpful conversations. Wayne Lewis assisted during a portion of the ETC observations.

This research was supported in part by the National Aeronautics and Space Administration under grant NSG-7339. In the development phase of the Explosive Transient Camera, we benefited greatly from the assistance of R. Doane, J. Settlemyre, K. Cramer, R. Barnes, B. Powell, and the technical and telescope support staff at the Kitt Peak National Observatory. Initially, Dr. G. Burbidge, and later, Dr. S.C. Wolff, in their roles as Directors of the Kitt Peak National Observatory, were extremely supportive of the arrangements needed to establish the ETC on Kitt Peak.

## REFERENCES

1. B. Katz, D. Driscoll, K. Millyard, B. Wazers, M. Zalcik, J. Adair, A. Gada, W. Hayes, R. Kelsch, R. McWatters, R. Rokosz, J. Zehethofer, A. Fullerton, R. Lyons, and M. McCall, "Optical Flashes in Perseus," *Ap. J. (Letters)*, 307, L33 (1986)
2. G.R. Ricker, J.P. Doty, W.H.G. Lewin, J.V. Valleria, and R.K. Vanderspek, "The Explosive Transient Camera: An Instrument for Identification of Gamma-Ray Burst Optical Counterparts," in: *High Energy Transients in Astrophysics*, ed. S.E. Woosley (AIP Conf. Proc. No. 115) Amer. Inst. of Physics, New York, p. 669 (1984)
3. R.K. Vanderspek, 1985, Ph. D. thesis, Massachusetts Institute of Technology.
4. G.R. Ricker and R.K. Vanderspek, "Real-Time Searches for Optical Flashes Associated with Gamma-Ray Bursts: Methods and First Results," this issue.
5. A. MacRoberts, "Observer's Notes," *Sky and Telescope*, 69, 148 (1985)
6. A. MacRoberts, "Observers Notes," *Sky and Telescope*, 70, 54 (1985)
7. B.E. Schaefer, "A Probable Optical Counterpart to a Gamma-Ray Burster," *Nature* 294, 722 (1981)
8. S.A. Woosley, "The Theory of Gamma-Ray Bursts," in: *High Energy Transients in Astrophysics*, ed. S.E. Woosley (AIP Conf. Proc. No. 115; New York, AIP), 485 (1984)
9. K.M.V. Apparao, and S.M. Chitre, "Optical Flashes - A Clue to the Origin of Gamma-Ray Bursts," preprint (1982)
10. H. Pedersen, J. Danziger, K. Hurley, G. Pizzichini, C. Motch, S. Illovaisky, N. Gradmann, W. Brinkmann, G. Kanbach, E. Rieger, C. Reppin, W. Trumper, and N. Lund, "Detection of Possible Optical Flashes from the  $\gamma$ -Ray Burst Source GBS0526-66," *Nature* 312, 46 (1984)
11. E.P. Mazets, S.V. Golenetskii, V.N. Ilyinskii, V.N. Panov, R.L. Aptekar, Yu.A. Guryan, M.P. Proskura, I.A. Sololov, Z.Ya. Sokolova, T.V. Kharitonova, A.V. Dyatchkov, and N.G. Khavenson, "A Catalog of Cosmic Gamma-Ray Bursts from the Konus Experimental Data," *Astrophys. Space Sci.* 80, 3 (1981)
12. R.W. Klebesadel, W.D. Evans, J.G. Laros, I.B. Strong, T.L. Cline, U. Desai, B.J. Teegarden, C. Barat, K. Hurley, M. Niel, G. Vedrenne, I.V. Estulin, A.V. Kuznetsov, and V.M. Zenchenko, "A Catalog of Gamma-Ray Bursts with Earth-Crossing Times," *Ap. J. (Letters)* 259, L51 (1982)
13. E.E. Fenimore, private communication.
14. J.G. Laros, private communication.
15. A. Zytkow, private communication.
16. W.H.G. Lewin and J. v. Paradijs, private communication.
17. N. Gehrels, preprint (1985)
18. R.K. Wallace, S.A. Woosley, and T.A. Weaver, "The Thermonuclear Model for X-ray Transients," *Ap. J.* 258, 716 (1982)
19. B.A. Fryxell and S.E. Woosley, "A Two-Dimensional Model for  $\gamma$ -Ray Bursts," *Ap. J.* 258, 733 (1982)
20. B.E. Schaefer, H.V. Bradt, C. Barat, K. Hurley, M. Niel, G. Vedrenne, T.L. Cline, U. Desai, B.J. Teegarden, W.D. Evans, E.E. Fenimore, R.W. Klebesadel, J.G. Laros, I.V. Estulin, and A.V. Kuznetsov, "Two Probable Optical Flashes from Gamma-Ray Bursters," *Ap. J. (Letters)*, 286, L1 (1984)
21. S.A. Rappaport and P.C. Joss, "On the Binary Nature of Cosmic Gamma-Ray Burst Sources," preprint (1984)
22. T.J. Moffet, "UV Ceti Flare Stars: Observational Data," *Ap. J. Suppl.* 273, 29, 1 (1974)
23. G.A. Gurzadyan 1980, *Flare Stars*, Pergamon Press.
24. Satellite Situation Report 1985, NASA Goddard Space Flight Center, Vol. 25, No. 3.

## Appendix H

*Deep CCD Imaging of the Optical Flash Error Region Near GBS 1810+31*  
Ricker, G.R., Ajhar, E., A., Luu, J. P., and Vanderspek, R. M., 1986 *Ap. J. (Letters)*.

## DEEP CCD IMAGING OF THE OPTICAL FLASH ERROR REGION NEAR GBS 1810+31

George R. Ricker, Edward A. Ajhar, Jane P. Luu, and Roland K. Vanderspek

Department of Physics and Center for Space Research,  
Massachusetts Institute of Technology

### ABSTRACT

Hudec (1986) has reported the detection of three bright transient optical images ( $4 < m_B < 7$ ) from the same celestial location on archival photographic plates taken in 1946 and 1954. The reported location of the object is  $\alpha_{1950} = 18^h 9^m 27^s \pm 3^s$  and  $\delta_{1950} = +31^\circ 23.0' \pm 0.5'$ ; this location is empty on the POSS "O" prints ( $B > \sim 20$ ). The proximity of the celestial coordinates of this bright object to the error region of the  $\gamma$ -ray burster GBS 1810+31 (Laros *et al.* 1985) may make it a candidate for the  $\gamma$ -ray burst source counterpart. We have used a CCD imager to search the error region associated with the optical transients in the B and R bands. We report the celestial coordinates and the B and R magnitudes of the fourteen objects found in the optical error region. A possible flare star origin for the phenomena reported by Hudec is discussed.

### I. INTRODUCTION

The phenomenon of  $\gamma$ -ray burst sources has been, and continues to be, an enduring astrophysical mystery. Since the initial  $\gamma$ -ray discoveries



made with the *Vela* satellites in the late 1960's (Klebesadel *et al.* 1973), no optical, X-ray, or radio counterparts have been established for a single one of the more than 400  $\gamma$ -ray burst sources detected to date (Baity, Hueter and Lingenfelter 1984; Laros 1987). Schaefer and co-workers have reported interesting results on archival optical flash events associated with three different  $\gamma$ -ray error boxes (Schaefer *et al.* 1984). However, none of these three events has been confirmed either by recurrences or by other observers. Recently, a report by Hudec (1986) of *recurrent* optical flash events from the same location near ( $\sim 6.5$  arcminutes displacement) the  $\gamma$ -ray burst source GBS 1810+31 (Laros *et al.* 1985) has appeared. All three of these flashes occurred in the "pre-Sputnik" era (*i.e.*, 2 flashes in 1946 and 1 in 1954), and thus are not subject to the problem of confusion with "glints" caused by reflected sunlight from artificial satellites. This latter problem was particularly highlighted by the "Perseus Flasher" episode, in which an photographed optical flash of apparent astronomical origin (Katz *et al.* 1986) was subsequently shown to be due to a tumbling artificial satellite (Maley 1987; Vanderspek, Zachary, and Ricker 1986). The importance of attempting to refine the location of Hudec's event to study the stellar and galactic composition of the  $\sim 1$  square arcminute error box reported by Hudec (1986) led to the observations reported here.

## II. OBSERVATIONS

Deep images of the optical error region were made with MIT's

MASCOT CCD instrument (Meyer and Ricker 1980; Dewey and Ricker 1980) on 1986 November 26 on the 2.4m telescope at the McGraw Hill Observatory<sup>1</sup>. Five minute exposures were made through Mould B and Mould R filters. The Landolt (1983) standard star 95-96 was observed to calibrate the photometry. Sections of the CCD images in B and in R with the optical error region indicated are shown in Figure 1 and Figure 2, respectively.

### III. DATA ANALYSIS

The astrometry was performed in the following manner. The celestial coordinates of 20 stars on the CCD image which were also visible on the Palomar Survey "E" plate were calculated. A mapping (Podobed 1965) between the celestial coordinates and positions of the 20 stars on the CCD image was determined with a least-squares fit of the stars' coordinates to their positions on the CCD image. From this mapping, the position of the optical error region on the CCD image and the celestial coordinates of any objects found inside the error region were calculated.

The photometry was performed on bias-subtracted, unflattened CCD images. The pixel size was 0.58" by 0.58". An array size of 5 by 5 pixels was used to measure the fluxes which determine the magnitudes of the ob-

---

<sup>1</sup> The McGraw Hill Observatory is located on Kitt Peak and is operated jointly by the University of Michigan, Dartmouth College, and the Massachusetts Institute of Technology.

jects found. The first step was to measure the sky level on each image in the area around the Landolt standard or in the area of the optical error region. The standard deviation of the sky level ( $\sigma_{\text{sky}}$ ) and the flux of the standard were used to determine the detection threshold ( $3\sigma_{\text{sky}}$ ) and the magnitude limit. Finally, the optical error region was searched for all 5 by 5 arrays whose flux was above the detection threshold. The magnitudes in B and in R for these arrays were then calculated.

#### IV. RESULTS

The deep B and R images of the optical error region revealed fourteen objects whose positions and magnitudes are reported in Table 1. The  $1\sigma$  error in the celestial coordinates is 0.61 arcsec. The magnitude limits for a 99.9% detection probability are  $m_R = 21.1$  and  $m_B = 22.0$ . The statistical error in the B and R magnitudes is  $< 0.2$ . The  $B-R$  reported in Table 1 is an instrumental magnitude difference, which is closely related to the magnitude difference on the Mould system. For 4 objects, the value of  $B-R$  is quite uncertain, due to the object's faintness of the blue CCD image and its spectral type; these instances are designated by lower limits on  $B-R$ .

Bushouse (1985) gives empirical transformations of instrumental to standard colors for an RCA CCD and Mould filters. As the spectral response of the RCA CCD is similar to that of the Texas Instruments virtual-phase CCD used in the MASCOT, the color corrections of Bushouse (1985) apply to the magnitudes listed in Table 1. Calculations

show that the color corrections to B, R, and B-R are small compared to the uncertainty in B, R, and B-R; hence, the B-R quoted in Table 1 reflects a B-R in the standard system to the precision of the photometry.

## V. DISCUSSION

One possible explanation of the source of the archival optical flashes is that they are events from a single flare star. Isolated flare stars are typically M stars which can brighten considerably in the U- and B-bands, with risetimes of up to a few minutes and durations of  $\sim 10$ –60 minutes (Gurzadyan 1980). Empirical studies show the flare frequency  $f$  to be an exponential function of the star's absolute magnitude  $M_V$ :  $f \propto 10^{0.15M_V}$  (Gurzadyan 1980). Thus, intrinsically fainter stars will tend to flare more frequently. This calculated flare frequency is not a constant for a given star: the frequency of events from a given flare star has been seen to vary by factors of 2–5. Empirical studies also show that the probability of a flare star brightening by an amount  $\Delta B$  goes roughly as  $e^{-\alpha \Delta B}$ , where  $\alpha \sim 1$  (Gurzadyan 1980). (*N.B.*: Although this relationship has been shown to be roughly valid for  $\Delta B < \sim 5$ , we will assume that it applies for larger values of  $\Delta B$  as well).

Using these empirical data, a rough scenario for a flare star creating the optical transients detected by Hudec (1986) can be constructed. For example, an M5 dwarf of  $M_V = 15$  at a distance of 100 pc would be seen to have an apparent magnitude of  $B = 21.5$ . The archived optical

transients reported by Hudec (1986) would have had a peak brightness of  $B_{\text{peak}} = 4-7$  if the image was created by an optical flash of one-second duration. Scaling directly from this estimate, if the image was, instead, created by a flare star event of thirty-minute duration, the peak magnitude of the flare would be  $B = 12-15$ . A flare star would therefore have to brighten by  $\Delta B \sim 10$  in order to create the transient image. From the relations given in Gurzadyan (1980), the rate of flares from the M dwarf is nominally  $\sim 2$  flares/hour, and the probability of a  $\Delta B = 10$  flare is  $\sim e^{-10} = 4.5 \times 10^{-5}$ . The resultant rate of  $\Delta B = 10$  flare events from an M dwarf of  $M_V = 15$  is  $\sim 1$  per year; the rate from an M dwarf of  $M_V = 10$  is  $\sim 1$  per 7 years. Hudec has reported two flares detected  $\sim 5$  months apart; given the random nature of flare events from any given flare star, a flare star with a nominal rate of bright flares of  $\sim 1$  per year could be the source of the flares. In addition, as Hudec scanned archival plates totalling over 1800 hours of cumulative exposure time, the probability of his detecting a bright flare from a flare star with a nominal rate of bright flares of 1 per year is  $\sim 20\%$ .

The number density on the sky of potential flare star candidates can be estimated from the constraints of the quiescent brightness ( $m_{\text{B quiescent}} > \sim 20$ ) and of estimates of the flare magnitude and duration. Assuming the flare star is an M star and that  $\sim 50\%$  of all M stars exhibit flare activity (J. Linsky 1987), the number of flare star candidates can be calculated from the number density of M stars in the local neigh-

borhood as a function of  $M_V$  (Allen 1976) and the limits on the distance to the flare star as a function of  $M_V$ . The lower limit on the distance of any M star of absolute magnitude  $M_V$  is calculated from the condition that  $m_{B \text{ quiescent}} > 20$ ; the upper limit is the distance at which a flare of  $\Delta B = 12$  would be necessary to create the transient, or 300pc, whichever is smaller. Simple calculations indicate one such flare star source per  $\sim 80$  square arcminutes. As Hudec (1986) evidently searched an area of at least 100 square arcminutes, the probability of a flare star being in the search field is not small. From these rough estimates of possible flare star densities and rates, it is clear that a flare star origin of the optical transients detected by Hudec cannot be excluded.

If a flare star is the source of the optical transients, the quiescent flare star could be recognized from its large value of B-R. Typical values of B-R for main sequence stars are 0.0 for an A0 star, 1.1 for a G0 star, 1.6 for a K0 star and 2.5 for an M0 star (Allen 1976). Table I includes several candidates for stars of high B-R: the most plausible are B, D, I, and J (although the R image of I could have been caused by a cosmic ray). Further multi-band photometry and spectroscopy of these sources must be done in order to be able to identify them as flare star candidates.

## VI. CONCLUSION

Based on the observations reported here, a possible explanation for the recurrent optical flash phenomena reported by Hudec (1986) as be-

ing due to a flare star with an unusually large amplitude appears plausible. Testing of this hypothesis by searches for small amplitude flares among the fourteen objects catalogued here based on CCD imagery will be time-consuming, but is possible in principal. Follow-up photometry of the Hudec field at even fainter limiting magnitudes in at least 3 colors should permit classification of the objects reported here. Spectroscopic examination of interesting color-excess objects should be attempted.

## VII. ACKNOWLEDGEMENTS

This research was supported in part by the National Aeronautics and Space Administration under grants NSG-7339 and NSG-7643. We gratefully acknowledge many useful suggestions and guidance in the use of the McGraw-Hill 2.4m telescope facility by M. Johns. The concerted efforts of G. Luppino and G. Mitsuoka were essential in bringing the MASCOT and its operating system to its current user-friendly state. Helpful suggestions on the photometric analysis were made by M. Bautz. We thank K. Hurley and B. Schaefer for useful discussions of optical flashes and for initially drawing our attention to the work of R. Hudec.

TABLE 1

Positions and Magnitudes of Objects Found in the Error Region

Object	$\alpha_{1950}^*$	$\delta_{1950}^{**}$	$m_R$	$B - R^\dagger$
A	$18^h 9^m 23.76^s$	$+31^\circ 22' 41.4''$	21.0	1.4
B	$23.91^s$	$23' 15.9''$	20.9	$> 1.8$
C	$24.42^s$	$22' 48.6''$	19.8	1.4
D	$24.54^s$	$23' 04.2''$	21.0	$> 1.7$
E	$25.18^s$	$22' 36.3''$	19.7	0.6
F	$26.04^s$	$22' 39.4''$	19.0	1.7
G	$26.41^s$	$22' 54.8''$	19.4	1.9
H	$26.84^s$	$22' 45.1''$	20.7	0.5
I $\ddagger$	$26.85^s$	$22' 36.2''$	20.5	$> 2.2$
J	$26.89^s$	$22' 40.8''$	20.5	2.2
K	$29.00^s$	$22' 38.3''$	20.6	1.0
L	$29.51^s$	$22' 35.0''$	18.6	0.4
M	$29.57^s$	$23' 12.3''$	21.5	0.5
N	$29.84^s$	$23' 17.6''$	19.1	1.3

\* Error in right ascension is  $\pm 0.035^s$  ( $1\sigma$  level of confidence).\*\* Error in declination is  $\pm 0.61''$  ( $1\sigma$  level of confidence).† Instrumental  $B - R$ , not Johnson standard (see section IV).

‡ Possibly a cosmic ray.



## REFERENCES

- Allen, C. W. 1976, *Astrophysical Quantities* (London: The Athlone Press).
- Baity, W. A., Hueter, G. J., and Lingenfelter, R. E. 1984 in *High Energy Transients in Astrophysics*, ed. S. Woosley (AIP Press, New York), p. 434.
- Bushouse, H. 1985, in *National Optical Astronomy Observatories Newsletter*, No. 4, p. 14.
- Dewey, D., and Ricker, G. R. 1980, in *Applications of Digital Image Processing to Astronomy*, ed. D. Elliot (S. P. I. E. 264, Bellingham, WA), p. 42.
- Gurzadyan, G. A. 1980, *Flare Stars* (New York: Pergamon Press).
- Hudec, R. 1986, *Inf. Bull. Var. Stars* (Budapest), submitted.
- Katz, B., et al. 1986, *Ap. J. (Letters)*, 307, L33.
- Klebesadel, R. W., Strong, I. B. and Olson, R. A. 1973, *Ap. J. (Letters)*, 182, L85.
- Landolt, A. U. 1983, *A. J.*, 88, 439.
- Laros, J., et al. 1985, *Ap. J.*, 290, 728.
- Laros, J. 1987, private communication.
- Linsky, J. 1987, private communication.
- Meyer, S. S., and Ricker, G. R. 1980, in *Applications of Digital Image Processing to Astronomy*, ed. D. Elliot (S. P. I. E. 264, Bellingham, WA), p. 33.

Podobed, V. V. 1965, *Fundamental Astrometry* (Chicago: University of Chicago Press).

Schaefer, B. E. 1981, *Nature*, 294, 722.

Schaefer, B. E., et al. 1984, *Ap. J. (Letters)*, 286, L1.

Vanderspek, R. K., Zachary, D. S., and Ricker, G. R. 1986, *Advances in Space Research*, 6, No. 4 (in the press).

## Figure Captions

### Figure 1:

A B band CCD image of the error box for the optical flash source reported by Hudec (1986). An integration time of 300 seconds through a Mould B filter was utilized. Candidate objects are identified in Figure 2. The rectangular box shown is 61 arcseconds N-S by 78 arcseconds E-W, centered at the position given by Hudec (1986).

### Figure 2:

An R band CCD image of the error box for the optical flash source reported by Hudec (1986). An integration time of 300 seconds through a Mould R filter was utilized. Candidate objects are designated A-N (see Table 1). The rectangular box shown is 61 arcseconds N-S by 78 arcseconds E-W, centered at the position given by Hudec (1986).

### **Address of Authors**

Edward A. Ajhar:

MIT Center for Space Research

Room 37-540

77 Massachusetts Ave.

Cambridge, MA 02139

(617) 253-7466

Jane P. Luu:

MIT Center for Space Research

Room 37-518

77 Massachusetts Ave.

Cambridge, MA 02139

(617) 253-7466

George R. Ricker:

MIT Center for Space Research

Room 37-527

77 Massachusetts Ave.

Cambridge, MA 02139

(617) 253-7532

Roland K. Vanderspek:

MIT Center for Space Research

Room 37-524

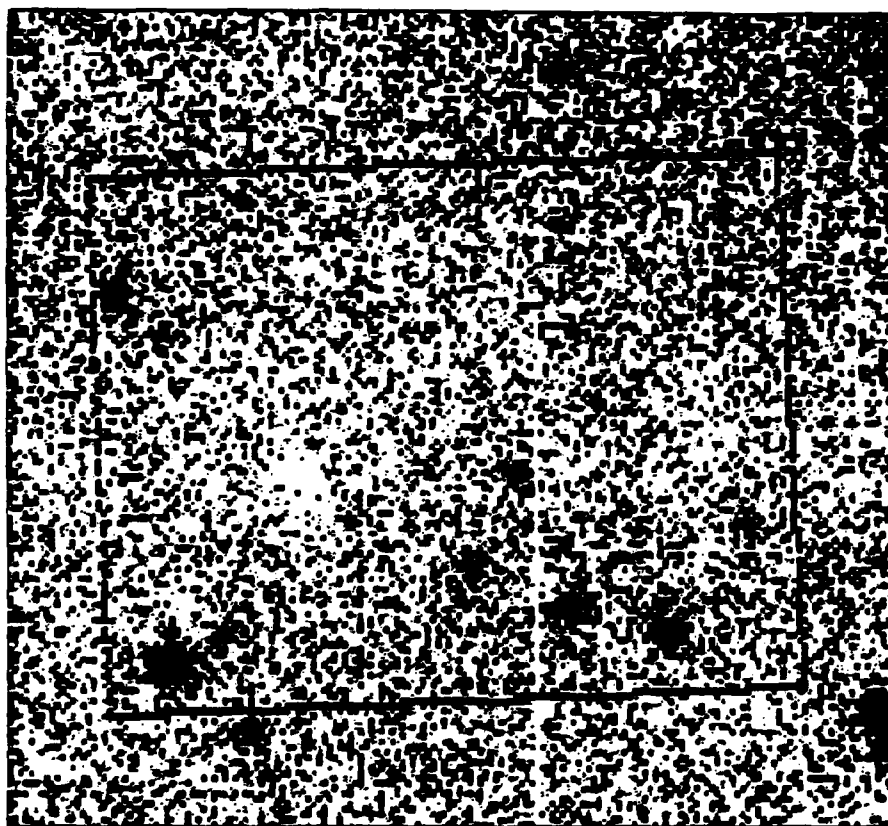
77 Massachusetts Ave.

Cambridge, MA 02139

(617) 253-7466

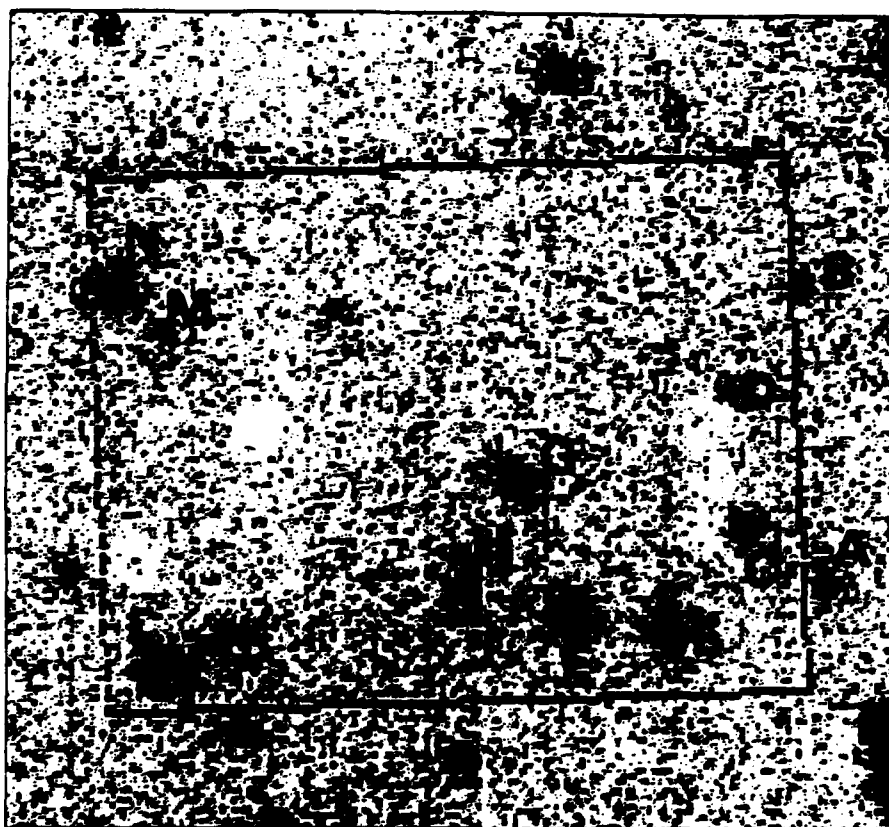
**E**

**N**



N

E



## Appendix I

*The Effect of Artificial Earth Satellites on ETC Observations, 1988,*  
Vanderspek, R.K.



## The Effect of Artificial Earth Satellites on ETC Observations

### 1. Motivation for concerns with Artificial Satellites.

Since the inception of the ETC program, it has been clear that artificial Earth satellites (AES) might have a profound effect on ETC observations. If the rate of "false" events from moving or "glinting" AES is too large, the ETC will spend a large fraction of its operating time processing AES events, thereby reducing the effective observing time for celestial optical flashes. A high event rate from AES will also reduce the effectiveness of the RMT by increasing the probability that it is monitoring a flash from an AES when a real celestial optical flash is detected by the ETC.

As originally proposed, the ETC was to be sited at two locations, separated by ~1.4 km, on Kitt Peak. The parallax associated with this baseline would be enough to recognize an optical flash from an AES to an altitude of ~1000 km. As seen in Figure C-1, a large fraction of the AES population has an apogee larger than 1000 km. Because of this fact, we have contemplated increasing the baseline between the sites in order to be able to reject AES in higher orbits. A baseline of 100 km, for example, would enable the ETC to reject AES at altitudes well beyond geosynchronous orbit.

In order to determine the real effects of AES on ETC observations, we have performed rough analyses of the AES population in near-Earth orbit and calculated typical and worst-case scenarios for the rate of contamination by sunlit AES. With these data, we can develop a strategy of reducing the probability of a false event from an AES for use while the ETC is still situated only at Site 1. This strategy includes pointing the ETC preferentially into the Earth's shadow, to reduce the number of sunlit satellites in the ETC's field-of-view. Note that these analyses concentrate on events occurring within  $60^\circ$  of the zenith, since the ETC will not observe sources less than  $30^\circ$  from the horizon.

### 2. Satellite populations

Since the launch of Sputnik 1 in 1957, the number of satellites in Earth orbit has increased steadily (Figure C-2). NORAD regularly tracks ~6000 objects in Earth orbit measuring larger than 10 cm (a dramatic view of the satellite population density, as tracked by NORAD, is given in Figure C-3). Recent observations, theoretical models and direct measurements have shown that the population of objects in Earth orbit larger than 1 mm

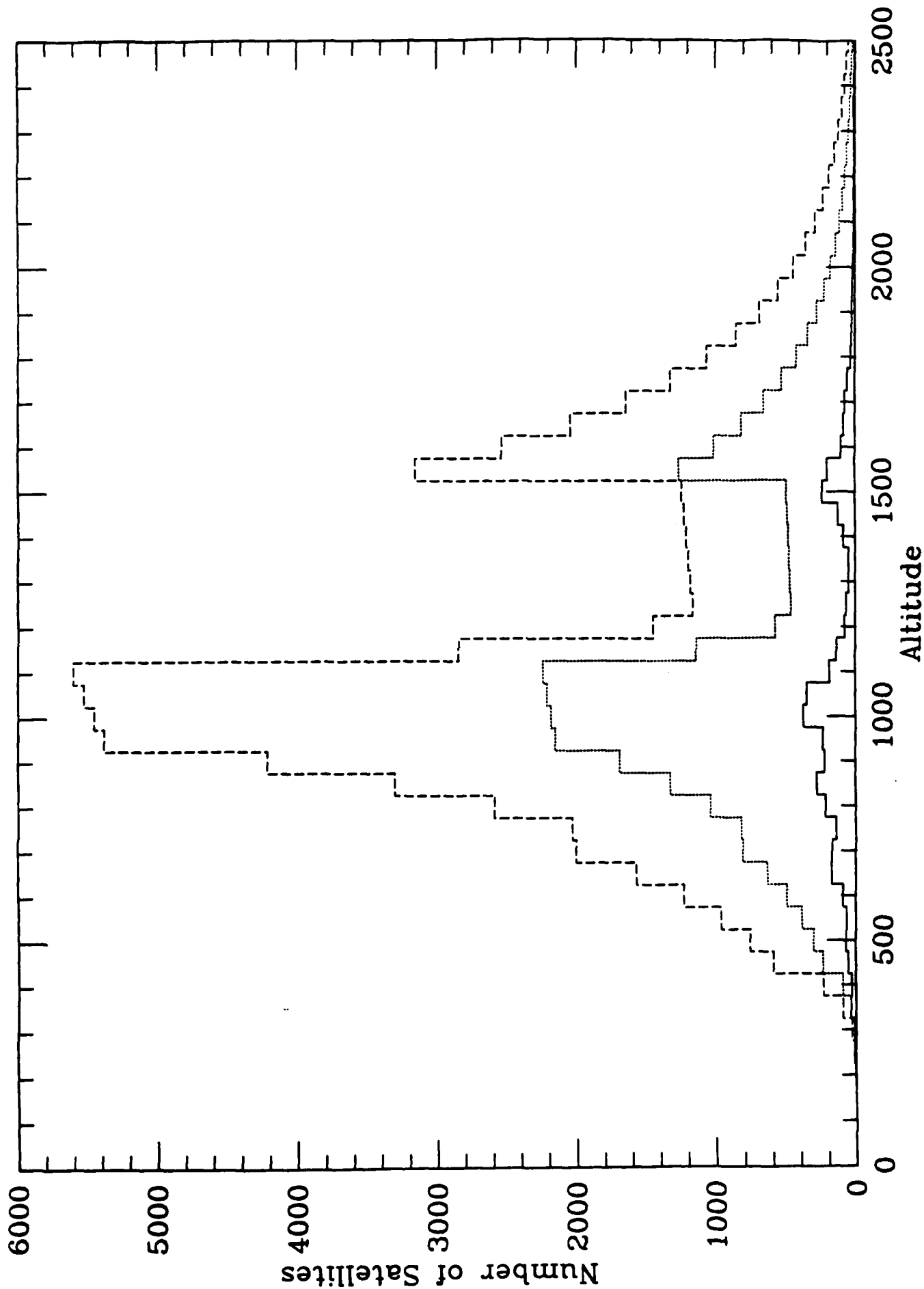
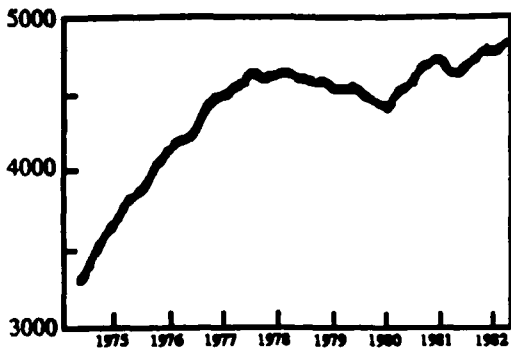
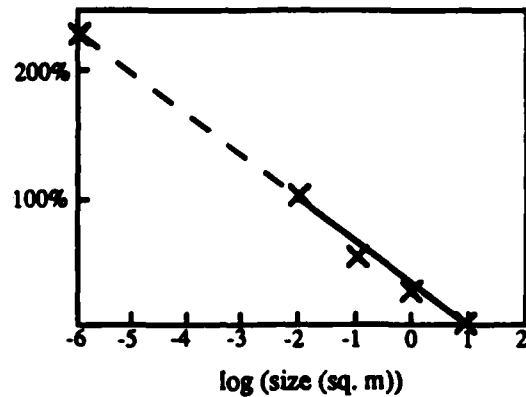


Figure C-1: Number of satellites as a function of satellite altitude at apogee (compiled from Kessler (1985) and Sehnal (1985)). The solid curve plots the number of NORAD-tracked objects (size > 10 cm); the dotted and dashed curves plot the number of objects larger than 1 cm and 1 mm, respectively (from models of Kessler (1985) and Sehnal (1985)).



**Figure C-2:**

A plot of the number of NORAD-tracked objects (measuring larger than 10 cm in size) since 1975 (Kessler 1985).



**Figure C-4:**

The roughly linear relationship between the log of the area of an orbiting object and the fraction of all orbiting objects with larger areas (from Sehnal (1985)). The curve is calibrated so that the fraction of all objects with areas larger than 100 sq. cm. is 1.0.

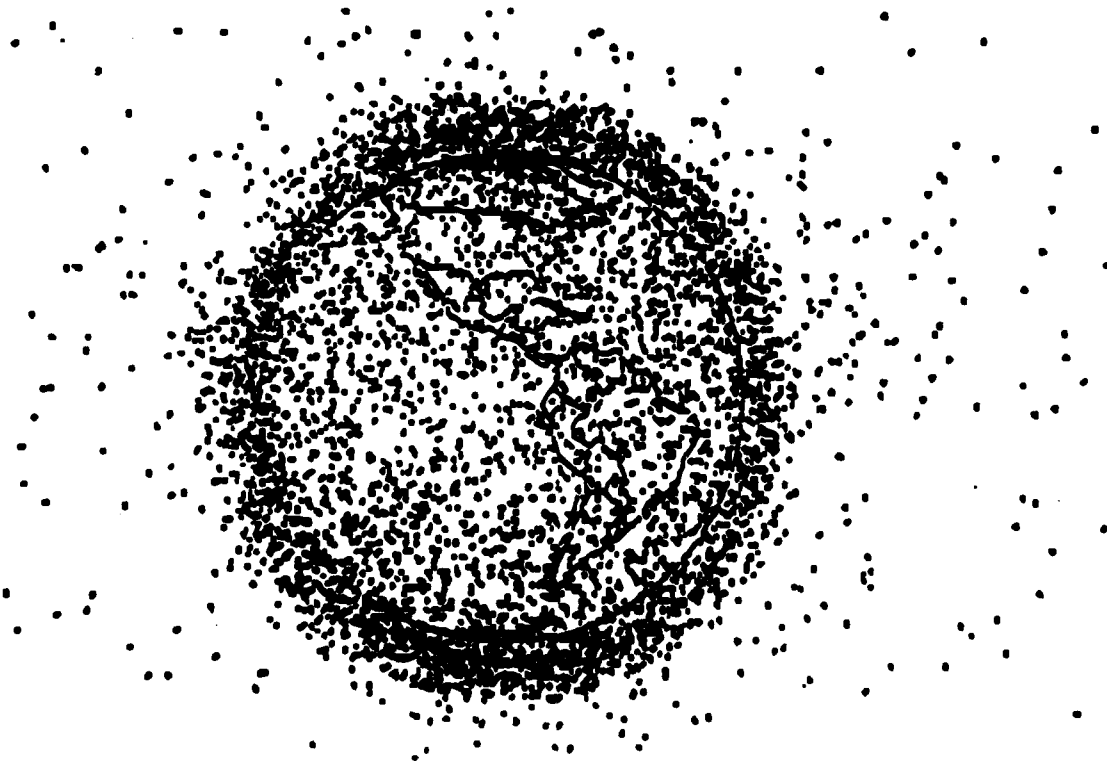


**Figure C-3:**

A snapshot of the Earth and some of its orbiting artificial satellites, taken from Maley (1987). The sharp decrease in the number of satellites occurs at an altitude of ~1000 km (cf. Figure C-1).

may be an order-of-magnitude higher. Most of the objects smaller than 10 cm are the results of explosions or collisions in Earth orbit: indeed, roughly half of the NORAD-tracked objects are the direct results of 27 known explosions in Earth orbit (Kessler 1985 and Table 3.4). Models of the distribution of debris in Earth orbit give estimates of ~40000 objects in space: plots of the density and number of AES versus limiting size and altitude are given in Figure C-1 (taken from Kessler 1985 and Sehnal 1985). Measurements of the distribution of AES size versus frequency yield a roughly linear relationship between the number of AES with area  $> A_0$  and  $\log(A_0)$  (Figure C-4; Sehnal 1985 and Kessler 1985).

### 3. Types of Events from AES

For the purposes of this analysis, we have taken satellites to have one of three general shapes: spherical, cylindrical, or flat. Surfaces are assumed to be smooth and mirror-like for simplicity of calculation. Some satellites may consist of a combination of two or more shapes (e.g. a cylindrical body with flat solar panels). A sunlit satellite in Earth orbit will have a certain signature, based on its shape (see Figure C-5). A flat surface will act as a plane mirror (with a certain albedo) and reflect the sunlight into a beam with a solid angle equal to that of the Sun; a cylindrical surface will

<u>Responsible Nation</u>	<u>Payloads in Orbit</u>	<u>Debris in Orbit</u>	<u>Total</u>
<u>Articles</u>			
USA	519	2530	3049
USSR	954	1843	2797
UK	9	1	10
CANADA	14	0	14
FRANCE	14	21	35
JAPAN	30	39	69
ALL OTHERS	89	26	115
<b>TOTAL</b>	<b>1629</b>	<b>4460</b>	<b>6089</b>

Table 3.4: Distribution of payloads and debris in catalog of objects tracked by NORAD as of September 10, 1986 (from Aviation Space, Fall 1986).

reflect sunlight into a hollow cone with half-angle equal to the angle of incidence of the sunlight and thickness equal to the angular diameter of the Sun; a spherical surface will reflect sunlight in all directions.

The first conclusion of this analysis is that *only spherical surfaces will be constantly visible: cylindrical and flat surfaces will create glints*. Because the brightness of a satellite is inversely proportional to the solid angle into which it reflects sunlight, flat surfaces are brighter than cylindrical surfaces, which are brighter than spherical surfaces (for a constant cross-sectional area). Calculations of this effect yield that, for a given cross-sectional area, *reflections from flat surfaces are 13 magnitudes brighter than from spherical surfaces; reflections from cylindrical surfaces are 6 magnitudes brighter than from spherical surfaces*.

#### 4. Reflections from Spherical Satellites

Spherical AES will have a relatively constant brightness, varying somewhat as the distance of the AES from the observer varies in its orbit. Spherical AES can create false events in the ETC when they move into a patch of sky that is normally empty: the ETC will register the increase in brightness and indicate that the AES is a celestial optical flash. Spherical AES with orbital altitudes less than ~1000 km can be rejected on the basis of their parallax. Spherical AES in general will have a streaked appearance, the length of which is a function of exposure time and AES altitude (see Figure C-6). Spherical AES with orbital altitudes greater than ~1000 km may be rejected on the basis of this streaking, or by the fact that they will create collinear events during later integrations. Note that spherical AES with large attached flat surfaces will also have the capability of creating glints (see sections below).

#### 5. Glints from Flat or Cylindrical Satellites

Glints are created by AES with flat or cylindrical surfaces, as discussed above. A glint from a flat surface is highly directional and depends very much on the orientation of the surface; thus, the probability of a randomly-oriented flat surface producing a glint is equal to the solid angle of the reflected beam divided by the solid angle of the entire sky. This probability is equal to the solid angle of the Sun divided by  $4\pi$ , or  $6.3 \times 10^{-6}$ .

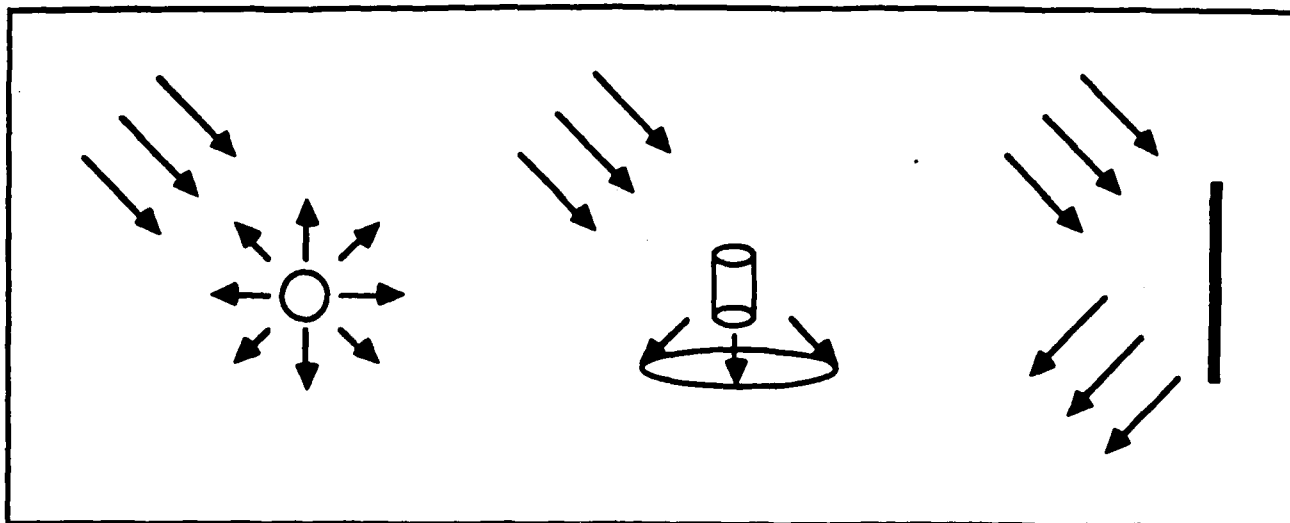


Figure C-5: Types of reflections from various satellite geometries. Assuming satellite surfaces are mirror-like, spherical satellites reflect sunlight in all directions; cylindrical satellites reflect sunlight into a hollow cone; flat satellites reflect sunlight into a narrow beam.

A glint from a cylindrical surface is more probable, because of the larger solid angle subtended by the reflected light. A rotating cylindrical surface, will, in general, produce either zero, two or four glints per rotation, depending on the orientation of the rotation axis to the plane including the Sun, AES, and observer. The probability of seeing a glint from a cylindrical surface at any instant is the ratio of the solid angle subtended by the reflected light to the solid angle of the entire sky; for a cylindrical surface, is  $2\pi(\text{angular size of the Sun})/4\pi$ , or 0.005.

## 6. Calculation of Event Rates

Our understanding of the effects of satellite geometry can be used to make a worst-case estimate of the rate of detection of all satellites of a given geometry as a function of magnitude. For flat and cylindrical satellites, we calculate the number of satellite glints per steradian per hour for zenith angles less than  $60^\circ$ ; for spherical satellites, we calculate the number of satellites visible per steradian. For this analysis, we assume that all satellites are sunlit; in Section H, we introduce a discussion of the effects of the Earth's shadow.

We make worst-case estimates for each of the three geometries, assuming in each case that all known satellites are of one geometry. In the case of flat and cylindrical satellites, for which we calculate rates of glinting, we assume that the satellites rotate chaotically

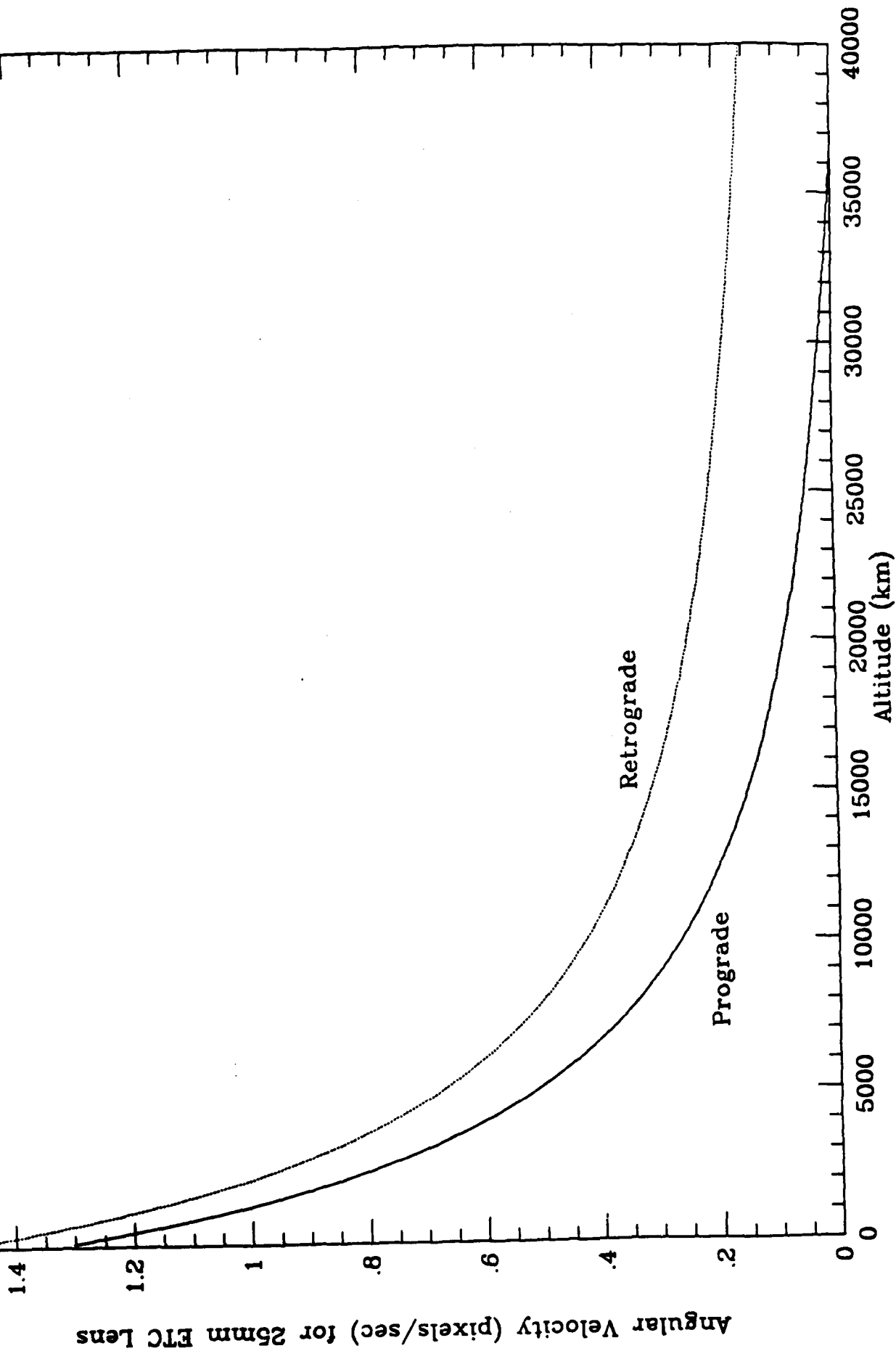


Figure C-6: Angular velocity of a satellite in a circular orbit as a function of orbital altitude. The ETC pixel size with a 25 mm lens is 3.1 arc-minutes. The upper curve corresponds to a satellite in a retrograde orbit; the lower curve is for a prograde orbit.

(randomly) with an arbitrary (but plausible) period of one second; the rate of glints decreases linearly with increasing rotation period. We are given the number of AES as a function of altitude (Figure C-1) and the distribution of AES cross-sectional areas (Figure C-4). In order to calculate the rate of detections, we have to make the following further assumptions:

- 1) Satellite orbits are distributed evenly in geocentric latitude and longitude (from Shara and Johnston 1985; the number density of satellites is well within a factor of two of the average density for that altitude at most latitudes).
- 2) All orbits are circular (from Shara and Johnston 1985; most AES in the Satellite Situation Report have eccentricities  $< 0.2$ , and debris from the destruction of such a satellite will have similar eccentricities).
- 3) All satellites have an albedo of 0.8.
- 4) Geometrical effects introduce a factor of 0.7 into the brightness of the glint for flat and cylindrical satellites.

For each orbital altitude, the fraction of the full  $4\pi$  steradians of the satellites orbit with a zenith angle less than  $60^\circ$  as seen from the Earth is calculated: that fraction times the number of satellites in orbit at that altitude gives the number of satellites visible at any time. The distribution of magnitudes from satellites at that altitude is calculated from the distribution of satellite sizes in Figure C-4. Note that because the distribution of areas in Figure C-4 has  $N(A > A_0)$  proportional to  $\log_{10}(A_0)$ , and because the magnitude of the glint is a linear function of  $\log_{10}(A_0)$ , the number of satellites with a magnitude  $m < m_0$  is a linear function of  $m_0$ . This effect is visible in Figures C-7a and C-7b, which show the number of satellites per steradian as a function of magnitude, and the number of satellites per steradian brighter than a given magnitude as a function of magnitude.

The rate of glints from a cylindrical or flat surface is calculated in a similar manner. For each orbital altitude, the fraction of satellites visible and the distribution of magnitudes from those satellites are calculated. The rate of glints per hour is calculated by multiplying the number-versus-magnitude distribution by the probability of a glint occurring. For a randomly-tumbling satellite, the probability of a glint per second is the probability of a glint occurring divided by the tumble period. The results of these calculations are shown in Figures C-8 and C-9; the tumble period is assumed to be one second.



### G. Duration of Glints from AES

As mentioned above, the ETC will be able to reduce the number of false events due to AES by recognizing the streak created by AES of steady brightness; the real contamination problem comes from glints from AES which have a duration of the order of one second. The duration of a satellite glint roughly equals the angular diameter of the Sun divided by  $2\pi/P$ , or  $.0016 \cdot P$ , where  $P$  is the rotation period of the satellite. For slowly-rotating satellites, the glint duration can be long enough that it creates a noticeable streak on the CCD (for satellites with a fixed orientation to the Sun, the glint duration is  $\sim 10$  seconds for low-Earth-orbit satellites; see also Figure C-6).

### H. Earth Shadow

In order to determine which times of year and which times of day are most likely to yield illuminated AES, we have calculated the fraction of the night sky which is sunlit as a function of orbital altitude for several dates and times during the year. As seen in Figure C-10, which shows an observer at Kitt Peak at midnight at the vernal equinox, the solid angle subtended by that part of an AES orbit that is in Earth shadow is a function of altitude: the solid angle decreases asymptotically to the limit of the solid angle of the Sun. Figures C-11, C-12, and C-13 plot, in zenith projection at Kitt Peak, the fraction of the night sky in Earth shadow as a function of orbital altitude at various times of the night at the vernal equinox and the summer and winter solstices. Note that the part of the sky with a zenith angle of less than  $60^\circ$  (indicated by a thick circle) is completely sunlit for AES with orbital altitudes less than 2000 km near evening or morning twilight and mostly sunlit for most of the summer's nights; the winter sky, on the other hand, is very dark for most of the night, and therefore much free from AES contamination.

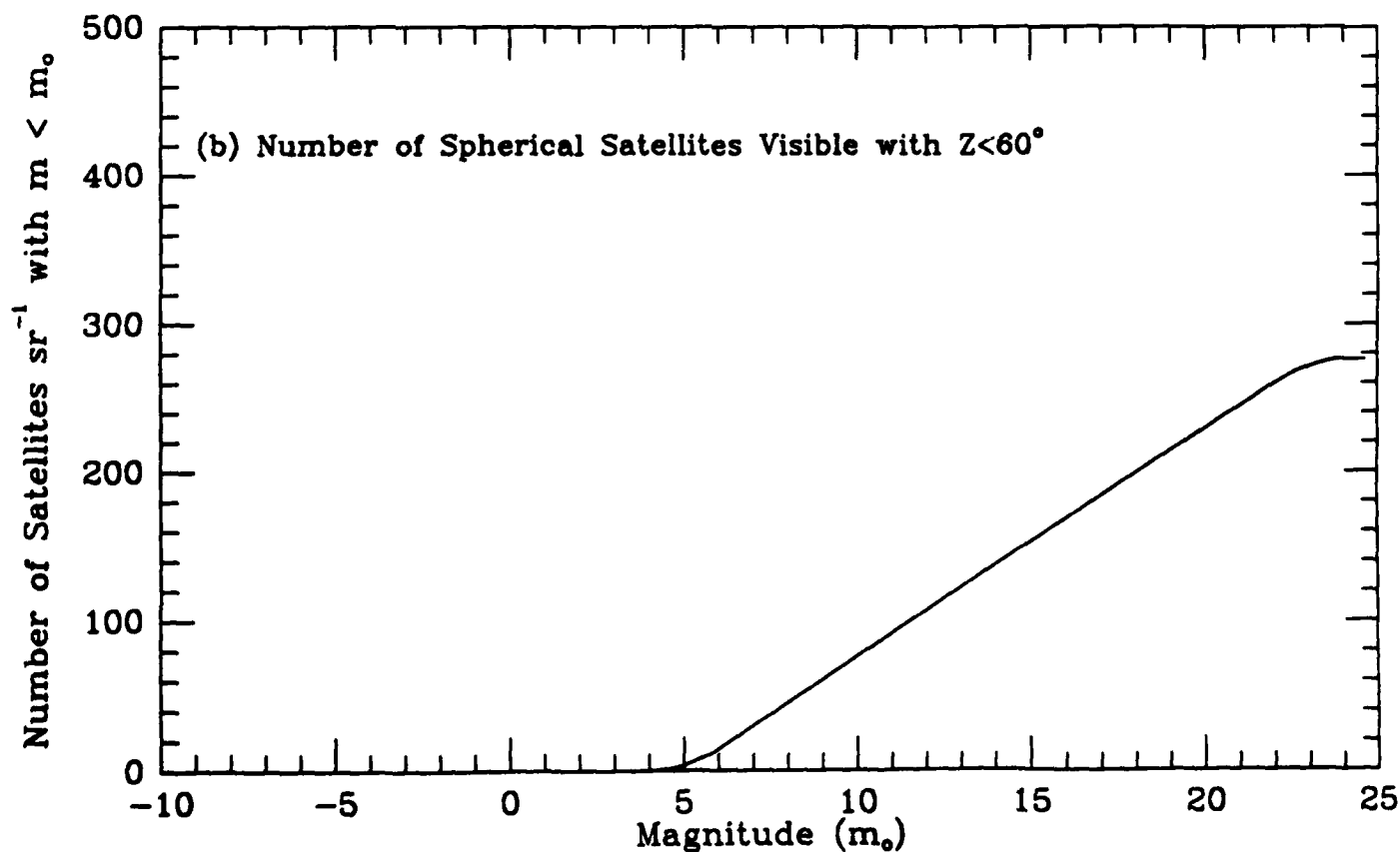
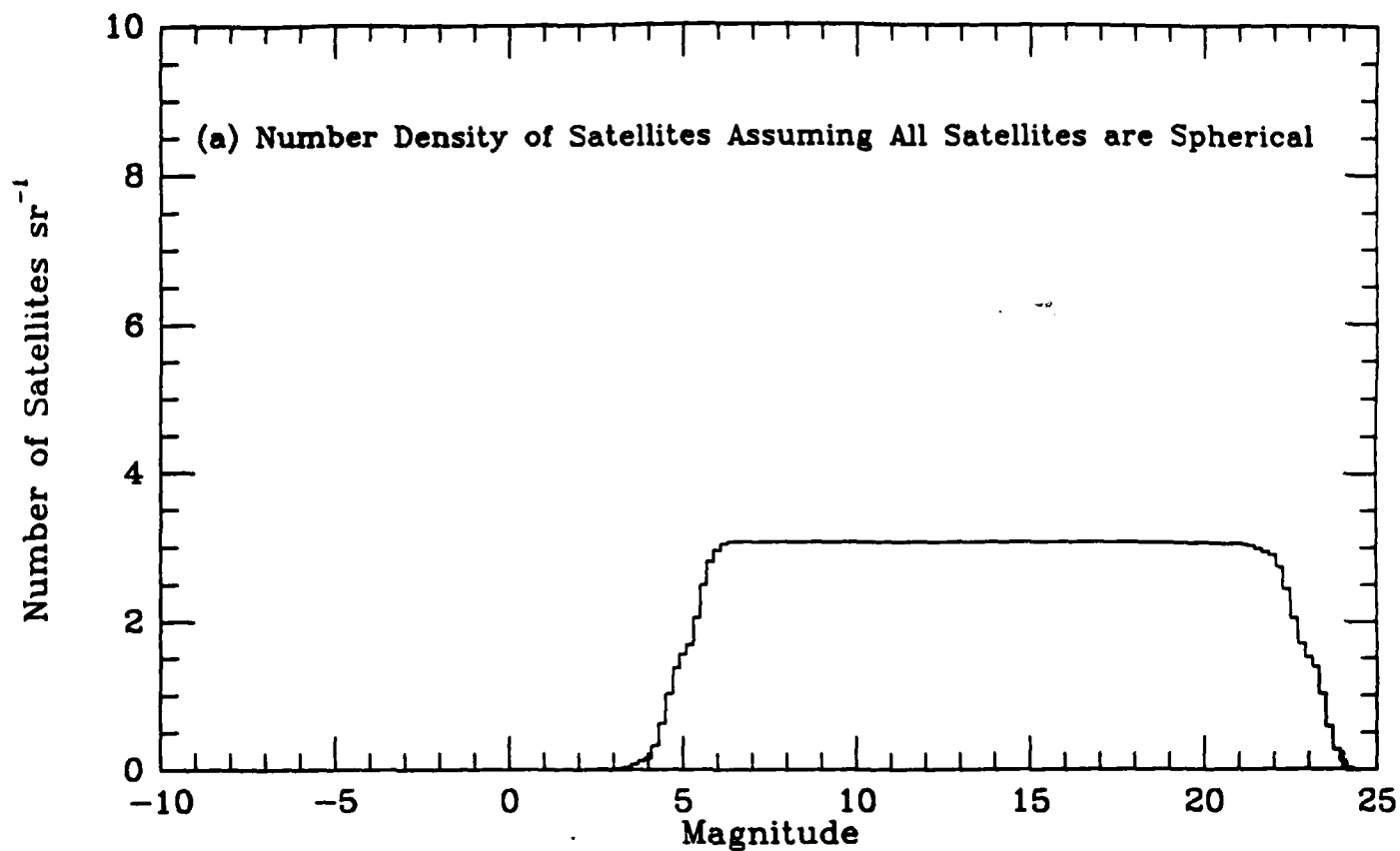


Figure C-7: Upper limit on the number of satellites visible with  $z < 60^\circ$ , assuming all satellites are spherical.

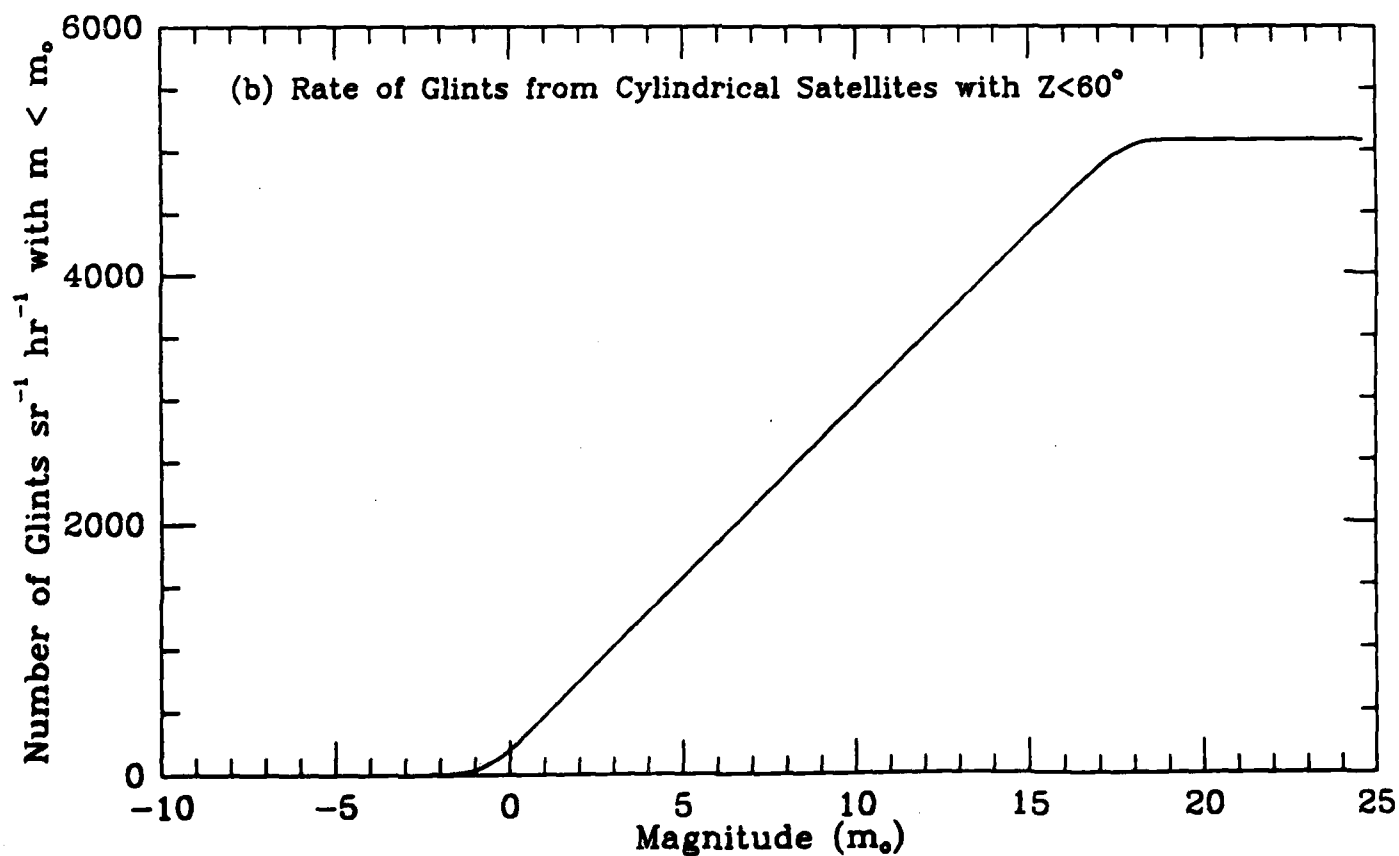
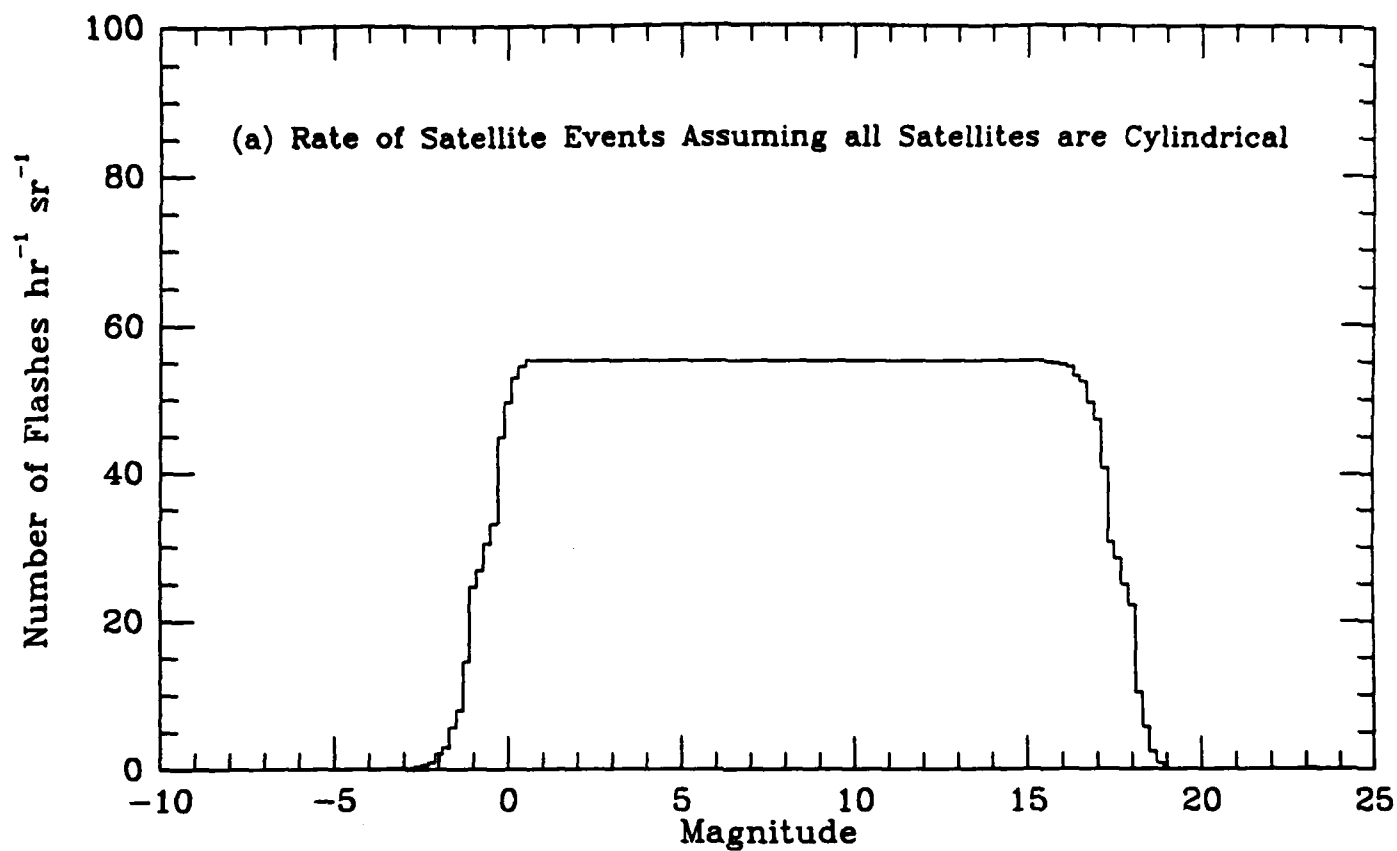


Figure C-8: Worst-case estimate of the rate of glints from satellites, assuming all satellites are cylindrical.

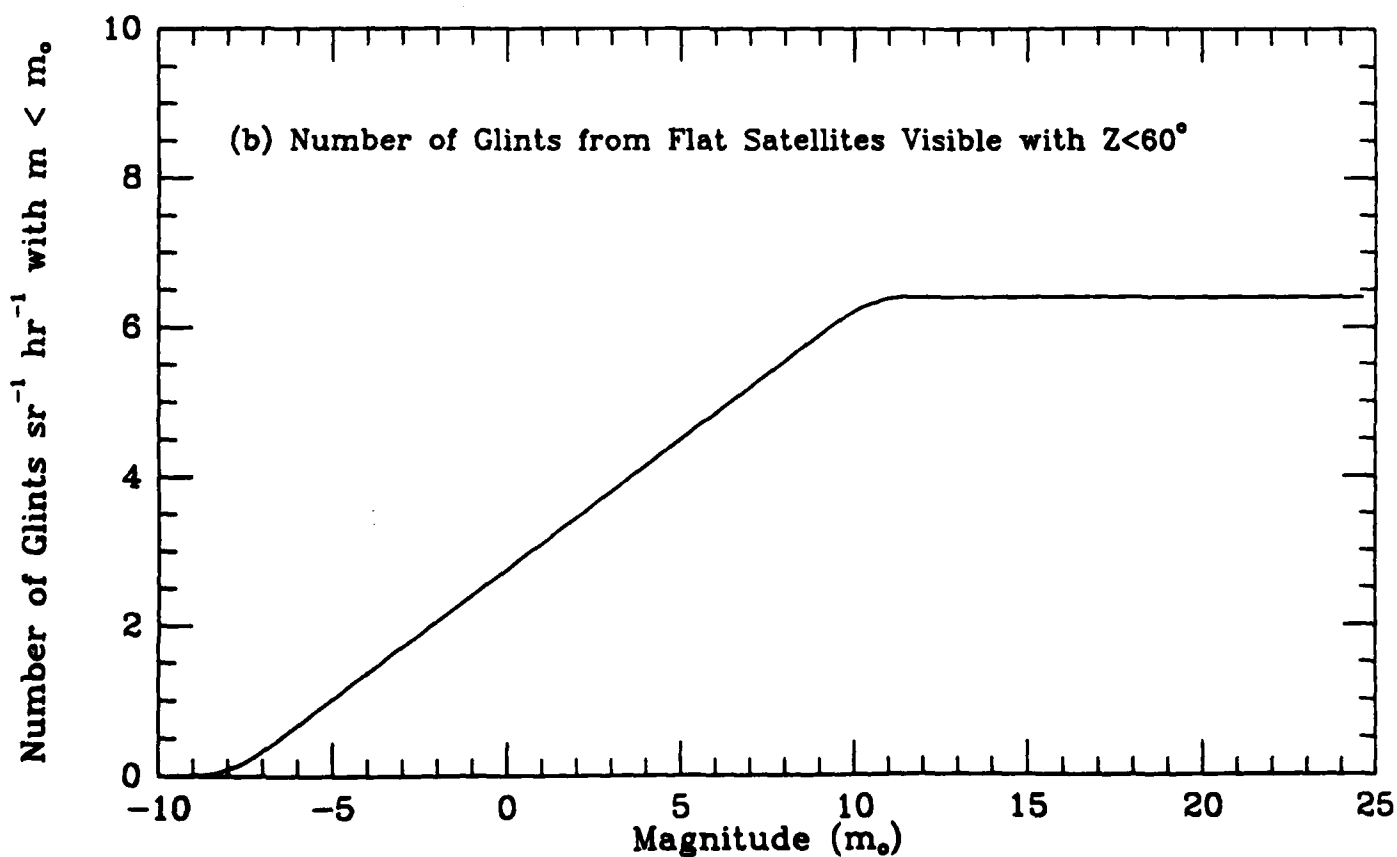
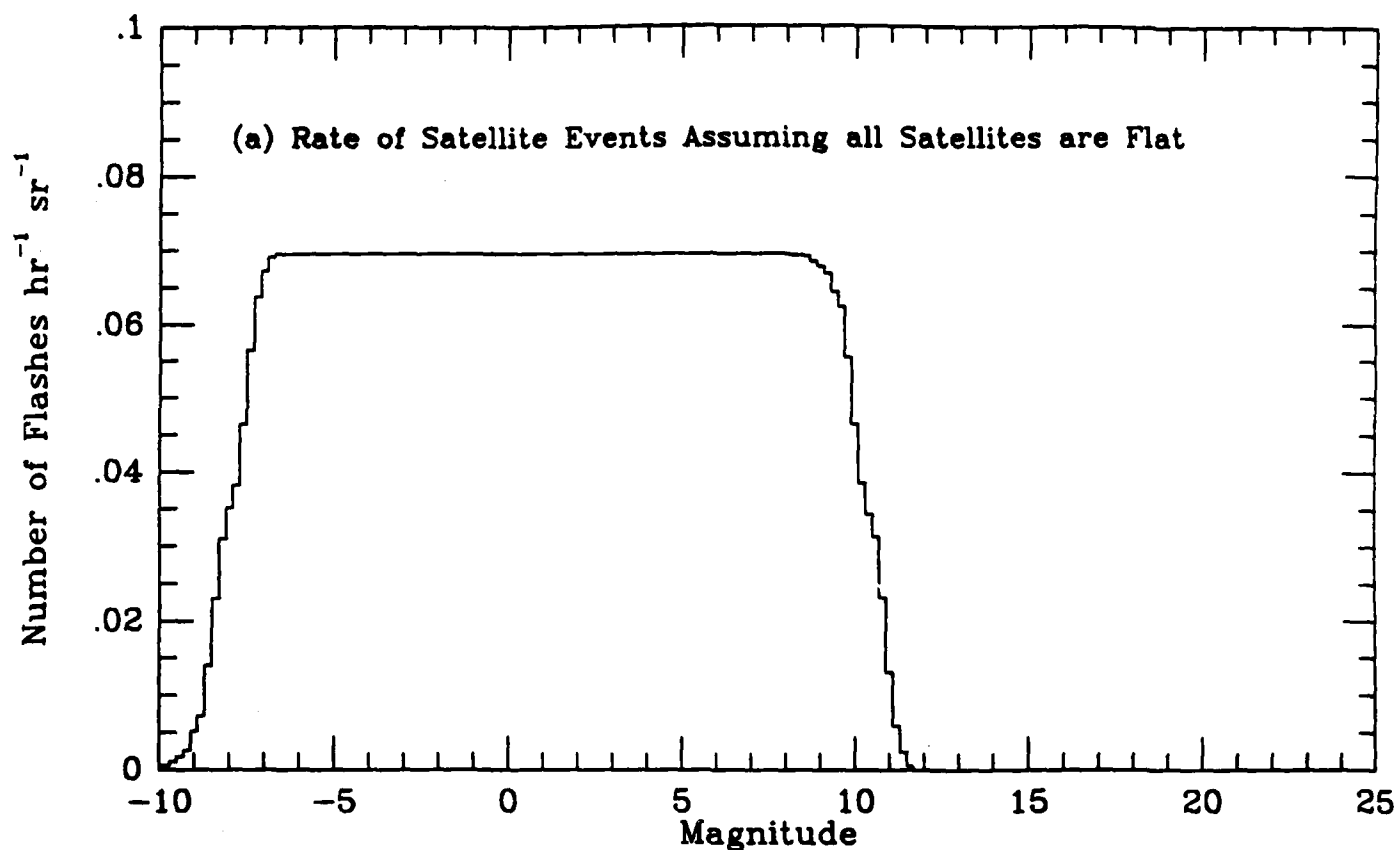


Figure C-9: Worst-case estimate of the rate of glints from satellites, assuming all satellites are flat.

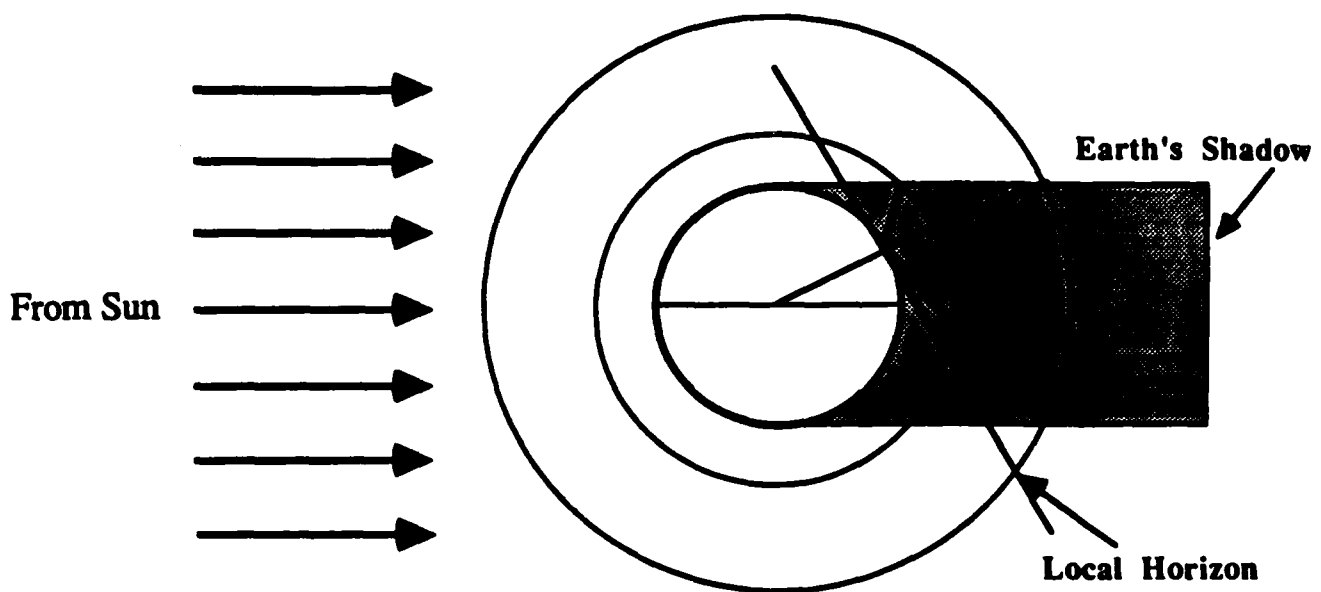


Figure C-10: Effect of orbital altitude on fraction of a satellite's orbit in Earth shadow. Note that as the orbital altitude increases, the solid angle including satellites in Earth shadow decreases (see Figures C-11, C-12, and C-13).

For the purposes of the calculations of the rate of satellite detections, the fraction of the night during which orbital altitudes below 2000 km are in Earth shadow has been calculated as a function of the day of the year (Figure C-14).

## 9. Interpretation of Results

The plots in Figures C-7, C-8, and C-9 are worst-case estimates of the probability of detection of satellites of a certain geometry, assuming all known satellites are of the same geometry. The plot in Figure C-7b of the number density of spherical satellites shows that the total number of satellites in the cone of  $Z < 60^\circ$  at any site is, on average,  $\sim 1000$ . The visibility of these satellites depends on, among several things, the actual geometries of the satellites and the fraction of the satellite in Earth shadow.

The rate of glints from cylindrical surfaces given in Figure C-8 is clearly improbable, since it would predict naked-eye flashes at a rate of  $\sim 100$  per minute for  $z < 60^\circ$ . This exaggerated number can be partially explained by 1) the fact that most satellites are not cylindrical, but rather spherical or multi-faceted (King-Hele, 1966), and 2) the period of tumbling of such satellites is not one second. Cylindrical bodies are generally associated with larger satellites and rocket casings; the end-over-end tumbling of such bodies required

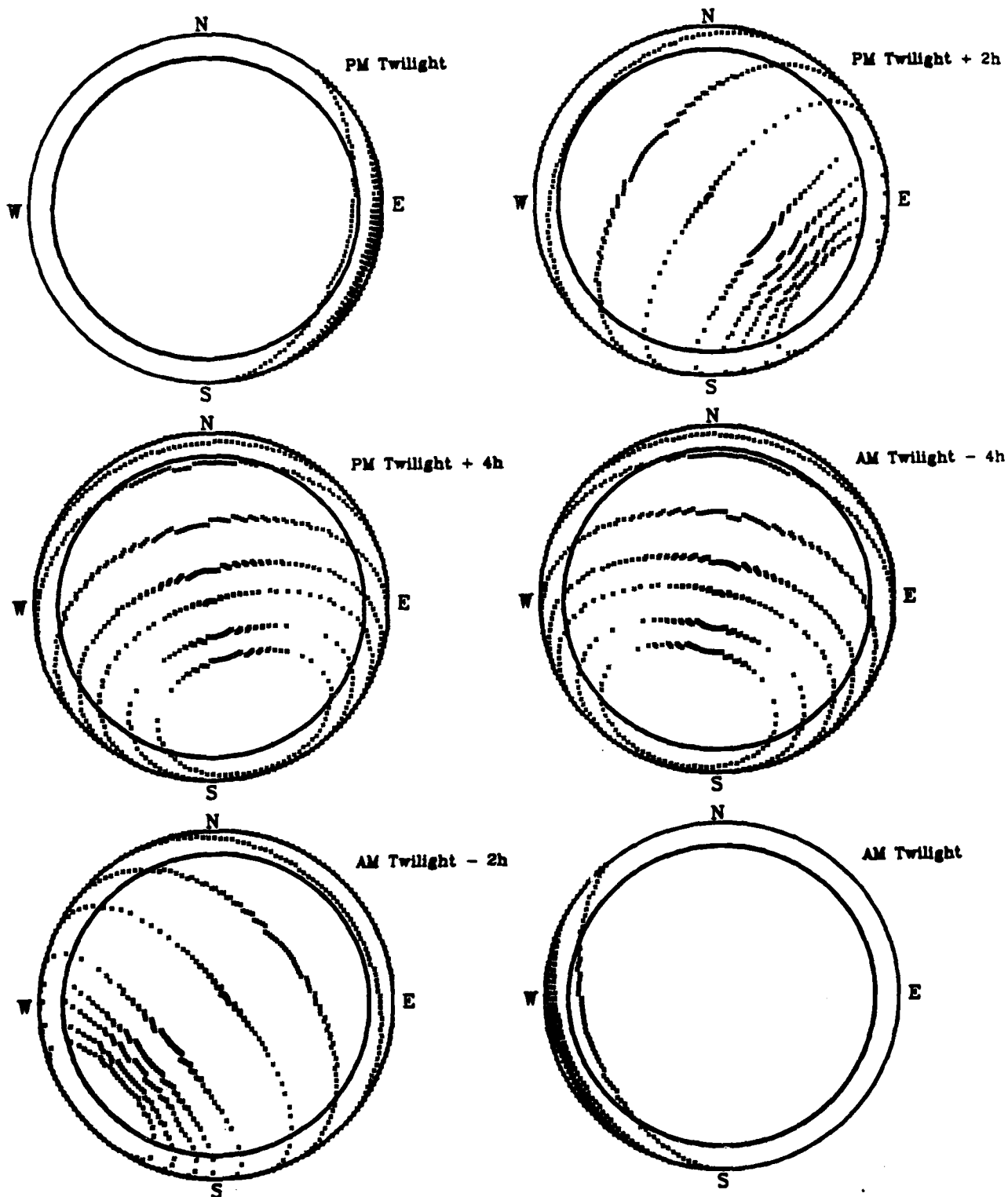


Figure C-11: Zenith projection of the edge of the Earth's shadow for various orbital altitudes and times at Kitt Peak on March 21. The smallest enclosed curve corresponds to an orbital altitude of 10000 km. The next circles correspond to altitudes of 7000, 5000, 3000, 2500, 2000, 1500, 1000, and 500 km, respectively (cf. Figure C-10).

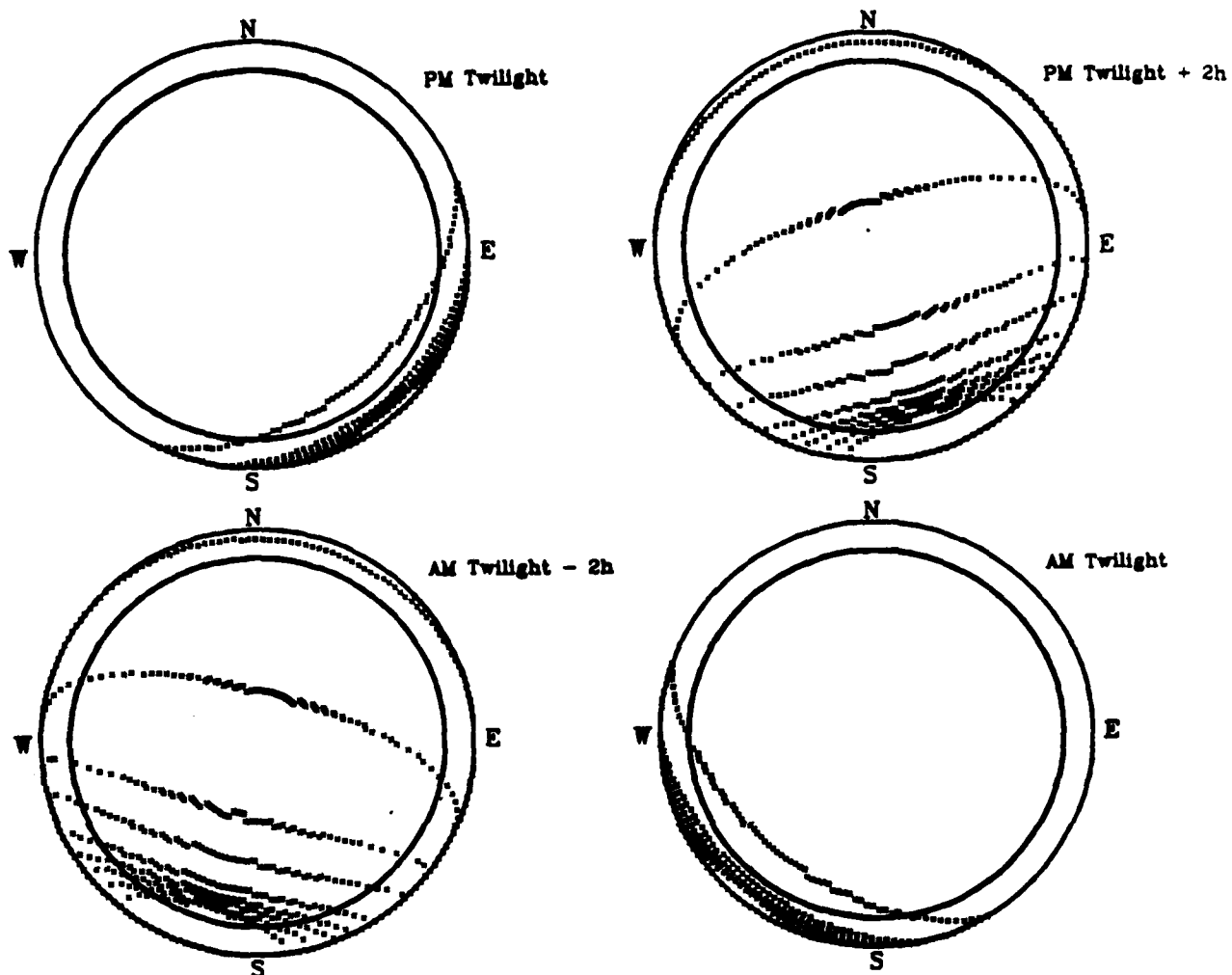


Figure C-12: Zenith projection of the edge of the Earth's shadow for various orbital altitudes and times at Kitt Peak on June 21. The smallest enclosed curve corresponds to an orbital altitude of 10000 km. The next circles correspond to altitudes of 7000, 5000, 3000, 2500, 2000, 1500, 1000, and 500 km, respectively (cf. Figure C-10).

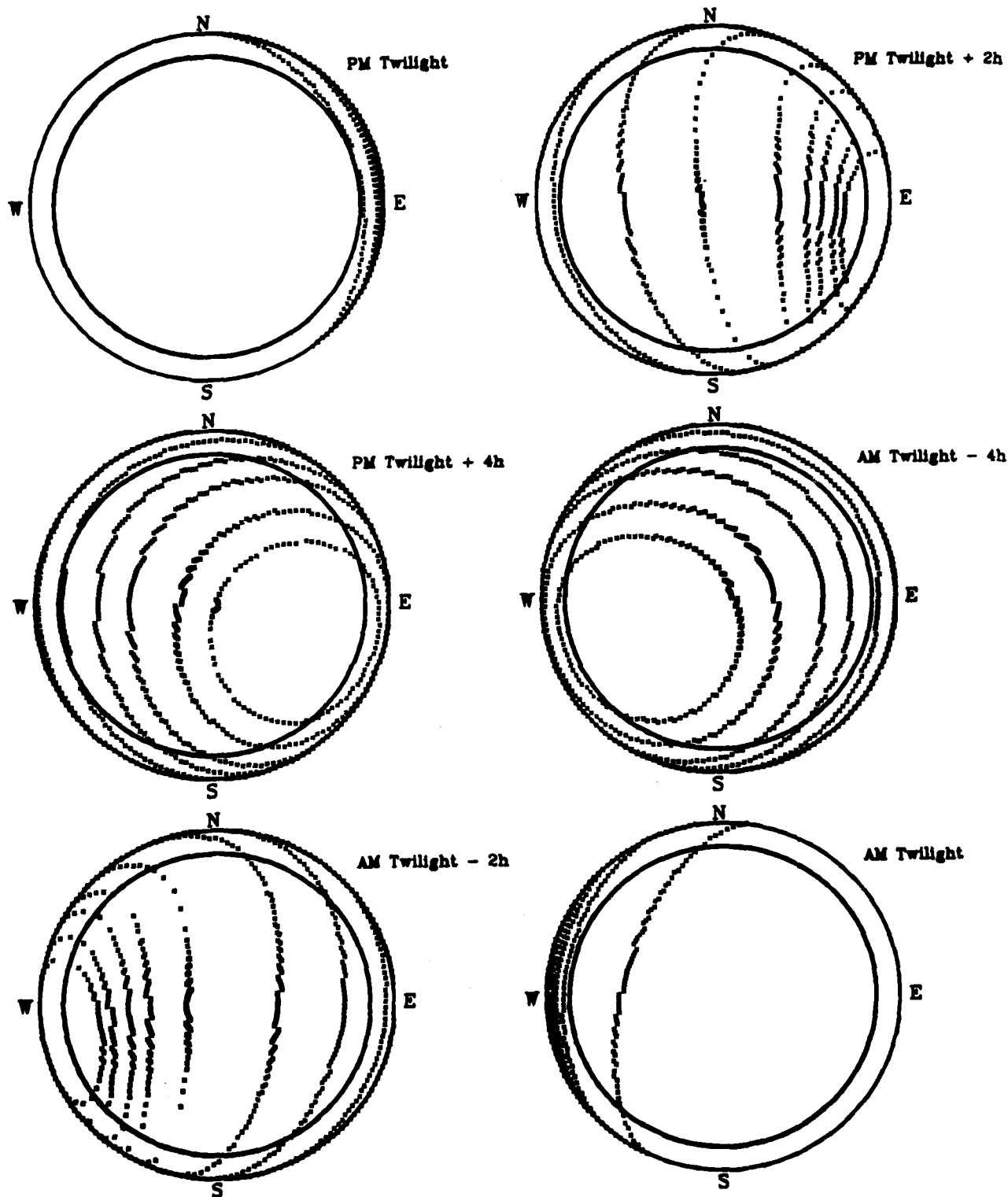


Figure C-13: Zenith projection of the edge of the Earth's shadow for various orbital altitudes and times at Kitt Peak on December 21. The smallest enclosed curve corresponds to an orbital altitude of 10000 km. The next circles correspond to altitudes of 7000, 5000, 3000, 2500, 2000, 1500, 1000, and 500 km, respectively (cf. Figure C-10).



Fraction of  $Z < 60^\circ$  in Earth Shadow

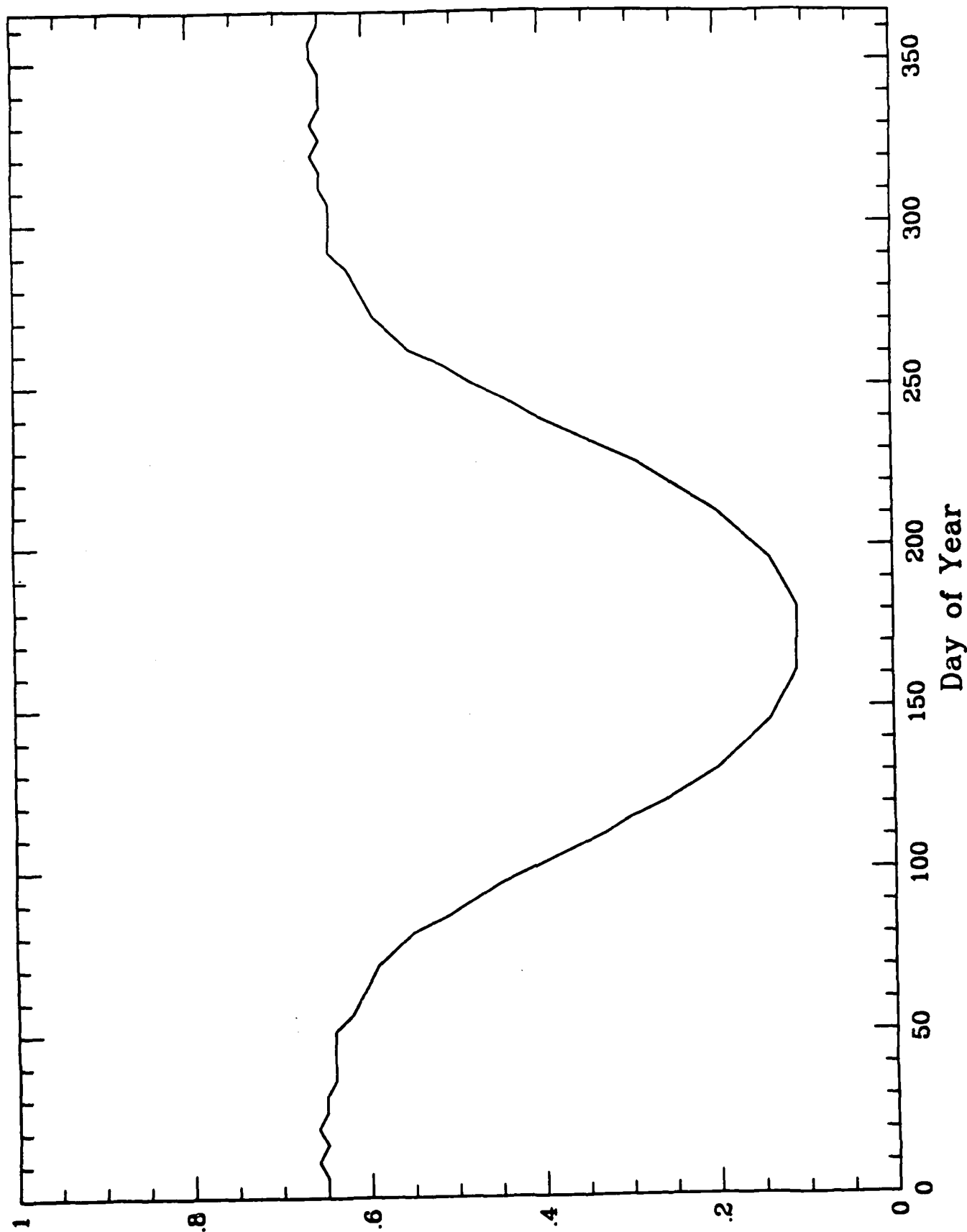


Figure C-14: Fraction of the night sky with zenith angle  $z < 60^\circ$  which is in Earth shadow for satellites with orbital altitudes under 2000 km. Fraction is averaged over time between evening twilight and morning twilight.

to create short glints is usually associated with the re-entry of the body into the Earth's atmosphere. Because of the typical large moment of inertia associated with a large body, such short rotation periods ( $P \sim 1$  sec) are difficult to achieve. If the rotation period of a cylindrical body is higher by a factor of 30-100, the glint rate will drop by a factor of 30-100.

The rate of glints from flat satellites is probably fairly realistic. Most pieces of debris produced by collisions or explosions in orbit will be relatively flat, and therefore capable of creating glints (a slight curvature to a flat piece will tend to spread the reflected light out into a wide beam; this will result in fainter glints, but a proportionally higher rate of glinting). A large fraction of satellites are either equipped with attached solar panels or have multifaceted bodies (which are capable of creating a continuous stream of short, bright glints). *Figure C-9 implies that the completed ETC will detect up to ~10 glints per hour; if the RMT were to devote five minutes to the analysis of the "post-burst" brightness of an unrecognized satellite glint, it would spend ~80% of its observing time monitoring empty space where a satellite glint recently occurred!*

The difficulty created by glints from flat surfaces in orbit can be reduced somewhat by observing into the Earth's shadow as much as possible (Figures C-11, C-12, and C-13). The plot in Figure C-14 indicates that the Earth's shadow is more favorably situated in winter than in summer. Since most satellites have orbital altitudes  $< 2000$  km, Figure C-14 indicates that *from September-April, the bulk of Earth satellites would be in Earth shadow for ~70% of the available dark hours.* The summer months (May-August) would, however, have a high rate of satellite contamination.

## 10. Conclusion

The ETC will have to cope with the large number of objects in Earth orbit and the optical signatures thereof: steady streaks of light, slowly-rising, slowly-fading glints, or short, point-like glints. If the ETC were to be located only at Site 1 on Kitt Peak, it would have to be able to recognize these optical signatures or operate in a manner as to reduce the associated rate of events. Pointing into Earth shadow or observing only from September to March are options in reducing event rates from satellites.

If the ETC were to be located at two sites separated by ~1.4 km on Kitt Peak (see Figure 1), it would be able to use parallax to reduce the rate of events from orbiting objects by ~50%. The imposition of the pointing and observing restrictions mentioned above would help to reduce further the rate of false events.

*If the ETC were to be located on two peaks separated by ~100 km, it would be able to use parallax to recognize and reject optical events from all orbiting sources of optical flashes. The ETC would be able to operate year-round, with no need for pointing or observing restrictions.*

## Appendix J

*Deep Optical and Radio Searches for a Quiescent Counterpart to the Optical Transient Source OTS 1809+31.* 1989, Ricker, G.R., Mock, P.C. , Ajhar, E.A., and Vanderspek, R.K. *Astrophys. J.*, 388, No. 2, 983.

## DEEP OPTICAL AND RADIO SEARCHES FOR A QUIESCENT COUNTERPART TO THE OPTICAL TRANSIENT SOURCE OTS 1809+31

GEORGE R. RICKER, PATRICK C. MOCK, EDWARD A. AJHAR, AND ROLAND K. VANDERSPEK

Department of Physics and Center for Space Research, Massachusetts Institute of Technology

Received 1988 July 14; accepted 1988 August 17

### ABSTRACT

Hudec has reported the detection of three bright transient optical images from the same celestial location on archival photographic plates taken in 1946 and 1954. The optical transient has been localized by Hudec to  $\alpha_{1950} = 18^{\text{h}}9^{\text{m}}26^{\text{s}}.29 \pm 0^{\text{s}}.03$ ,  $\delta_{1950} = +31^{\circ}23'19''.7 \pm 0''.6$  and has been designated OTS 1809+31. This celestial location is empty on the Palomar Observatory Sky Survey blue prints ( $B > \sim 20$ ). Estimates of the duration of the archived transients ( $< \sim 1$  minute) place an upper limit on the peak burst magnitude of  $8 < m_B < 11$ , indicating that the source of the transient brightened by over 10 mag. We have performed a deep CCD search in four colors for the quiescent counterpart of the optical transients. We find no source at the location of the optical transients to  $m_B = 24.5$ ; however, we detected 18 objects in the vicinity of the quoted coordinates which are consistent with the source having a proper motion  $\mu < 1'' \text{ yr}^{-1}$ . A search at 6 cm with the VLA revealed no source in the  $\mu < 1'' \text{ yr}^{-1}$  circle to a  $3\sigma$  limiting flux of 83  $\mu\text{Jy}$ .

*Subject headings:* gamma-rays: bursts — stars: individual (OTS 1809+31) — stars: variables

### I. INTRODUCTION

The phenomenon of the gamma-ray burster (GRB) continues to be an astrophysical mystery. Since the initial GRB detections made with the *Vela* satellites in the late 1960s (Klebesadel, Strong, and Olson 1973), no definitive optical, X-ray or radio counterpart has been established for any of the more than 400 GRBs detected to date (Hurley 1983 and references therein; Baity, Hueter, and Lingenfelter 1984; Laros 1987). In a promising new approach to the GRB problem, Schaefer and co-workers examined archived photographic plates in a search for optical transients associated with GRBs. They have reported the discovery of optical transient images in three different GRB error regions (Schaefer 1981; Schaefer *et al.* 1984); however, none of the three events has been confirmed either by recurrences or by other observations. In 1984, Pedersen *et al.* reported the photoelectric detection of three optical transient events possibly associated with the GRB source GBS 790305.

Recently, Hudec (1987) reported the detection of recurrent optical transients from the same location near the GRB error region GBS 1810+31 (Laros *et al.* 1985). The proximity of the optical transient to the GRB error region was responsible for its discovery; however, its large distance ( $\sim 5'$ ) from the  $3\sigma$  GRB error region makes it highly improbable that the optical transient is associated with the GRB (Laros 1987, personal communication). All three of the flashes reported by Hudec occurred in the pre-Sputnik era (i.e., two flashes in 1946 and one in 1954) and thus are not subject to the problem of confusion with glints caused by sunlight reflected from artificial satellites.

The optical transients reported by Hudec have peak magnitude of  $4 < m_B < 7$ , when normalized to a 1 s burst duration. Hudec also reports an upper limit on the duration of the transients of  $\sim 1$  minute, which places an upper limit on the burst magnitudes of  $8 < m_B < 11$ . As the error region of the transients is empty to  $m_B \sim 20$ , the transient source must have brightened by more than 10 mag. In an effort to identify a possible quiescent counterpart to the optical transient, deep CCD images of the error region were made in four colors in

1987 June. In order to explore the possibility that the source might be close to the solar system ( $d < 20$  pc), a region of the sky corresponding to a proper motion  $\mu$  of  $< 1'' \text{ yr}^{-1}$  since 1946 was examined. The results of the analysis of these observations, as well as of several hours of 6 cm observations with the VLA, are presented below.

### II. OPTICAL OBSERVATIONS

The OTS 1809+31 field was observed 1987 June 21–23 with MIT's MASCOT CCD instrument on the 2.4 m telescope at the McGraw-Hill Observatory.<sup>1</sup> The images were made through Mould *B*, *V*, *R*, and *I* filters in a series of 10–60 minute exposures. The total exposure time was 121 minutes in *B*, 80 minutes in *V*, 51 minutes in *R*, and 100 minutes in *I*. The standard star Landolt 110–340 (Landolt 1983) was imaged each night in all colors as a photometric calibration reference. The observations were made under photometric conditions with a typical seeing disk measuring  $1.5$  FWHM.

#### a) Data Reduction

The CCD images were reduced using procedures from the YARP image-processing package (Tonry 1988). Each image was bias subtracted, flattened, and cleaned. An image was flattened by creating a normalized two-dimensional polynomial representation of the sky level across the image and dividing that normalized representation of the sky into the image. CCD defects and cosmic rays were repaired by parabolic interpolation with an interactive clean program. The reduced images were registered and a subarray centered near OTS 1809+31 was extracted. The subarrays were stacked for more precise photometry.

A circle of radius  $41''$  centered on OTS 1809+31 on the stacked images, corresponding to a proper motion of  $\mu < 1'' \text{ yr}^{-1}$  since the first flash, was searched for faint sources. Stellar objects in the field were identified using FOCAS (Valdes 1987).

<sup>1</sup> The McGraw-Hill Observatory is located on Kitt Peak and is operated jointly by the University of Michigan, Dartmouth University, and the Massachusetts Institute of Technology.

TABLE 1  
CELESTIAL COORDINATES OF THE 18 SOURCES DETECTED NEAR OTS 1809 + 31

Object	Right Ascension	Declination	Distance to OTS 1809 + 31
1.....	18 <sup>h</sup> 9 <sup>m</sup> 25 <sup>s</sup> .87	31°22'39".5	40.6
2.....	18 9 26.72	31 22 41.0	39.1
3.....	18 9 26.70	31 22 44.8	35.3
4.....	18 9 24.29	31 22 48.3	40.6
5.....	18 9 26.26	31 22 54.8	24.9
6.....	18 9 24.40	31 23 3.7	29.1
7.....	18 9 24.91	31 23 6.9	21.9
8.....	18 9 29.27	31 23 12.5	39.0
9.....	18 9 27.74	31 23 10.5	20.8
10.....	18 9 27.80	31 23 15.1	20.0
11.....	18 9 25.60	31 23 16.4	9.5
12.....	18 9 23.76	31 23 15.6	32.8
13.....	18 9 24.14	31 23 31.0	29.9
14.....	18 9 24.76	31 23 35.9	25.5
15.....	18 9 26.16	31 23 36.8	17.2
16.....	18 9 25.76	31 23 41.1	22.5
17.....	18 9 26.58	31 23 43.7	24.3
18.....	18 9 26.87	31 23 48.9	30.1

The threshold for detection was typically set to  $\sim 2\sigma$ . Eighteen sources were detected in the searched area. All objects were detected in all colors except for one which was below threshold in the *B* band.

#### b) Astrometry

The celestial coordinates of the detected sources were calculated in a two-step procedure from the coordinates of SAO stars near the error region. First, the positions of  $\sim 20$  SAO stars and of  $\sim 20$  field stars visible in the CCD images were measured on the POSS "E" plate. A linear least-squares fit of the reduced coordinates of the SAO stars to their measured positions was used to calculate the celestial coordinates of the field stars to a  $1\sigma$  precision of  $0.64''$  (Podobed 1965). Then, the coordinates of the field stars were used in a similar procedure to calculate the celestial coordinates of the sources in the error circle from the positions on the CCD images of the field stars and sources. The ultimate  $1\sigma$  precision of the fit was  $0''.74$ . The celestial coordinates of the detected sources and their distance from the OTS 1809 + 31 coordinates are included in Table 1. For OTS 1809 + 31, the coordinates of  $\alpha_{1950} = 18^h9^m26^s.29$ ,

$\delta_{1950} = 31^\circ23'19''.7$  were assumed (K. Hurley, private communication from R. Hudec).

#### c) Photometry

The magnitudes of the detected objects in the field were measured in two steps. The magnitudes of the bright objects in the *B*, *V*, *R*, and *I* images from June 21 were calibrated with the images of the Landolt standard star 110—340 taken that same night. The images from all three nights were added to obtain a set of *B*, *V*, *R*, and *I* stacked images, respectively. The magnitudes of the detected objects in the stacked images were calculated from the magnitudes of the bright objects in the images of June 21. All photometric measurements were made with FOCAS. A fixed, approximately circular aperture of 69 pixels (radius =  $3''.3$ ) was used for all images because it yielded the best overall signal-to-noise ratio. Airmass corrections were calculated from the standard Kitt Peak extinction coefficients (Barnes and Hayes 1984). The instrumental magnitudes were corrected to Mould *BVR*I magnitudes using the measured MASCOT color-corrections (M. Bautz 1988, private communication). The measured limiting magnitudes ( $3\sigma$  level of confidence) are  $m_B = 24.5$ ,  $m_V = 23.7$ ,  $m_R = 22.8$ , and  $m_I =$

TABLE 2  
MAGNITUDES OF THE 18 SOURCES DETECTED NEAR OTS 1809 + 31

Identification Number	<i>B</i>	$1\sigma$	<i>V</i>	$1\sigma$	<i>R</i>	$1\sigma$	<i>I</i>	$1\sigma$
1.....	21.31	0.17	19.66	0.13	18.69	0.11	17.08	0.08
2.....	21.92	0.17	20.89	0.13	20.23	0.11	18.99	0.08
3.....	21.27	0.17	20.53	0.13	20.31	0.11	19.33	0.08
4.....	21.92	0.17	20.50	0.13	19.57	0.11	18.63	0.08
5.....	21.91	0.17	20.26	0.13	19.29	0.11	17.99	0.08
6.....	22.92	0.18	21.74	0.14	20.83	0.12	19.10	0.08
7.....	24.33	0.28	23.02	0.19	21.73	0.15	20.34	0.10
8.....	22.66	0.17	21.80	0.14	21.09	0.13	20.15	0.09
9.....	24.72	0.33	23.36	0.24	22.12	0.18	20.87	0.12
10.....	23.78	0.21	22.33	0.15	21.27	0.13	20.59	0.10
11.....	24.40	0.28	22.98	0.20	22.01	0.17	20.92	0.12
12.....	22.90	0.17	21.28	0.13	20.37	0.11	19.22	0.08
13.....	23.55	0.20	22.40	0.16	21.41	0.13	20.86	0.13
14.....	22.80	0.18	21.89	0.14	21.59	0.14	19.84	0.08
15.....	23.15	0.18	21.76	0.14	20.92	0.12	19.89	0.09
16.....	21.53	0.17	20.10	0.13	19.28	0.11	18.18	0.08
17.....	> 24.5	0.3	23.16	0.20	22.70	0.26	21.47	0.19
18.....	24.52	0.28	22.78	0.17	22.15	0.19	21.31	0.15

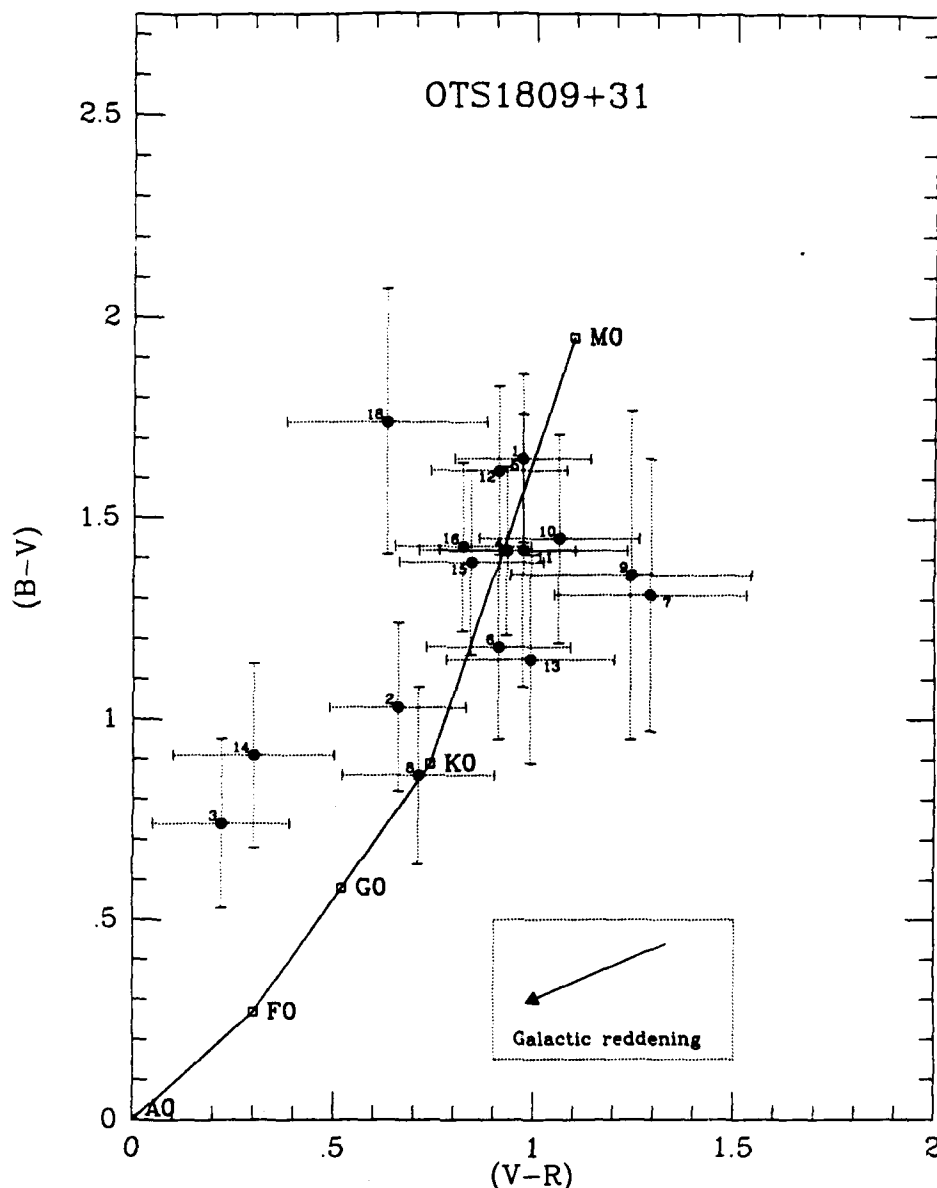


FIG. 1.—A plot of  $B-V$  vs.  $V-R$  for the 18 sources detected near OTS 1809+31. The main sequence, taken from Allen (1976) is indicated by the line in the figure. The reddening correction to the edge of the Galaxy was taken from Sandage (1972).

22.0. The color-corrected magnitudes are listed in Table 2 and  $(B-V)$  versus  $(V-R)$  is plotted in Figure 1.

## II. RADIO OBSERVATIONS

The OTS 1809+31 field was observed in 1987 April at the National Radio Astronomy Observatory<sup>2</sup> with the VLA in the 6 cm and 20 cm bands. The total observation times were 46 minutes at 6 cm and 21 minutes at 20 cm. The data were reduced and mapped with the AIPS program (AIPS Cookbook, NRAO 1986).

No significant sources were detected in the OTS 1809+31 field. The 6 cm map had an rms noise of  $32 \mu\text{Jy}$ , and the maximum detected flux for a point source in the field was  $83 \mu\text{Jy}$ . The 20 cm map had an rms noise of  $180 \mu\text{Jy}$ , and the

maximum detected flux for a point source in the field was  $460 \mu\text{Jy}$ . There were no extended objects detected in the center of either the 6 cm or 20 cm maps.

## III. ANALYSIS

The colors and celestial coordinates of the detected sources were analyzed for characteristics that might be associated with the quiescent counterpart of Hudec's optical flashes. However, as the nature, distance, and velocity of the quiescent source are all unknown, such an association is difficult to make. We have therefore examined the colors and coordinates of the detected sources in an attempt to identify one which is significantly different from the others, which are presumed to be field stars or galaxies.

The color-corrected color-color diagram in Figure 1 shows that the colors of objects within the  $41''$  error circle are consistent with those of field stars of type G-M (Allen 1976). If any of

<sup>2</sup> The National Radio Astronomy Observatory is operated by Associated Universities, Inc., under contract with the National Science Foundation.

the sources were extragalactic, the interstellar reddening would introduce a small color correction term (Sandage 1972) shown in Figure 1. Even with the color correction due to reddening, none of the sources have colors significantly different from those of field stars.

Figures 2-4 shows that none of the detected sources is consistent with the location of the optical transient (N.B.: There is a discrepancy of  $\sim 13''$  in the localization of OTS 1809+31 between this paper and that of Hartmann *et al.* 1989: in neither case, however, is there a source at the reported location of the optical transient). Therefore, either we have not detected the quiescent counterpart to the optical transient or the source of OTS 1809+31 has moved. If the source of OTS 1809+31 has moved and is one of the detected sources, a program of deep observations of the field in 1-2 yr will be sufficient to identify any of the 18 detected sources as high proper-motion objects (such "second epoch" observations of OTS 1809+31 have

already been made; Mock, Vanderspek, and Ricker 1989, analysis in preparation). Hudec (1987) has reported an upper limit on the proper motion of the source of OTS 1809+31  $2''.5 \text{ yr}^{-1}$  EW and  $5'' \text{ yr}^{-1}$  NS, which would be easily detectable over a baseline of 1 yr using current observational techniques.

#### IV. DISCUSSION

As no candidate quiescent counterpart to OTS 1809+31 has been established, the nature of the source of the optical transients remains a mystery. Assuming the optical transients had a duration of 1 minute (the upper limit of Hudec *et al.* 1987), the faintest of the three archived bursts had a peak magnitude of  $m_B \sim 11$ . If any of the 18 objects detected in the  $1'' \text{ yr}^{-1}$  error circle is the quiescent counterpart, the burst amplitude was  $\Delta B \geq \text{mag}$ ; if the source is in the error circle and has not been detected,  $\Delta B \geq 13.5 \text{ mag}$ .

Thus OTS 1809+31 probably underwent three bursts of

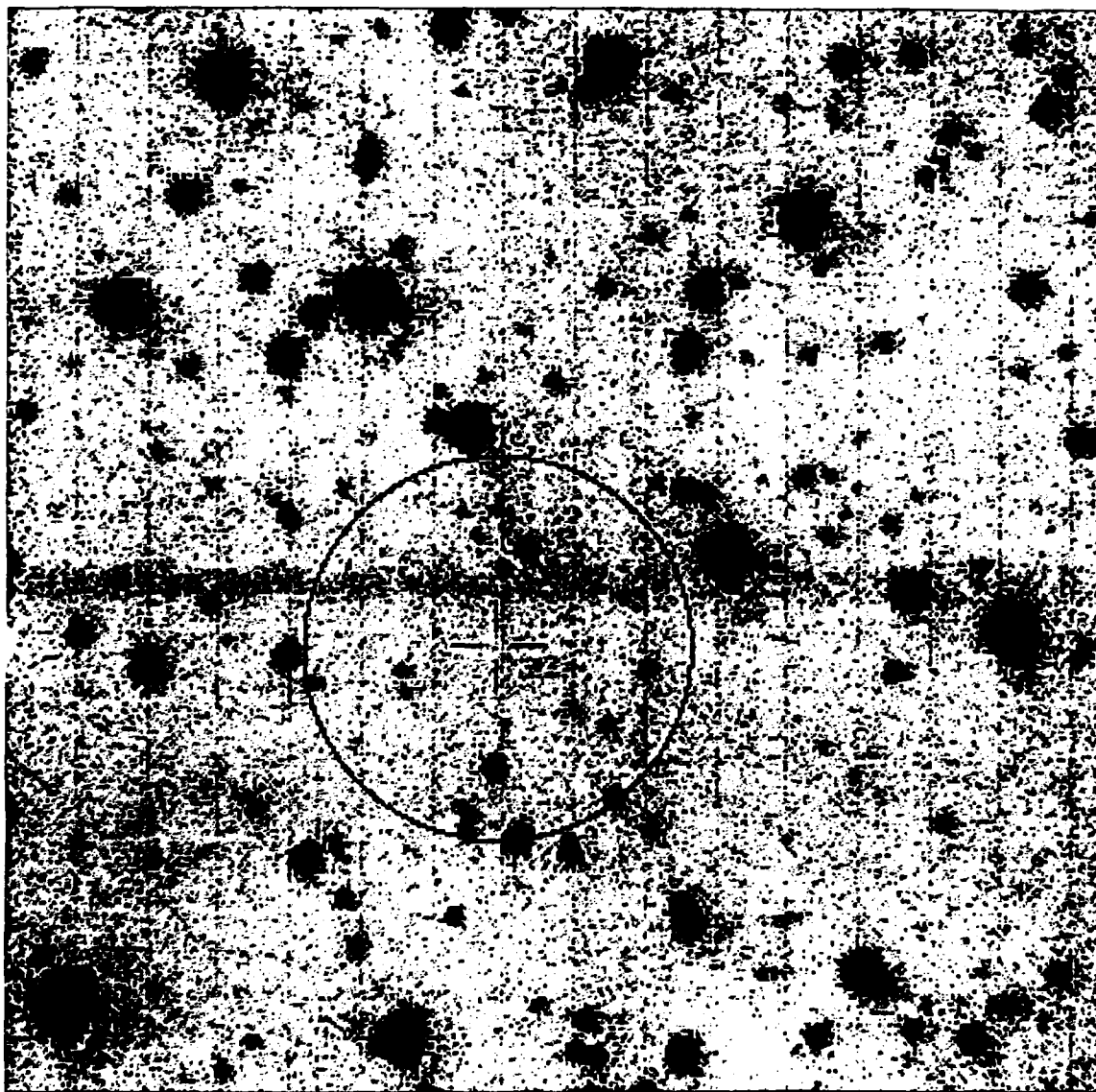


FIG. 2.—A  $3.5 \times 3.5$  Mould R finding chart for the field near the source OTS 1809+31. The circle is centered on the coordinates of 1809+ OTS ( $\alpha_{1950} = 18^{\text{h}}09^{\text{m}}26^{\text{s}}.29$ ,  $\delta_{1950} = 31^{\circ}23'19''.7$ ) and has a radius of  $41''$ . The horizontal artifact crossing the circle is a diffraction spike from the nearby fifth magnitude star 104 Her.



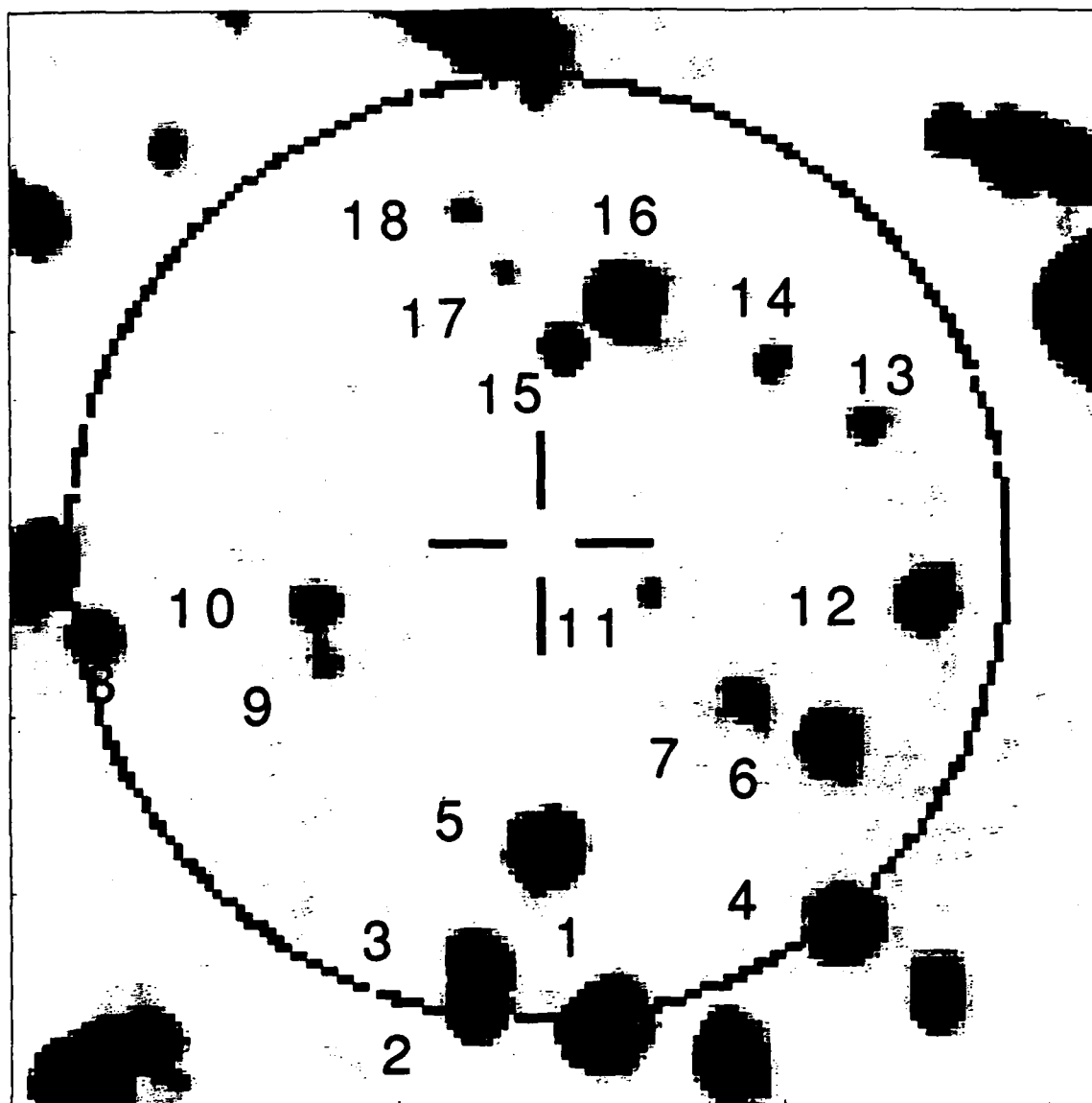


FIG. 3.—A 20 minute exposure in a Mould R filter of the field near OTS 1809+31. The circle is centered on the coordinates of 1809+31 OTS ( $\alpha_{1950} = 18^{\text{h}}09^{\text{m}}26^{\text{s}}.29$ ,  $\delta_{1950} = 31^{\circ}23'19''.7$ ) and has a radius of  $41''$ . The cross hairs are  $6''.6$  in length. The identification numbers of the 18 sources for which color information has been derived (Table 2 and Fig. 1) are given.

$\Delta B > 10$  mag of duration  $\tau_B < 60$  s, two of which occurred only months apart. Of all known sources of optical transients, only gamma-ray bursts are capable of such explosive bursts. Cataclysmic variables are known to produce large-amplitude bursts ( $\Delta B = 2\text{--}14$  mag), but have much longer burst durations ( $\tau_B = \text{months to years}$ ) (Robinson 1976). X-ray bursts (Grindlay *et al.* 1978) produce short-duration optical bursts, but the burst amplitude is only  $\Delta B = 1\text{--}2$  mag. Flare stars are capable of large-amplitude ( $\Delta B = 1\text{--}6$  mag) bursts with duration  $\tau_B = 10\text{--}60$  s and are known to recur often (Gurzadyan 1980). Although no flare of  $\Delta B = 10$  mag has yet been recorded, the possibility of its occurring should not be excluded.

Gamma-ray bursts (GRBs) are thought to produce large ( $\Delta B \sim 20$  mag) optical transients on short time scales ( $\tau_B < 300$  s) (Schaefer 1981; Schaefer *et al.* 1984). Several published models of GRBs explain optical radiation from a GRB source, both during the GRB (London and Cominsky 1983; Woosley

1984; Rappaport and Joss 1985; Melia 1987; Hartmann, Woosley, and Arons 1988) and independent of the GRB (Tremaine and Zytlow 1986). Although OTS 1809+31 is not thought to be associated with the nearby ( $\sim 6'$  distant) gamma-ray burst GRB 730325b (J. Laros, private communication), the source of the optical transients could be an undiscovered GRB source.

In addition to the above association, it is of course possible that OTS 1809+31 may be the prototype of an entirely new class of astrophysical phenomenon.

#### V. CONCLUSION

We have made deep *BVR* observations of a  $41''$  circle centered on the coordinates of OTS 1809+31. No source was detected ( $3\sigma$  level of confidence) at the coordinates of OTS 1809+31 brighter than  $m_B = 24.5$ ,  $m_V = 23.7$ ,  $m_R = 22.8$ , and  $m_I = 22.0$  in the optical and  $F_{6\text{ cm}} = 83\ \mu\text{Jy}$  and  $F_{20\text{ cm}} = 460$

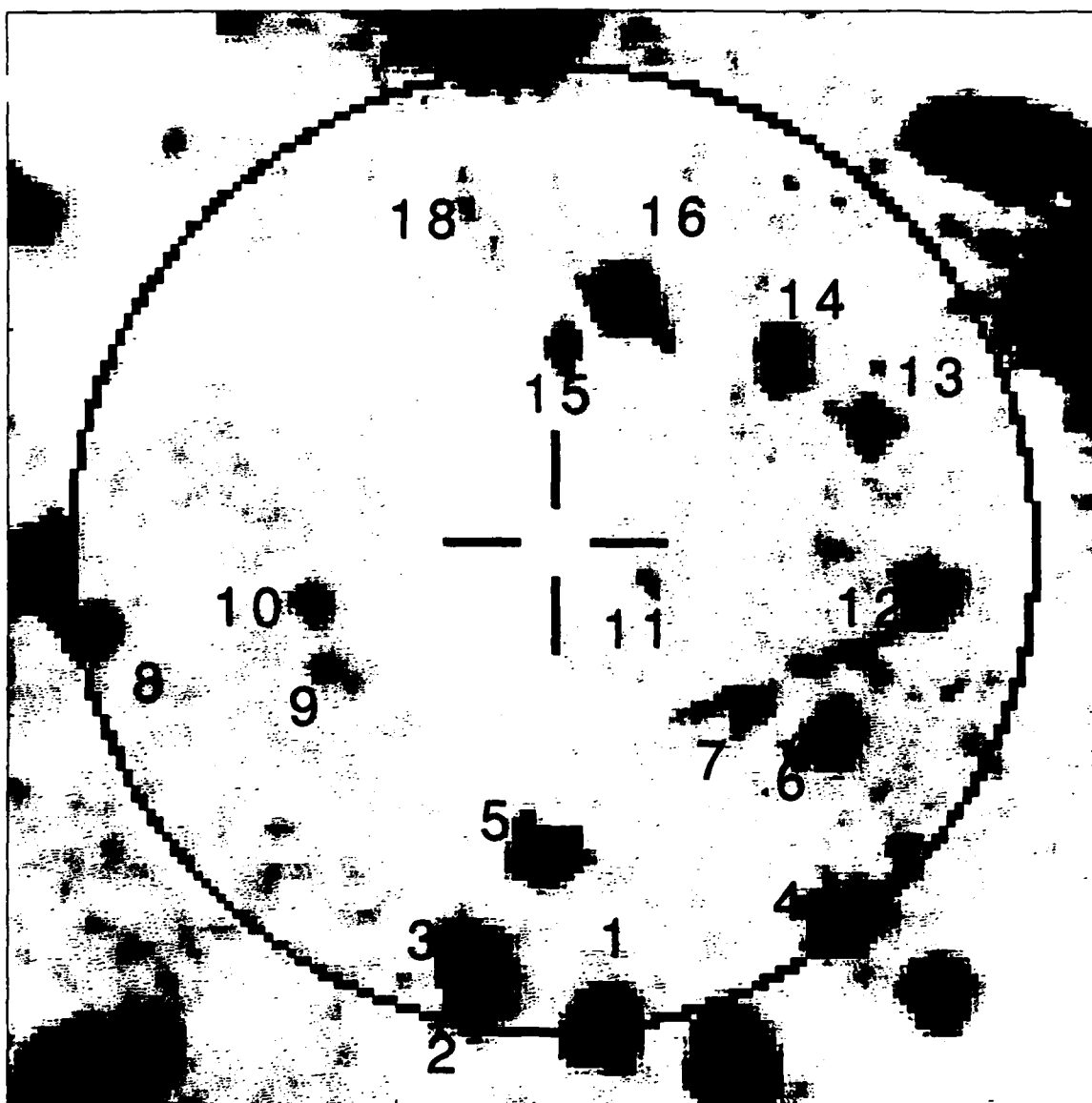


FIG. 4.—A 120 minute exposure in a Mould B filter of the field near OTS 1809+31. The circle is centered on the coordinates of 1809+31 OTS ( $\alpha_{1950} = 18^{\text{h}}09^{\text{m}}26^{\text{s}}.29$ ,  $\delta_{1950} = 31^{\circ}23'19''.7$ ) and has a radius of  $41''$ . The cross hairs are  $6.6''$  in length. The identification numbers of the 18 sources for which color information has been derived (Table 2 and Fig. 1) are given.

$\mu\text{Jy}$  in the radio. Eighteen sources were found to be within  $\sim 41''$  of the OTS 1809+31 coordinates, and none of the sources could be distinguished from field stars. The quiescent counterpart to OTS 1809+31 was not identified. If it is a high-proper-motion object and brighter than the threshold quoted above, observations in 1 or 2 yr should allow its motion to be detected.

We would like to thank K. Hurley for his communication of the precise coordinates of OTS 1809+31, as well as for useful discussions regarding the work of Hudec and Hartmann. We would also like to thank D. Hartmann, R. Hudec, and W. Wenzel for useful discussions and communications regarding

the astrometry of the OTS 1809+31 field. We would like to thank J. Klavetter for giving us part of his telescope time and for his assistance with the optical observations, M. Bautz for his help with FOCAS and with the MASCOT color corrections, J. Tonry for his help with the data reduction software, and A. Akmal for his help in analyzing the data. We extend our special thanks to the staff at the McGraw-Hill Observatory for their help with the optical observations, and the NRAO staff at the VLA Observatory for their help with the radio observations and analysis.

This research was supported in part by the National Aeronautics and Space Administration under grant NSG-7339.

#### REFERENCES

- Allen, C. W. 1976, *Astrophysical Quantities* (London: Athlone).  
 Baity, W. A., Hueter, G. J., and Lingenfelter, R. E. 1984, in *AIP Conf. Proc. 115, High-Energy Transients in Astrophysics*, ed. S. E. Woosley (New York: AIP), p. 434.  
 Barnes, J. V., and Hayes, D. S. 1984, *IRS Standard Star Manual* (Tucson: Kitt Peak National Observatory).  
 Grindlay, J. E., et al. 1978, *Nature*, **274**, 567.  
 Gurzadyan, G. A. 1980, *Flare Stars* (New York: Pergamon).

- Hartmann, D., et al. 1989, *Ap. J.*, **336**, 000.  
Hartmann, D., Woosley, S. A., and Arons, J. 1988, preprint.  
Hudec, R., et al. 1987, in *Adv. Space Res.*, Vol. 8, No. 2-3, *The Physics of Compact Objects Theory and Observations: Proc. of Symposium 27 of the COSPAR Plenary Meeting, Sofia, Bulgaria (1978 July)*, ed. N. E. White and L. G. Filipov (New York, Oxford: Pergamon), p. 665.  
Hurley, K. 1983, *Adv. Space Res.*, Vol. 3, No. 4, p. 163.  
Klebesadel, R. W., Strong, I. B., and Olson, R. A. 1973, *Ap. J. (Letters)*, **182**, L85.  
Landolt, A. U. 1983, *A.J.*, **88**, 439.  
Laros, J. G., et al. 1985, *Ap. J.*, **290**, 728.  
———, et al. 1987, *Ap. J. (Letters)*, **320**, L111.  
London, R. A., and Cominsky, L. R. 1983, *Ap. J.*, **275**, L59.  
Melia, F. 1987, preprint.  
NRAO 1986, *AIPS COOKBOOK* (Charlottesville: NRAO).  
Pedersen, H., et al. 1984, *Nature*, **312**, 46.  
Podobed, V. V. 1965, *Fundamental Astrometry* (Chicago: University of Chicago Press).  
Rappaport, S. A., and Joss, P. C. 1985, *Nature*, **314**, 242.  
Robinson, E. L. 1976, *Ann. Rev. Astr. Ap.*, p. 119.  
Sandage, A. 1972, *Ap. J.*, **178**, 1.  
Schaefer, B. E. 1981, *Nature*, **294**, 722.  
Schaefer, B. E., et al. 1984, *Ap. J. (Letters)*, **286**, L1.  
Tonry, J. 1988, *YARP User's Manual*.  
Tremaine, S., and Zytlow, A. N. 1985, preprint.  
Valdes, F. 1987, *FOCAS USER'S MANUAL* (Tucson: Kitt Peak National Observatory).  
Woosley, S. A. 1984, in *High-Energy Transients in Astrophysics. AIP Conf. Proc. 115*, ed. S. E. Woosley (New York: AIP), p. 485.

EDWARD A. AJHAR: MIT Center for Space Research, 70 Vassar Street, Room 37-524, Cambridge, MA 02139

PATRICK C. MOCK: MIT Center for Space Research, 70 Vassar Street, Room 37-538, Cambridge, MA 02139

GEORGE R. RICKER: MIT Center for Space Research, 70 Vassar Street, Room 37-535, Cambridge, MA 02139

ROLAND K. VANDERSPEK: MIT Center for Space Research, 70 Vassar Street, Room 37-527, Cambridge, MA 02139

## Appendix K

*Three Faint Objects in the Optical Error Region of GBS2251-02, 1989,*  
Vanderspek, R.K., Ricker, G.R.

# Three Faint Objects in the Optical Error Region of GBS2251-02

Roland K. Vanderspek and George R. Ricker

Center for Space Research of the Massachusetts Institute of Technology  
Cambridge, MA 02139

## Abstract

We report the detection of three faint objects in the error box associated with the archival optical flash discovered in the error region of the gamma-ray burst GBS2251-02 (Schaefer, *et al.* 1984). Magnitudes of these objects were determined in B and V bands; an R-band upper limit was also determined. The values of B-V and V-R for these objects, designated a, b, and c, are consistent with those of field stars. Further observations are recommended, especially in R-band, in a search for variability (see, *e.g.*, Schaefer, *et al.* 1984) and high proper motion (see Ricker, Vanderspek, and Ajhar 1986).

## I. Introduction

Since the first detection of a gamma-ray burst (GRB) in 1969 (Klebesadel, Strong, and Olson 1973), the nature of the source of GRBs has remained a mystery. Because the error region associated with the typical gamma-ray burst is large (measuring tens of arc-minutes to degrees on a side), deep searches for quiescent counterparts have been impractical. The few error regions that are small enough for a practical deep search have been studied in several wavebands; these studies have yielded no positive identification of a quiescent GRB source (see *e.g.* Chevalier, *et al.* 1981, Fishman, Duthie, and Dufour 1981, Laros, *et al.* 1981, Apparao and Allen 1982, Pizzichini, *et al.* 1985, Ricker, Vanderspek, and Ajhar 1986).

The discovery by Schaefer (1981) and Schaefer, *et al.* (1984), that transient optical radiation may be associated with GRBs has drastically improved the chances of detection of a quiescent GRB source, primarily because optical radiation can be localized much more accurately than gamma-rays. The error regions of the three optical transients discovered in archived images of GRB error regions are orders-of-magnitude smaller than the standard GRB error region, and so have lent themselves perfectly to a focussed deep search for a quiescent counterpart in several wave bands (Hjellming and Ewald 1981, Pizzichini, *et al.* 1982, Pedersen, *et al.* 1983, Schaefer, Seitzer, and Bradt 1983, Schaefer and Ricker 1983). Deep optical searches of two such error regions (associated with archived optical transients photographed in 1944 and 1928) have yielded several candidates for the quiescent counterpart (Pedersen, *et al.* 1983, Schaefer, Seitzer, and Bradt 1983); as yet, however, no positive identification has been made.

We report here the results of deep CCD observations of the error region of the archived optical flash discovered in the error region of GBS2251-02 (the 1901 optical transient of Schaefer, *et al.* 1984). A total of 6.0 hours of integration in three colors have resulted in the detection of three faint objects (designated a, b, and c) in this error region. Although these objects have colors consistent with those of field stars, further observations, especially in R-band, is warranted.

## II. Procedure

Data were taken during dark time on 30 September and 1 October 1986 with MIT's MASCOT (references) on the McGraw-Hill 2.4m telescope on Kitt Peak. The MASCOT's sensors are TI4849 virtual-phase CCDs, measuring 584x390 22.3  $\mu\text{m}$  pixels; the plate scale for these observations was 0."6/pixel. Data were taken through Mould B, Mould V, and Mould R filters; the total integration times in these filters were 2.40 hours, 2.09 hours, and 1.51 hours, respectively. Photometric and astrometric calibrations were made with exposures of the CCD photometry standard NGC2264 (Christian, *et al.* 1985).

The data consist of a series of 600-second exposures of the area near the optical error region. The

telescope was offset by  $\sim 30''$  in random directions between exposures. The random offsets allow a flat field to be created from the images themselves, using the technique of "median stacking." In median-stacking  $N$  images, the value of a pixel in the median-stacked image is the median of the values of that pixel in the  $N$  image frames. If the images are offset from one another, the median-stacked image is a representation of the typical sky during the time the images were taken.

The CCD images of the field were all bias-subtracted and segregated by color. In each color, a normalized copy of each image was used in the creation of a sky flat field via median stacking. Each field was then flattened by the sky flat. The flattened images were then aligned by integral pixel shifts and then stacked. The resultant B-band image is shown in Figures 1. The small rectangle indicates the error region of the optical flash detected by Schaefer, *et al.* (1984).

The B-band image of the optical error region revealed three faint objects, designated a, b, and c. Two of the objects were detected with FOCAS (reference); the third is faintly visible below the first two. Inspection of the V-band image revealed faint objects at the site of the B-band detections; FOCAS was able to detect the brightest of these objects (a). No distinct images were detectable on the R-band image.

The celestial coordinates of the a, b, and c were calculated in the B-band image with respect to  $\sim 10$  nearby stars, whose celestial coordinates are given in Ricker, Vanderspek and Ajhar (1986). The locations on the CCD image of the reference stars and a, b, and c were calculated by cross-correlating their images with that of an artificial star of similar point-spread-function. A linear least-squares fit of the locations of the reference stars to their celestial coordinates yielded the celestial coordinates of a, b and c in the B-band image; the precision of the fit was  $0.''4$ . These coordinates were used to calculate the locations of a, b, and c on the V-band and R-band images. (This was necessary primarily because of the indistinctness of the R-band images of a, b, and c. The centroids of the V-band images of a, b, and c, calculated both from the least-squares fit and directly from the images, compared well).

The brightnesses of a, b, and c were measured using simple box photometry centered on the measured or (in the case of the R-band images) calculated centroids of the sources. A curve of

growth (fraction of total starlight enclosed in the box versus box size) was calculated using field stars. The measured brightnesses of a, b, and c were corrected for finite box size and atmospheric effects.

The magnitudes of the sources were calibrated in B-, V- and R-bands using photometric reference stars in the field of NGC2264 (Christian, *et al.* 1985). The brightnesses of several stars (numbers 239, 243, 245 and 252) in the field of NGC2264 were measured, corrected for atmospheric effects and finite box size (as above) and used to calculate the relationship between measured brightness and stellar magnitude. This relationship was seen to be accurate to  $\pm 0.1$  magnitudes (??).

### III. Results

Table 1 lists the coordinates, magnitudes, color differences, and associated uncertainties of the three sources (a, b, and c) detected in the optical error region of GBS2251-02.

The B and V-band images of the optical error region show the three detected sources clearly; each source has been detected with  $S/N > 3$ . In the R-band image, however, the three sources are detected with  $S/N$  between 2.5 and 3.0; thus, the R-band magnitudes given in Table 1 are the three-sigma upper limits on source detection.

A color-color plot of the error region, calculated from the stacked images using FOCAS, is shown in Figure 2. Because of the rather large error bars associated with the values of B-V and V-R for a, b, and c, the colors of a, b, and c cannot be distinguished from those of field stars.

### IV. Conclusion

The present body of scientific knowledge on gamma-ray bursts does not exclude any of the three detected objects from being the quiescent gamma-ray burst source. All three sources have colors



consistent with those of other stars in the field. Further observations of these sources, especially in the red, are necessary for more conclusive results. In addition, deep exposures of this field at future epochs should be used in a search for high proper motion in these or other nearby objects.

## V. Acknowledgements

The authors gratefully thank Dr. Marshall W. Bautz for his assistance during the reduction and analysis of the data, specifically in the use of FOCAS and the concept of median stacking. Edward Ajhar was also helpful in discussions regarding the photometry and astrometry of the sources. Dr. Matthew Johns was helpful in learning how to use the new telescope operating system. Dr. John P. Doty and Nerissa Zolty contributed the median-stacking software. Dr. Doty was also present during several helpful discussions.

## V. References

Allen, C.W. 1976, "Astrophysical Quantities", London, The Athlone Press.

Apparao, K.M.V and Allen, D. 1982, *Astron. Astrophys.* **107**, L5.

Chevalier, C., *et al.* 1981, *Astron. Astrophys.* **100**, L1.

Christian, C.A, *et al.* 1985, *P.A.S.P* **97**, 363.

Fishman, G.J., Duthie, J.G., and Dufour, R.J. 1981, *Astrophys. Space Sci.* **75**, 135.

Helfand, D.J. and Long, K.S. 1979, *Nature* **282**, 589.

Hjellming, R.M. and Ewald, S.P. 1981, *Ap. J.* **246**, L137.

Klebesadel, R.W., Strong, I.B., and Olson, R.A. 1973, *Ap. J.* 182, L85.

Laros, J.G., *et al.* 1981, *Ap. J.* 245, L63.

Pedersen, H., *et al.* 1983, *Ap. J.* 270, L43.

Pedersen, H., *et al.* 1984, *Nature* 312, 46.

Pizzichini, G. 1982, in "Gamma-Ray Transients and Related Astrophysical Phenomena," eds. Lingenfelter, R.E., Worrall, D.M., and Hudson, H.S., AIP Conf. Proc. No. 77 (New York, AIP), 101.

Pizzichini, G., *et al.* 1985, *Ap. J.*, submitted.

Ricker, G.R., Vanderspek, R.K., and Ajhar, E.A. 1986, in *Advances in Space Research*

Schaefer, B.E. 1981, *Nature*, 294, 722.

Schaefer, B.E., Seitzer, P., and Bradt, H.V. 1983, *Ap. J.* 270, L49.

Schaefer, B.E., and Ricker, G.R. 1983, *Nature* 302, 43.

Schaefer, B.E., *et al.* 1984, *Ap. J.* 286, L1.

Valdes, F., *FOCAS Manual*

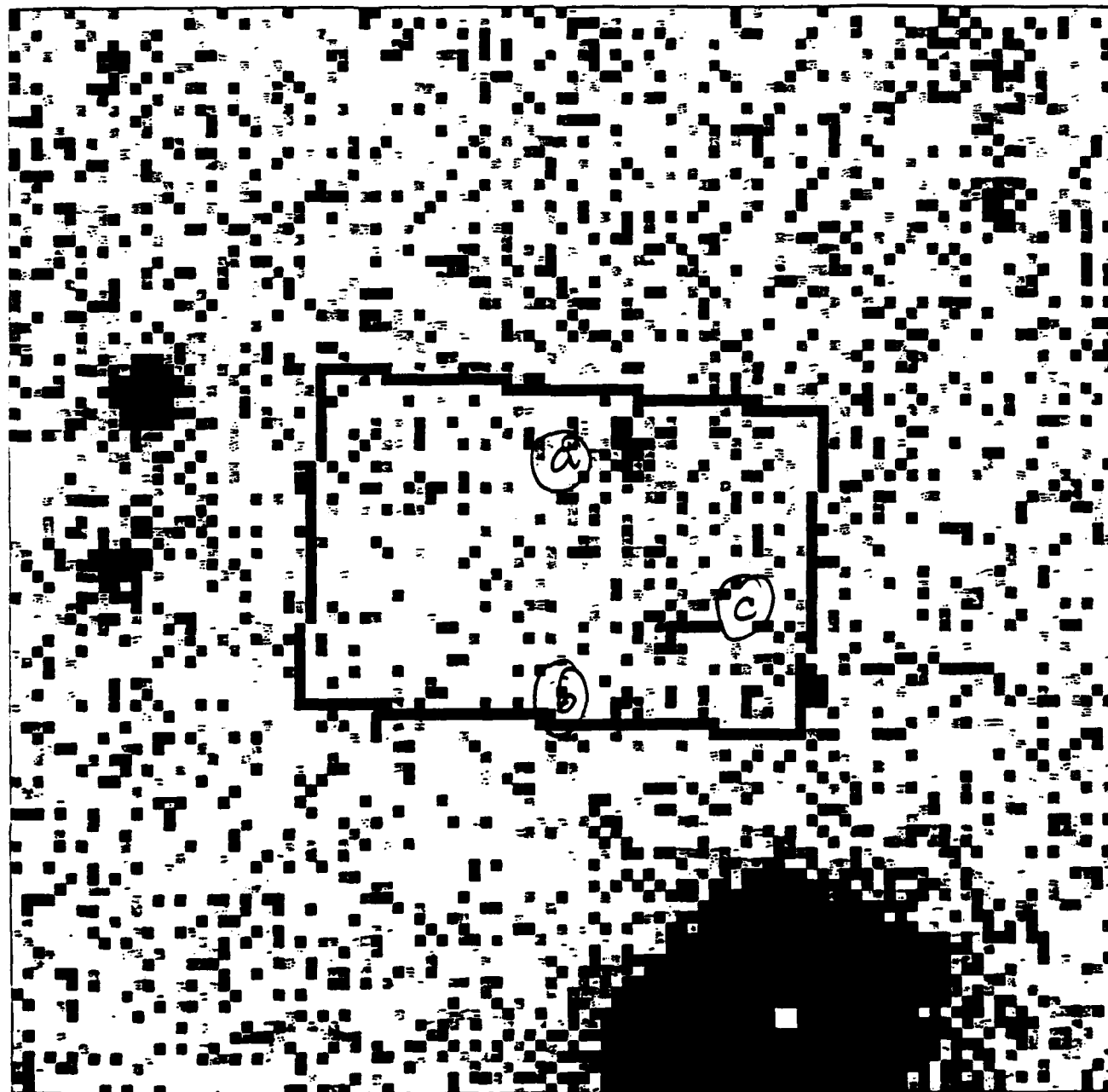
Star	R.A.	Dec.	B	V	R	B-V	V-R
a	22 <sup>h</sup> 51 <sup>m</sup> 38.00 <sup>s</sup>	-2°31'26.2"	23.8±0.2	23.5±0.3	>23.2±0.4	0.3±0.3	<0.4±0.5
b	22 <sup>h</sup> 51 <sup>m</sup> 38.03 <sup>s</sup>	-2°31'39.7"	24.1±0.3	23.6±0.3	>23.2±0.4	0.4±0.5	<0.4±0.5
c	22 <sup>h</sup> 51 <sup>m</sup> 38.19 <sup>s</sup>	-2°31'36.0"	24.0±0.3	23.5±0.3	>23.2±0.4	0.7±0.4	<0.3±0.5

Table 1: The celestial coordinates and B, V, and R magnitudes of the three faint objects (a, b, and c) detected in the optical error region of GBS2251-02, shown in Figure 1. The R magnitudes given are the three-sigma upper limits on source detection; it should be noted, however, that a,b, and c were all measured in the R-band with  $S/N > 2.5$ . The three-sigma upper limits in B- and V-bands are 24.1 and 23.8, respectively. The rms error in the celestial coordinates is 0."4.

## Figure Captions

**Figure 1:** The stacked B-band image of the optical error region associated with GBS2251-02. This image was made of a total of 8600 seconds of exposure with MIT's MASCOT on the McGraw-Hill 2.4m telescope on Kitt Peak. The rectangle indicates the error box associated with the optical transient discovered in this field by Schaefer, *et al.* (1984). The three sources detected in this image are labelled a, b, and c. Measured magnitudes and coordinates of these sources are given in Table 1.

**Figure 2:** A color-color diagram of thirteen field stars and the three sources a, b, and c detected in the optical error region associated with GBS2251-02. The values of V-R of a, b, and c are all upper limits.



430

330

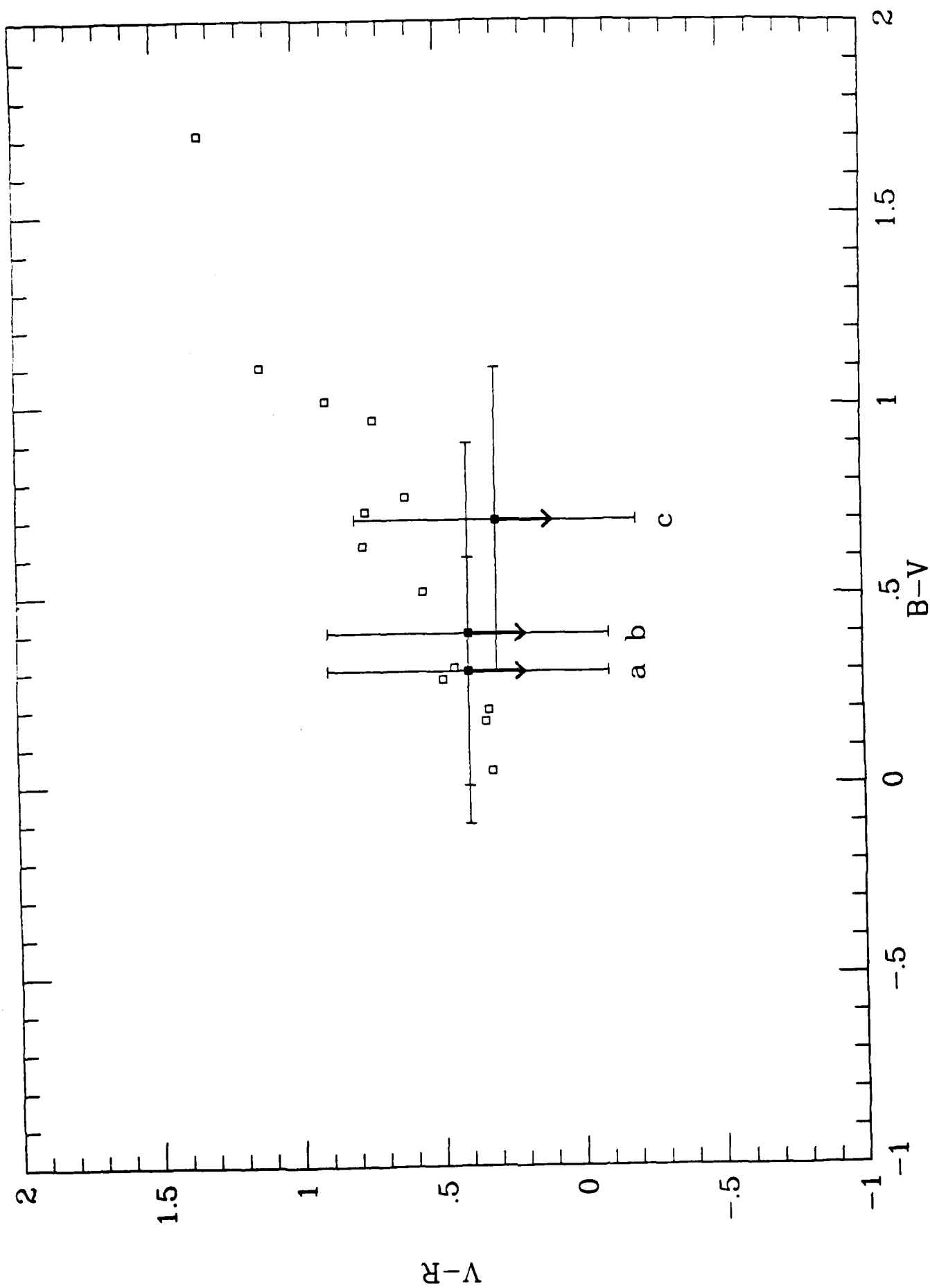
Stack.fig

0 20.0 35.0

200

300

Figure 1



## Appendix L

Vanderspek, Roland K. Ph.D. Thesis, Department of Physics,  
Massachusetts Institute of Technology, 1986. *The Explosive Transient  
Camera: A Wide Field Sky Monitor of Celestial Optical Flashes.*

**THE EXPLOSIVE TRANSIENT CAMERA:  
A WIDE-FIELD SKY MONITOR OF CELESTIAL OPTICAL FLASHES**

by

**ROLAND KRAFT VANDERSPEK**

A.B., University of California, Berkeley (1980)

**SUBMITTED TO THE DEPARTMENT OF PHYSICS  
IN PARTIAL FULFILLMENT OF THE  
REQUIREMENTS OF THE DEGREE OF**

**DOCTOR OF PHILOSOPHY**

at the

**MASSACHUSETTS INSTITUTE OF TECHNOLOGY**

© Massachusetts Institute of Technology, 1985



Webster's New Collegiate Dictionary defines *plenary* as  
"complete in every aspect: absolute, unqualified."

Roget's International Thesaurus, Third Edition, adds:  
(56.12)

full, filled, replete, ample, good, plump, *plenary*, pleny  
[naut.], pregnant, flush, round; brimful, brimming; chock-  
full, chuck-full, choke-full, chug-full [dial.], chock or  
chuck [coll.], cram-full, topfull; jam-full, cramp-full,  
cram-jam-full, jam-packed, pack-jammed, jam-up, full-up  
[all slang]; stuffed, packed, crammed; bursting, ready to  
burst, fit to bust [slang]; as full as a tick, as full as a  
vetch, as full as an egg is of meat, packed like sardines or  
herrings; replete with, crawling or oozing with; saturated,  
capacitated [coll.]; congested, overfull.

The Explosive Transient Camera:  
A Wide-Field Sky Monitor of Celestial Optical Flashes

by

ROLAND KRAFT VANDERSPEK

Submitted to the Department of Physics on November 14, 1985,  
in partial fulfillment of the requirements for  
the Degree of Doctor of Philosophy in Physics

ABSTRACT

The discovery in 1973 (Klebesadel, et al., 1973) of the phenomenon of gamma-ray bursts (GRBs), seen as short (durations of 1-60 seconds), sudden (risetimes of less than a second) outbursts of  $\gamma$ -rays from deep space, has led to intense efforts to discover the source of these mysterious emissions. Observations in the last ten years with a series of interplanetary and terrestrial satellites have led to hundreds of detections of GRB events. Analyses of observational data support the hypothesis of a highly-magnetized ( $10^{12-13}$  Gauss) neutron star as the source of GRBs, yet the low precision of localization of most GRBs (tens of arc-minutes to degrees) has hindered the a posteriori identification of a quiescent counterpart to a GRB source in any energy band. To date, no convincing quiescent optical counterparts to GRB sources have been established. The discovery by Schaefer (1981) of transient optical radiation from a small GRB error region, recorded on an archived photographic plate in 1928, led to the hope the precision of localization of GRB sources might be greatly improved through the detection of optical radiation emitted during the GRB.

In 1982, the *Explosive Transient Camera* (ETC), a wide-field sky monitor sensitive to celestial optical flashes with risetimes of the order of one second, was proposed as a ground-based counterpart to gamma-ray satellites with the expressed intent of detecting optical radiation from outbursting GRBs (Ricker, et al., 1983). In 1983, construction was begun of a sub-unit of the plenary ETC, designed to test the feasibility of a full wide-field ETC. This thesis discusses the motivation, design, construction and implementation of the ETC test unit. Calculations of estimated event rates from several known sources of celestial optical transients in the plenary ETC are presented. In addition, this thesis includes the presentation and discussion of results from observations made the test unit, which comprise *the most complete wide-field search for celestial optical flashes to date*. The observations with the ETC test unit covered a solid-angle-time product of 3.0 steradian-hours and included the error regions of GRB1200+21 (24 November 1978), GRB1152+20 (1 January 1979) and GRB1140+20 (2 May 1979) (Baity, et al., 1984) as well as the flare stars V475 Her, Ross 867 and Ross 868 (Gurzadyan, 1980). The observations were expected, based on assumptions presented within, to have detected optical transient events from 1.5 flare stars and 0.008 GRBs. These observations resulted in the determination of a new upper limit on the celestial optical flash rate of 2.2 optical flashes per hour per steradian at  $10^{\text{th}}$  magnitude, lower by a factor of 10 than the previous best upper limit determined by Schaefer, Vanderspek, Bradt and Ricker (1984).

Thesis Supervisor: Dr. George R. Ricker

Title: Senior Research Scientist

# TABLE OF CONTENTS

Chapter 1: Introduction .....	1
Chapter 2: Motivation .....	2
Chapter 3: Theories of Radiation from GRBs .....	9
Chapter 4: The Concept of the Explosive Transient Camera .....	19
Chapter 5: ETC Operations .....	24
Chapter 6: The ETC Test Instrument .....	27
Chapter 7: The ETC Overseer Computer .....	31
Chapter 8: The ETC Trigger Processor .....	39
Chapter 9: The Instrument Control Electronics .....	46
Chapter 10: Expected Results .....	51
Chapter 11: Results of Observations with the ETC .....	57
Chapter 12: Future Work .....	68
Chapter 13: Acknowledgements .....	72
References .....	74
Appendix A: The Overseer Computer Software .....	78
Appendix B: The Trigger Processor Software .....	79
Appendix C: The Instrument Control Electronics Software .....	80
Appendix D: ETC-specific Driver Code .....	81
Appendix E: ETC Computational Algorithms .....	82
Appendix F: Thermal Analysis of the ETC .....	83

## CHAPTER 1

### Introduction

In 1969, orbiting  $\gamma$ -ray satellites intended to detect  $\gamma$ -rays from nuclear explosions in near-Earth orbit detected unusual, sudden flashes of  $\gamma$ -rays from deep space (Klebesadel, et al., 1973). Analysis of the flashes showed that 1) the bursts were not created by the interaction of high-energy particles with the  $\gamma$ -ray detectors and 2) that the Earth or Sun were not the sources of the  $\gamma$ -rays, and therefore that the  $\gamma$ -rays were cosmic in origin. Several hundred of these flashes, dubbed gamma-ray bursts (GRBs), have been detected by balloon- and satellite-borne  $\gamma$ -ray detectors since 1969. Despite the large number of GRB detections, the source of GRBs has largely remained a mystery, primarily due to the low precision of localization of most GRBs.

Many of the observed characteristics of GRBs provide clues to the source, location and mechanism of GRB production. The short risetimes of many GRBs (typically 10-200 ms; one lower than 200  $\mu$ s; Mazets, et al., 1981) point to a small  $\gamma$ -ray emitting region ( $<60$ -1000 km). This fact, combined with the detection in some GRB spectra of line features which can be interpreted as gravitationally-redshifted  $e^+e^-$  annihilation radiation (near 400 keV) and cyclotron resonance features (near 50 keV) and the detection of pulsations in the tails of a few GRB light curves suggest that a GRB originates near the surface of a highly-magnetized ( $10^{12}$  Gauss) neutron star. Due to the large error regions of typical GRBs, this association has not been confirmed by observations of a quiescent GRB source.

In 1981, B. Schaefer of MIT discovered an optical flash on an archived photographic plate in the atypically-small error region of a known GRB (Schaefer, 1981). This discovery made clear the possibility that GRBs may emit optical radiation during outburst. Schaefer's finding is very significant, since the detection of optical radiation from an outbursting GRB would permit precise localization of the burst source, thus leading to more meaningful follow-up observations in all energy bands. Since 1981, two further archived optical flashes from GRB error regions have been found by Schaefer (Schaefer, et al., 1984), further supporting the claim that GRB sources can emit bursts of optical radiation.

In 1983, a program was initiated at MIT to design and construct an instrument capable of detecting and precisely locating optical flashes from GRBs in real time. This instrument, known as the Explosive Transient Camera (ETC), was to be a wide-field sky monitor sensitive to tenth-magnitude optical flashes with risetimes of the order of one second. The instrument would operate automatically, and would be able to provide the location of an optical flash with sub-arc-minute precision within a fraction of a second after its detection (Ricker, et al., 1984).

The design, construction and testing of the initial stage of the Explosive Transient Camera is the subject of this thesis. The following four chapters will discuss the motivation and concept of the ETC, as well as some of the possible mechanisms for the production of optical light from GRBs. Thereafter, the ETC instrumentation will be presented in detail. Finally, estimates of event rates from known possible sources of optical flashes, both celestial and terrestrial, are presented, as well as the results of observations made with the ETC test unit. These observations, made during March and May of 1985, comprise the *most sensitive wide-field search for optical flashes made to date*. These observations have defined an upper limit of 2.2 optical flashes per hour per steradian at a visual magnitude of  $m_v < 10$ , a factor of 10 lower than the previous best limit defined by the work of Schaefer, Vanderspek, Bradt and Ricker (1984).

## CHAPTER 2

### Motivation

#### Introduction

This chapter is intended to give the reader an overview of the history and morphology of detected gamma-ray bursts. More detail on GRB morphology can be found in reviews by Mazets (1981), Cline (1983), and Hurley (1983). Following the morphology, a review of observations at quiescence of GRB sources at other energies is given, with an emphasis on follow-up work in the optical band. The chapter concludes with a comparison of present methods of searching for optical flashes from GRBs, indicating the pressing need for a dedicated all-sky monitor for optical flashes, such as the Explosive Transient Camera.

#### 2.1. Gamma-Ray Burst Morphology

Gamma-ray bursts were first discovered in 1973 by the Los Alamos Group from data taken with Air Force Vela satellites to detect  $\gamma$ -rays from nuclear explosions in space (Klebesadel, et al., 1973). In the discovery paper from the Los Alamos group, a GRB was reported as generating an intense burst of gamma-rays (fluence  $S \geq 10^{-5}$  erg cm $^{-2}$ ) with a risetime of a fraction of a second. Since 1969 a series of interplanetary and terrestrial satellites, (including the Vela satellites, the Soviet Venera spacecraft, the Pioneer Venus Orbiter, ISEE-3, Prognoz 7, Helios-B, IMP-6 and IMP-7) have detected more than 100 bursts (Cline, 1983; Baity, 1984).

##### 2.1.1. Characteristics of Typical GRB

The characteristics of detected GRBs vary over a wide range: it is therefore difficult to present information about a "typical" GRB. (See Baity, et al. (1984) and references within for a complete review of GRB observations). GRBs as a group can be described by characteristics common to all bursts and the range of values of these characteristics in detected bursts. The GRBs detected to date are distributed roughly isotropically over the celestial sphere (Hurley, 1983). The peak fluxes of detected GRBs range from  $10^{-2}$  to  $10^{-7}$  erg cm $^{-2}$ s $^{-1}$ . The fluences,  $S$ , of all GRBs detected to date are between  $10^{-3}$  and  $10^{-8}$  erg cm $^{-2}$ . The number of burst sources  $N(>S)$  having a fluence greater than a value  $S$  roughly follows a power law,  $N(>S) \sim S^{-\alpha}$ , where  $\alpha \approx 3/2$  for values of  $S > 10^{-5}$  erg cm $^{-2}$  and upper limits indicate  $\alpha \approx 0.7$  for  $S < 10^{-5}$  erg cm $^{-2}$ . A plot of  $\log N(>S)$  vs.  $\log S$  is shown in Figure 2.1.

The light curves of most GRBs are characterized by a fast rise (risetimes of  $\sim 50$ -1000 ms) and an exponential decay (decay times of 1-30 seconds). Total durations of typical GRBs range from less than one second to minutes. A few GRB sources have shown periodic pulsations (periods of 4-10 seconds) during the decay of the brightness of the GRB (Mazets, et al., 1979b; Wood, et al., 1981). A few "typical" GRB light curves are shown in Figure 2.2.

The spectra of GRBs can, in general, be fit by a power-law function,  $F(\nu) \sim \nu^{-1} e^{h\nu/kT}$ , where  $F(\nu)$  is the flux (in cm $^{-2}$ s $^{-1}$ erg $^{-1}$ ) of  $\gamma$ -rays of energy  $h\nu$ . Typical GRB temperatures ( $kT$ ) fall in the range of 100 to 500 keV. The spectra show substantial time variations, presumably due to changes in the physical characteristics of the  $\gamma$ -ray source (Mazets, et al., 1981). Some GRB spectra show line features at energies in the range of 30-70 keV. Roughly 15% of all GRB spectra show an emission feature near 400 keV (Cline, 1983). A few characteristic GRB spectra are shown in Figure 2.3.

These characteristics allow one to make a rough sketch of the source of the GRB. Many workers in the field argue that GRBs are associated with neutron stars with strong ( $\sim 10^{12}$  Gauss) magnetic fields,

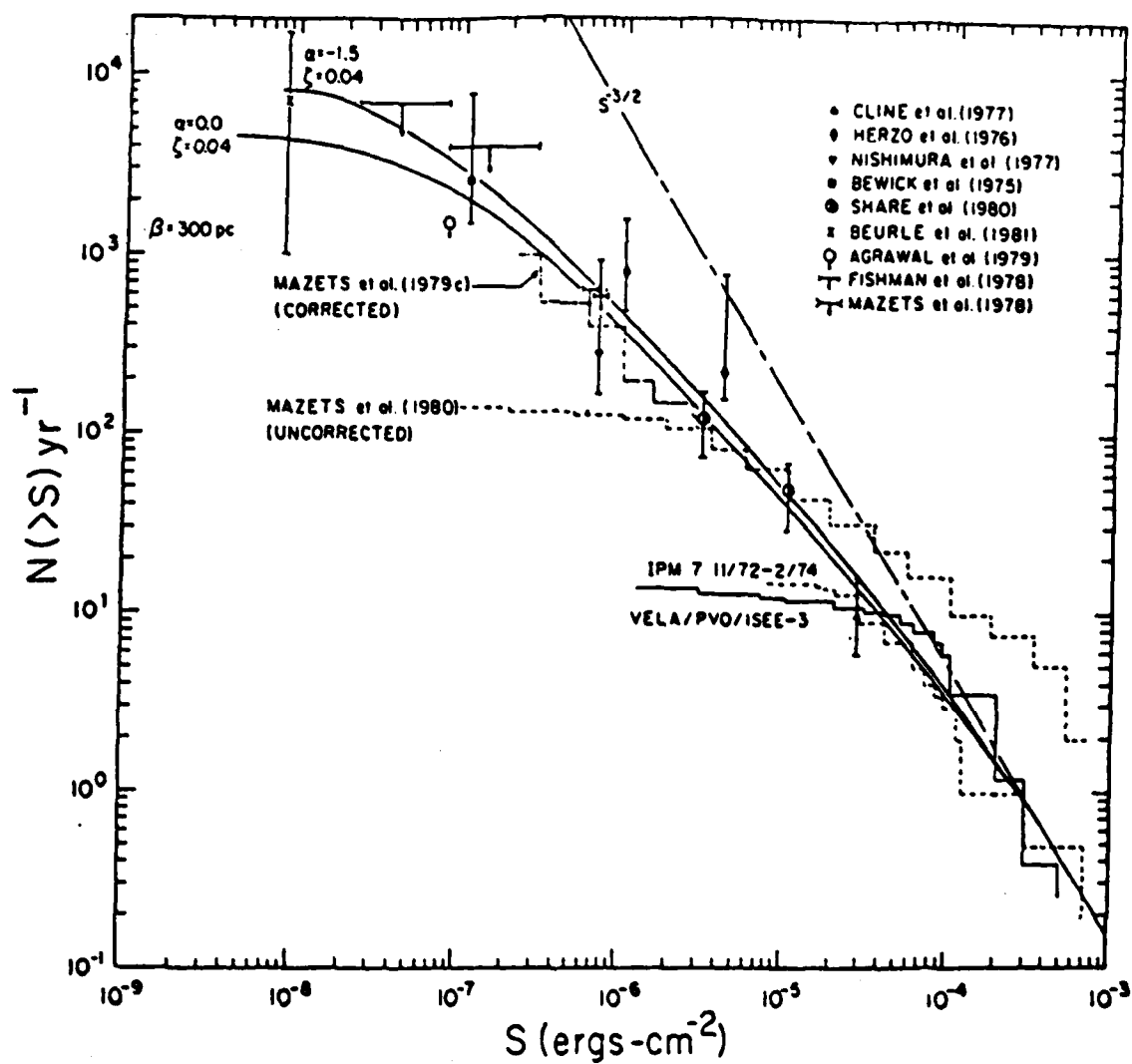


Figure 2.1: The  $\log N(>S) - \log S$  curve for detected GRBs, taken from Jennings (1982). The solid lines indicate the results of disk models of GRBs with an intrinsic luminosity distribution.

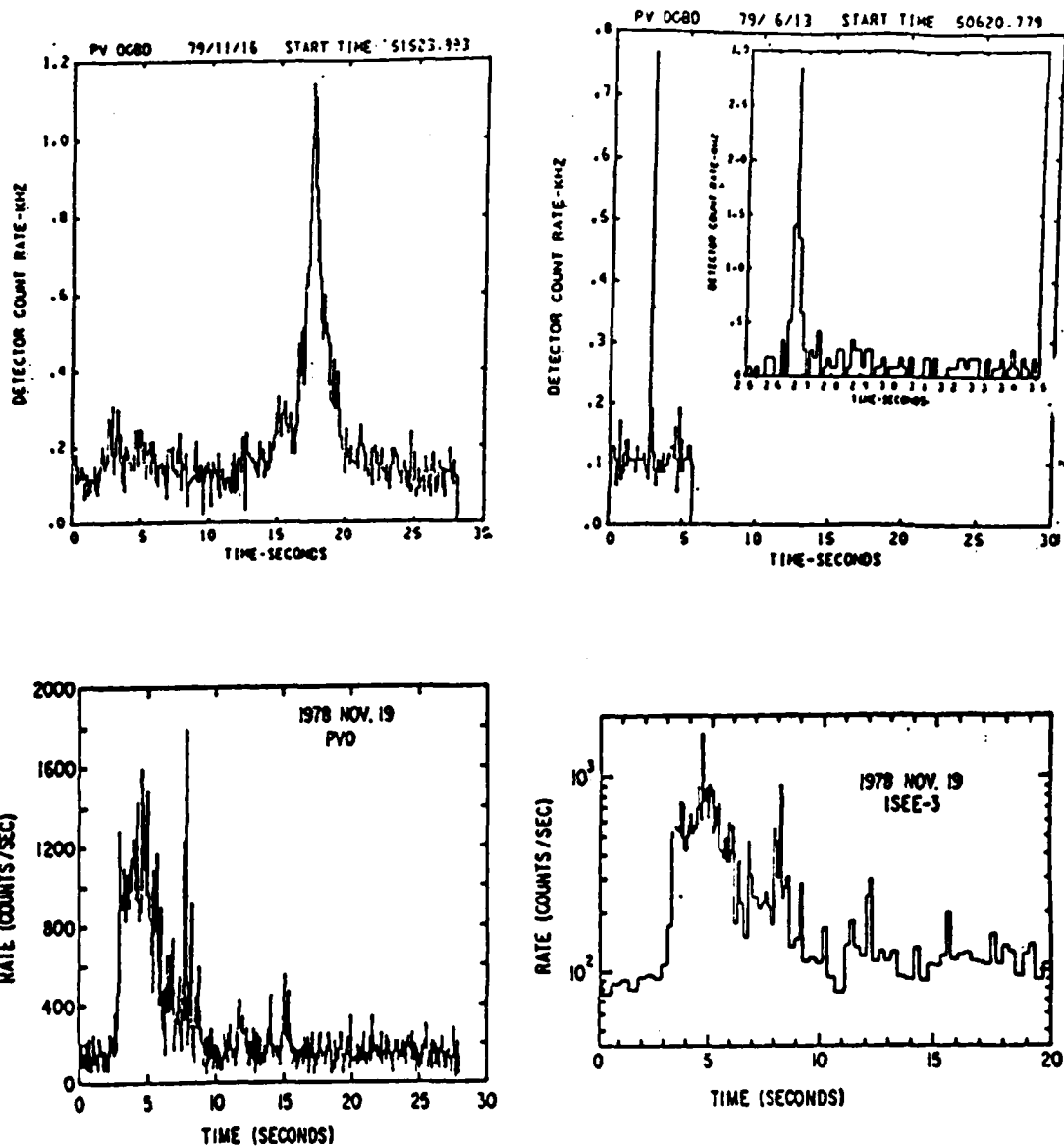


Figure 2.2: Four GRB light curves. Figures (a) and (b), taken from Klebesadel (1982) and Cline (1983) show the lightcurves with the slowest and second-fastest rise to peak recorded to date. Figures (c) and (d) are two views of a GRB whose lightcurve is typical of the GRB phenomenon.

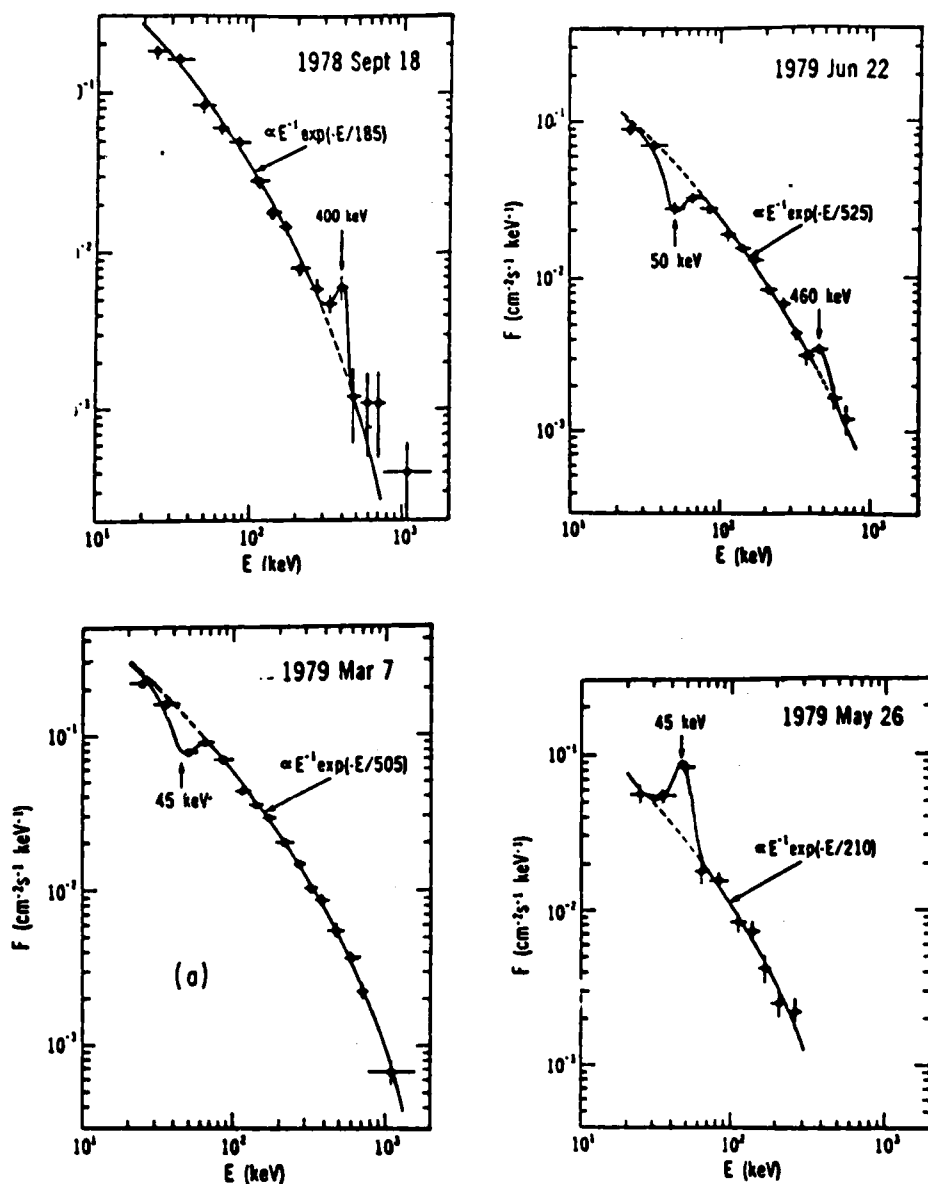


Figure 2.3: Four GRB spectra, taken from Teegarden (1982). The spectra show the standard  $(1/E)\exp(-E/kT)$  dependency, along with line features present in ~15% of all GRB spectra. The 30-70 keV feature is interpreted as being due to cyclotron radiation in a high magnetic field and the ~400 keV feature as 511 keV positron-electron annihilation line gravitationally-redshifted in the gravitational field of a neutron star.



based on the following interpretations:

- 1) The short burst risetimes ( $\sim 50$  ms) point to a source size  $< 10^9$  cm.
- 2) The line features near 30-70 keV can be interpreted as the cyclotron resonance features in a  $10^{12}$ - $10^{13}$  Gauss magnetic field.
- 3) The emission features near 400 keV are consistent with the 511 keV  $e^+e^-$  annihilation line gravitationally redshifted in the field of a neutron star.
- 4) The brief pulsations (with periods of 4-10 second) are reminiscent of a slow pulsar.

### 2.1.2. GRB0528-66: An Atypical GRB

On 5 March, 1979, nine interplanetary and terrestrial satellites detected an exceptionally strong GRB from the direction of the Large Magellanic Cloud (Mazets, et al., 1979b). This burst, designated GRB0528-66 from its celestial coordinates, has significantly added to the controversy surrounding GRBs because of its many unique characteristics (Cline, 1982):

- 1) A very fast risetime (200 microsecond) - - shorter than any other burst.
- 2) An extremely high peak flux ( $2 \times 10^{-3}$  erg/cm<sup>2</sup>/s) - - an order of magnitude higher than the flux detected from any other GRB.
- 3) A very soft spectrum ( $kT_{\text{burst}} \sim 30$  keV) - - softer than that of almost all other GRBs.
- 4) Prolonged, repetitive afterpulses ( $\sim 8$  second period), lasting much longer than those of any other detected GRB (see Figure 2.4).
- 5) The possible association of the GRB source with a known celestial object: the error box of GRB0528-66,  $20'' \times 80''$  in size, contains part of the supernova remnant N49 in the Large Magellanic Cloud.
- 6) The burst source has been seen to recur more than a dozen since the initial burst, although none of the recurrences had a fluence greater than  $10^{-3}$  of the original burst (Golenetskii, et al., 1984). It is the only GRB source to recur more than a few days after the original burst.

The unique characteristics of GRB0528-66 have lent much support to the theory that a neutron star is the source of a GRB. In particular, the short risetime ( $< 0.2$  ms, limited by instrument precision) points to an emission source size of less than 60 km. In addition, the strong 8-second pulsations favor a rotating neutron star as the source of the burst. Finally, the association of the error region with the supernova remnant N49 - - if it is true - - strongly favor the neutron star remnant of the supernova as the source of the GRB.

It is this last point - - the possible association of the GRB with the LMC - - that has stirred the most controversy. The probability of the GRB error region randomly overlapping the supernova remnant is small. Yet, if the association is correct, the total energy of the burst was prodigious: the total energy would have been  $5 \times 10^{44}$  ergs, assuming isotropic emission, and the average luminosity during the first 120 ms of the burst would have been  $\sim 3 \times 10^{45}$  ergs/second, or  $\sim 10^{12} L_{\text{sun}}$ . The possible association of GRB0528-66 with the LMC lends support to the theory that GRBs are generally located at

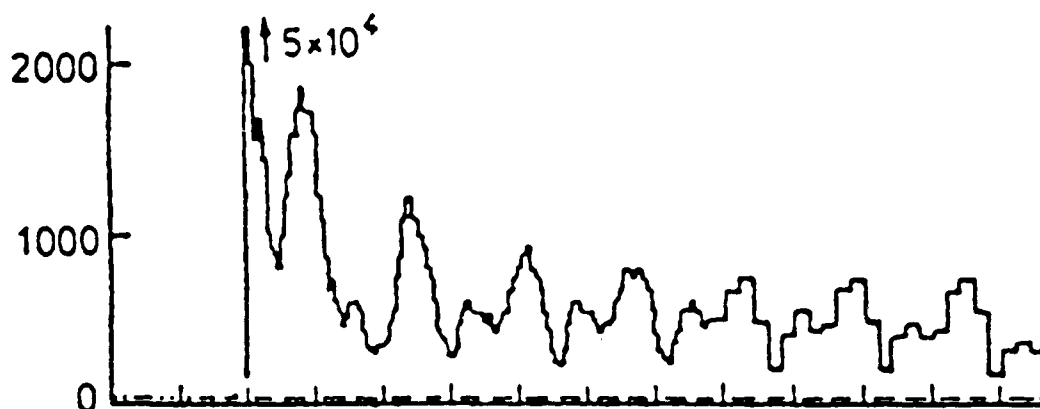
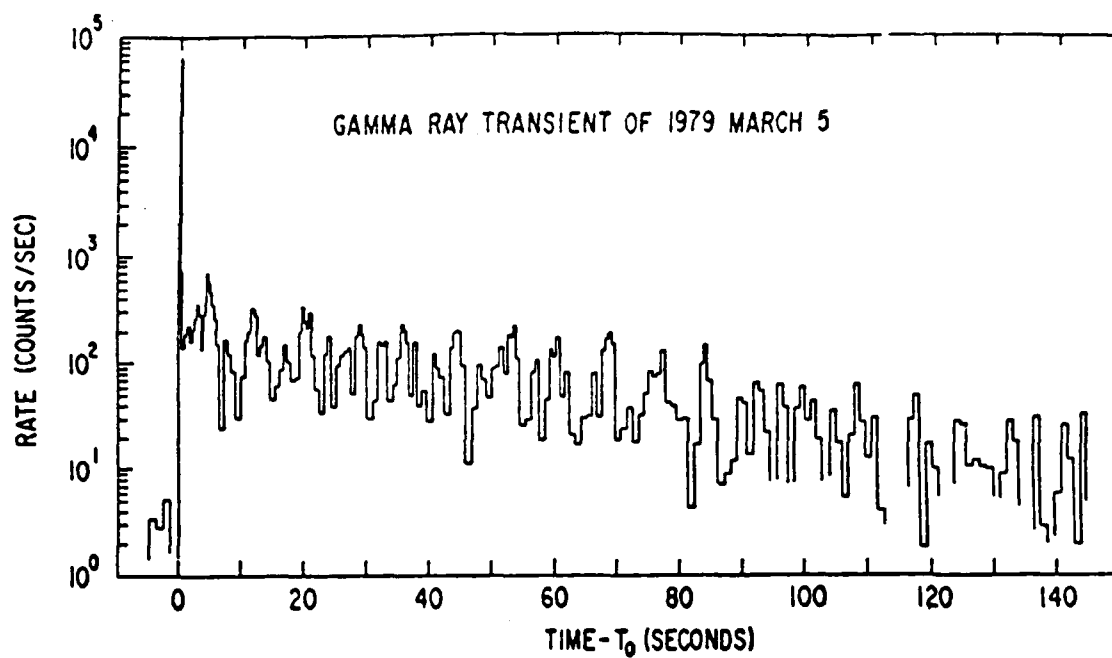


Figure 2.4: The light curve of the peculiar GRB0528-66 (5 March 1979) as seen by ISEE-3 (above) and Venera 12 (below; both taken from Cline (1983)). Note the fast rise to peak, the high peak flux and the strong 8s pulsations.

distances of 50-500 kpc from the Earth: this idea is discussed further in section 2.4.

### 2.1.3. GRB source localization

The precision of localization of  $\gamma$ -ray detectors used on balloon gondolas and  $\gamma$ -ray satellites is generally low. Consequently, a single  $\gamma$ -ray satellite detecting a GRB cannot provide the precise coordinates of the outbursting GRB. The celestial coordinates of an outbursting GRB can be determined much more precisely by measuring the difference in arrival times of  $\gamma$ -rays at three or more satellites detecting the burst. The precision of the localization of the burst increases with the number of detecting satellites (see Figure 2.5 and its caption). Typical error regions determined by this method have dimensions ranging from tens of arc-minutes to degrees. Several ( $\sim 10$ ) bursts have been detected by many widely-separated satellites and have been localized to a precision of a few arc-minutes. Such small error regions allow for reasonable searches for the quiescent GRB source. Despite this, no GRB has yet been positively associated with any other celestial object (see section 2.2).

### 2.1.4. GRB Source Distances

Since no definite correlation exists between a GRB source and another celestial object, the distances to GRB sources are unknown. An estimate of source distance or the population as a whole can be made by determining the spatial distribution of the GRB population: whether the GRBs we see are generally local ( $d < 300$  pc), belong to a disk or halo population, or are extragalactic.

Some insight into the question of GRB source distances can be gained by examining the  $\log N(>S) - \log S$  distribution of GRBs, shown in Figure 2.1. Jennings and White (1980) and Jennings (1982) have attempted to reconcile models of GRB source distribution with the  $\log N(>S) - \log S$  curve. An infinite spherical distribution of GRB sources around the Sun follows an  $N(>S) \sim S^{-3/2}$  function, while a disk population follows  $N(>S) \sim S^{-1}$ . The  $S^{-3/2}$  function is superimposed on Figure 2.2. The actual  $\log N - \log S$  curve roughly follows  $N(>S) \sim S^\alpha$ , with  $\alpha \approx 0.7$  for  $S < 10^5 \text{ erg cm}^{-2}$ . The monoluminosity models of GRB distribution of Jennings and White (1980) could not account for this value of  $\alpha$ . Jennings (1982) has calculated a theoretical  $\log N - \log S$  distribution based on a galactic population of GRB sources with an intrinsic luminosity function. His calculations show that the observed  $\log N(>S) - \log S$  curve can be explained by varying parameters in his model: most notably, biasing the concentration of the luminosity function of GRBs toward low-luminosity bursts permitted a good match to the observed  $\log N(>S) - \log S$  curve. However, in a recent paper, Jennings (1985) questions the validity of using GRB statistics in determining the distance scale to GRBs.

The nearly-isotropic distribution of GRB sources on the celestial sphere is an indication of the nature of the GRB population (Jennings, 1982). This isotropy favors models that visible GRBs belong to either a local population of GRB sources ( $d < 200$  pc) or that place GRB sources in an extended halo about the galaxy ( $d \sim 50\text{-}200$  kpc). A disk population of visible GRBs is excluded by the lack of concentration of GRBs in the plane of the galaxy. Models of GRB source population in a halo of  $\sim 10$  kpc radius about the center of the galaxy are not considered because there is no concentration of GRBs in the galactic hemisphere containing the galactic center. The validity of an extragalactic population of GRBs is reduced by the absence of associations of GRBs with known extragalactic objects, as well as by the unimaginable energetics involved in the creation of a GRB at extragalactic distances.

There is no definitive proof for either a local or extended halo distribution. The association of the GRB0528-66 with the LMC may be considered in favor of an extended halo distribution, but 1) this association is not definite and 2) GRB0528-66 is generally considered an anomalous event (because of its many unique features) and its association with the LMC would not be considered contrary to the concept of a local GRB population.

## 2.2. Observations of Known GRB Sources

The *a posteriori* observation of GRB source is difficult for two reasons:

- 1) GRBs do not repeat regularly or often (only two GRBs have been seen to recur:

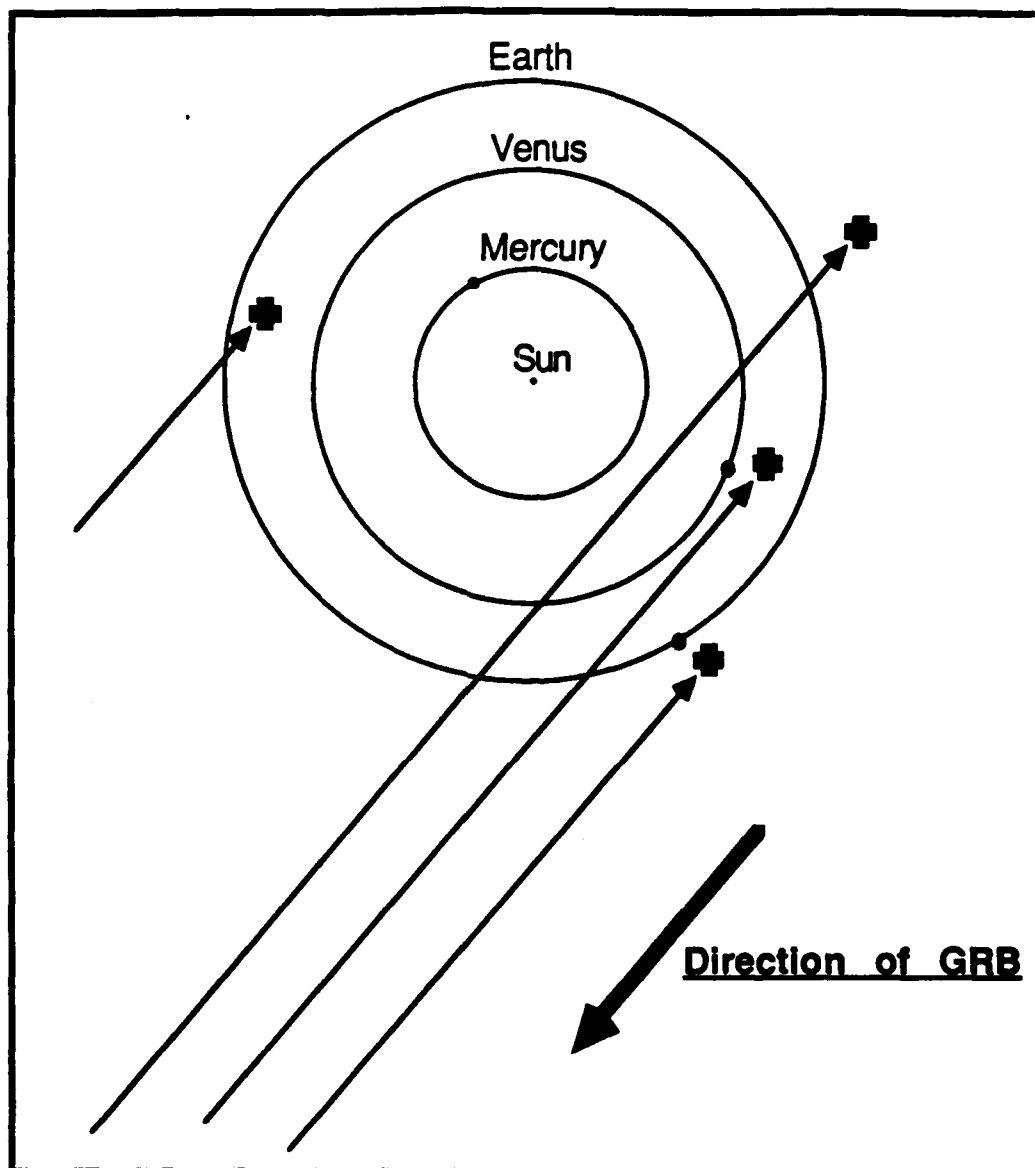


**Figure 2.5: Gamma-ray Burst Arrival-Time Localization Method.** The location of a gamma-ray burst in space is determined from the differences in the arrival times of the gamma-ray wavefront at several terrestrial and interplanetary satellites. Detection of the GRB by two satellites allows localization of the burst source to an annulus on the celestial sphere. Detection by three satellites allows localization to two diametrically opposite "diamonds" formed by crossings of two inclined annuli. If the GRB is detected by at least four satellites, the localization is unique.

GRB0528-66 (5 March 1979a) has reburst more than a dozen times since the initial outburst (Golenetskii, et al., 1984) and the source GRB1900+14 recurred twice within four days of the initial event (Mazets, et al., 1981)).

- 2) The GRB error boxes are generally too large for a reasonable follow-up observation. Only a few ( $\sim 10$ ) error boxes are small enough for sensible follow-up work (Hurley, 1982).

Most of the follow-up observations of GRB sources are intended to detect the GRB source in quiescence at various energies. Few attempts have been made, to date, to detect radiation from a GRB source during outburst. The error regions of GRB0528-66 and GRB0116-29 (19 November 1978) have been most extensively searched: the former because of its unique features and the latter because of the discovery of an archived optical transient in its error region (Schaefer, 1981). Cline (1983) provides an excellent detailed review of the observations of these and other GRB sources. The results of observations of several error regions are briefly summarized below.

### 2.2.1. Radio Observations

Hjellming and Ewald (1981) searched the error region of GRB0116-29 for quiescent radio emission at 6 and 18 cm with the VLA. They found three point radio sources (designated B, C and Q) inside the error region: one (Q) is also located inside the error circle of a weak X-ray source detected by Einstein (Pizzichini, et al., 1985; see section 2.2.3). None, however, is consistent with the error box of the associated archived optical transient (section 2.2.4.2).

### 2.2.2. Infrared Observations

Infrared observations of the error regions of GRB2312-50 (6 April 1979) and GRB0528-66 and of the radio sources in the error region of GRB0116-29 were carried out by Apparao and Allen (1982) on the 3.9m Anglo-Australian telescope. The error region of GRB2312-50 was seen to be empty to  $J=17.5$ . Their observations of the point radio sources detected by Hjellming and Ewald (section 2.2.1) revealed a  $J=18.4$  magnitude object consistent with one of them (B), but no source consistent with the error circle of a weak X-ray source in the field (Pizzichini, et al., 1985; section 2.2.3). The search of the error region of GRB0528-66 was confusion-limited and resulted in no reliable detection.

Schaefer and Ricker (1983) searched the error box associated with the archived optical transient in the error region of GRB0116-29 (section 2.2.4.1). They found no infra-red sources in the error box to a limiting magnitude of  $K=18.8$ .

Recently, B. Schaefer searched the IRAS data base for infra-red sources in the 23 smallest known GRB error regions. The sensitivity of the observations used in the search varied considerably: Schaefer reports no infra-red sources detected with an estimated average  $4\sigma$  sensitivity of  $\sim 1$  Jansky (B. Schaefer, private communication).

### 2.2.3. X-ray Observations

Pizzichini, et al. (1985) report observations of five GRB error regions (those of GRB2008-22 (4 November 1978), GRB0116-29, GRB1704+01 (21 November 1978), GRB0528-66 and GRB2312-50) with the Einstein Observatory. Although no overwhelming evidence for the existence of quiescent X-ray counterparts in any of the regions was found, X-ray observations of the error regions of GRB0116-29 and GRB0520-66 have yielded some positive results. The optical and  $\gamma$ -ray error regions of GRB0116-29 are consistent with the error circle of a weak ( $\sim 10^{-13}$  erg/cm<sup>2</sup>/sec - - a  $3\sigma$  level-of-confidence detection) X-ray source (Pizzichini, et al., 1981), which may be a quiescent X-ray counterpart. The supernova remnant N49, which is included in the error region of GRB0528-66, was also detected by Einstein (Helfand and Long, 1979).

## 2.2.4. Optical Observations

Optical observations of GRBs have been carried out in a variety of ways. These optical searches have looked for optical radiation from both quiescent and outbursting GRB sources.

### 2.2.4.1. Search for Quiescent Optical Counterparts

Deep searches of several small GRB error boxes with large telescopes have been carried out by Chevalier, et al. (1981), Fishman, et al. (1981), Laros, et al. (1981), Pedersen, et al. (1983), Schaefer and Ricker (1983), Schaefer, Seitzer and Bradt (1983), among others. The investigation of the error region of GRB0116-29 has uncovered several faint ( $m_v \approx 22$ ) sources, including an apparently highly-variable ( $\Delta m \approx 2$ ) object (Schaefer, Seitzer and Bradt, 1983; Schaefer and Ricker, 1983; Pedersen, et al., 1983). No definite quiescent optical counterpart to GRB0116-29 has yet been confirmed.

The error region of GRB2312-50 is empty to a limiting visual magnitude of 22.5 (Laros, 1981). The error region of the GRB1412+78 (13 June 1979) contains  $>5$  faint ( $m_v = 22$ ) objects (Vanderspek, Ajhar and Ricker; work in progress). The error region of GRB0528-66 contains the supernova remnant N49 (Cline, 1982).

### 2.2.4.2. Searches for Optical Light from an Outbursting GRB

Optical transient events have been noted in the literature for more than half a century. In addition to transient events of short timescales from known astrophysical objects, such as cataclysmic variables and flare stars, several unknown optical transient events have been reported. Klemola (1983) reports two possible optical transient events, first recognized by Hertzsprung (1927) and Popovic (1982). Although the Hertzsprung object has been recently recognized as a plate defect by Schaefer (1983), the Popovic object, which was seen as a fifth-magnitude event with a duration of less than 20 minutes, remains without explanation or verified quiescent counterpart. In addition, recent analysis of SEC Vidicon meteor observations made in 1969 revealed that the 4<sup>th</sup>-magnitude double star  $\beta$  Cam underwent a 0.7 magnitude brightening in a period of 0.25 seconds (Wdowiak and Clifton, 1985).

In 1981, B. Schaefer of MIT began a survey of historic photographic plates of three small GRB error regions, in the hope of finding an optical transient which may have been associated with a GRB. In the scanning of plates stored at the Harvard plate archives totalling roughly three years of exposure, Schaefer discovered three transient images which are now generally accepted as being optical flashes from historical GRBs (Schaefer, 1981; Schaefer, et al., 1984). The three events were of magnitude 3.0, 6.6 and 4.3, assuming the optical radiation was emitted in one second. Schaefer reported an upper limit on the total duration of the optical bursts of  $\tau < 500$ s. The ratio of optical fluence in the three archived optical transients,  $S_{opt}$ , to the  $\gamma$ -ray fluence,  $S_\gamma$ , of the associated GRB is roughly  $10^{-3}$  for each of the three bursts.

Schaefer's work initiated an entirely new approach to GRB research: it created the hope that the location of GRB sources could be precisely determined by observing optical light emitted during a GRB. His work has sparked a series of new, real-time searches for optical counterparts to outbursting GRBs: some of these experiments are described below.

#### 2.2.4.2.1. Pic du Midi SIT TV Flash Search

In the summer of 1982, Kevin Hurley and collaborators (Hurley, private communication) observed the night sky at Pic du Midi with a wide-field lens on a SIT TV camera in an effort to measure the optical flash background rate and perhaps detect an optical counterpart to a GRB. The Pic du Midi system records images of the night sky at video rates, which are viewed after the fact by a human worker. Its time resolution was 0.04 seconds and its sensitivity  $m = 5.5$ . Because of its low angular resolution (one degree), the Pic du Midi system cannot differentiate between head-on meteors and real celestial optical flashes, thus making them reliant on simultaneous detection of a GRB by a  $\gamma$ -ray satellite to confirm any optical counterpart. In over 100 hours of observations with a three-steradian field-of-view, no optical counterparts to GRBs have been reported.

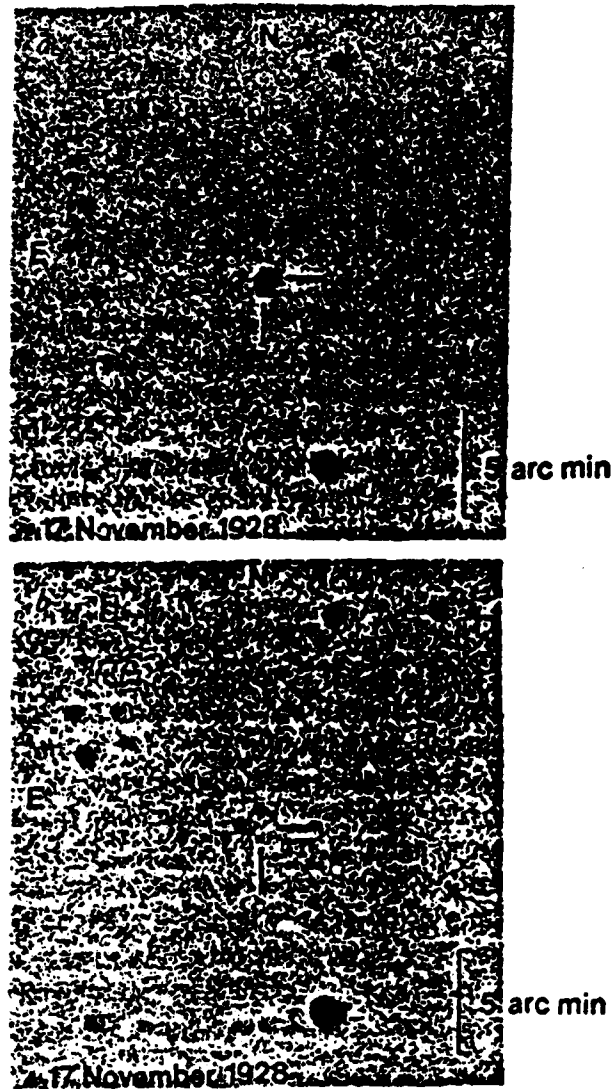


**Figure 2.6:** The archived optical transient in the field of GRB0116-29 (19 November 1978), discovered by Schaefer (1981). The upper plate shows the transient event, found on a 45 minute exposure taken in 1928. The lower plate was taken of the same field 45 minutes before the upper plate. The lack of trailing of the burst image puts an upper limit of 500s on the burst duration. The ratio of 1928 optical fluence to the 1978 gamma-ray fluence is 0.001.

#### 2.2.4.2.2. Two-Schmidt Sky Survey

In October, 1982, a unique set of observations designed to detect celestial optical flashes was carried out (Schaefer, Vanderspek, Bradt and Ricker, 1984b). Simultaneous observations of several patches of sky were made with identical 0.4m Schmidt telescopes located at the Cerro Tololo Inter-American Observatory in Chile and at Kitt Peak National Observatory in Tucson, Arizona. Two telescopes were used in order to confirm any optical flashes detected, thus eliminating local sources of optical flashes. In addition, the 6000 km baseline between the sites allowed the use of trigonometric parallax to recognize sources of optical flashes within  $\sim 10$  AU of the Earth. A total of 890 square-degree-hours (0.27 sr-hrs) of observations were made, with a median one-second sensitivity of 13th magnitude. No flashes were detected, resulting in a  $3\sigma$  upper limit on the celestial optical flash rate of 54 flashes/hr/sr at 13th magnitude and 22 flashes/hr/sr at  $10^{\text{th}}$  magnitude.

#### 2.2.4.2.3. GRB0528-66 Monitoring

Holger Pedersen and co-workers at the European Southern Observatory (ESO) have recently monitored the error box of the peculiar GRB0528-66 (5 March 1979) with a photometer mounted on a 50 cm telescope (Pedersen, et. al., 1984). The aperture of the photometer matched the shape of the  $3\sigma$  level-of-confidence error region of GRB0528-66. The output of the photometer was stored on magnetic tape. The ESO team has published the detection of three significant optical flashes in 910 hours of observation of the error region of GRB0528-66. No coincident gamma-ray events were detected by any satellite operating at the time. Pedersen notes, however, that none of these bursts could have been detected at  $\gamma$ -ray energies by any of the satellites, based on the ratio  $L_{\gamma}/L_{\text{opt}} \approx 10^3$ .

Pedersen's method, although quite sensitive, suffers from the inability to reject terrestrial sources of optical flashes. The detector is a simple photometer without any anticoincidence detector, so that any object moving quickly through the field of view, such as a satellite or meteor, could create a light curve similar to that of an optical flash. Indeed, the three detections may be consistent with a meteor or satellite crossing the detector field (see Chapter 11).

#### 2.2.4.2.4. Conclusion

The discoveries by Schaefer (1981; Schaefer, et al., 1984) of optical transients associated with GRBs have demonstrated that bursts of optical radiation can be expected from GRB sources. The detection and study of optical radiation from GRBs would lead to better understanding of the GRB phenomenon. In addition, a comparison of the characteristics of the optical and  $\gamma$ -radiation would provide greater insight into the mechanism of the production of  $\gamma$ -rays and optical light in GRBs. Optical detections of outbursting GRBs would lead to a more precise source localization than presently possible with  $\gamma$ -ray satellites, leading to more fruitful *a posteriori* observations of the GRB source.

The methods for searching for optical light from GRBs described in the preceding section are all effective for searching for flashes from limited regions of the sky, yet are ineffective as general monitors of optical flashes from GRBs. To be more specific:

- (1) Hurley's Pic du Midi sky monitor has the advantage of a dedicated, wide-field instrument, yet the data collected must be analyzed after the fact, in real time, by a human observer. This method is time-consuming and fraught with human frailties. In addition, the low detector resolution and the absence of a coincidence detector limit the effectiveness of the method in general.
- (2) Schaefer's archived plate method leaves thousands of plates at the investigator's disposal, yet no optical flash detected can ever be confirmed as coming from a GRB. In addition, the method is very time-consuming, since each plate must be visually scanned by the investigator.
- (3) The Two-Schmidt survey method combines large viewing solid angle with a moderately large observing time, and with its use of coincidence is effective as a survey method. However, it



relies on the acquisition of observing time on two telescopes at the same time, and suffers from the long analysis time of Schaefer's method.

- (4) Pedersen's monitoring of GRB0528-66 has the advantage of a being done with a dedicated telescope, but its small field-of-view limits the applicability of the method to a single object. In addition, its lack of anticoincidence detector significantly reduces its reliability as a detector of optical flashes from a point source. (This limitation has been recognized by the ESO team, and they are planning to incorporate a second, imaging instrument operating in coincidence with their photomultiplier detector).

Ideally, it would be desirable to assemble an instrument which combines the positive features of all methods: a dedicated, automated, wide-field detector of sudden optical flashes with coincidence detectors to confirm any flashes. Such an instrument is the *Explosive Transient Camera* (ETC), described in the following chapters.

## CHAPTER 3

### Theories of Radiation from GRBs

#### Introduction

Since the discovery of GRBs (Klebesadel, et al., 1973), many theories have been proposed to explain the phenomenon of the GRB. It is only in the last ten years that the understanding of the GRB has progressed to the point where the number of GRB detections has exceeded the number of models attempting to explain GRBs. The increased number of detected GRBs has enabled workers in the field to cull out implausible theories of the mechanism and space distribution of GRBs. Still, because of the large number of unknown facts about GRBs, many theories can still explain the observed characteristics of GRBs.

With the discovery in 1981 of transient optical radiation from a GRB error region (Schaefer, 1981), new data about GRB sources have become available. As a result, several new theories of the production of optical radiation from GRB sources have been proposed since 1981. The discovery of transient optical radiation from a GRB source has introduced new constraints on the theories of GRB emission which would predict optical radiation from the same source. Only a few self-consistent models of transient  $\gamma$ -ray and optical radiation from a GRB source have emerged since 1981.

This chapter is designed to give the reader an overview of the most accepted theories of the production of gamma-rays and of optical light during a gamma-ray burst. Space limitations dictate that the discussion of these theories be in the form of short explanations: the reader should refer to the appropriate reference for more detailed information about a specific model. Ventura (1983), Katz (1984), and Lamb (1984) also provide excellent reviews of the physics and proposed theories of  $\gamma$ -ray emission from GRB sources.

#### 3.1. Models of Gamma-Ray Production in GRBs

Any theory of GRB production and source location must be able to explain the most common observed characteristics of GRBs:

- 1) Short risetimes (0.05 - 1 second).
- 2) Spectral shape  $N(E) \sim E^{-1}e^{-E/kT}$ , with  $kT \approx 100$ -500 keV.
- 3) Total energies (based on detected fluences ranging from  $10^{-3}$  to  $10^{-8}$  erg/cm<sup>2</sup> and an assumption of the distance to the source).
- 4) Line features near 30-70 keV and near 400 keV in some burst spectra.
- 5) Pulsations (4-10 second periods) in a few (2-3) burst lightcurves (Mazets, et al., 1979b; Wood, et al., 1981).
- 6) Low quiescent flux in energy bands from radio to  $\gamma$ -rays.
- 7) An estimate of the recurrence rates of some GRBs of the order of  $1 \text{ yr}^{-1}$  (Schaefer and Cline, 1985), based on the detection of three archived optical transient events of Schaefer, et al (1984a).

Because of the wide variety of detected GRB characteristics, it is possible that no single GRB theory can explain every characteristic of every observed GRB.

### 3.1.1. GRB Spectral Shape and Features

The physics explaining the continuum shape and low-energy features of a GRB spectrum are in principle independent of the physics explaining the other GRB characteristics. The energy dependence of the GRB continuum spectra ( $E^{-1}e^{-E/kT}$ ) are consistent with the emitting material being an optically-thin plasma. The 30-70 keV line features are consistent with cyclotron emission (or absorption) lines from an optically-thin plasma in a high ( $\sim 10^{12}$  Gauss) magnetic field.

The energy dependence of the continuum spectra can be described by a variety of different models. Liang (1984b) points out that single-temperature thermal bremsstrahlung or inverse-Compton models cannot explain GRB continuum spectra because the high-energy cutoff (at a few times  $kT$ ) predicted by these models has not been observed. The thermal synchrotron model of Liang (1984a) fits the observed spectra well out to high energies and predicts the 30-70 keV line features. However, Liang (1984a) notes that the exponential continuum shape can be explained by any number of models. (For a good review, see Lamb (1984)).

### 3.1.2. The Energy Sources of GRBs

As discussed in section 2.1.1, the observed characteristics of GRBs (short risetime, pulsations, gravitationally-redshifted  $e^+e^-$  line) point to a neutron star as the source of the burst. Various energy sources have been proposed to power the burst, including the neutron star's gravitational and rotational energy, the gravitational energy of impacting matter and the nuclear energy of matter on the surface of the neutron star. These energy sources will be discussed in the sections below.

Several models of the energy source of GRBs require a companion star and/or an accretion disk. The existence of a companion has profound consequences for the detection of a quiescent source: any companion star or accretion disk would most likely be more visible than the neutron star primary in the optical band, and any significant accretion onto local ( $d < 200$  pc) neutron stars will create an X-ray flux detectable at the Earth (see Rappaport and Joss (1985) and section 3.1.2). These models are also important in the discussion of mechanisms producing optical burst radiation to follow in section 3.3.

Most models of the source of the total energy of GRBs are based on an assumption of the distance to the GRB source. The theories of  $\gamma$ -ray production from a local ( $d < 500$  pc) distribution of GRB sources will propose total burst energies in the range of  $10^{35}$ – $10^{39}$  erg (based on the range of detected fluences of  $10^{-3}$ – $10^{-7}$  erg/cm<sup>2</sup>). The theories of  $\gamma$ -ray production from an extended-halo population of GRBs ( $d > 50$  kpc), or to explain GRB0528-66 (5 March 1979) as being in the LMC, derive total burst energies of  $10^{39}$ – $10^{43}$  erg.

It should be noted that the Eddington luminosity for a  $1.4M_{\text{solar}}$  neutron star is  $\sim 10^{38}$  erg/s. Any GRB mechanism which predicts significantly super-Eddington luminosities has to contend with a fraction of the total burst energy going into the kinetic energy of matter driven from the surface of the neutron star by radiation pressure (Colgate and Petschek, 1981). One proposed means of avoiding this problem is to confine the ejected matter near the surface of the neutron star with a large surface magnetic field, thereby increasing the  $\gamma$ -ray production efficiency of the burst (Woosley and Wallace, 1982).

The following sections contain discussions of some of the more widely-accepted mechanisms for the production of GRBs. Each section is based on the source of the energy of the GRB, as follows:

- 1) Sudden accretion of matter onto a neutron star, which liberates  $\sim 10^{20}$  ergs of gravitational energy per gram of accreted matter.
- 2) Thermonuclear detonation of accreted matter on the surface of the neutron star, which liberates  $\sim 10^{38}$ – $10^{39}$  ergs in  $\gamma$ -rays (Woosley and Wallace, 1982).
- 3) Physical changes in the state of the neutron star, which may liberate large amounts

of energy (up to  $\sim 10^{46}$  ergs).

The energies quoted here are total energies liberated by the particular mechanism. The energy of the GRB in  $\gamma$ -rays depends of the efficiency of the burst mechanism.

### 3.1.2.1. GRB Production by Sudden Accretion onto a Neutron Star

The sudden accretion of matter on to a neutron star involves the collision of a 5-10 km solid body with a neutron star. Various theories have been put forth describing the effects of such a collision. A body approaching close enough (within  $\sim 10^5$  km) to a neutron star is broken up tidally and continues to orbit the neutron star as a stream of particles. These particles can lose enough of their angular momentum to the neutron star's magnetic field to strike the star, releasing  $GM_{NS}/R_{NS} \equiv 10^{20}$  ergs per gram of accreted matter in gravitational energy. Most of this energy would appear as thermal X-rays from the heated neutron star's surface, but nuclear collisions and non-thermal radiation from infalling and re-ejected material could lead to an appreciable  $\gamma$ -ray flux (Colgate and Petschek, 1981).

Colgate and Petschek (1981) and Van Buren (1981) discuss event rates based on impacts of interstellar asteroids onto neutron stars, while Joss and Rappaport (1983) propose the *in situ* formation of asteroids in a cold accretion disk. Harwit and Salpeter (1973) and Tremaine and Zytlow (1985) explore the energetics and event rate of collisions of comets from a comet cloud about a neutron star or white dwarf.

#### 3.1.2.1.1. Collision of an Asteroid with a Neutron Star

Colgate and Petschek (1981) analyze the direct collision of a 5 km body with a neutron star. In their model, the body is tidally disrupted within  $\sim 10^8$  cm: the resulting matter is deformed tidally and thermally into a long ( $\sim 10$  km), thin ( $\sim 3$  mm) curtain of matter, which strikes the neutron star surface along a line of magnetic longitude. The total impact time of the matter is of the order of  $\sim 1$  ms. The impact sends up a plume of plasma, which then radiates in the magnetic field of the neutron star. The total gravitational energy available for the burst is  $\sim 10^{40}$  ergs from a body with  $m \equiv 5 \times 10^{19}$  g. A strong surface magnetic field is required in this model to confine the bursting material. If no magnetic field is present, the efficiency of the GRB would be low because the impact energy is converted to the kinetic energy of material ejected by radiation pressure.

This model does not require any neutron-star companion or accretion disk and does not predict any detectable quiescent flux in any energy band. However, the recurrence rate based on the random collision with an asteroid-sized body with a neutron star has been estimated to be low (a few times  $10^{-7}$  yr $^{-1}$ ; Newman and Cox (1980)). Calculations by Van Buren (1981) of the rate of collisions of interstellar asteroids deflected by gravitational interactions with a planetary system about the neutron star (thereby increasing the collision cross-section of the neutron-star system) have yielded slightly higher, yet similarly low collision rates ( $\sim 10^{-6}$  yr $^{-1}$ ).

Joss and Rappaport (1983) have proposed the possibility of the condensation of iron-nickel bodies at a rate of up to  $\sim 1$  yr $^{-1}$  from a cold accretion disk about a neutron star. In their scenario, the neutron star is in a close orbit with a low-mass companion from which matter had been accreting for several billion years. When the companion mass drops below a certain level, the rate of accretion to the disk and onto the neutron star drops steadily. The viscosity of the disk may then very well decrease, in which case the disk cools slowly until the temperature is such that iron-nickel grains could condense out of the disk. These grains would settle into a thin plane inside the accretion disk and condense into asteroid-sized bodies by a series of inelastic collisions. The resulting body could then possibly give up its angular momentum to the neutron star's magnetic field, causing it to strike the neutron star surface and create a GRB as in the model of Colgate and Petschek (1981).

This scenario has many positive aspects. The recurrence rate estimated by Joss and Rappaport agrees well with the estimates of Schaefer and Cline (1985). The absence of accretion onto the neutron star's surface accounts for the absence of a quiescent X-ray flux. In addition, the existence of an accretion disk and companion has important implications for some theories of the generation of optical radiation, as will be seen in section 3.3.

### 3.1.2.2. Impact of a Comet onto a Neutron Star

Harwit and Salpeter (1973) have proposed that GRB could be produced on a regular basis by impacts onto a neutron star of comets from a comet cloud surrounding the neutron star. In their model, comets straying within  $\sim 10^5$  km of the neutron star are tidally broken up into a stream of smaller bodies which spread along the comet's orbit. Comets with periastron distances much less than  $10^5$  km are compressed and heated and spread into a set of orbits about the neutron star. Disrupted comet matter could lose its angular momentum to the magnetic field of the neutron star and then be guided onto the surface of the neutron star along magnetic field lines. Such a collision of a comet of mass  $3 \times 10^{17}$  g would release  $\sim 3 \times 10^{37}$  erg of gravitational energy: if  $\sim 3\%$  of the available energy were released in the GRB (a very uncertain estimate),  $\sim 10^{36}$  ergs of energy would be available for the burst.

Harwit and Salpeter did not discuss a key aspect of the creation of GRBs by the impact of comets from a comet cloud about the neutron star: the retention of the comet cloud by the neutron star during the formation of the neutron star. Their model has been reanalyzed by Tremaine and Zytzkow (1985). Besides rediscussing the basic aspects of the collision of a comet with a neutron star, Tremaine and Zytzkow address the problem of the retention of the comet cloud during the formation of the neutron star. They conclude that it is indeed possible to create a neutron star without losing the cloud of comets present around the parent star, thus enabling the system to be a possible source of GRBs.

In their paper, Tremaine and Zytzkow note that a cloud of comets orbit a star at a mean distance of  $\sim 20,000$  AU is very loosely bound to the star (the escape velocity is of the order of 1 km/s). If, during the creation of a neutron star from the parent star, the neutron star is given a peculiar velocity significantly greater than  $\sim 1$  km/s, the comet cloud will not remain bound to the neutron star. Measurements of pulsar radial velocities indicate that many neutron stars are created with high peculiar velocities, presumably due to asymmetries in the supernova explosion creating the neutron star. At typical velocities of  $\sim 100$  km/s, such a neutron star would escape a cloud of comets at a mean distance of 20,000 AU from the progenitor star (which has an escape velocity of the order of 1 km/s) within  $10^3$  years. Tremaine and Zytzkow discuss four scenarios for the creation of a neutron star with low enough peculiar velocity so that the comet cloud remains bound. These scenarios are:

- 1) The symmetric type II supernova explosion of a single massive star. Tremaine and Zytzkow quote results of calculations by Hills (1983) that imply that a good fraction (roughly half) of the comets in high eccentricity orbits would remain bound during a sudden mass loss by the central star. The fraction of type II supernovae that satisfy this criteria is unknown.
- 2) The creation of a neutron star in a cataclysmic variable due to mass accretion by the white dwarf until its mass exceeds the Chandrasekhar limit. The result is a binary system, generally including a neutron star and a low-mass secondary. Those systems which would retain their comet cloud would have secondaries with masses less than  $0.03 M_{\text{sun}}$ . (This binary system is very similar to one proposed by Rappaport and Joss (1985) to explain optical flashes from GRBs (see section 3.3)).
- 3) The creation of a neutron star from a white dwarf accreting matter from a giant companion in a wide binary orbit. Tremaine and Zytzkow propose that the resulting system would be a neutron star in orbit with the white dwarf core of the giant companion. The peculiar velocity of the resulting system would be small due to the its large period.
- 4) The merging of a close pair of white dwarfs, possibly creating a Type I supernova and/or neutron star.

The analysis of the physics of the interaction of the comet with a neutron star is similar to the analysis of Colgate and Petschek (1981). The comet is tidally disrupted at a distance from the neutron star dictated by the tensile strength of the cometary material. Gravitational forces compress the disrupted comet into a long, thin stream of conducting material, which can lose angular momentum to the neutron star's magnetic field through the generation of Alfvén waves. If the energy loss by the cometary material is not large enough to allow the material to strike the neutron star, the probability is high that the material will impact the neutron star in a following passage. Indeed, since the maximum impact parameter for accretion on the first encounter is relatively small, most bursts will occur when the comet is disrupted on the first pass by the neutron star and accretes on the second pass. The total time in which the cometary material strikes the neutron star depends on the extent of its spread during previous encounters with the neutron star. GRBs of duration 0.1 to 30 seconds are in principle allowed by this model, with burst times less than one second restricted to comets with an impact parameter of less than a few hundred kilometers.

The estimated rate of impacts onto the neutron star by comets "straying" near the neutron star is  $\sim 10^{-4} \text{ yr}^{-1}$  for either a solitary neutron star or one in a binary system. Tremaine and Zytkow note that Hills (1981) has pointed out that a close encounter of the comet cloud with a field can create a relatively brief period (duration  $\sim 30,000$  years) of high comet influx into the neutron star system. During these periods, the observed impact rate is enhanced: burst recurrence rates of  $\sim 1 \text{ yr}^{-1}$  are easily explained by this model. As a result, the mean impact rate increases to  $\sim 10^{-3} \text{ yr}^{-1}$ . Tremaine and Zytkow emphasize that these numbers are conservative and fairly uncertain, and that the rates could be much higher.

The intriguing possibility of creating bursts of optical radiation by impacting a comet onto the white dwarf companion of the neutron star is discussed further in section 3.3.1.

#### 3.1.2.2.1. Unstable Accretion of Interstellar Matter

Lipunov et al. (1982) propose that interstellar material can accumulate as an envelope of matter in the magnetosphere of a highly-magnetized neutron star. When enough matter has accumulated, the envelope becomes unstable and accretes quickly onto the poles of the neutron star, releasing  $\sim 10^{37}$  ergs of gravitational energy. The accretion rate, and therefore the recurrence time, is very sensitive to the neutron star velocity. Slower neutron stars will accumulate mass more quickly than faster ones and will therefore recur more often. Lipunov estimates a recurrence time of  $(0.1 \text{ years}) \cdot (0.1V)^3$ , where  $V$  is the neutron star's velocity in km/sec. According to this model, then, a neutron star with  $V=100$  km/sec will therefore recur every  $\sim 100$  years.

#### 3.1.2.3. GRB Emission from the Detonation of Accreted Matter

Woosley and Wallace (1982) and Fryxell and Woosley (1982) propose models of GRB production in which matter accreted onto a neutron star from a companion star or accretion disk ignites explosively to create a gamma-ray burst. Matter (mostly hydrogen) accreting from an accretion disk onto a neutron star accumulates on the surface of the neutron star and fuses non-explosively into helium. The accreted matter can collect in a kilometer-sized area, either due to the funneling of the matter onto the poles of the neutron star by the strong magnetic field or due to the presence of "wrinkles" in the magnetic field at the neutron star surface (Woosley and Wallace, 1982). The accreted hydrogen and helium form a "blister" on the surface of the neutron star. The blister measures tens of meters deep and has a surface area of the order of  $\sim 1\text{-}10 \text{ km}^2$ . The matter in the blister will tend to spread over part of the neutron star surface: the extent of the spread determines the total mass of the blister at the time of detonation, and so the energy of the burst. When the pressure and temperature at the base of the blister reach the point where helium at the base of the blister undergoes runaway thermonuclear fusion, a blast wave of fusion propagates through the blister, releasing  $10^{38}\text{-}10^{39}$  ergs in  $\gamma$ -rays per  $\text{km}^2$  of accreted matter. The hot ( $T = 10^9\text{-}10^{10} \text{ K}$ ) plasma thrown up by the explosion interacts with the magnetic field of the neutron star, creating the GRB.

It should be noted that matter accreting onto the surface of a neutron star will emit X-rays. Depending on the distance to the source and the mass transfer rate, these X-rays may be detectable at the Earth. According to Rappaport and Joss (1985, equation 4), the quiescent X-ray flux of GRB0116-29 ( $10^{-13}$  erg/cm<sup>2</sup>/s; cf. section 2.2.3) is such that the recurrence time between bursts is  $4 \times 10^5$  years if the source is at 100 pc, 3500 years at 1 kpc and four months at 100 kpc, assuming isotropic emission.

Application of this model to GRB0116-29 (19 November 1978) presents some difficulties. The apparent detection of two bursts from this source within 50 years imply an accretion rate which would create the detected X-ray flux if the source is at a distance of  $\sim 8$  kpc. On the other hand, a total burst energy of  $\sim 10^{38}$  ergs places GRB0116-29 (fluence =  $3.2 \times 10^{-4}$  erg/cm<sup>2</sup>) at a distance of 50 pc from the Earth. Since all models of optical radiation from GRBs favor a local ( $d < 100$  pc) population of GRB sources, it is probable that either this model does not apply to GRB0116-29 or the X-ray flux is from a serendipitous source in the error region of GRB0116-29.

### 3.1.3. GRB Emission from Phase Changes inside a Neutron Star

A phase change inside a rotating neutron star is usually seen as a starquake accompanied by a release of energy from the neutron star. Pulsar "glitches", where the period of a pulsar changes suddenly and discontinuously, are thought to be associated with some change in the physical state of the neutron star. The amount of energy release in a neutron star glitch is roughly  $E_{\text{total}}(\Delta P/P)$ , where  $\Delta P$  is the change in the neutron star rotational period  $P$ . Pulsar glitches have been observed at intervals of  $\sim 10$  years, so each glitch model would allow recurrence times of the order of 10 years.

In pulsar-glitch models of the production of GRBs, the starquake in the neutron star causes a sudden change in the magnetosphere of the neutron star, which creates a strong electric field near the neutron star surface. This electric field pulls charged particles from the surface of the neutron star, which then radiate in the neutron star magnetosphere. The fraction of the energy released by the glitch that appears in fast particles and the total energy radiated in  $\gamma$ -rays is model-dependent.

Several theories of GRB production from starquakes have been proposed, with different results. Mitrofanov (1984) has calculated that a starquake in an old pulsar could release of the order of  $10^{46}$  ergs of the gravitational energy of the neutron star ( $\sim 10^{53}$  ergs), based on the assumption that the change in the neutron star period is accompanied by a change in the neutron star radius, and that  $\Delta P/P = \Delta R_{\text{ns}}/R_{\text{ns}}$ . Pacini and Ruderman (1974), on the other hand, calculate total energies of  $\sim 10^{35}$  ergs, assuming the GRB derives its energy from the rotational energy of the neutron star ( $E_{\text{rotational}} = 10^{45}$  erg for a neutron star with a period of 6s).

The starquake model of GRBs are, in principle, capable of creating the short risetimes (10-500 ms) seen in GRBs. If the source of the GRB energy is the rotational energy of the neutron star, the characteristic timescale of radiation of energy is the time needed for an Alfvén wave to cross the neutron star magnetosphere, which is about 1 ms (Lamb, 1984). If the energy source is the gravitational energy of the neutron star, the characteristic timescale of energy conversion is the orbiting time of a particle just above the neutron star surface, which is  $\sim 0.1$  ms (P. Joss, private communication).

Because of the six orders of magnitude difference in the burst energy predicted by the models of Pacini and Ruderman (1974) and Mitrofanov (1984), the mean distances to GRB sources predicted by the two theories differs by three orders of magnitude. As a result, the two theories prefer different source distributions: Pacini and Ruderman have proposed a local GRB source population, while Shklovskii and Mitrofanov (1985) have proposed an extended-halo GRB source population based on the model of Mitrofanov (see section 3.2).

---

\*Assuming the X-rays are emitted isotropically from the neutron star: if the emission occurs in a small area on the surface of the neutron star, the distance to the source will decrease as the ratio of the emission area to the area of the neutron star. However, any significant concentration of emission onto one spot on the surface of the neutron star would most likely be noticed as the neutron star rotates; yet, no reports of pulsations in the quiescent X-ray flux have been published.

### 3.2. The Distribution of GRB Sources

Since GRBs are thought to originate near the surface of neutron stars, some insight into the space density of GRB sources can be gained by an analysis of the space density of neutron stars. Isotropy arguments (section 2.1.4) point to a spherical distribution of detected GRB sources about the Earth. The GRB sources are either close to the Earth ( $d < 100\text{--}300$  pc) or in an extended halo about the Galaxy ( $d = 50\text{--}200$  kpc).

The present best estimate of the rate of creation of neutron stars is  $\sim 0.03 \text{ yr}^{-1}$  (Shklovskii and Mitrofanov, 1985). If this rate has persisted throughout the life of the Galaxy ( $\sim 10^{10}$  years), there have been  $N_{\text{ns}} = 3 \times 10^8$  neutron stars created in our Galaxy. If only a fraction,  $f_{\text{GRB}}$  of these neutron stars are responsible for GRBs observable by present instruments (perhaps because only a fraction of all neutron stars can create GRBs, or perhaps because only a fraction of all neutron stars are close enough to be detected in outburst), then there are  $f_{\text{GRB}} N_{\text{ns}}$  observable GRB sources in the Galaxy.

If one can assign some sort of mean recurrence time,  $\tau_{\text{rec}}$ , to GRBs as a population, then the observed GRB detection rate (of the order of  $30 \text{ yr}^{-1}$ ) can be compared with the expected rate  $f_{\text{GRB}} N_{\text{ns}} / \tau_{\text{rec}}$ . From this comparison, it is clear that if every neutron star is a potential site of a detectable GRB ( $f_{\text{GRB}} = 1$ ), the mean recurrence time is  $\sim 10^7$  years. On the other hand, if the recurrence time of about one year calculated by Schaefer and Cline (1985) is correct, the value of  $f_{\text{GRB}}$  is  $\sim 10^{-7}$ .

Shklovskii and Mitrofanov (1985) point out that typical pulsar peculiar velocities are high ( $\sim 100\text{--}200$  km/s) and that, therefore, the galactic population of old pulsars is spherically distributed within  $100\text{--}200$  kpc of the center of the Galaxy. It is not clear whether this statement can be made of neutron stars in general. First, the observable pulsars make up only a small fraction ( $< 10\%$ ) of the expected number of young (age  $< 10^6$  years) neutron stars in the Galaxy. Second, Tremaine and Zytlow (1985) have suggested four scenarios for the production of neutron stars with low peculiar velocities (cf. section 3.1.2.2), implying that not all neutron stars are born with velocities typical of pulsars. Neutron stars as a group have some intrinsic velocity function: the validity of the use of pulsars as a tracer of this function is questionable.

Shklovskii and Mitrofanov have used the arguments listed above and suggested that GRBs belong to a class of "switched-off" radio pulsars. These old pulsars all have high peculiar velocities ( $> 100$  km/s) and populate an extended halo about the Galaxy at a mean distance of  $\sim 100$  kpc. The old pulsars create GRBs through the mechanism proposed by Mitrofanov (1984), described in section 3.2.3.3. Shklovskii and Mitrofanov suggest that high peculiar velocity, early pulsar activity and late GRB activity are intimately related: only fast, old pulsars are capable of bursting. Because the fast pulsars are far away from the plane of the Galaxy before they start their bursting phase, no nearby GRBs can be expected. In this case, the value of  $f_{\text{GRB}}$  is just the fraction of all neutron stars capable of pulsar activity and, therefore, of GRB activity. If this value is roughly 0.05 (from the ratio of the number of known pulsars to the number of neutron stars expected to have been created in one pulsar lifetime ( $\sim 10^6$  years)), then there are roughly  $10^7$  GRB sources; the average recurrence time is, then,  $\sim 5 \times 10^5$  years.

On the other hand, perhaps most ( $> 50\%$ ) neutron stars are potential GRB sources, and the observed GRBs are distributed close to the Earth. The fraction,  $f$ , of all neutron stars capable of GRBs would be dictated by the mechanism of the burst: if, for example, all GRB sources are in binary systems, then the value of  $f$  would be dominated by the fraction of binary systems which would allow and survive the transformation of one member into a neutron star.

It is interesting to examine the specific case where  $\tau_{\text{rec}} \equiv 1 \text{ yr}$  and  $f_{\text{GRB}} \equiv 10^{-7}$ . If all neutron stars are evenly distributed within  $100$  kpc of the center of the Galaxy, and all neutron stars are GRB sources, then the nearest  $10^7 N_{\text{ns}}$  GRB sources would be located within  $300$  pc of the Earth. If  $\tau_{\text{rec}} = 10 \text{ yr}$ , the distance scale increases to  $\sim 600$  pc. Pacini and Ruderman (1974) have suggested that GRB sources are distributed in a disk  $2$  kpc thick in the plane of the Galaxy. If the radius of this disk is  $15$  kpc, the nearest  $300$  GRB sources (corresponding to  $\tau_{\text{rec}} = 10$  years) are located within  $70$  pc of the Sun.



### 3.3. Optical Radiation from Gamma-Ray Burst Sources

Since the discovery of transient optical radiation from outbursting GRB sources, several theories have been published attempting to explain its existence. The number of theories has remained small to date, much lower than the number of theories originally proposed to explain  $\gamma$ -ray emission from GRBs. The emission of optical light is much more strongly constrained by observations than the emission of  $\gamma$ -rays. Specifically, any theory of optical emission from GRBs must satisfy the following requirements:

- 1) The ratio of gamma-ray to optical fluence,  $F_\gamma/F_{\text{opt}}$ , must be of the order of  $10^3$ . This value was determined from the three archived optical flashes found by Schaefer (1981) and Schaefer, et al. (1984a), assuming a short ( $< 5$  second) optical burst time. This ratio could drop by a factor of several if the duration of the optical flashes significantly exceeds a few seconds (Rappaport and Joss, 1985).
- 2) The quiescent blue magnitude of the object  $m_b > 23$ , based on various deep searches of small GRB error regions.
- 3) The duration of the optical flash,  $\tau_{\text{opt}}$ , must be less than  $\sim 500$  seconds, based on the limit of image trailing in the 1928 archived optical flash found in the error region of GRB0116-29 (Schaefer, 1981).

The theories describing optical emission from GRBs describe the emission as being either 1) an integral part of the burst emission spectrum, or 2) a by-product of the burst (such as in the absorption of high-energy photons from the burst and their re-emission at optical wavelengths). Each of these types of emission model brings new restrictions on the mechanism producing the optical radiation.

It has been noted by several workers in the field that if the mechanism of emission of optical radiation is thermal, the radiation cannot be emitted at or near the surface of a neutron star because of the neutron star's low surface area. (Katz (1985) calculated that the brightness temperature of the archived 1928 optical flash was  $\sim 10^{16}$  °K (based on an estimate of  $m_v = 3$  for  $\tau_{\text{opt}} = 1$ s; if  $\tau_{\text{opt}} = 500$ s,  $T_b$  is still greater than  $10^{15}$  °K). Because typical temperatures seen in GRBs are of the order of  $10^9$  °K, Katz concluded that any mechanism producing optical radiation from the surface of a neutron star must not be thermal in nature.)

Schaefer and Ricker (1983) calculated that if the optical emission process is thermal, the emission must come from a region of radius  $\geq 10^8$  cm (for a GRB source distance of  $\sim 50$  pc) in order to be able to explain the optical flux at the Earth. Katz (1985) also noted that if the optical light is the result of thermal reprocessing of  $\gamma$ -rays from the burst in a neighboring object (a companion star and/or accretion disk), the quiescent temperature of the reprocessing surface must be  $\sim 1600$ °K to be able to explain the 20 magnitudes difference between the quiescent and outburst visual magnitudes.

Several theories for the production of optical light from GRBs have been proposed to date:

- (1) Tremaine and Zytlow (1985) noted that thermal optical and UV radiation would be produced by the impact of a comet onto the surface of a white dwarf. This interaction would lead to optical/UV bursts with no GRB counterpart.
- (2) Woosley (1984) proposed that optical light could be produced by cyclotron radiation at a distance of  $\sim 10^8$  cm from a highly-magnetized, outbursting neutron star. Woosley's assumptions on the structure and content of the neutron star magnetosphere are rather uncertain, yet are critical to the details of his model. For this reason, Woosley states that his results are uncertain but that the observational criteria could "in principle" be satisfied.
- (3) London and Cominsky (1983) first investigated the reprocessing of  $\gamma$ -rays from a GRB on a main-sequence companion star. Their model, which did not work for a main-sequence

companion, was improved by work of Rappaport and Joss (1985), whose model is able to explain the observed characteristics.

All of these theories point to a local ( $\sim 100$  pc) distribution of GRB sources. Some details of these theories are listed below.

### 3.3.1. The Impact of a Comet onto a White Dwarf

An interesting possibility presented by the model of Tremaine and Zytlow (1985) is for the creation of GRBs from neutron star impacts of comets from a comet cloud about the neutron star (cf. section 3.1.2). In the case of the formation of a neutron star by accretion of matter from a giant companion, impacts of comets onto the white dwarf remnant of the giant companion could give rise to bursts of radiation in the UV and optical bands from the heated surface of the white dwarf. The gravitational energy released in the impact is inversely proportional to the radius of the star impacted, so the ratio of optical to  $\gamma$ -ray burst energy would be  $R_{NS}/R_{WD}$ , or  $\sim 10^{-3}$ , which is consistent with observations. Typical quiescent absolute magnitudes of white dwarfs of  $M=11-16$  yield source distances of  $\sim 250-2500$  pc (given that the minimum quiescent visual magnitude of a GRB source is  $\sim 23$ ). The intriguing aspect of this theory is that optical and  $\gamma$ -ray bursts would not be simultaneous, since comet impacts onto the white dwarf are independent of impacts onto the neutron star. The impact rate onto the two stars would be comparable, so the  $\gamma$ -ray and optical burst rates from the system would be comparable.

This theory can also easily be extended to solitary white dwarfs which have retained their Oort cloud. The same analysis of event rates applies to a solitary white dwarf as to a solitary neutron star: the average impact rate is  $\sim 10^{-3} \text{ yr}^{-1}$ , with periods of comet storms when an average impact rate of  $\sim 1 \text{ yr}^{-1}$  can easily be achieved.

### 3.3.2. Self-absorbed Cyclotron Emission

Woosley (1984) proposes that optical radiation emitted from a GRB is cyclotron radiation intrinsic to the GRB itself. In his model, gamma-rays from the burst strike and accelerate electrons in the neutron star magnetosphere (whether from a burst wind or from accretion). These electrons then gyrate in the magnetic field of the neutron star and emit cyclotron radiation. The  $\gamma$ -ray emitting region near the neutron star is optically thick to the cyclotron fundamental frequency and its first  $\sim 100$  harmonics, leading to self-absorption of the cyclotron radiation. Due to Doppler smearing of the lines and the magnetic field gradient (assuming a roughly dipole magnetic field about the neutron star), the emitted radiation is the Rayleigh-Jeans tail of a blackbody spectrum, spanning the energy range from the cyclotron fundamental to the  $\sim 100$ th harmonic.

In a dipolar magnetic field with surface strength of  $\sim 10^{12}$  Gauss about a neutron star, the cyclotron energy at a distance of  $10^8$  cm is 0.046 eV ( $27 \mu\text{m}$ ), so the emitted spectrum, which spans a factor of  $\sim 100$  in energy, covers the range of  $\sim 2700 \text{ \AA}$  to  $27 \mu\text{m}$ , which includes the optical band. With this model and taking into account the large uncertainties in the magnetic field strength and distribution and the electron density distribution about the neutron star, Woosley states that the observed ratio of  $F_{\gamma}/F_{\text{opt}}$  of  $\sim 10^3$  could be achieved. The duration of the optical flash would be the same as that of the GRB ( $\tau_{\text{opt}} \leq 100\text{s}$ ), and the intrinsically faint neutron star satisfies the criterion of a faint quiescent source.

Because of its general applicability, the Woosley model of optical radiation from GRBs should be valid in any case: i.e., optical radiation should be emitted from virtually every GRB at some level. The validity of the application of this model to the optical transient events detected to date depends on whether the observed ratio of  $F_{\gamma}/F_{\text{opt}}$  can be achieved.

### 3.3.3. Reprocessed Gamma-Radiation

London and Cominsky (1983) have proposed that optical radiation could be produced by the reprocessing of GRB  $\gamma$ -rays in a close companion star. They have roughly calculated the brightness of the absorbing surface of a close (separation  $\sim 10^{11}$  cm) main-sequence or white-dwarf companion. They concluded that although this scenario would indeed produce optical light, it was inadequate to explain the observed quiescent criteria. Specifically, they found that their proposed binary companion

object was too bright and should be detectable if it were a main-sequence star or white dwarf. (As a reference, a star of  $m_v = 23$  at a distance of 100 pc has an absolute magnitude of 18. Typical white dwarfs have absolute magnitudes of 11-16 and main sequence stars have absolute magnitudes of up to  $M \approx 9$ ).

Rappaport and Joss (1985) improved on the analysis of London and Cominsky by considering a low-mass brown dwarf as a companion. They found that this system could produce optical radiation which satisfied the observed criteria over a range of companion masses, burst energies and source distances. Their model favors a companion mass of  $M_c < 0.05 M_{\text{solar}}$ , quiescent temperature  $T_{\text{quiescent}} < 1800^\circ \text{K}$  and burst energy  $E_b < 10^{38} \text{ erg}$ ; the favored distances range from  $< 50 \text{ pc}$  to  $< 250 \text{ pc}$  for Schaefer's three archived optical transients (Schaefer (1981) and Schaefer, et al. (1985)).

### 3.4. Discussion

The previous sections have outline the various theories for the production of  $\gamma$ -rays and optical bursts. Many possible stellar systems were proposed to explain GRBs and optical transients. However, only a few stellar systems were able to act as the source of both GRBs and optical transients. These scenarios are the most important for instruments such as the Explosive Transient Camera, since one can hope to learn about GRB sources from optical transients directly associated with the GRB itself.

The model of optical radiation from GRBs proposed by Woosley predicts optical burst radiation from virtually all GRBs, regardless of the GRB production mechanism. The optical burst would have a duration comparable to that of the GRB, and the optical light curve would be very similar to the  $\gamma$ -ray light curve, after accounting for the smearing of the optical light curve features over the larger optical emission region. The Woosley model of optical radiation from GRBs would therefore predict optical transients of short duration (a few seconds) with light curves that track the  $\gamma$ -ray light curve well.

On the other hand, the models of Rappaport and Joss (1985) and Tremaine and Zytlow (1985) both predict optical burst durations of tens to hundreds of seconds. All of these models require  $\gamma$ -ray/optical burst sources to be in binary systems. The only scenario of the model of Tremaine and Zytlow that allows GRBs and optical transients from the same binary system places the neutron star in a wide binary orbit with a white dwarf. The optical and  $\gamma$ -ray bursts are created by the impact of a comet with the white dwarf and the neutron star, respectively. In principle, of course, the  $\gamma$ -ray burst could be created by many of the  $\gamma$ -ray production mechanisms described above. The model of Rappaport and Joss puts the neutron star in a close binary orbit with a low-mass dwarf star. In their model, GRBs are created by virtually any mechanism described in section 3.3. The optical radiation would be  $\gamma$ -radiation from the neutron star, reprocessed in the surface layer of the companion star.

Both optical reprocessing models predict similar optical burst durations, consistent with the upper limit of Schaefer (1981). The model of Rappaport and Joss predicts optical burst duration of  $< 500\text{s}$ . In order to satisfy the constraint of  $F_{\text{opt}}/F_{\text{b}} = 10^3$ , the model of Tremaine and Zytlow predicts that the temperature of the white dwarf surface during outburst is  $\sim 9000^\circ \text{K}$ , so that most of the thermal energy of the burst emerges in the blue band. In that case, the burst duration would be  $\sim 100\text{s}$  (based on a total burst energy of  $10^{33} \text{ ergs}$  and a white dwarf radius of  $10^9 \text{ cm}$ ).

Both of these models explicitly predict that the  $\gamma$ -ray and optical burst rates from such systems should be similar. The main difference between the models is the timing of the  $\gamma$ -ray and optical bursts. Woosley (1983) and Rappaport and Joss (1985) predict simultaneous optical and  $\gamma$ -ray bursts, while Tremaine and Zytlow implicitly predict independent GRBs and optical transients. The prediction of the model of Tremaine and Zytlow that isolated white dwarfs will not be able to differentiate between the models, since the calculated optical transient rate from solitary white dwarfs is very low (see Chapter 10).

## CHAPTER 4

### The Concept of the Explosive Transient Camera

#### Introduction

The discovery in 1981 of an apparent optical transient associated with a gamma-ray burst error region (Schaefer, 1981) sparked the interest in trying to detect optical light from a GRB source in outburst. Specifically, it became clear that an instrument to monitor the full sky for optical transient events was needed to complement the  $\gamma$ -ray detectors currently in operation in deep space. Data taken from  $\gamma$ -ray and optical transient detectors operating in parallel would provide useful information about the nature and mechanism of GRBs.

In early 1982, George Ricker and co-workers at MIT began the conceptual development of an automated, wide-field instrument to detect celestial optical flashes from space. This instrument, dubbed the Explosive Transient Camera (ETC), would be sensitive to increases of brightness of celestial objects on timescales of 1-4 seconds. The design, construction and testing of a sub-unit of the plenary ETC began in the Spring of 1983.

The ETC would be a very effective ground-based sky monitor, combining a large viewing solid angle ( $\sim 1.5$  steradians) with the large observing time available to a dedicated, automated instrument. As a detector of celestial brightenings on timescales of 1-4 seconds, the ETC would investigate an entirely new range of parameter space in astronomy, since most astronomical measurements are made on timescales of minutes to hours (standard imaging or spectroscopic observations) or milliseconds (photometric studies with photomultiplier tubes). It is quite possible, therefore, that the ETC may detect optical transients with no astrophysical precedent.

The following chapters describe the ETC test instrument and the operations of the ETC in detail. This chapter discusses the ETC as it will stand in its final configuration; a description of the operation of the ETC will follow in Chapter 5. Chapters 6 through 9 describe the test instrument and the details of the software-controlled operation, data flow and instrument control in the ETC.

#### 4.1. The Plenary ETC

The plenary ETC will consist of 32 CCD cameras monitoring the night sky. Each CCD camera consists of a wide-field lens illuminating a cooled CCD, resulting in a  $15^\circ \times 20^\circ$  field-of-view. The 32 CCD cameras will monitor 16  $15^\circ \times 20^\circ$  fields: two CCD cameras will monitor a given patch of sky. In this way, the ETC will operate in coincidence: no optical flash detected in one camera will be considered real unless confirmed by the detection of a flash at the the same celestial coordinates in the other camera monitoring the field. Operating the CCD cameras in coincidence virtually eliminates the possibility of the detection of false optical flashes due to local effects, either in the CCD or in the immediate vicinity of the cameras.

The two sets of 16 CCD cameras will be located on two sites separated by  $\sim 1.5$  km on Kitt Peak, near Tucson, Arizona. (Site 1 is located on the summit of Kitt Peak; Site 2 will be located on the southwest ridge of Kitt Peak, near the picnic area and the NRAO 12m telescope: see Figure 4.1). Sources of optical flashes located in the Earth's atmosphere can be recognized by virtue of the parallax afforded by the distance between the two sites. The precision of localization of an optical flash by an ETC camera is 1.5 arc-minutes, sufficient to recognize (and reject as non-celestial) sources of optical flashes at altitudes of up to 3000 km.

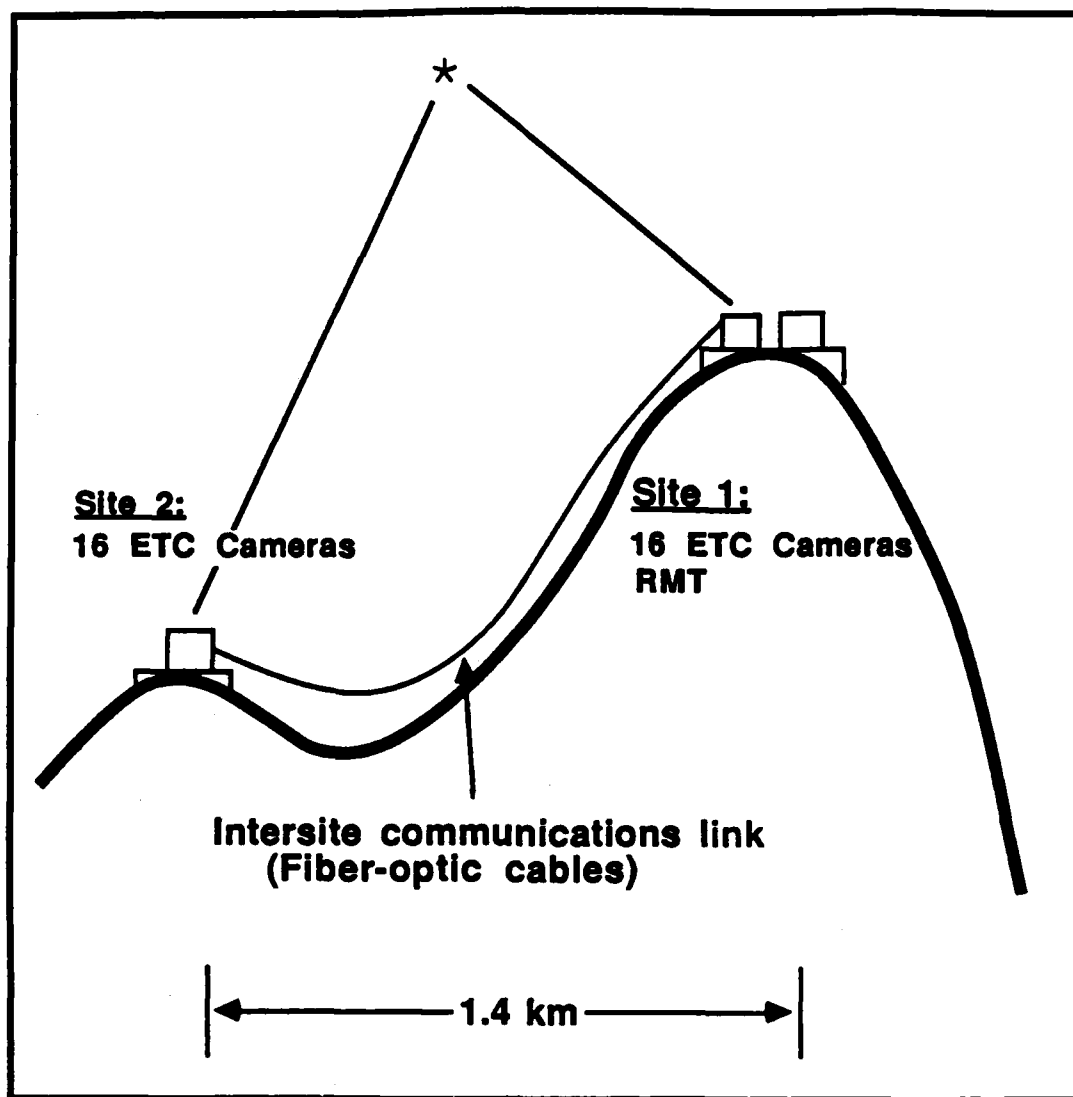


Figure 4.1: The proposed layout of the full-up ETC at Kitt Peak. Site 1, presently the location of the ETC test unit, is the former Airglow Laboratory and Twelve-Inch Schmidt Dome on the summit of Kitt Peak. Site 2 is to be located on the southwest ridge at Kitt Peak, several hundred meters east of the sites of the NRAO and McGraw-Hill telescopes. Intersite data flow will likely be over fiber-optic cable. The Rapidly Moving Telescope (RMT) will be located in the refurbished Airglow Laboratory adjacent to the ETC dome at Site 1. Through the use of two sites, terrestrial sources of optical flashes (such as satellites and meteors) can be eliminated by the use of parallax afforded by the separation between the sites.

## 4.2. ETC Observations

The sixteen cameras at each site will be mounted on two sidereal drives, which will track the sky in order to avoid the smearing of stellar images (see Figure 4.2 for an illustration of the layout of eight ETC cameras on one tracking drive). Each set of eight cameras will begin observations at a predetermined hour angle east of the meridian and monitor the sky for about two hours. The drives will then slew back to their original hour angles and monitor a new patch of sky for the next two hours.

The plenary ETC will be entirely automatic. Operations will be initiated by a human user: the ETC computers will then be in complete control of the the ETC instrument and operations. The ETC will operate between evening and morning astronomical twilight, and then only under photometric or nearly-photometric conditions. The continuous monitoring of weather sensors near each site will allow the ETC control computer to know whether precipitation is present or imminent and thus whether the protective dome should be closed or not opened. The ETC will be able to tell whether the sky is cloudy from an analysis of stellar brightnesses in the CCD camera images; thus, the ETC will be able to judge the quality of the night sky and from this, to be able to determine whether observations should commence or continue. Synthesized voice communication will allow for telephone calls for human assistance or intervention if required.

Observations with the ETC consist of a series of contiguous, short (1-4 second) exposures of the night sky. The observations are controlled and directed by a small, powerful microprocessor known as the *Overseer* computer; the real-time analysis of ETC image data (at a rate of  $10^5$  bytes/camera/second) is done by a *Trigger* processor associated with each camera. The plenary ETC will consist of one Overseer computer, 32 CCD cameras and 32 Trigger processors analyzing CCD image data in parallel. During observations with the ETC, all CCD images are read out simultaneously at regular intervals of 1-4 seconds. Since the duty cycle of the ETC is 100% (i.e., a new integration in each CCD commences immediately after the readout of an image), the ETC computer system must complete its analysis and storage of image data in less than an exposure time. When the exposure time of an image has expired, the CCDs are read out in parallel: the output of each CCD is amplified and digitized and sent to a dedicated Trigger processor, which analyzes the image for sudden brightenings by an arithmetic comparison of the image to its immediate predecessor. The location on the CCD of any optical flashes detected by a Trigger processor are sent to the Overseer computer, which calculates the celestial coordinates (right ascension and declination) of the event from its location on the CCD. After all Trigger processors have finished image analysis, the Overseer computer compares the celestial coordinates of the events reported by the Trigger processors during the last analysis period. If the Trigger processors associated with a pair of cameras pointing at the same patch of sky report events from the same celestial coordinates (to a programmed precision), the reports are considered to have come from a true celestial optical flash.

In the time between the end of the analysis of the image data by the Trigger processors and the readout of the images being exposed concurrently, the Overseer computer will record and analyze data from any celestial flashes detected in this or previous images. The data stored from a flash are taken from both cameras detecting the event, and include  $30' \times 30'$  image subarrays centered on the flash and on several photometric standards near the flash. These data are moved from the Overseer computer's volatile memory and stored on magnetic tape at regular intervals. If, in subsequent exposures, the Overseer computer determines that the brightness of a flash has returned to its quiescent level or has subsided below the detection threshold of the ETC, it will no longer store data from that flash event.

The celestial coordinates of any confirmed celestial flash will be sent upon detection to the Rapidly Moving Telescope (RMT; Teegarden, et al., 1984) (presently under construction at the Goddard Space Flight Center), which will be located in a building adjacent to the building housing ETC Site 1. The RMT (see Figure 4.3) consists of a 7" telescope pointing down at a two-axis gimbaled mirror, capable of slewing to any spot on the sky within one second with an accuracy of one arc-second. The RMT, with a one-second image sensitivity of  $m_v \sim 14$  ( $10\sigma$  significance), will take contiguous  $<1s$  exposures of the event and store data from the event until the brightness of the event drops below the detection threshold of the RMT.

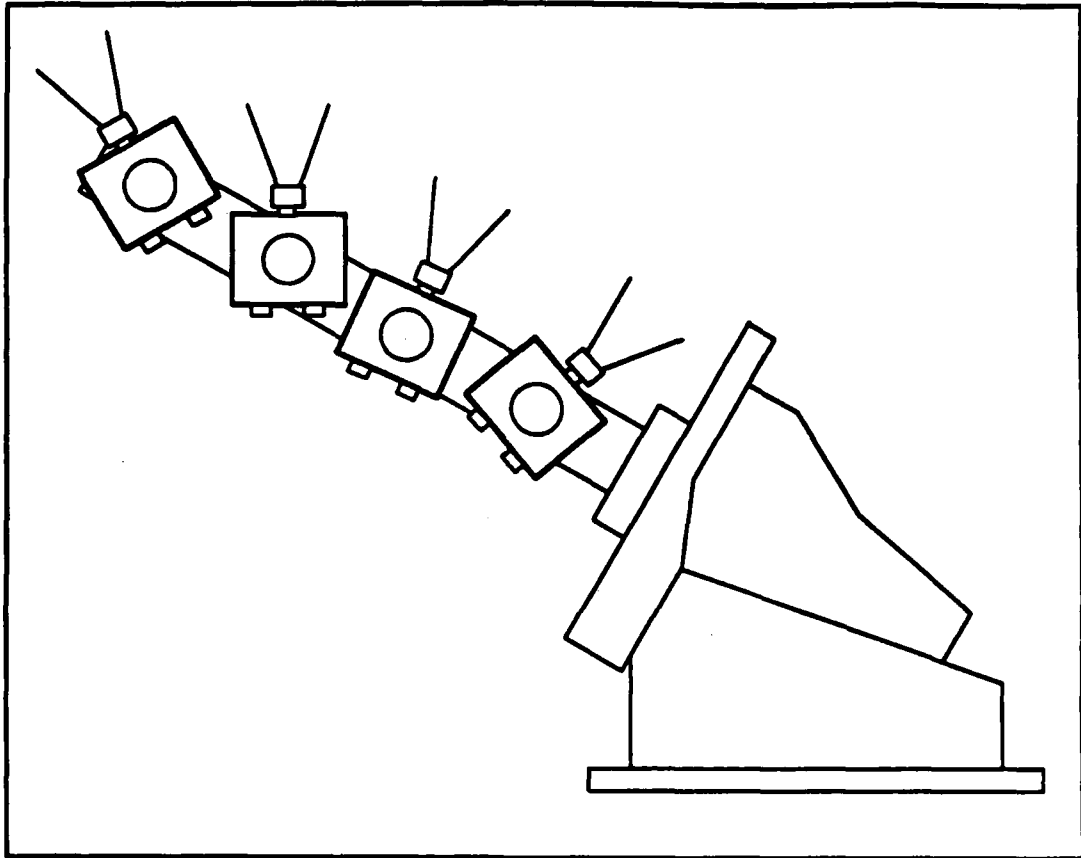


**Figure 4.2:** A schematic layout of the future ETC tracking mount, showing four of eight CCD cameras.

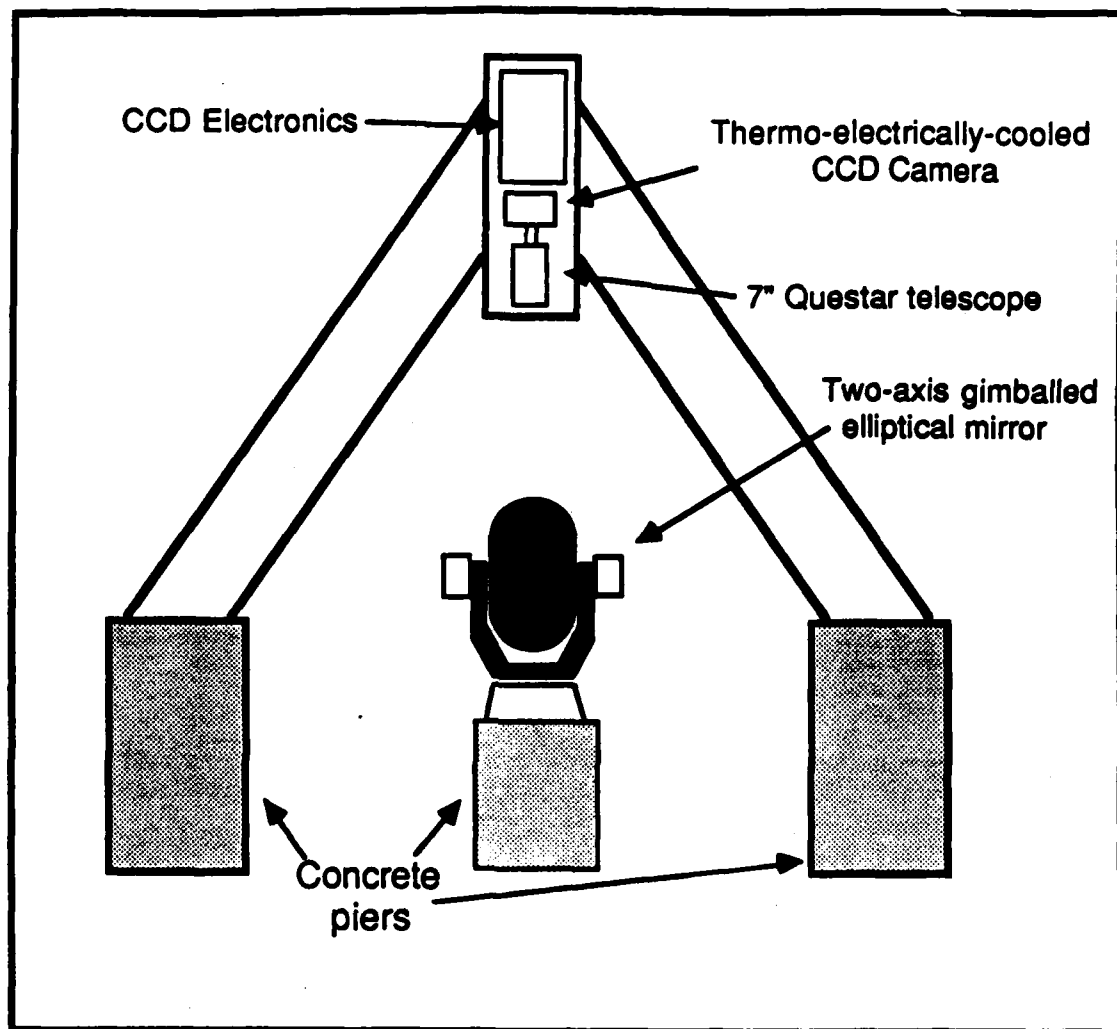


**Figure 4.3:** Cross-sectional view of Rapidly Moving Telescope (RMT) presently under construction at the Goddard Space Flight Center. The two-axis gimbaled mirror can slew to any part of the sky within one second with arc-second accuracy. Light is reflected from the mirror into the aperture of a standard 7" Questar telescope and then focussed onto a thermoelectrically-cooled CCD. The field of view of the RMT is 5x8 arc-minutes. The sensitivity of the RMT is  $m \approx 14$  in a one-second exposure (ten sigma level-of-confidence).



### 4.3. The Sensitivity of the Plenary ETC

The sensitivity of the ETC can be described in two ways: 1) the sensitivity of a single camera in imaging the sky and 2) the sensitivity of a single camera to the detection of an event. The sensitivity of an ETC camera as an imaging device is given by the equation

$$q_i = \frac{S}{(S + \sigma_R^2 + B\tau)^{1/2}} \quad (4.1)$$

where  $q_i$  is the significance of the detection in a single camera,  
 $S$  is the signal at the CCD (in electrons)  
 $\sigma_R$  is the CCD readout noise (in electrons/pixel),  
 $B$  is the sky rate per pixel at the CCD (in electrons/second/pixel)  
 $\tau$  is the exposure time (in seconds)

An image of signal  $S$  electrons in one CCD pixel will be detected at a signal-to-noise ratio  $q_i$  in a CCD camera of readout noise  $\sigma_R$  and sky brightness  $B\tau$ .

The sensitivity of the ETC to the detection of a brightening in a CCD image frame differs from the  $q_i$  because a difference measurement from two image frames is necessary to detect a brightening. Because both images have an associated sky noise and readout noise, the total noise associated with the difference between the images is larger than the total noise associated with a single image. In the calculation of the total noise of the difference of two images, the sky and readout noises must be taken into account twice. The formula for the significance of a difference detection is, then,

$$q_d = \frac{\Delta S}{(\Delta S + 2\sigma_R^2 + 2B\tau)^{1/2}} \quad (4.2)$$

where  $q_d$  is the significance of a difference detection in a single camera, and  $\Delta S$  is the signal level (in electrons) above the sky+bias level in the CCD. (This equation is a specific instance of equation 11.1 for the situation where the star is not visible before the event).

In order to relate the detected signal  $S$  to stellar magnitudes, one must have a complete understanding of the effects of absorption due to the various media between the star and the CCD. A star which is seen as  $N$  photons/s/cm<sup>2</sup>/A at the top of the atmosphere will be measured as  $e_a e_f e_w e_c N \Delta \lambda \tau$  electrons at the CCD, where  $e_a$ ,  $e_f$ ,  $e_w$ , and  $e_c$  are the transmissivities of the atmosphere, filter, lens and window, respectively;  $e_c$  is the efficiency of the CCD (in e<sup>-</sup>/photon);  $e_v$  is the averaged effect of the reduction of overall lens transmissivity due to vignetting;  $A$  is the area of the lens; and  $\Delta \lambda$  is the bandpass of the filter (in A). When the fact that the point-spread-function of the lens spreads the image charge over several pixels is taken into account, the number of electrons in the peak pixel of a stellar image is  $e_a e_f e_w e_c e_v N \Delta \lambda \tau$ , where  $e_p$  is the fraction of a stellar image in the highest pixel of the image (see Figure 4.4 for a schematic illustration of the transmissivity of the ETC CCD camera system). Thus, given a detected signal of  $S$  electrons above the sky+bias level in a CCD, the value of  $N$  can be calculated as  $N = S / (e_a e_f e_w e_c e_v A \Delta \lambda \tau)$ . For visual magnitudes, the value of  $N$  can be related to  $m_v$  by the formula  $N = 1.05 \times 10^{13} 10^{-0.4 m_v}$  photons/cm<sup>2</sup>/A.

The sky rate,  $B$  electrons per pixel per second, can be calculated from the sky brightness,  $H$  photons/cm<sup>2</sup>/s/m<sup>2</sup>/A, as  $B = e_f e_w e_c A H \tau \Delta \Omega \Delta \lambda$  electrons/pixel at the CCD, where  $\Delta \Omega$  is the solid angle subtended per pixel. The value of  $H$  is  $2.35 \times 10^{-6}$  in V-band (5000A to 6000A).

The values of the above variables projected for the full-up ETC are tabulated in Table 4.1 along with the expected ETC threshold sensitivity to detected events, as calculated from equation 4.2. The plenary ETC can be expected to detect a flash at a signal-to-noise ratio of 10 at visual magnitude  $m_v = 10.3$  in a one-second exposure and at 11.3 in a four-second exposure. (A  $10\sigma$  flash detection in the ETC is achieved by  $7\sigma$  flash detections in each of two cameras in the ETC; a  $7\sigma$  flash detection corresponds to a level of confidence of 0.9999997 in a single pixel (this level of confidence does not correspond directly to that given by Gaussian statistics: cf. Chapter 11 and Figure 11.3)). Note from Table 4.1 that the *a posteriori* signal-to-noise ratio of a detected event is greater than the detection

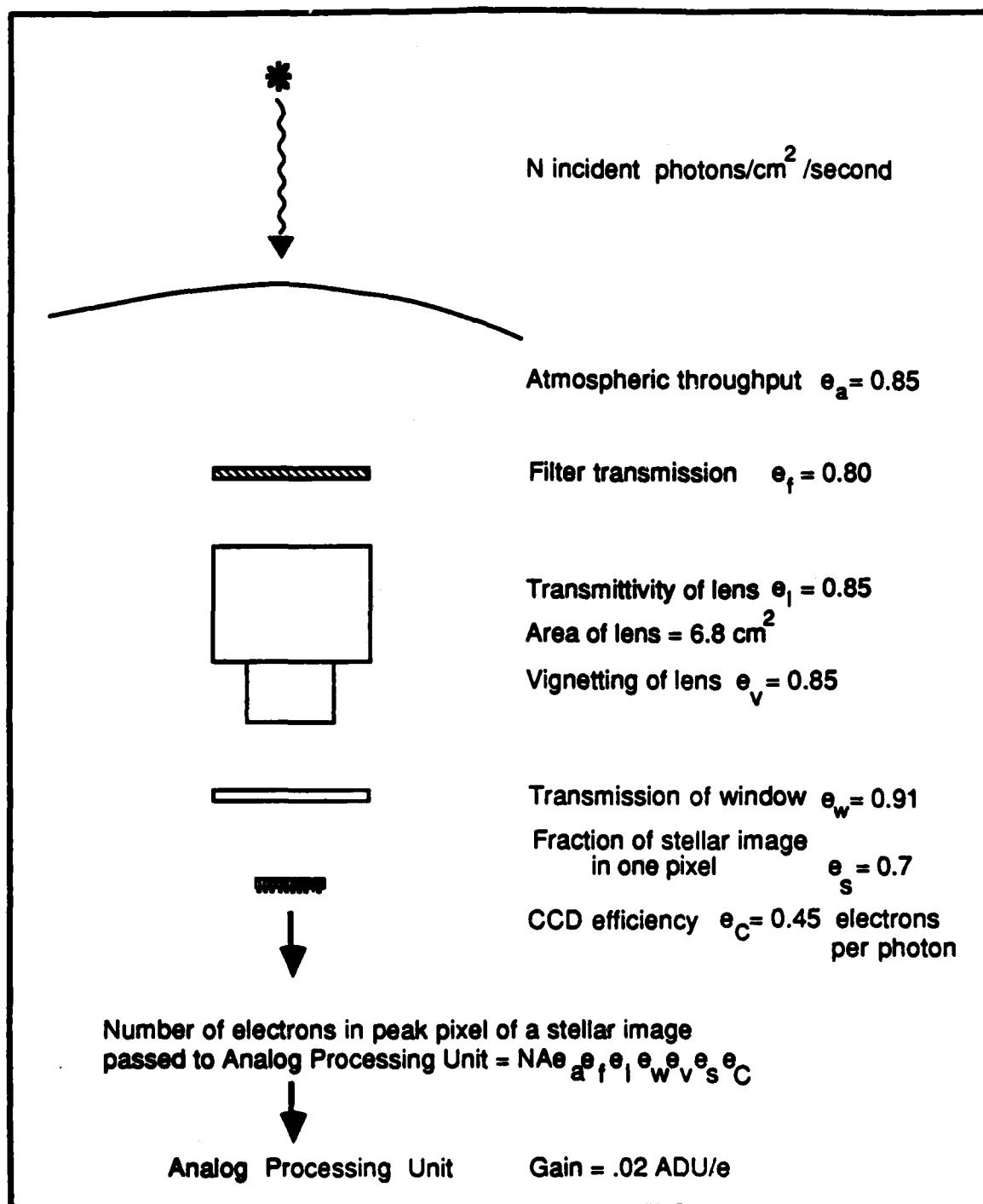


Figure 4.4: This figure schematically represents the path of photons incident to the Earth's atmosphere in reaching the ETC as digitized data. The values given here are those corresponding to the ETC test unit (see Chapter 11).

signal-to-noise ratio, because the signal electrons from the full stellar image can be taken into account. These *a posteriori* detection sensitivities are also listed in Table 4.1, under "full image sensitivity".

#### 4.4. The Sky Coverage of the Plenary ETC

The ideal arrangement of the ETC's sixteen 15x20 degree fields-of-view on the night sky is one that maximizes the observed solid angle coverage of the CCD cameras while minimizing atmospheric effects. The total solid angle is maximized by minimizing the overlap of adjacent fields. Atmospheric effects, which include a reduction of atmospheric transmissivity and an increase in image and field distortion, increase with zenith angle. Atmospheric effects are, in general, minimized by minimizing the mean angular distance of all fields-of-view from the zenith.

The mapping of the sixteen ETC fields-of-view is dependent on the structural constraints of the ETC instrumentation. The sixteen cameras at each site are divided into eight pairs: each pair of cameras is structurally required to point at the same right ascension. The relative right ascensions of all

CHARACTERISTICS OF THE CCD CAMERAS OF THE PLENARY ETC		
	Symbol	Value
Focal length	F	25 mm
f-number	f	0.85
Area	A	6.8 cm <sup>2</sup>
Angular size	$\Omega$	9.55 '2
Bandpass	$\Delta\lambda$	4500Å - 7500Å
Sky brightness	H	2.4x10 <sup>-6</sup> ph/cm <sup>2</sup> /s/Å
Atmospheric transmissivity	$e_a$	0.85
Filter transmissivity	$e_f$	1.0 (no filter)
Lens transmissivity	$e_l$	0.8
Window transmissivity	$e_w$	0.95
CCD efficiency	$e_c$	0.53 e <sup>-</sup> /photon
CCD gain	1/g	12 e <sup>-</sup> /adu
CCD readout noise	$\sigma_R$	25 e <sup>-</sup>
Stellar image splitting	$e_s$	0.7
10 $\sigma$ event sensitivity (1s)		10.3
10 $\sigma$ event sensitivity (4s)		11.3
10 $\sigma$ event sensitivity (10s)		11.8
10 $\sigma$ full image sensitivity (1s)		10.7
10 $\sigma$ full image sensitivity (4s)		11.7
10 $\sigma$ full image sensitivity (10s)		12.2

Table 4.1: Optical Characteristics of Plenary ETC

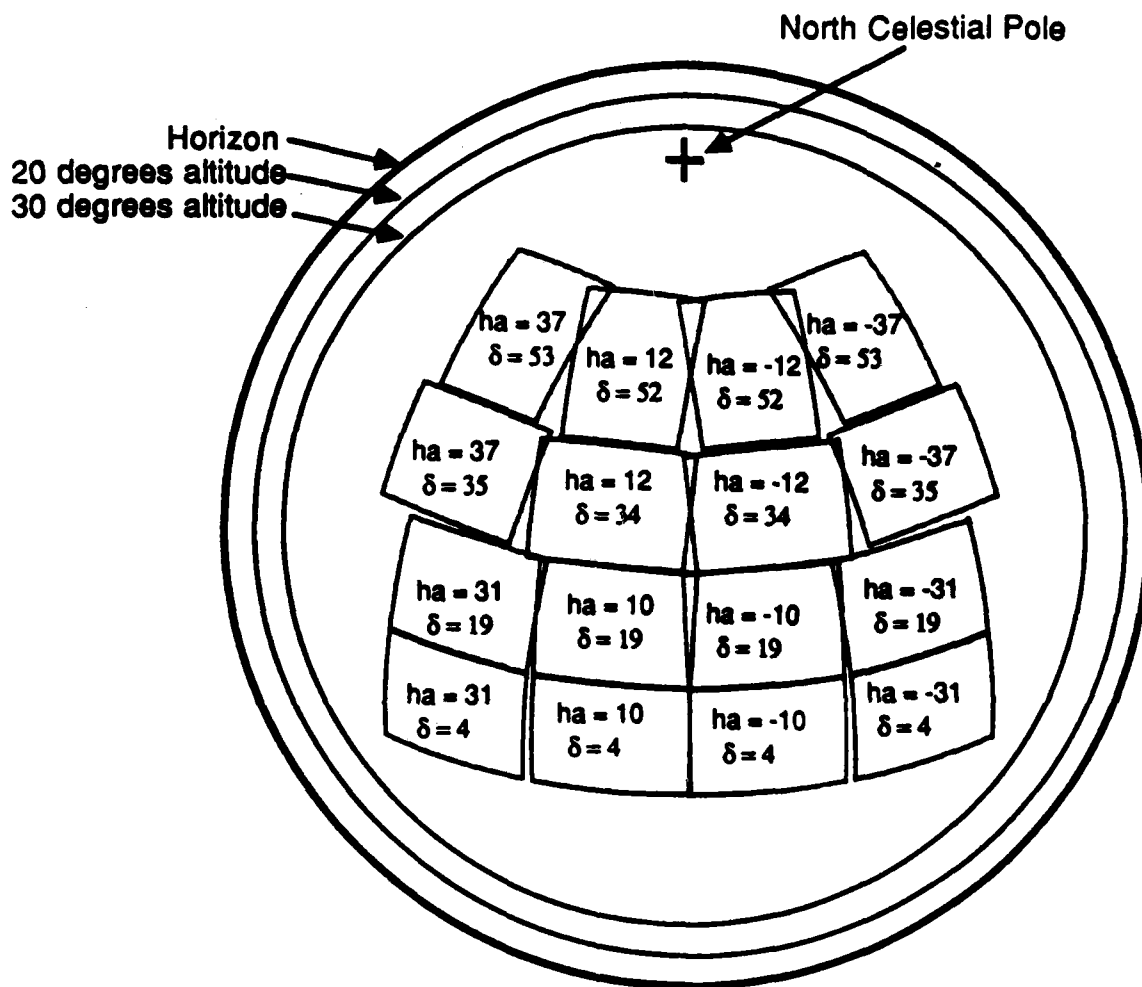


**Figure 4.5:** Possible layout of the plenary ETC camera fields-of-view on the night sky. The view shown is a zenith projection from Kitt Peak. Coordinates inside each field are the coordinates of the field center. Each field-of-view has an angular size of 15 x 20 degrees.

pairs is continually variable, as is the declination of each individual ETC camera.

The problem of finding an analytic method to find the ideal orientation of the fields-of-view was presented to a graduate mathematics seminar led by Professor Dan Kleitman, the chairman of the mathematics department at MIT. This group concluded that a simple analytic solution was not possible: they suggested that an adequate solution could be found by trial-and-error, mapping the fields-of-view onto the night sky by hand according to the structural constraints. Figure 4.5 shows the result of such a trial-and-error analysis: the proposed layout of the sixteen ETC camera fields-of-view.

#### 4.5. Survey Capabilities of the Plenary ETC

The ETC will operate under photometric conditions during dark and grey time (in the period between third and first quarters of the Moon) at Kitt Peak. Thus, the ETC could potentially observe ~180 nights per year. Given that the mean night is nine hours long, if half of these nights are clear enough to allow observations, then the ETC will observe roughly 820 hours per year. Combining this with the observed ETC efficiency of ~75% (see Chapter 11) leads to the estimate of the time the ETC is actually observing per year of 616 hours. The total observing solid angle of the plenary ETC is  $16 \times 282^{\circ 2} = 4512^{\circ 2} = 1.37$  steradians. The total actual solid-angle-time product of the plenary ETC, taking all above considerations into account, is 850 sr-hours per year.

An estimate of event rates from known sources of celestial optical flashes can be made from the estimate of the observing time per year of the plenary ETC and the analysis presented in Chapter 10. Specifically, the value of 850 sr-hrs observed per year yields direct estimates of event rates from Figure 10.6. Given the sensitivities of event detection listed in Table 4.1, the ETC can be expected to detect optical flashes from GRBs at a rate of 0.5 per year for one-second exposures, 4 per year for four-second exposures and 8 per year for ten-second exposures.\* In addition, the ETC should detect 14, 420 and 3800 flare stars per year in one-, four- and ten-second exposures, respectively, assuming a mean flare risetime of 30 seconds (see Chapter 10).

---

\*Assuming the duration of the optical burst to be five seconds.

## CHAPTER 5

### ETC Operations

#### Introduction

The plenary ETC is intended to be a completely independent, automated instrument completely under computer control. It must be able to think and react with the flexibility of a human observer, but more quickly and more consistently. In addition, the operation and data storage of the ETC must occur smoothly and efficiently. As a result, controlling software for the ETC instrument is quite complex. Through its interactions with the peripheral computers, the ETC software must control every aspect of ETC operations. In addition, it must operate in a fashion that assures that any and every failure mode which we can possibly anticipate is rendered "failsafe"

This chapter is intended to give the reader an overview of ETC operations, ranging from the highest (day-to-day) level to the lowest (second-to-second) level. (Extensive details of the ETC software are given in chapters 7, 8 and 9.)

#### 5.1. ETC Instrument Control

All aspects of ETC operations are controlled by computer. In the plenary ETC, the control system will be set into operation by a human user, and then operate for months at a time with no significant human interaction. The only exceptions to this complete computer control are 1) when the system detects an instrument failure and requests human help, 2) the periodic replacement of magnetic storage media and 3) the periodic cleaning of optical surfaces.

The computers controlling the ETC are divided into three distinct units. Each computer has a specific set of tasks and works independently of the others. The master computer is a small, powerful Motorola 68000-based computer known as the *Overseer* computer. The Overseer computer is responsible for controlling and coordinating ETC operations and thus is in a very real sense the "brain" of the ETC.

The Overseer computer controls ETC hardware operations and data flow through two sets of slave computers. The first, the *Instrument Control Electronics* (ICE), is the Overseer computer's link to the system's CCD cameras and most of the ETC instrumentation. The ICE is truly a slave computer, having no independent control over any part of the system: it simply executes commands given by the Overseer computer.

The second, the *Trigger* processor, on the other hand, is more of an "idiot savant": its primary responsibility is to analyze incoming CCD data quickly and efficiently. Each Trigger processor analyzes data from a single ETC camera: the plenary ETC will therefore include 32 Trigger processors. Each Trigger processor accepts successive images from its associated camera and examines them for flash events. Any potential events detected by a Trigger processor is reported to the Overseer computer at the time of detection.

ETC operations consist of the reading out and analysis of contiguous, precisely-timed exposures of the night sky. Data flow in the ETC is initiated by the Overseer computer, which, at the end of an exposure, commands the ICE to read out all CCDs. The CCD image data is amplified and digitized in the ICE and then sent to the Trigger processors, which analyzes the image for any significant brightenings by, among other things, comparing it to the preceding exposure. Reports of brightening are sent from the Trigger processor to the Overseer computer over RS-232 serial link, while image data is transferred over a custom high-speed serial link (HSSL) at a rate of 250 kpixels/second. After the analysis and any data storage are completed, the next image is read out for analysis.

## 5.2. A Typical Observing Night

A typical observing night for the ETC is moonless and nearly photometric, and is about nine hours long. The ETC begins operations shortly before astronomical twilight, when an on-board clock alerts the Overseer computer that it is time to observe. The Overseer computer then commands all sidereal drives to slew to their designated starting points, generally two hours east of the meridian, and then to begin tracking the sky. The Overseer computer then checks all weather sensors to make sure that it is safe to open the protective dome. If so, the Overseer computer opens the dome with a command to the ICE (a flow diagram of the setup operation is given in Figure 5.1).

Once the dome is open, the Overseer computer analyzes images of the night sky for patchy clouds or an extended cloud cover, since any clouds in the field-of-view can create false optical flashes by briefly covering a star in an ETC field. The Overseer computer compares the brightnesses of stellar images in a CCD exposure to their expected brightness: if the transmissivity of the atmosphere is high enough ( $>80\%$ ) and if no individual stars are significantly dimmer than expected (e.g., due to patchy clouds), the Overseer computer initiates observations.

A single observation cycle consists of monitoring a given patch of sky for about two hours, after which the sidereal drives will be commanded to slew back to their initial position. A new observation cycle then begins, with all cameras observing a new patch of sky. This method assures that the cameras will always be observing at or near the meridian, so that the effects of atmospheric extinction are minimized.

### 5.2.1. An Observation Cycle

An observation cycle consists of a series of short (1-4s) contiguous exposures of the night sky taken simultaneously by all CCD cameras. (A flow diagram of an exposure cycle is given in Figure 5.2; a timing diagram of an ETC exposure can be found in Figure 5.3). The exposures are timed by the Overseer computer's high-precision countdown timer (the *frame timer*). Near the end of an exposure, the Overseer computer notifies all Trigger processors that data transfer is imminent. When the frame timer expires, the Overseer computer commands the ICE to read out all CCDs. The CCD images from each camera are transmitted to the corresponding Trigger processor: each Trigger processor then analyzes its image for brightenings by, among other things, comparing the image to its direct predecessor (see Chapter 8 for details). Any potential flash candidate noted by a Trigger processor is reported to the Overseer computer in the form of a *candidate report*, which lists the location on the CCD of the potential flash. The Overseer computer converts this location to celestial coordinates, and stores the coordinates in a table. By comparing the celestial coordinates of all candidate reports from a given exposure, it can use a coincidence requirement to determine whether a legitimate celestial flash has been detected.

Any confirmed celestial flash is added to the Overseer computer's *active flash list*. In the time after the analysis of a set of images by the Trigger processors and before the next set of images is read out, the Overseer computer collects and stores image data from each flash in the active flash list. This data, which consists of small subarrays (9x9 pixels) centered on the locations of the flash and several nearby photometric standards, is transferred from the appropriate Trigger processor to the Overseer computer at the request of the Overseer computer. If the Overseer computer determines that a flash has subsided to its pre-event brightness, it removes the flash from the active flash list: after this point, no further data from the flash is collected.

The Overseer computer will report the coordinates of any confirmed celestial flash to the RMT (see section 4.1.2), which will immediately slew to the coordinates of the flash and collect data from the flash until the flash brightness has subsided below the detection threshold of the RMT.

This series of exposures will continue until the end of the observation cycle. The Overseer computer will automatically interrupt the observation cycle periodically in order to a) check the sky conditions by measuring atmospheric throughput, b) recalibrate the mapping of CCD location to celestial coordinates (see section 7.1.4.2) and c) store onto magnetic tape any data taken in the last observing period.

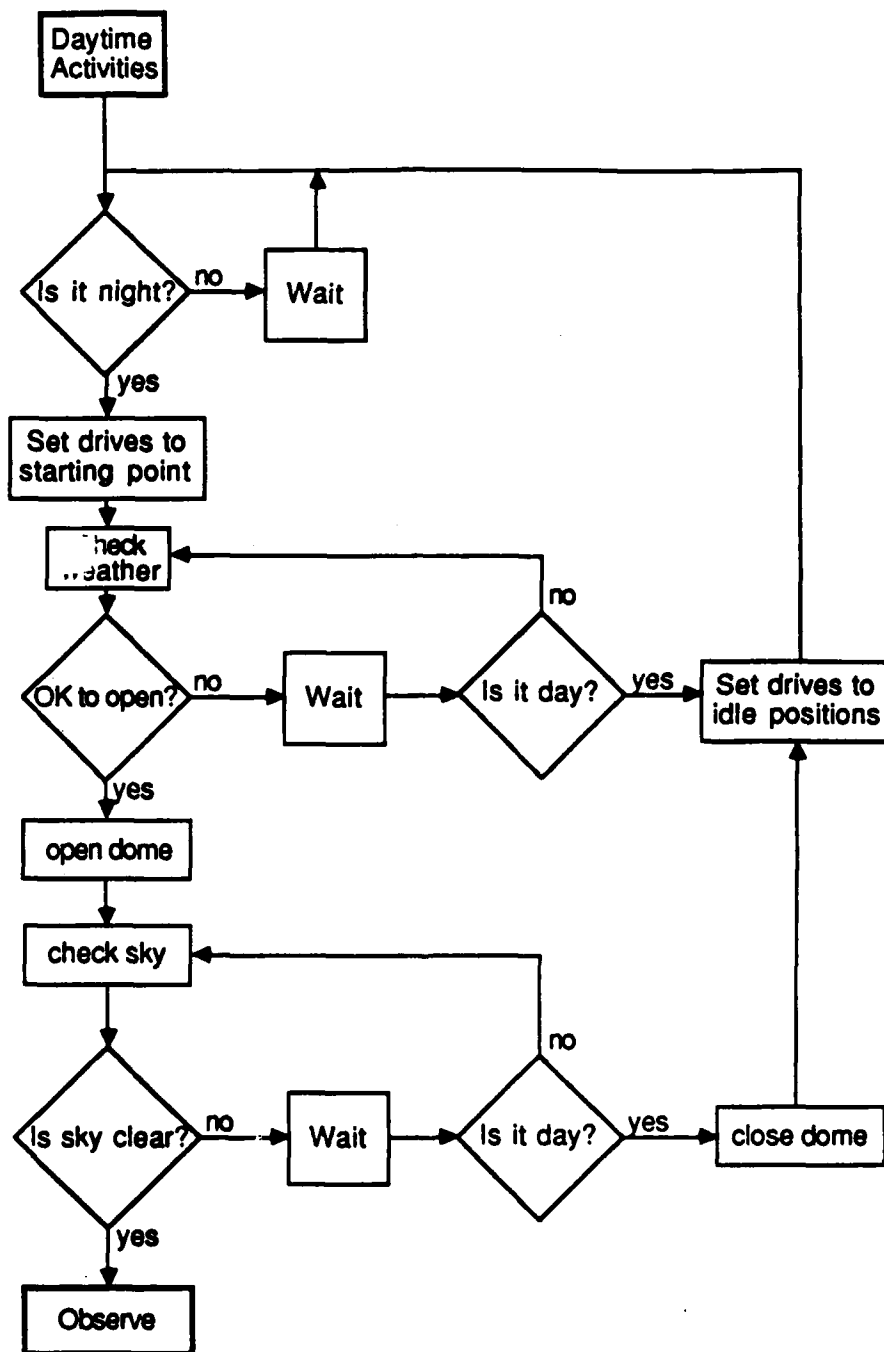


Figure 5.1: Flow chart of the setup of ETC operations



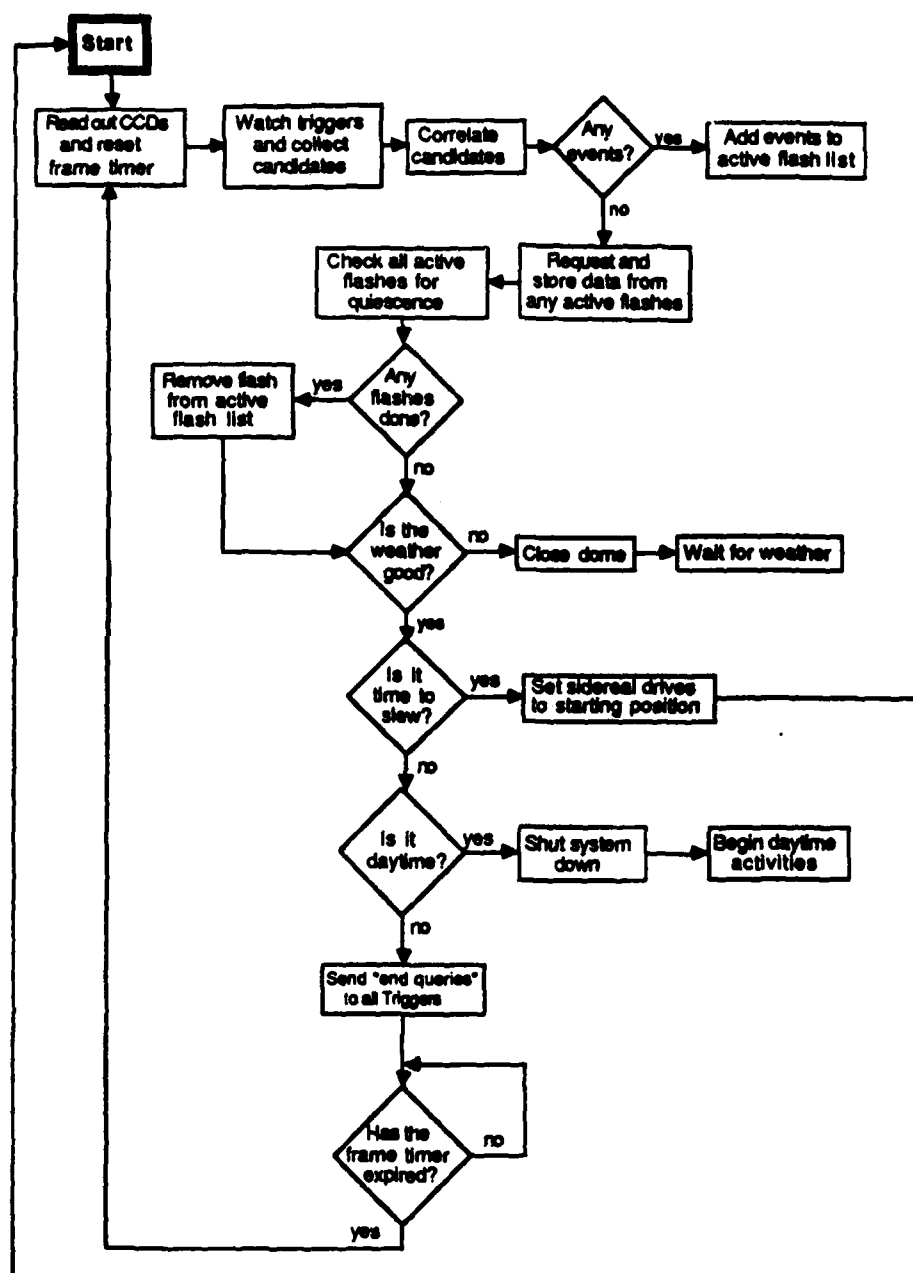
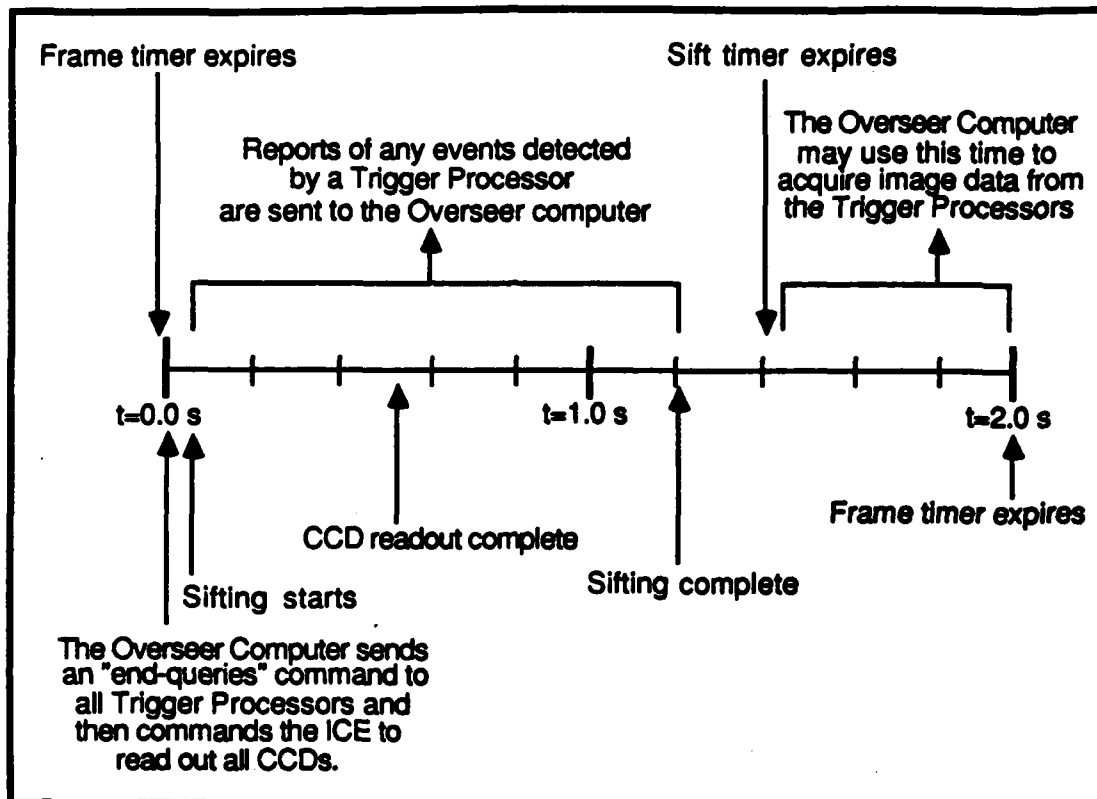


Figure 5.2: Flow chart of an ETC exposure cycle during observations.



**Figure 5.3: ETC exposure cycle timing diagram.** This figure schematically describes the sequence and timing of events during a single exposure cycle. Soon after the CCDs are read out, each Trigger processor begins the process of analysis (sifting) of the incoming CCD image data. Any event detected by a Trigger processor are reported to the Overseer computer, which tabulates and correlates them as they come in. Sifting continues until completion or until the sift time expires, whichever comes first. After the sift timer expires, the Overseer computer has time to request data from the Trigger processors. Immediately before the frame time expires and the CCDs are to be read out, the Overseer Computer issues an "end queries" command to the Trigger processors, notifying them of incoming data. (See text for details).

In addition, observations can be unexpectedly interrupted for the following re

- 1) Data has been taken from the maximum allowable number of flashes. If more than a certain number of flashes (presently 6) are detected in any observing period, the Overseer computer must interrupt operations in order to store this data on magnetic tape.
- 2) The weather sensor reports impending precipitation. A protective dome is then automatically closed and the Overseer computer halts operations.

#### **5.2.2. End of the night**

When the Overseer computer's onboard clock reports that the observing night is over (generally shortly after morning astronomical twilight), the Overseer computer will shut the system down. The last data are stored onto magnetic tape, the mounts are slewed to the meridian and locked into position and the dome is closed. The Overseer computer can then proceed with any daytime activities, which potentially include some further reduction of stored data, the analysis of cosmic-ray interactions with the CCDs or the transmission via modem of collected data to MIT. Otherwise, the Overseer computer waits for night to fall, when the cycle begins anew.

## CHAPTER 6

### The ETC Test Instrument

#### Introduction

The completed ETC will consist of 32 CCD cameras and their associated hardware located at two sites on Kitt Peak. The instrument described in this thesis is a sub-unit of the plenary ETC, intended to test the concept and design of the Explosive Transient Camera as a whole. The expansion of this instrumentation to the complete, 32-camera ETC requires the construction of several copies of this sub-unit and their integration with the ETC system as a whole.

The test unit is a four-camera "mini-ETC" set up at Site 1 at Kitt Peak (see Figure 4.1). The test unit is controlled by a complete Overseer computer (the same Overseer computer which will control the plenary ETC). The CCDs and ETC instrumentation are controlled by a set of Instrument Control Electronics (ICE), which respond to commands issued over RS-232 serial link by the Overseer computer. Image data from the four CCD cameras is analyzed for sudden brightenings by four parallel Trigger processors, which communicate with the Overseer computer over RS-232 serial links. (A schematic layout of the data and communications paths in the prototype ETC can be found in Figure 6.1). The ETC sub-unit is completely functional, and through the Overseer computer and Trigger processor software is able to conduct observations in a semi-automatic mode.

#### The ETC Test Unit

The ETC test unit was constructed between May, 1983 and October, 1984, at the Center for Space Research's Balloon Laboratory at MIT. The test unit consists of four cooled-CCD cameras mounted on a sidereal drive, sharing a common vacuum and cooling source.

The test unit's CCD cameras were based on an existing  $\text{LN}_2$ -cooled CCD camera used in X-ray experiments at MIT. As the ETC is intended to be a completely automatic sky-monitoring instrument, the use of expendables (such as  $\text{LN}_2$ ) which require daily human maintenance must be avoided. As a result, a closed-cycle refrigerator, which can run unattended for months or years without maintenance, is used to cool the CCD cameras.

Detailed design for several important elements of the ETC test unit was performed by DFM Engineering, Inc., of Longmont, Colorado. The cameras, support structure and sidereal drive were all constructed by DFM Engineering, Inc. The test unit's CCD cameras, each with a field-of-view of  $15^\circ \times 20^\circ$ , are mounted on a single sidereal drive in order to track the sky during an observation. The interface between the cameras and the drive is the *manifold*: the cameras are mounted to the manifold, which in turn is mounted to the sidereal drive. The expansion probe of the closed-cycle refrigerator is situated on the axis of the manifold: the CCDs in the cameras are kept at a temperature of  $\sim -85^\circ\text{C}$  by thermal contact to the expansion probe.

A picture of the ETC test unit is shown in Figure 6.2, and a sketch of the manifold and cameras, giving views of the insides of both, is in Figure 6.3. A sketch of the ETC prototype building and the layout of the instrument in the building can be seen in Figure 6.4. Detailed descriptions of each aspect of these figures can be found in the figure captions and in the text of this chapter.

The following sections describe each part of the ETC test unit in some detail.

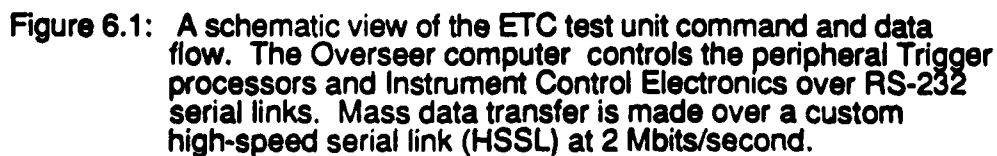


**Figure 6.1:** A schematic view of the ETC test unit command and data flow. The Overseer computer controls the peripheral Trigger processors and Instrument Control Electronics over RS-232 serial links. Mass data transfer is made over a custom high-speed serial link (HSSL) at 2 Mbits/second.



Figure 6.2: A view of the ETC instrument during test operations. The four ETC cameras are mounted on the manifold, which is mounted to the sidereal drive. The vacuum hose at lower left runs from the ion pump (not in picture) to the base of the manifold. In this picture, the four cameras are outfitted with three 75 mm lenses and one 25 mm lens. (See Figure 6.4 for a complete schematic overview of the ETC instrument.)

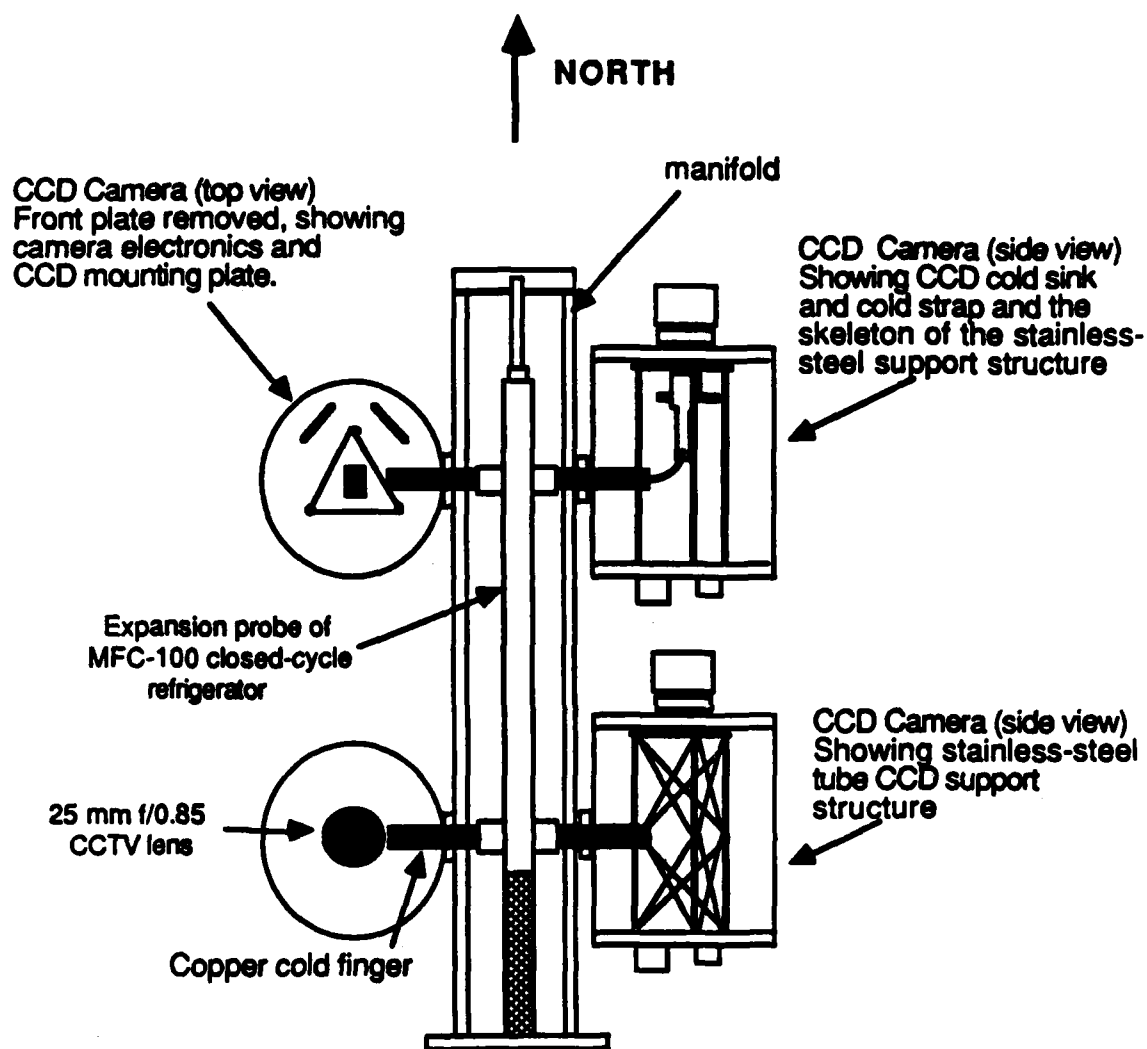


**Figure 6.3:** Cross-sectional view of the ETC prototype instrument. View is of manifold and four cameras, showing various aspects of the instrumentation.

## 6.1. The ETC CCD Camera

The ETC CCD camera consists of a cooled CCD placed at the focal plane of a 25mm lens. A vacuum-tight aluminum camera body houses the CCD, its thermal-control heater unit, its protection electronics and an output signal preamplifier. Signals from the Instrument Control Electronics (ICE) reach the CCD through the connectors in the camera back plate. (A sketch of an ETC CCD camera is included in Figure 6.3).

### 6.1.1. Camera Body Construction

The camera body is cylindrical, measuring 7" length by 6" diameter. Four bolts through the side of the camera body fasten the camera body to the manifold. Small (1.5 inch) holes in the camera body and manifold at the camera/manifold interface allow the manifold and camera to share a common vacuum cavity as well as create room for a thermal path from the CCDs to the cooling probe inside the manifold.

The CCD rests on an aluminum cold sink, which makes thermal contact with the cooling probe through a braided copper strap, as described in section 6.3. The temperature of the cold sink (and therefore of the CCD) can be measured with a thin-film, temperature-sensitive resistor mounted on the cold sink. The temperature of the cold sink can be raised by passing current through a 25 ohm, 10 Watt power resistor mounted on the cold sink.

A thin, triangular aluminum plate with a rectangular opening for the CCD imaging area presses the CCD against the cold sink, assuring good thermal contact. This triangular plate is mounted on a structure of thin-walled stainless steel tubing extending up from the back plate of the camera. The thinness of the wall and length of the tubing create a large thermal resistance between the CCD and the back plate.

Electrical connections to the camera contents are made through two hermetically-sealed connectors in the back plate of the camera. A 32-pin connector feeds the CCD clocking signals, power to the preamplifier and the signals to and from the CCD temperature sensor and heater from the ICE to the CCD camera. A 6-pin connector feeds the preamplified CCD output signal out of the housing.

### 6.1.2. The ETC Optical System

The CCDs are Texas Instruments virtual-phase devices, consisting of an array of 390 x 584 22.3  $\mu\text{m}$  pixels. They are divided into imaging and memory halves, and are operated in "frame-store" mode. In frame-store mode, an exposure made in the imaging area can be clocked quickly (in a few milliseconds) into the memory area. Then, as the first image is being read out into the processing circuitry at a slower rate (in about 0.5 seconds), the imaging area can be collecting photons from the next exposure, assuring a duty cycle of nearly 100%.

The camera lens used in the ETC survey is a commercial 25mm, f/0.85 CCTV lens manufactured by Kowa, Inc, of Japan. It is a wide-field lens (focal plane scale = 2.3 degrees per millimeter) with a large collecting area (6.8  $\text{cm}^2$ ) due to its low f-number. Its back-focal-distance, unfortunately, is quite low (4.5 mm), thereby requiring that the CCD imaging area be within 1.5 mm of the front plate of the camera.

The chromatic aberration of the lens allows good focus to be achieved only with the use of a filter (typical  $\Delta\lambda = 1000 \text{ \AA}$ ). Even then, the point-spread-function of the lens is such that a point source is imaged onto two to four pixels at image center. The off-axis reduction in response of this lens is also significant: the vignetting of the lens is ~30% at an image radius of 5 mm. The average loss of transmissivity over the CCD due to vignetting is ~15%. Typical images made by the ETC are shown in Figure 6.5.

### 6.1.3. The Internal Electronics of the CCD camera

CCD clocking signals entering the camera body pass through the internal protection electronics. The protection electronics prevent voltage spikes on CCD clocking lines from reaching the CCD. The



CCD output signal is fed directly into the preamplifier inside the CCD camera. The preamplifier has a gain of  $\sim 25$ , and its output travels to the analog signal processor board in the ICE through the 6-pin connector in the camera back plate.

## 6.2. Manifold

The manifold is a hollow aluminum cylinder, 24" long by 4" diameter, flattened on two sides. Two holes in each flattened side locate the camera mounting points. A unique design of the interface between camera body and manifold allow for a continuous rotation of the cameras parallel to the flattened face while holding vacuum, so that the declination of each camera is continuously adjustable.

The cooling probe of the closed-cycle refrigerator is located along the axis of the manifold. The mounting flange of the expansion probe of the closed-cycle refrigerator mounts with an O-ring seal to the southern end of the manifold. To prevent cantilevering, the northern end of the expansion probe is supported by means of a short thin-walled stainless-steel tube (for a large thermal resistance) between the tip of the probe and the end cap of the manifold.

The manifold is bolted to a short aluminum spacer which is bolted onto the disk of the sidereal drive. The flexible hose from the cooling probe is wrapped once around this spacer to assure that the stress on the hose from the motion of the drive is longitudinal, since the hose is very sensitive to axial twists.

## 6.3. CCD Cooling System

The cooling probe is the expansion head of the MFC-100 freon-based closed-cycle refrigerator manufactured by FTS Systems, Inc. The MFC-100 is a 1/2 horsepower, two-stage closed-cycle refrigerator, quoted to deliver  $\sim 200$  Watts of cooling power at  $-80^\circ\text{C}$ . The MFC-100 pumps liquid freon through a flexible line to the expansion head, where it evaporates and cools the head. The gaseous freon returns along a second, parallel flexible line to the refrigerator's condenser.

Thermal contact from the expansion head to the CCD cold sinks is made at four points on the expansion head which appear at the camera mounting ports on the manifold. Short (4") threaded copper rods screw into tapped bosses on the expansion head and extend  $\sim 2$ " into each camera housing. A short metal strap completes the thermal path from the end of the copper rod to the CCD cold sink (see Figure 6.3).

## 6.4. Vacuum System

The ETC camera and manifold system is kept at a pressure of  $\sim 4 \times 10^{-6}$  Torr by a 20 l/s Vacuon pump. Rough vacuum ( $\sim 5$  microns Hg) is achieved using a standard  $\text{LN}_2$ -trapped oil roughing pump; a sorption pump reduces the pressure to  $\sim 10^{-5}$  Torr, where the ion pump is safely started.

The pressure of the system is reduced significantly when the refrigerator is in use, since the expansion probe acts as a cryopump, adsorbing many of the molecules leaking into the system. On the other hand, when the electronics inside the camera head are powered up, the outgassing of the warm elements of the electronics raises the pressure a small, but noticeable amount ( $\sim 2 \times 10^{-6}$  Torr).

The ion pump is mounted at the back of the sidereal drive. A flexible metal hose connects it to the manifold. Vacuum access to the manifold is a 2.75" Conflat flange located at the southern end of the manifold.

## 6.5. Sidereal Tracking Drive

The sidereal drive is a polar-mount tracking drive for small telescopes designed and built by DFM Engineering of Boulder, Colorado (this drive is in its concept a twin to the 2.4m telescope recently constructed at the McGraw-Hill Observatory on Kitt Peak). The unit has a 14" steel disk which is friction-driven by one of the two rollers upon which it rests: one roller is driven by the tracking motor, the other by the slewing motor. The manifold bolts directly to the steel disk.

The tracking drive motor is a standard 1 RPM DC motor. The rate of tracking can be varied by a thumbwheel switch mounted on the drive. The slewing motor is a 0.88 amp Slo-Syn stepper motor, which is controlled by a stepper motor controller circuit in the ICE. The maximum slewing rate is greater than 40 degrees/minute. Both motors and the clutches associated with each are controlled by the Instrument Control Electronics.

The angle of the friction disk about the polar axis can be measured through a synchro shaft encoder mounted directly onto the southern end of the polar axis of the drive. The shaft encoder delivers three 400 Hz signals, mutually 120° out of phase, to a synchro-to-digital converter (SDC) in the ICE. The SDC can calculate the absolute angle of the shaft encoder to 14-bit precision from the relative amplitudes of the three signals.

Electrical connections between the ICE and the tracking drive pass through a 14-pin cable. This cable contains signals for clutch control, motor control, synchro input and output. The drive is powered with standard 115 VAC; the stepper motor is powered by a 24 Volt, 6 amp power supply located near the sidereal drive.

#### 6.6. Thermal Analysis of the ETC

The operating temperature of the CCD is determined by the cooling rate of the closed-cycle refrigerator and the ambient warming of the chips and how each varies with temperature. The rate of cooling is determined by the cooling power of the MFC-100 and the thermal resistance of the metal strap between the cold copper rods and the CCD cold sink. The ambient warming of the chip is due to heat gain through conduction and radiation from the walls of the camera. The final temperature of the CCDs cannot be calculated exactly because the variation of the cooling power with final temperature is not known. The various rates of heating and cooling are analyzed in Appendix F. This analysis shows that the heat gain by the cold surfaces in the CCD cameras is insignificant when compared to the cooling power of the MFC-100 at -80°C. Therefore, the minimum temperature of the CCDs should be well below -80°C.

#### 6.7. ETC Site 1

The ETC test unit is located in the former twelve-inch Schmidt observatory, a two-story circular building on Kitt Peak, near Tucson, Arizona. The second story is covered with a 16' dome with a 42" slit. The angle subtended by the open slit is ~24°, (as seen by the ETC cameras), which is slightly smaller than a single ETC camera's field-of-view. Because the diagonal angular length of an ETC field is 25°, partial occultation by the dome can occur for some camera orientations. The ETC test instrument views the sky through this slit: the dome is rotated at appropriate intervals to prevent substantial occultation of a camera's field-of-view by the dome. For the plenary ETC, the dome will be replaced by a roll-off roof to allow coverage of the entire night sky. Schematic views of the ETC dome and contents can be seen in Figure 6.4.

The ETC instrument is mounted on a 2' x 2' concrete pier in the second story. The Instrument Control Electronics and ion pump are located near the test instrument in the second story. The vacuum roughing stages are located on the first floor and are plumbed to the upstairs vacuum through a network of vacuum plumbing. The closed-cycle refrigerator is located on the first floor: the flexible hose to the cooling probe feeds through a 6" hole in the floor between.

The first floor is primarily occupied by the Overseer computer, Trigger processors and all user peripherals (e.g. color graphics display, printer, terminals, magnetic tape drives, etc.). Cables leading to the ICE are fed through holes in the ceiling.

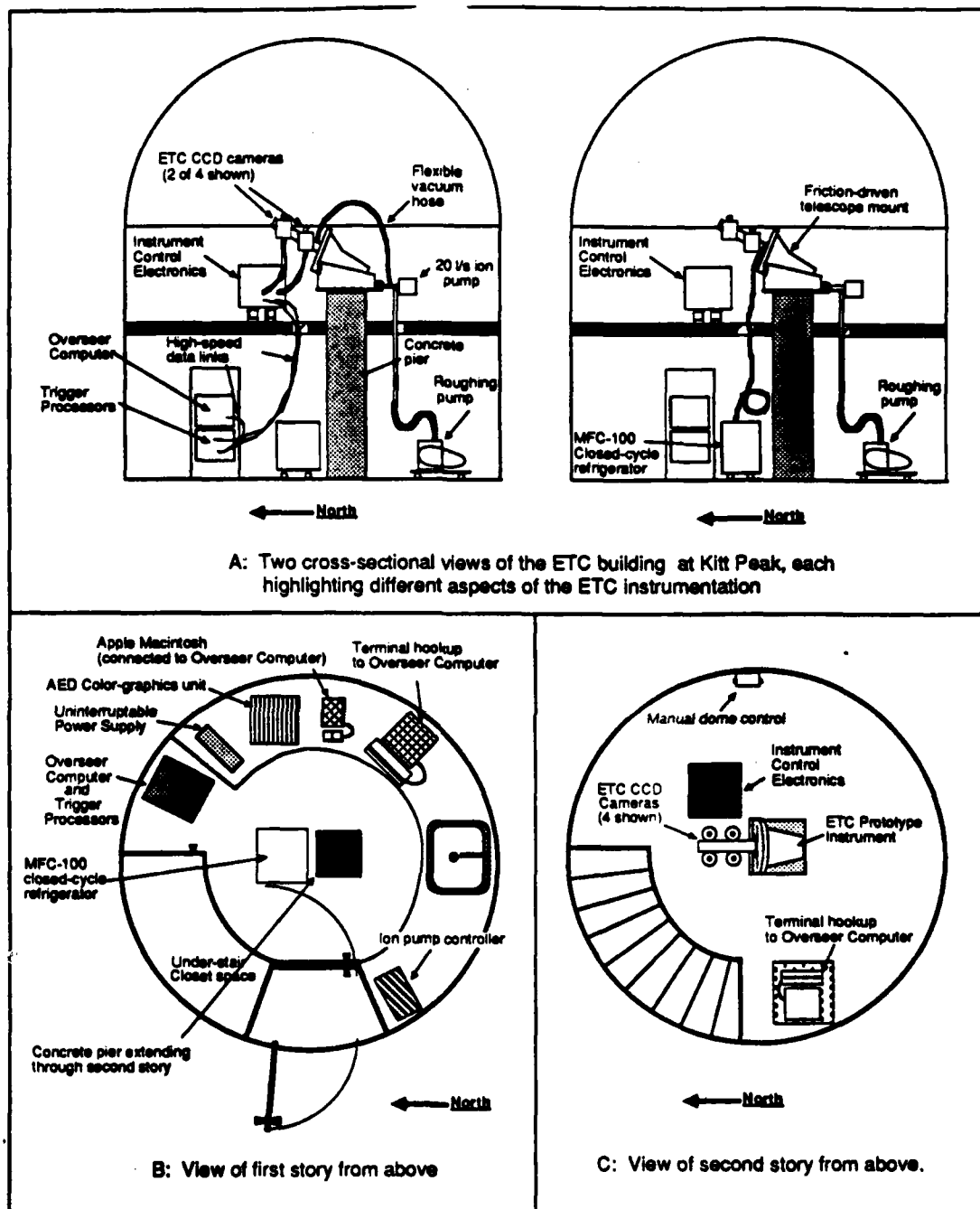
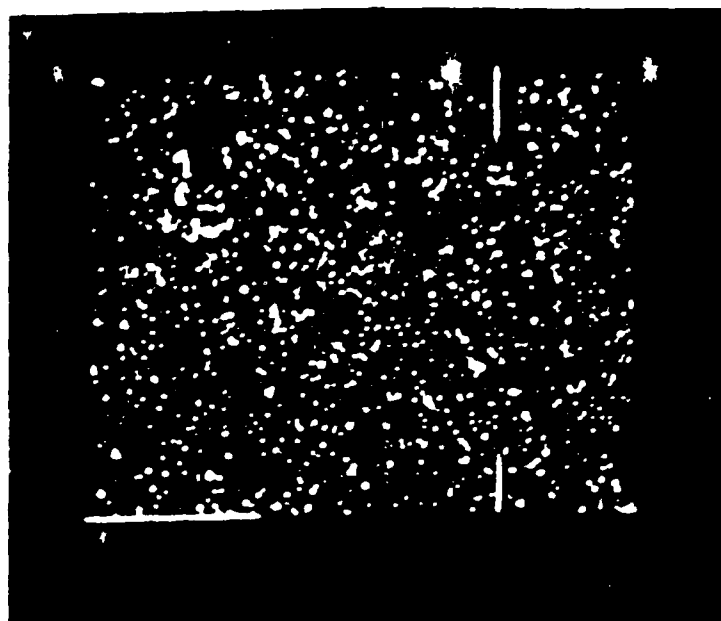
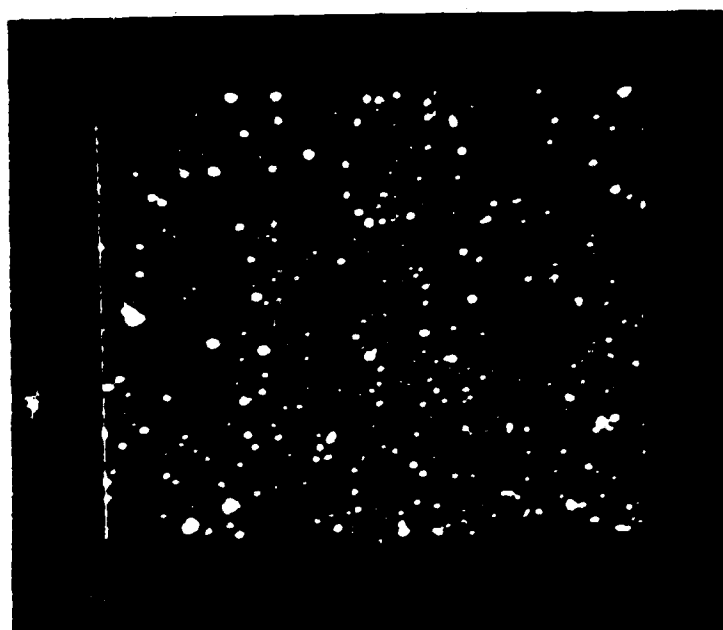


Figure 6.4: Schematic representation of the ETC test instrument within its building at Site 1 on Kitt Peak.



(a)



(b)

**Figure 6.5:** Two ten-second exposures made with ETC camera C. The images were made through a) the ETC 25 mm lens, as described in section 6.1.2, and b) a high-quality 75 mm lens. The vertical streaks visible in Figure 6.5a are due to a column defect in the CCD in camera C.

## CHAPTER 7

### The ETC Overseer Computer

#### Introduction

The Overseer computer is a fast, powerful microcomputer that is the center of organization for the ETC. It controls the ETC through software written in C. Through RS-232 serial links, the Overseer communicates with and controls the peripheral instrumentation of the ETC. The Overseer computer is capable, through its sophisticated control software, of making the ETC a completely automated observational instrument.

This chapter describes the Overseer computer hardware and software in some detail. The full complement of Overseer computer software is located in Appendix A.

#### 7.1. Overseer Computer Hardware and Peripherals

The Overseer computer is a powerful microcomputer based on the single-board, Motorola 68000 microprocessor. It is the third "generic" computer developed and constructed at the Center for Space Research at MIT for use in X-ray and optical astronomy. The Overseer computer consists of eight Multibus computer boards, which, together, control the Overseer computer operation, data flow and several peripheral units responsible for data storage and display.

The Overseer computer consists of the following hardware:

- 1) A PM68K 8 MHz, 68000-based CPU board.
- 2) A Rodime RO204 20 Mbyte, 5.25" Winchester disk.
- 3) A Konan Taisho disk-controller board, which controls the system's Winchester and floppy-disk drives.
- 4) A Texas Instruments TMM40020-04 512 kbyte memory board, used as CPU core memory.
- 5) A high-speed serial link (HSSL) receiver board, used for the high-speed (2 Mbits/second) acquisition of image data from the Trigger processors.
- 6) A second TMM40020-04 memory board, used as dedicated memory for the HSSL.
- 7) Two Central Data Corporation octal serial I/O boards. Through these boards, RS-232 serial connections can be made to sixteen peripheral units, including terminals, modems and other computers (specifically, the ICE and Trigger processors - see chapter 5). Data rates can be varied between 110 and 19200 baud.
- 8) An Omnibyte OB68K230 parallel I/O board, which allows for communication with any peripheral over parallel interface.
- 9) A Ciprico Tapemaster tape drive controller board, which controls the Cipher tape drive used for mass storage of image data.

- 10) An AED 512x512 color graphics monitor for the inspection of CCD image data. Images are transferred to the AED over parallel interface.
- 11) A GC-1000 WWV receiver. The GC-1000 receives WWV signals and can communicate the time to the Overseer computer via serial link.
- 12) A Tandon 101-4 5 1/4" floppy disk drive.
- 13) A Cipher F880 1600 bpi streaming magnetic tape drive.

The Overseer computer runs Pacific Microcomputer's Unix Version 7 operating system. Programs written in C and 68000 assembler control all aspects of the Overseer computer. The high-speed serial link (HSSL) receiver card, the only completely custom-built card in the Overseer computer, is the receiving end of a high-speed data link developed at MIT. The transmitters are mounted on the Triggers and are used to transfer image data to the Overseer computer at ~250 kpixel/second. More details on the Multibus HSSL can be found in section 8.1.2. The HSSL has its own 512 kbytes of RAM for image data storage.

Three custom-built circuits on the OB68K230's prototyping area play key roles in the operation of the ETC. One circuit is used to transmit image data to the AED color graphics unit. A second circuit makes use of signals available on the OB68K230 board. These signals, when sent to a Trigger processor, reset the Trigger processor to its start-up state. The third circuit taps a high-precision (4  $\mu$ s) timer on the OB68K230 board and makes it available to the Overseer computer for the precise timing of CCD images (the *frame timer*).

## 7.2. Interprocessor Communication

The Overseer computer communicates with both the Instrument Control Electronics and the Trigger processors in its execution of ETC operations. All communication with the ICE and the Trigger processors takes place over RS-232 serial link at 4800 baud. The Overseer computer has the control software for the ICE and the Trigger processors stored on disk; when necessary, the Overseer computer downloads the software to the particular unit over RS-232 serial link. A schematic diagram listing possible Overseer computer commands or requests to the Trigger processors and the ICE is given in Figure 7.1.

### 7.2.1. Overseer computer-ICE communication

The primary communication between the Overseer computer and ICE is in the form of commands to the ICE. Most Overseer computer commands to the ICE require no response from the ICE. In the interest of time, there is no handshaking between the Overseer computer and the ICE in time-critical situations (since the Overseer computer can generally establish independently whether a command to the ICE was properly executed). The only situation where a handshaking by is used is to inform the Overseer computer that a command which takes substantial time to execute (such as the slewing of the sidereal drive) has been completed.

### 7.2.2. Overseer Computer-Trigger Processor Communications

Communications from the Overseer computer to a Trigger processor are divided into two types: those during the analysis of image data by the Trigger processors ("sift" mode - see section 8.3.1) and those after the analysis, where the Overseer computer can make requests for data from the Trigger processors ("query" mode).

Sift mode in the Trigger processors is initiated by a command from the Overseer computer immediately before reading out the CCDs. In sift mode, the Trigger processors analyze incoming data and report any events to the Overseer computer via serial link. The Overseer computer's job during sift mode is to listen and wait for "candidate reports" and the analysis-ending "sift-termination report". (For

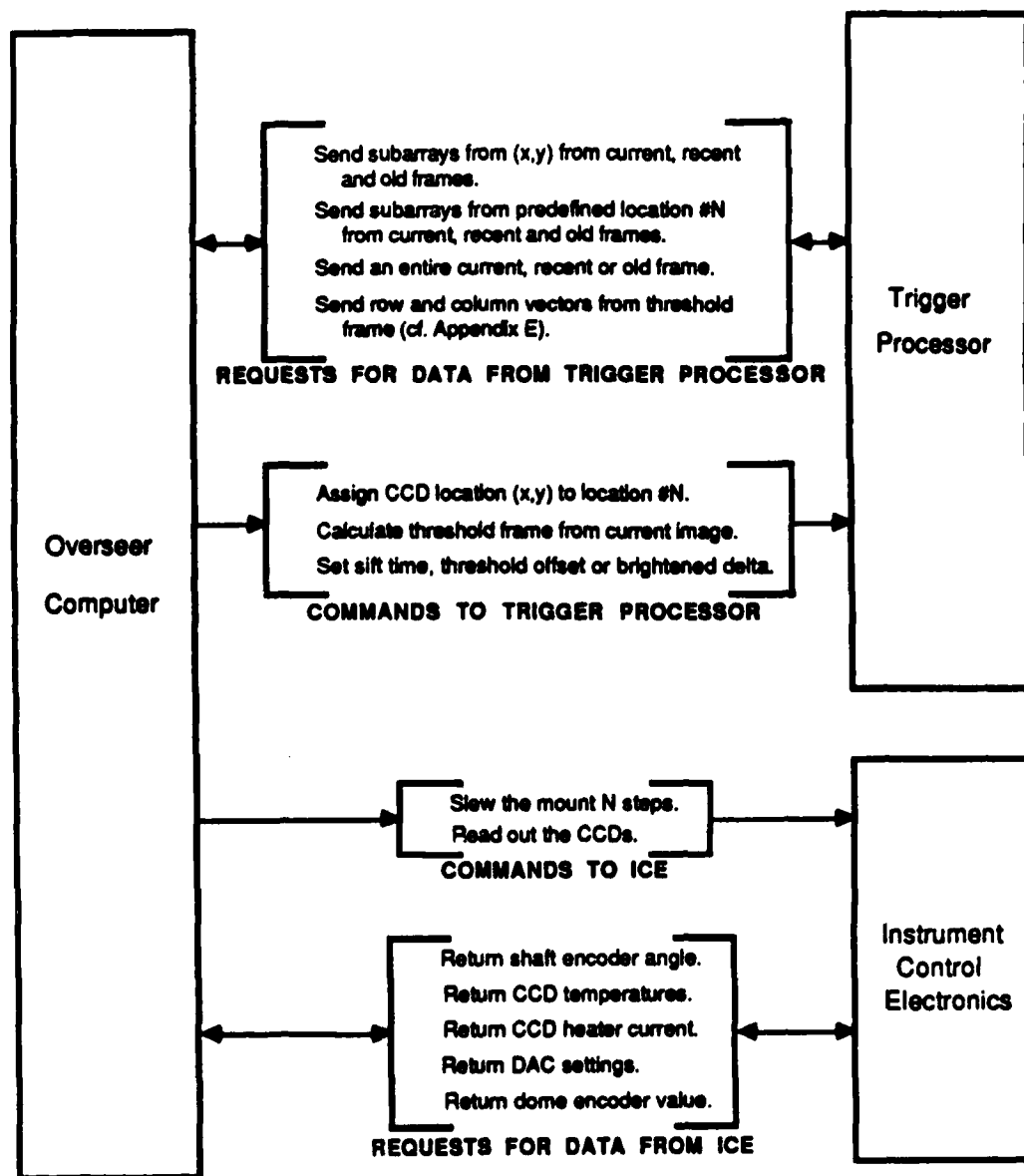


Figure 7.1: Schematic summary of Overseer communications with the ICE and Trigger Processors.

more detail on Trigger processor analysis procedures, see Chapter 8). A single handshaking byte is returned to the Trigger processor after every candidate report for efficiency.

After transmitting the sift-termination report, which marks the end of sift mode in the Trigger processors, the Trigger processors are automatically in query mode and are open to requests from the Overseer computer. The commands from the Overseer computer now take the form of requests for data or organizational commands. The requests for data include:

- 1) Send an image subarray of any size from any part of the CCD.
- 2) Send 9x9 image subarrays from a predefined location corresponding to either a flash or a standard star.
- 3) Send an entire image.
- 4) Send the row and column vectors whose vector sum make up the threshold image (cf. section 8.3.2.1 and Appendix E).

All image data is transferred to the Overseer computer over the high-speed serial link at 2 Mbits/second.

The organizational commands from the Overseer computer to the Trigger processors include the following:

- 1) Assign to a given location (x,y) on the CCD a number corresponding to a standard *star image located at that spot on the CCD*.
- 2) Calculate a threshold frame from the frame presently in memory (cf. section 8.3.2.1 and Appendix E).
- 3) Set the parameters used in the analysis of image data by the Triggers: sift time, threshold offset, and brightened delta (see Chapter 8).

### 7.3. Overseer Computer Utility Routines

Overseer computer utility routines are larger subsections of the ETC Overseer computer software which are too detailed to be included in the general overview of chapter 4, yet play a major role in the operation of the Overseer computer during observations. A description of these routines follows.

#### 7.3.1. Timekeeping

The Overseer computer has two system clocks. The first clock, associated with the CPU board of the Overseer computer, keeps year, month, day and time to a precision of 5 milliseconds. This clock is used for recording the time of events. It can be set by the user or, via software, with the GC-1000 WWV receiver. The GC-1000 clock receives WWV time signals and can transmit the precise date and time over RS-232 serial link on command. Thus, the Overseer computer can set the day-date clock from information received from the GC-1000 WWV clock.

The second system clock is used for timing CCD exposures: the Overseer computer's day-date clock is inadequate for this task because of low precision and its long access time. For these reasons, the 10 MHz clock from the Overseer computer's parallel I/O board (the OB68K230) is used for exposure timing. The OB68K230's timer has a precision of 4 microseconds and can act as a countdown timer, so that once the timer is set (for example, at the beginning of an exposure), it will count down until the time has expired, and then restart itself. The Overseer computer only needs to watch the timer and read out the next exposure when the frame timer expires.



Time in the ETC is stored in "modified Julian day" format for simplicity: a four-byte modified Julian day gives the year, date and time to a precision of one second. The modified Julian day is the Julian day minus 2400000.5 (Nautical Almanac, 1985): for reference, 12.00 UT on 1 June 1985 is modified Julian day 46216.5.

### 7.3.2. Astrometry

The Overseer computer must have a precise knowledge of the mapping of pixel location to celestial coordinates in each CCD in order to judge the validity of an optical flash based on whether it has the same celestial coordinates in two cameras. The Overseer computer can make a reasonably good estimate of this mapping given the details of the optical system: the focal length of the lens, the pixel size on the CCD, any first-order distortions in the lens and the angle of the rows and columns of the CCD with respect to lines of right ascension and declination. The sub-pixel precision necessary for the ETC is achieved by calculating the parameters of the astrometric mapping using the centroided location of several ( $\sim 20$ ) SAO standard stars in the field of the CCD and the celestial coordinates of those stars.

The mapping used in the ETC is a simple linear relation between pixel coordinates ( $x, y$ ) and the reduced coordinates ( $\xi, \eta$ ). The reduced coordinates are calculated from the celestial coordinates ( $\alpha, \delta$ ) in the tangent-plane approximation, given the celestial coordinates of the field center ( $\alpha_0, \delta_0$ ), as in Podobed (1965, p. 180).

$$\xi = \frac{\cos(\delta_0) \sin(\alpha - \alpha_0)}{\sin(\delta) \sin(\delta_0) + \cos(\delta) \cos(\delta_0) \cos(\alpha - \alpha_0)} \quad (7.1a)$$

$$\eta = \frac{\sin(\delta) \cos(\delta_0) - \cos(\delta) \sin(\delta_0) \cos(\alpha - \alpha_0)}{\sin(\delta) \sin(\delta_0) + \cos(\delta) \cos(\delta_0) \cos(\alpha - \alpha_0)} \quad (7.1b)$$

The mapping of pixel coordinates ( $x, y$ ) to reduced coordinates ( $\xi, \eta$ ) is

$$x = a_1 + b_1 \xi + c_1 \eta \quad (7.2a)$$

$$y = a_2 + b_2 \xi + c_2 \eta \quad (7.2b)$$

The values of the parameters of the mapping ( $a_{1,2}$  and  $b_{1,2}$ ) can be roughly estimated from details of the CCD optical system. For example, if a CCD has one axis oriented east-west, then ( $a_1, a_2$ ) are the coordinates of the center of the CCD,  $b_1$  and  $c_2$  are the focal-plane scale and  $b_2 = c_1 = 0$ .

The Overseer computer calculates the precise values of the astrometric parameters from the estimated values of these parameters in the following way. The Overseer computer has a rough idea of the celestial coordinates of the center of each CCD, since the declination of each camera is specified in software and the right ascension can be calculated from the hour angle of the camera and the sidereal time. The hour angle of the camera is easily calculated from the value of the synchro shaft encoder mounted on the polar axis of the drive: the mapping of shaft encoder units to hour angle is specified in software and does not change. Given these celestial coordinates of the center of a CCD, the rough calculation of the parameters of the astrometric mapping is sufficient to allow Overseer computer to estimate the locations on the CCD of several ( $\sim 20$ ) SAO stars to an accuracy of  $\sim 10'$ . In order to determine the locations of these stars on the CCD more precisely, the Overseer computer then acquires small image subarrays of each SAO star from the appropriate Trigger processor. The Overseer computer can then determine the location of each standard star on the CCD to a precision of  $\sim 0.1$  pixels with a simple interpolation algorithm (see Appendix D). The Overseer computer is now able to calculate the values of the astrometric parameters from a least-squares fit of the precise locations of the SAO stars to the celestial coordinates of the SAO stars. If the least-squares fit yields an rms deviation of predicted stellar coordinates from actual stellar coordinates of more than 0.5 pixels, the star with the highest residual to the fit is discarded and the least-squares fit is repeated. After iterating the above procedure until the rms deviation is below 0.5 pixels, the celestial coordinates of any stellar image on the CCD can be calculated by 1) determining the location of the image on the CCD precisely and 2) inverting equations

7.1 and 7.2 to map the precise image location onto its celestial coordinates with a final precision of better than 0.5 pixel.

The celestial coordinates of the SAO stars used in the above procedure are found in a file on disk which contains a portion of the SAO catalog. The celestial coordinates in the SAO catalog file are epoch 1950.0; therefore, all celestial coordinates used in the ETC are epoch 1950.0 for simplicity. The effects of stellar proper motions of the stars and differential precession across the field are insignificant when compared to 3' pixels. The effect of precession is ignored, since precession only introduces a rotation into the astrometric mapping, which is accounted for by the cross terms in the fit parameters.

### 7.3.3. Data Storage by the ETC

The data from flashes detected by the ETC is stored in an extensive data storage structure, diagrammed in table 7.1. The stored data includes:

- 1) 9x9 pixel subarrays about the flash event and local photometric standards from immediately before the detection and for the course of the flash.

FLASH EVENT DATA STORED BY THE ETC	
Data stored per observation cycle	Number of flashes detected. Data from all detected flashes.
Data stored from each detected flash	Number of exposures taken of the flash. Data from the flash.
Data stored from each flash	Subarrays from standard stars from old, recent and current frames. Coordinates and position of flash in both cameras detecting. Threshold frame information (see Appendix E). Data from all exposures.
Data stored from each exposure	Time of the exposure Data from each camera
Data stored from each camera	Subarrays around flash location. Subarrays around locations of standard stars.

Table 7.1: List of data stored from a flash event detected by the ETC.

- 2) Flash information, including the time of the flash, which CCD cameras detected it, the precise location of the flash on the detecting CCDs and the calculated flash coordinates.

During observations, the ETC stores data onto magnetic tape at thirty-minute intervals, including any data taken from detected flashes in that thirty-minute period. In addition, the ETC will always store data indicative of the operating conditions of the ETC in that period, regardless of whether flashes were detected (see table 7.2).

This archived information includes all pertinent information about the configuration of the CCD cameras, readout and sift times, and throughput and vignetting information. The ETC also regularly stores subarrays around five standard stars in the field of each CCD at the beginning and end of each thirty-minute observing period as an after-the-fact check of sky conditions.

ETC OPERATIONAL DATA STORED AT REGULAR INTERVALS	
Archives	All system constants (see section 7.1.5.3.10) Start and end times of cycle Coordinates, positions and magnitudes of all SAO standards used in each FOV Subarrays about all SAO standards at start and end of cycle
Camera data	Right ascension, declination of field center Focal length, f-number, area of lens Angle of CCD, angle of camera to north-south CCD gain, noise, bias level, total noise Trigger processor constants CCD temperature
Trigger processor data	Sift time
Mount data	Synchro units to hour angle calibration information Right ascension of mount Hour angle at start and end of observations
System data	Exposure time Interval at which to slew the mounts Interval at which to redo astrometry

*Table 7.2: Instrument Status Data Stored by ETC*

### 7.3.4. The ETC Overseer Computer Software

The Overseer computer software is completely written in C. It is divided into 19 modules, each restricted to a particular aspect of the Overseer computer software. Some overlap of functions is, of course, unavoidable. Nonetheless, the modulization of the code is an attempt to enhance the organization, readability and maintainability of the code.

This section will describe each module in some detail: further details can be found in the code and documentation found in Appendix A. All module names begin with two capital letters in order so that subroutines can be identified with the modules they are found in. (The ".c" suffix indicates a module written in C).

The modules are broken up into control, I/O and utility routines. Control routines are primarily concerned with the actual operation of the instrument and the flow of the data, and use utility routines to assist them. I/O routines are used to communicate with other processors.

#### 7.3.4.1. Control Routines

The ETC control routines are listed and briefly described below:

- ) S**T**art.c is the execution module: it simply executes E**N**try, which is the real entry-level module.
- ) E**N**try.c is the primary user-interaction module. Here the user chooses whether to start automatic observations (through O**PER**ations) or human-aided observations (through U**S**er), or to do some preliminary image location work (I**M**age).
- ) O**PER**ations.c is the node at which the Overseer computer software is directed into its various day-to-day modes. For example, during the day O**PER**ations will execute the "wait until dark" routine. When it gets dark, O**PER**ations will first execute the "set up the mounts" code, followed by the observation code. Any panic or failure flags in the observation code will return control of the code to O**PER**ations.
- ) O**B**servations.c is the module which controls all aspects of observations. It coordinates exposures, sets up and reads from Trigger processors, watches the and looks for peripheral failures. At the end of an observation cycle, it returns control to the module from which it was entered.
- ) U**S**er.c is the semi-automatic observation control code used in observations with the ETC test unit. It executes the observations automatically, but requires user assistance during setup to position the mount, to line up the cameras properly and to determine observation thresholds.
- ) I**M**age.c is a collection of user-interactive code used in determining the celestial coordinates of a CCD field center, in focussing a camera and in testing certain sift parameters.

#### 7.3.4.2. I/O Routines

The three I/O modules in the ETC Overseer computer software are:

- ) C**O**smac\_I**O**.c contains all software used in communication with the ICE, including downloading software.
- ) T**R**igger\_I**O**.c contains all software used in communication with the Trigger

processors, including downloading software.

- ) EXternal IO.c contains code to communicate with external instruments, such as the RMT.

#### 7.3.4.3. Utility Routines

The ETC Overseer software's utility routines are a collection of useful subprograms which are used during the execution of ETC operations.

- ) AStrometry.c consists of all astrometry routines for the ETC, including code to calculate the astrometric mapping parameters, given precise locations and coordinates of astrometric standards, as well as code to calculate celestial coordinates of a stellar given the precise location on a CCD, and vice versa (see section 7.1.4.2).
- ) DAtime.c contains code to determine whether it is day or night and code to wait for night if it is day.
- ) DEclarations.c contains look-up tables regarding the cameras and their operating parameters.
- ) DOme.c contains code to move and read out the location of the ETC building's dome.
- ) JPD.c is a module devoted to the software contributions of John Doty. These routines include faster algorithms for time-critical ETC operations, such as a fast median-filtering routine and a fast standard star choosing algorithm.
- ) PHotometry.c contains the system's photometry routine, which calculates the brightness above background of any array passed to it. It returns the sum over all pixels in the array of the difference between the brightness of the pixel and the sky+bias level in the same pixel.
- ) SAo.c contains all code pertaining to the SAO stars used as standards by the ETC. It is primarily used to select SAO stars for use as standards in a given field.
- ) UTility.c is a collection of various routines with general applicability. The reader is referred to Appendix A for more detail of its many features.
- ) WEather.c contains weather-detection software and is presently not implemented
- ) WWv.c is a module designed to read the precise time from the GC-1000 clock into the Overseer computer's day-date timer.
- ) The modules Globals.c and extern.h contain all initial declarations of system global variables.
- ) The module constants.h contains all system-wide fixed constants.

## CHAPTER 8

### The ETC Trigger Processor

#### Introduction

The ETC Trigger processors are responsible for real-time data reduction of in ETC. The Trigger processors are powerful microprocessors dedicated to the quick, efficient analysis of CCD image data taken by the ETC. Each Trigger processor is responsible for the analysis of the image data from one CCD camera: the job of a Trigger processor is to cull through the CCD image data and report significant brightenings to the Overseer computer. Through the Trigger processors, the rate of data leaving the ICE (~100 kbytes/second/camera) is reduced by four to six orders of magnitude before entering the Overseer computer. This efficient, dedicated method of data analysis is what makes the ETC a viable instrument for real-time astronomy at the one-second timescale.

#### 8.1. Trigger Processor Hardware

A Trigger processor in the ETC test unit consists of three Multibus (reference) boards in its own enclosure:

- 1) An Omnibyte OB68K1A 10 MHz microprocessor.
- 2) A Texas Instruments TMM40020-04 512 kbytes memory board.
- 3) A custom Direct Memory Access (DMA) board with a High Speed Serial data receiver/transmitter Link (HSSL).

The data from each ETC camera is transferred to Trigger processor memory over the HSSL receiver at ~250 kbytes/second. Image data from the CCDs is processed as it streams in. Information about an event detected by a Trigger processor is sent to the Overseer computer via an RS-232 serial link on the OB68K1A board.

##### 8.1.1. The Omnibyte OB68K1A

The Omnibyte OB68K1A single-board processor is a Motorola 68000-based microprocessor and supports code written in C and 68000 assembler. Two on-board EPROMs provide the OB68K1A with a power-up operating program, known as ETRM (ETC Trigger ROM Monitor), accessible by the Overseer computer via RS-232 serial link. Through ETRM, memory locations and I/O registers in the Trigger processor can be accessed by the Overseer computer or a human user. The Trigger software is stored as a file in the Overseer computer and is downloaded using ETRM: the executable Trigger software is stored in RAM on the OB68K1A board. via RS-232 serial link.

The Omnibyte OB68K1A board also includes a timer chip with which the Trigger processor times the data analysis process (the *sift timer*: see section 8.3.1). The precision of the on-board timer is better than 0.01 seconds.

##### 8.1.2. The Multibus DMA/HSSL board

The Direct Memory Access/High Speed Serial Link receiver/transmitter board consists of discrete circuitry linked to DMA circuitry which interacts through the Multibus with the Omnibyte OB68K1A board. The DMA/HSSL board is used for fast, uninterrupted transfer of data to and from the Trigger

processor's memory. Direct Memory Access (DMA) circuitry makes possible the hardware-controlled storage of data without wait states or software control. The High-Speed Serial Link (HSSL) allows for transfer of image data at a rate of 2 Mbits/second. The Trigger processor HSSL receiver circuitry accepts image data from the ICE, while the transmitter sends requested image data to the Overseer computer. Together, the DMA and HSSL are an efficient method of mass data transfer and storage which does not require any software intervention. This leaves the Trigger software free to analyze CCD image data *as it streams in*, making it possible to detect events before all the data has been received.

The DMA controller is based on the Motorola 68450 DMA chip. The controller has four transmitter/receiver channels and is controlled by bitwise manipulation of the 68450 registers. In the case of incoming data, the DMA circuitry is responsible for the control and organization of data and address bytes, making sure that each incoming byte goes where it is supposed to be in RAM. For outgoing data, the DMA circuitry must acquire the data from the requested memory locations and feed them to the data transmitter circuit in the correct order.

### 8.1.3. Trigger Processor Memory

The Trigger processor memory is broken up into the following sections:

- 1) Eight kbytes of read-only-memory (ROM) on two ROM chips on the Omnibyte board. ETRM firmware (section 8.1.1) is located in this ROM, so that the Overseer computer can communicate with the Trigger processors through ETRM immediately after power-up.
- 2) 32 kbytes of RAM on the Omnibyte OB68K1A board. The executable Trigger software is stored in this memory.
- 3) 512 kbytes of RAM on the TMM40020-04 Multibus memory board. This memory is used for frame and data storage and is large enough to hold four full 400x292 byte ETC frames.

## 8.2. Overview of Trigger Software

The software for the Trigger processors was written as part of a senior thesis project by Steven Rosenthal of MIT. It includes the code setting up the OB68K1A environment, the DMA control code, the ETRM firmware (the ETC Trigger ROM Module, described in section 8.1), as well as all of the real-time analysis software.

### 8.2.1. Trigger processor memory allocation

The Trigger processor memory is large enough for four 400x292 CCD images. The Trigger processor 512 kbyte memory is broken up into four image regions, with the remaining 45 kbytes of memory used for data storage. The four image areas are named the *current*, *recent*, *old* and *threshold* frames. In the *current* frame is stored the most recent image to enter the Trigger processor (data flowing into the Trigger processor is always stored in the current frame). The recent frame generally contains the image taken immediately prior to the current frame. During sifting, the current frame is compared to the recent frame. After sifting, as is explained below, the current frame becomes the recent frame, and the recent frame is overwritten with an incoming image.

The old frame is a frame of data taken at some point and set aside in memory, expressly designated to be the old, or archival, frame. It can be used as the comparison frame during sifting, but it generally is viewed as archival information. The threshold frame is a construction which is used in the first level of sifting (see section 8.3.2.1). It consists of a sky frame with the stars artificially removed. Frames being analyzed are compared to the threshold frame. The method of calculating the threshold frame is explained in detail below and in Appendix E.

The frame labels (current, recent, old and threshold) are not fixed to a memory location in the Trigger processor, but rather are names which can be dynamically attached to any of the four areas of memory. For example, in the sifting process, the current frame is always being compared to the recent frame. When the analysis of the current frame is over and a new image is to be read in, the current frame becomes the recent frame. Rather than move the data from the current frame into the memory locations associated with the recent frame, the names of the memory locations are simply swapped: the next image read in goes into the current frame, overwriting the old recent frame, while the old current frame is the new recent frame. In this fashion, the analysis of consecutive images can proceed quickly and without lengthy transfers of data within Trigger processor memory.

### 8.3. Trigger Processor Operations

The Trigger software runs in one of two states. In *sift mode*, the Trigger processor waits for CCD image data to come in across the HSSL from the ICE. As soon as the first byte of data enters the Trigger processor, analysis of the data begins. If, during the analysis, the Trigger processor discovers a candidate flash event, it will report the event (in the form of a *candidate report*) to the Overseer computer over the RS-232 serial link. The analysis continues until the entire image has been analyzed or the time allotted for analysis has been exceeded. In either case, the Trigger processor issues a *sift-termination report* to the Overseer computer: the sift-termination report indicates any errors that occurred in the analysis.

After the issuance of the sift-termination report, the Trigger processor automatically enters *query mode*, its other mode of operation. During sift mode, no communication is possible between the Overseer computer and Trigger processors, except for candidate and sift reports, since any communication can slow the processing of incoming data by the Trigger processor. The only exception to this is a handshaking byte sent from the Overseer computer to the Trigger processor after a candidate report. In query mode, the Trigger processor awaits commands or requests for data from the Overseer computer. During this period, the Overseer computer can check or change the operational parameters of the Trigger processor, as well as request transmission over the HSSL of arrays of data from any of the three data frames stored in Trigger processor memory. When appropriate (usually immediately before the next CCD image is to be read into the Trigger processor), the Overseer computer returns the Trigger processor to sift mode with the issuance of an "end queries" command.

If for some reason the software in a Trigger processor halts, the Trigger processor is left in a non-communicative, non-productive state: the Trigger processor will have to be reset, the Trigger software re-downloaded and re-executed. A signal on the RS-232 serial link acts as an Overseer computer-activatable reset. The reset is generated on the parallel I/O board of the Overseer Computer (see section 7.1), and is sent to the halted Trigger processor over an RS-232 serial link, followed by the reloading of the Trigger software.

#### 8.3.1. Sift Mode

In sift mode, the Trigger processor single-mindedly devotes itself to the analysis of incoming CCD data. As soon as the Trigger software recognizes the reception of the first byte of data from the CCD, it begins the process of data analysis; the DMA hardware in the HSSL stores the data automatically as it streams in. At the same time, the Trigger processor starts an internal countdown timer (the *sift timer*) which indicates the time at which sifting will be terminated, whether all the data has been analyzed or not. The sift timer, in conjunction with the Overseer computer's frame timer (section 7.3.1), assures that a known amount of time is spent in both sift and query modes, and that these times will not change from exposure to exposure.

At the onset of sifting, the Trigger processor allows data from several rows of the CCD image to stream into memory before beginning actual data analysis, to permit the sift algorithm to reference data in adjacent rows. The analysis of CCD data then begins. Because the HSSL transfers CCD data by DMA, the continuing storage of CCD image data proceeds without interrupting the analysis processes.



The analysis of a CCD image consists of sequentially passing each pixel of the image through the "sifter", which is described in the following section. The analysis of this image, known as the *current frame*, requires a *threshold frame* (see section 8.3.2.1 and Appendix E), as well as an image against which to compare the current frame to detect any brightening. This image, the *recent frame*, is the image taken immediately before the current frame.

If any portion of a CCD image is considered an event by the Trigger processor, the Trigger processor issues a *candidate report* to the Overseer computer over RS-232 serial link. This report consists of seven bytes and communicates the column and row numbers of the event, interpolated to a within a fraction of a pixel and reported in centipixels (.01 pixels), as well as the value of the triggering pixel in both the current and recent frames. The format of this report is included in Table 8.1. Upon receipt of the candidate report, the Overseer computer transmits a handshaking byte to the Trigger processor. The Trigger processor must receive this byte before it can issue any further reports. The handshaking byte is implemented to avoid having so many candidate events report to the Overseer computer that the Overseer computer falls behind in receiving incoming bytes and, as a result, does not receive all the report data.

When the Trigger processor's internal sift timer expires, the Trigger processor issues a *sift-termination report* to the Overseer computer over the RS-232 link and enters query mode, regardless of whether the sift has finished. If the sift is still in progress, it is terminated immediately. Use of DMA by the HSSL assures that any data still coming in over the HSSL are stored correctly in the Overseer computer memory. A sift-termination report consists of three bytes which indicate the type of sift and the status of the sift when the sift timer expired. The format of the sift-termination report is included in Table 8.1.

The first byte of the sift-termination report includes a three-bit binary error code which indicates any errors in the sift. Each of these bits, the lowest three bits in the byte, indicates an error in the sift when it is transmitted in the high state. The information passed is 1) the sift was aborted before completion (bit 0), 2) too few bytes were received (bit 1) and/or 3) no sifting was done (bit 2). (See Appendix B for more detail). The possible errors are:

- 0: Sift completed, no errors. The Trigger processor received all the image bytes and successfully completed the sift procedure in the allotted time.
- 1: Sift incomplete. The sift process was interrupted by the sift timer. The last two bytes of the sift-termination report indicate the number of rows successfully sifted.
- 2: Not enough data. The number of bytes received by the Trigger processor is not the same as the number of bytes expected. This error usually indicates a problem with the ICE or, more likely, the HSSL.
- 3: Sift incomplete and not enough data (see 1 and 2).
- 4: No sift. The Trigger processor had no image against which to compare the current image during the sift. Sifting was not attempted, but the image was placed in memory for use in future sifts.
- 5: Not possible.
- 6: No sift and not enough data (see 2 and 4).
- 7: Not possible.

Format of Trigger Processor Reports to the Overseer Computer	
Candidate Report	Column number of event in centipixels Row number of event in centipixels Value of event pixel in recent frame Value of event pixel in current frame Value of threshold offset
Sift-termination Report	Three-bit error flag (see section 8.3.1) Row number of sift termination (0 if sift completed)

Table 8.1: Format of Trigger processor Reports to the Overseer computer

### 8.3.2. Sifting

The real-time analysis, or sifting, of the CCD images is done with a series of *sift algorithms* which, together, represent all of the criteria for recognizing an event in the ETC. Each algorithm, or level of sifting, is a test of whether an image pixel meets a certain criterion. A pixel meeting the criterion of a given level is passed to the next level for further testing; a pixel rejected by any level is not analyzed further and the sifter proceeds to examine the next pixel. Any pixel passing all sift levels is considered by the Trigger processor to be an event candidate and becomes the subject of a candidate report to the Overseer computer.

Since an ETC image of  $10^5$  bytes must be analyzed in about one second, an average of 5-10 microseconds of sifting time is allowed per pixel. Because this time is so short, the first level of sifting is a quick, simple algorithm which rejects most pixels in an ETC image. The small fraction of the image pixels which pass the first level of sifting are analyzed in increasing detail (at the cost of a higher analysis time per pixel) by the next levels of the sifter.

The following subsections describe each level of sifting in detail, proceeding in the order of levels encountered by a triggering pixel.

#### 8.3.2.1. Level 1: Threshold Comparison

The first level of sifting is a check of whether the brightness of a pixel exceeds the expected sky brightness in a statistically significant way. This level is passed if the value of the current image pixel is greater than the value of the same pixel in the *threshold frame*, which is located in a specific area in Trigger processor memory. The value of each pixel of the threshold frame is the sum of the sky-plus-bias level in the image frame (in the absence of stars) and a constant integer offset, the *threshold offset* (specified by the Overseer computer).

The threshold frame is constructed at the request of the Overseer computer by the Trigger processor before the beginning of an observation cycle from a normal ETC image through the process of *median filtering*. This method, described in detail in Appendix E, removes all high-spatial-frequency images (such as stars) from the CCD image, leaving an image of the sky without the stars. The value of the threshold offset reflects a statistical criterion programmed into the ETC software. The value of threshold offset is determined by the level of statistical significance: the Overseer computer calculates the value of threshold offset from the total noise per pixel of the CCD image. The value of threshold offset is added to the value of each pixel of the median filtered image to create the threshold frame.

Use of a threshold frame permits high speed processing of incoming CCD image data. Because the threshold offset is already added to the median filtered image, the Level 1 test consists of a single comparison of single-byte values. The Level 1 test requires a processing time of 4.8 microseconds per pixel.

The pixels which pass Level 1 have a value exceeding the starless sky value by a few ADU. These pixels are usually a part of a stellar image, a "hot" CCD column or a cosmic ray. The fraction of a full image's pixels passing Level 1 and thereby reaching Level 2 is dependent on the value of threshold offset and the number of bright stars in the field of the CCD: the fraction is of the order of  $\sim 0.01$  to  $\sim 0.03$ .

#### 8.3.2.2. Level 2: Brightening Test

The second level test checks whether a pixel is significantly brighter than the same pixel in the recent frame. The second level is passed by those pixels whose value in the current frame exceeds their value in the comparison frame by an amount greater than a constant known as *brightened delta*, which is specified by the Overseer computer. The value of *brightened delta* is calculated in the same way as the value of threshold offset (see above). The pixels that pass Level 2 are potentially very interesting to the ETC: they consist of cosmic rays, hot pixels and, hopefully, flash events. The fraction of incoming pixels passing Level 2 depends very much on the value of *brightened delta* and the total noise associated with the image: it will generally be  $< 0.005$ .

#### 8.3.2.3. Level 3: Centering Test

A flash event may cause several adjacent pixels to brighten enough to pass Level 2. Since the sifter should only issue one candidate report per event and report the center of the event, the Level 3 test checks the pixels neighboring the current pixel to determine whether the current pixel is the center of the event.

The third level of sifting is passed if the current pixel brightened more than any of its immediate neighbors. The fraction of incoming pixels passing Level 3 is  $\sim 0.5$ .

#### 8.3.2.4. Level 4: Anti-streak Algorithm

The fourth level of sifting is a test of whether the current pixel is part of a streaked image. This tests for meteor trails and perhaps fast satellite or airplane trails. The Level 4 sift tests all pixels on the perimeter of a seven-by-seven pixel box centered on the pixel under consideration: if any of these pixels pass the Level 2 brightening test (section 8.3.2.2), the image is considered a streak and the pixel being analyzed is rejected. If any part of the box is off the edge of the CCD, the pixel is rejected.

Estimates of the rate of meteors which have trails short enough (in angular size) to falsely satisfy the anti-streak algorithm are given in Chapter 10.

#### 8.3.2.5. Level 5: Bright Star Test

This level was devised when it was noticed that pixels surrounding bright stars were frequently the subjects of candidate reports. These brightenings were interpreted as being due to a shifting of the stellar image on the CCD, perhaps due to local atmospheric effects or the effects of high shot noise near bright stars in the CCD. In order to recognize this effect, Level 5 checks whether the value of any of a pixel's immediate neighbors exceeds the value of the pixel by more than three times *brightened delta* (generally  $\sim 20$  ADU).

#### 8.3.3. Sift Parameters

The performance of the Trigger software can be controlled by the Overseer computer by changing one of several sift parameters during query mode. These adjustable parameters include:

- 1) The variable *threshold offset* is the criterion used in the first level of sifting (see

section 8.3.2.1).

- 2) The variable *brightened delta* is used in the second and fifth sifting levels (see sections 8.3.2.2 and 8.3.2.5).
- 3) The *sift time* is the upper limit on the amount of time allowed for sifting. The amount of sift time needed is dependent on the values of threshold offset and brightened delta, and should be sufficiently shorter than the exposure time to allow time for requests for data by the Overseer computer.

#### 8.3.4. Query mode

Query mode is the free time between the termination of sifting and the next "end-queries" report. This time is available to the Overseer computer for 1) changing Trigger processor parameters, 2) making requests for data, or 3) requesting calculation of a threshold frame. A list of possible requests was given in section 7.2.2 and Figure 7.1.

## CHAPTER 9

### The Instrument Control Electronics

#### Introduction

The Instrument Control Electronics (ICE) are a set of custom-built analog and digital electronics which control the instrumentation of the ETC. Through the ICE, the Overseer computer or a human user can interface with and control the ETC instrument (e.g., read out the CCDs, measure and adjust the CCD temperature, slew the telescope drive and read the hour angle of the mount). Such software manipulation of the instrument hardware is essential to the automated ETC.

#### 9.1. Instrument Control Electronics Hardware

The ICE are controlled directly by a single-board microcontroller, known as the "COSMAC" board, which is based on the RCA 1802 "COSMAC" microprocessor. Overseer computer communication with the ICE occurs over an RS-232 serial port on the COSMAC board.

The ICE are divided into two groups: the "digital" and "analog" electronics. "Digital" electronics consist of all those boards sharing a common bus with the COSMAC microprocessor board. The COSMAC bus is a well-defined standard, allowing for 16-bit wide memory addresses, 8-bit data and eight I/O lines for communications with other boards sharing the bus. All boards sharing this bus are directly controlled by the COSMAC.

The "analog" electronics are primarily concerned with CCD clock generation and CCD signal processing and transmission. The CCD clock generation ("driver") and CCD signal processing ("analog") boards are very noise-sensitive, since any noise present on these boards reduces the quality and consistency of the CCD images. For this reason, the analog electronics are physically separated and RF-shielded from the digital electronics to reduce the extent of infiltration of digital noise. The output and input signals from the Analog Electronics to the CCDs are wired directly from the analog back-plane to the cable connectors leading to the cameras.

The sections that follow give a general description of the function and layout of each board in the Instrument Control Electronics. More attention will be paid to the Analog Electronics, since they are more specific to the operation of low-noise CCD cameras and generally the more intricate boards of the ICE. A schematic diagram of the boards and the data and signal flow in the ICE is given in Figure 9.1.

#### 9.1.1. Digital Electronics

The ICE digital electronics consist of several boards which are necessary for primary computer and CCD control (the COSMAC, memory, sequencer and DAC boards). In addition, the digital electronics include boards which control details of the ETC instrumentation (CCD temperature control, shaft encoder readout, clutch control, stepper motor control and dome control boards).

##### 9.1.1.1. COSMAC Board

As mentioned above, the COSMAC controller board is based on the RCA 1802 "COSMAC" microprocessor. The COSMAC is an eight-bit, bit-level controller: higher-level control is made possible by a FORTH-like language developed for the COSMAC. This code is stored in a set of four "boot ROMs", so the COSMAC is in a user-accessible state immediately after power-up.

The COSMAC board contains a UART (Universal Asynchronous Receiver/Transmitter) for serial communication at data rates from 300 to 9600 baud. Higher level instruction code can be created for

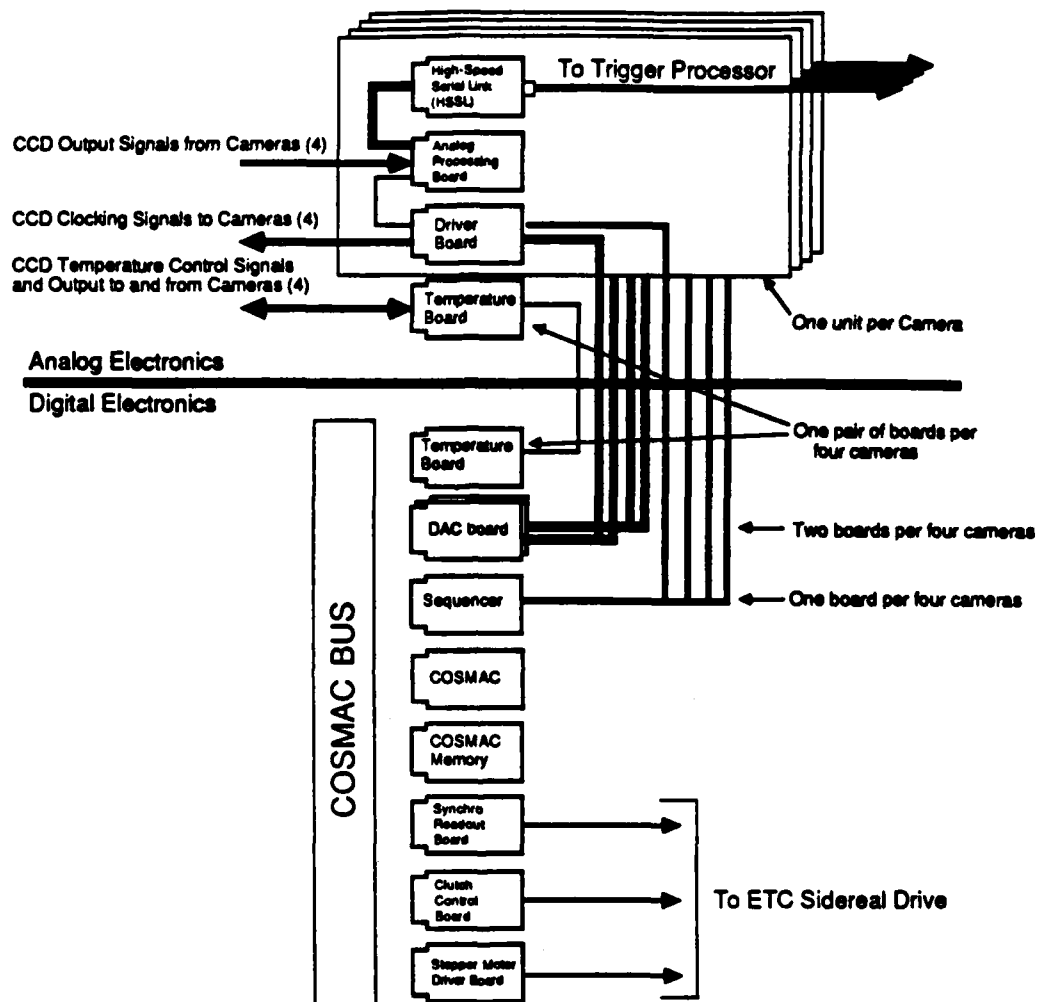


Figure 9.1 : Layout of the Instrument Control Electronics into Analog and Digital electronics

the COSMAC and loaded into the COSMAC from another processor (e.g. the Overseer computer) over the RS-232 serial link. The collection of higher-level code for the ETC's Instrument Control Electronics, known as the operating system, contains intermediate level building blocks, the Sequel compiler (see section 9.1.1.3) and upper-level instrument control code. A copy of the basic operating system and command definitions can be found in Appendix C.

#### 9.1.1.2. COSMAC Memory Board

The COSMAC memory board provides 16K of RAM to the COSMAC board through 8 2K RAM chips. The COSMAC memory board also houses the four 2K "boot ROMs" which store the COSMAC start-up instructions. The memory available to the COSMAC is allocated in part to certain peripheral boards of the Digital Electronics: the major portions of the COSMAC memory are reserved for the boot ROMs and the Sequencer compiler (see section 9.1.1.3). In addition, many small control functions of the Digital Electronics are accessed through memory locations, rather than through the available I/O lines. A map of the functions of memory locations of the ETC four-camera test unit is shown in Table 9.1 (see the appropriate subsections for details of the control functions).

#### 9.1.1.3. Programmable Sequencer

The Sequencer is responsible for the creation of the timing of the CCD clocks (see discussion of the CCD clocking in sections 9.1.2 and Figure 9.2). The sequencer, based on the Signetics 8x300 bipolar microcontroller, is run at 8 MHz, producing pulses 250 ns wide. The sequencer can produce up to 16 distinct streams of programmable timed pulses. The streams are generated by the sequential reading and execution (in 250ns steps) of 16-bit memory locations. The state of each of the 16 bits reflects the state of the appropriate stream in any given 250 ns time period: if a bit is high, the stream level is high.

The programming and sequential execution of the sequencer memory locations is done through a high-level language called Sequel, developed at MIT by John Doty, which runs in the COSMAC environment. The Sequel program as well as the stream execution memory are stored in fast-access RAM on the sequencer board.

In addition to the creation of the three clocks used to drive the CCDs, the sequencer is also responsible for timing operations in the analog processing of the CCD signal. The timing of the hold pulse in the analog processing chain is controlled by a sequencer stream (see Figure 9.2).

The signals from the Sequencer are fed to the Analog Electronics through a 26-pin flat ribbon cable to any of the driver boards. Since all the CCDs in the ETC test unit are timed identically, the sequencer signals are bussed along the Analog backplane to all the driver boards. Sequencer signals to the Analog boards are fed from the drivers along the backplane.

Memory location (hex)	Function
0000 - 1FFF	Boot ROM
7300 - 73F7	DACs
E000 - EFFF	Sequencer compiler
FF00 - FFFF	Device control

Table 9.1: COSMAC Memory Map

#### 9.1.1.4. DAC Board

The DAC board produces the analog voltages used in clocking out the CCDs (see section 9.1.2 and Figure 9.2). It is filled with 24 Digital to Analog Converters (DACs), each of which will produce a 0 to 10 Volt analog DC output based on an eight-bit digital input. The 24 DACs provide voltages to two cameras (three DACs per each of three tri-level CCD clocks and two bias voltages per CCD). The DAC signals are brought to each driver board on 26-pin flat ribbon cable connectors.

#### 9.1.1.5. CCD Temperature control

The CCD is cooled to  $-90^{\circ}\text{C}$  by a closed-cycle refrigerator. The temperature of the CCD can be held constant by passing a controlled amount of current through a power resistor mounted on the CCD cold sink. The temperature of the CCD is read via a thin film detector (a temperature-dependent resistor). The temperature of the CCD is controlled by an analog feedback loop which regulates the current through the power resistor to within  $\pm 1^{\circ}\text{C}$ .

#### 9.1.1.6. Stepper motor driver board

The slewing of the ETC telescope mount is done with a 0.88 amp stepper motor mounted on the telescope drive. The stepper motor driver board is designed to provide power to any winding or any combination of windings of a stepper motor given the appropriate low-level software command. Thus, the motor can be stepped by a series of commands powering the windings of the stepper in the correct sequence. The stepper motor in the ETC is stepped as quickly as the software will allow ( $\sim 500$  steps/second), which is sufficient to slew the mount at a rate in excess of 40 degrees per minute.

#### 9.1.1.7. Synchro readout board

The synchro readout board services the synchro shaft-angle encoder on the ETC tracking mount. It utilizes a CMOS synchro-to-digital converter, which converts the three 400 Hz signals from the synchro shaft-angle encoder on the polar axis of the telescope mount to a single 14-bit absolute shaft angle. This angle can be calibrated to give the absolute hour angle of the telescope mount. A 14-bit S/D gives an angular resolution of 1.3 arc-minutes, which is comparable to the angular size of an ETC pixel.

#### 9.1.1.8. Clutch control board

The clutch control board controls the motor clutches in the telescope drive. The drive has a slewing motor, a tracking motor and a clutch associated with each. In order to prevent both clutches from being engaged at the same time, they are controlled by a single double-pull, single-throw relay on the clutch control board.

#### 9.1.1.9. Dome Control Board

The dome at ETC Site 1 is equipped with an incremental encoder designed and built by Gerard Luppino of MIT. The output of the incremental encoder is monitored by circuitry on the dome control board. The dome encoding circuitry allows the determination of the location of the dome to 10-bit precision ( $\sim 21$  arc-minutes). The dome control card also includes circuitry which controls the two relays controlling the motion and direction of motion of the dome.

### 9.1.2. Analog Electronics

The primary function of the analog electronics is the acquisition, processing and transmission of image data from the CCDs. The clock signals used in reading out the CCD are created on the *driver* board using the timing signals from the *sequencer* and the voltages from the *DACs*. Each clock requires three DAC signals and two sequencer streams. When the CCDs are read out, the CCD output signal is amplified by a preamplifier inside the camera housing and sent to the *analog processing board*. Here the signal is sent through a delay line and several stages of amplification and digitized to 12 bits. These 12 parallel bits are sent to the High Speed Serial Link (HSSL) where they are converted to eight



serial bits and transmitted to the appropriate Trigger Processor. A schematic layout of the analog processing circuitry can be found in Figure 9.2a.

#### 9.1.2.1. Driver Board

The driver board creates CCD clocking signals by combining voltage levels from the DAC board according to timing signals from the sequencer. The CCD clocking signal is created by combining three analog voltage levels. One voltage level is always present in the clocking signals; the other two voltage levels are added to the clocking signal depending on the states of the two sequencer streams. The combination of the sequencer streams' timing and the three analog voltages allows for the production of the tri-level clocks used in reading out the CCDs. (See Figure 9.2c for a simplified schematic illustration).

Each driver board includes drivers for three separate CCD clocks and a bias voltage for the on-chip FET circuit. DAC and sequencer signals travel to the board over two flat ribbon cables. The CCD clocking signals are taken directly from the analog backplane to the cable connectors leading to the CCD cameras.

#### 9.1.2.2. Analog Board

When a CCD is read out, the output signal is passed through a preamplifier in the CCD camera housing. The preamplified CCD signal is then fed directly to the analog processing board. The CCD image information in the signal is separated from the signal background by an analog delay line and a balanced difference amplifier via correlated double sampling (see Figure 9.2b). The image signal is then passed through a software-controlled programmable variable-gain amplifier (PRAM), the gain of which is controlled by a sequencer stream, which is controlled by the COSMAC. The signal out of the PRAM is re-amplified, digitized to 12 bits and passed to the High Speed Serial Link.

#### 9.1.2.3. High Speed Serial Link (HSSL) board

The HSSL board accepts the 12-bit digital output from the Analog processor and converts it to an eight-bit serial stream readable by the HSSL receiver in the Trigger processor (see section 8.1.2). The twelve-to-eight-bit conversion is done through UV-erasable Programmable Read-Only Memory chip (EPROM) on the HSSL board, which maps its 12-bit input onto its 8-bit output based on a lookup table stored in its memory.

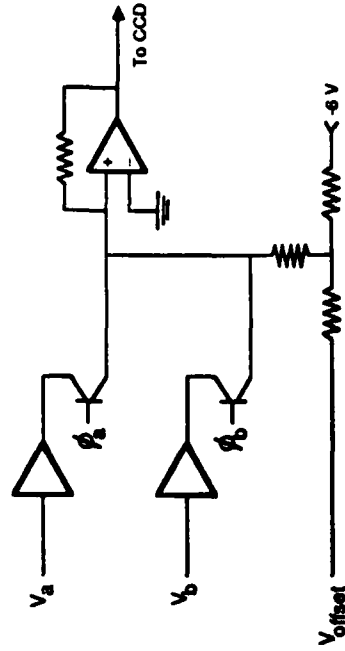
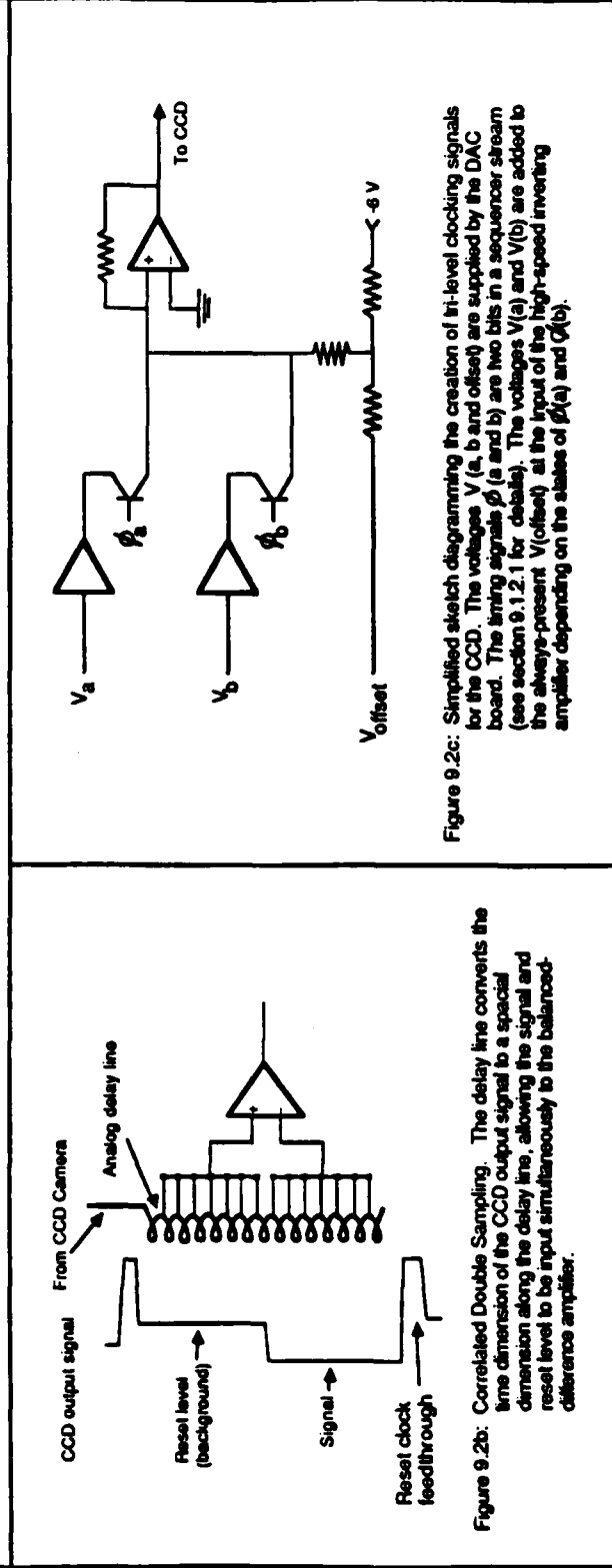
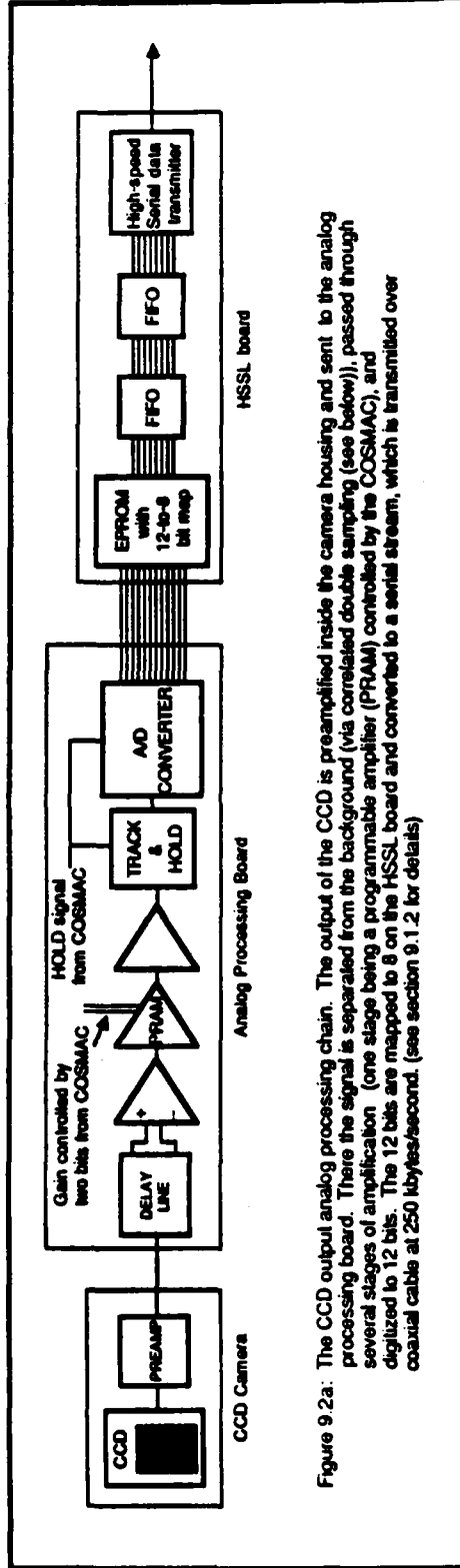
The high-speed serial link is based on the National Semiconductor DP8342/3 serial transmitter/receiver pair. The transmitter accepts 8-bit parallel data and transmits in a serial form readable by the receiver in the Trigger Processor. The receiver then translates the serial data back into parallel data. The transmitter/receiver pair in the ETC are run at 20 MHz, resulting in a 2 Mbit/second data transfer rate.

### 9.2. ICE Software

The Instrument Control Electronics are entirely controlled by low-level commands to the COSMAC microprocessor. A bit-level operating language was developed for the COSMAC microprocessor by Robert Goeke of MIT. This FORTH-like language was built upon to form a mid-level language, whose commands form the basis of the ICE software operating system.

The ICE control software consists of about four dozen mid-level commands to other boards on the COSMAC bus. Most commands involve the movement of data to and from locations in the ICE memory. The rest are commands to the sequencer, either to read out the CCDs or to change the CCD signal creation and analysis environment.

The ICE operating system and working software can be found in Appendix C. The bulk of the code defines the COSMAC software environment and the Sequel compiler. ETC control code is located near the back of the file.



## CHAPTER 10

### Expected Results

#### Introduction

Historically, it has generally been true that important scientific discoveries are made after the introduction of new instrumentation that opens the door to the investigation of an as-yet-unexplored physical regime. As a detector of optical flashes with risetimes of the order of one second, the ETC is investigating a relatively untouched region of parameter space in astronomy. The ETC has the potential to discover an entirely new class of astrophysical phenomena, characterized by brightness changes on the timescale of one second.

While the potential new discoveries of the ETC cannot be predicted, the detection of fast optical transients from astrophysical objects can be foreseen. The rate and brightness of optical flashes from GRBs and flare stars can be estimated from previous theories for expected transient optical radiation from the sources. By the same token, the rate and brightness of optical flashes from terrestrial sources, such as meteors and satellites, can be estimated.

As a bank of solid-state, electronic detectors, the ETC is also susceptible to local events which mimic optical flashes, such as cosmic rays and shot noise in the CCD. This chapter includes a discussion of the sources of events as seen by the ETC and estimates their expected rates. The results are graphed in Figures 10.3-10.7.

#### 10.1. Rate of Optical Flashes from Gamma-Ray Burst Sources

The expected rate of optical events from GRB sources is very uncertain at present, due to the lack of solid data on optical flashes from GRBs. A rough estimate can be made by convolving 1) the  $\log N$ - $\log S$  curve for detected GRBs (Jennings, 1982), 2) the ratio of  $F_{\text{opt}}/F_{\text{B}} = 750$  (for short ( $\sim 5$  second) optical bursts; Rappaport and Joss, 1985), 3) an estimate of the B-V for such a burst (Rappaport and Joss, 1985) and 4) an assumed fraction of GRBs which emit optical light.

The convolution of the  $\log N(>S)$ - $\log S$  curve for GRBs (see section 2.1.4) and the ratio of gamma-ray to optical fluence is straightforward, as it is a simple recalibration of the axes of the  $\log N(>S)$ - $\log S$  curve, based on the duration of the optical flash. Since the burst duration is rather loosely constrained by observation ( $\tau_{\text{burst}} < 500$  seconds), the optical event rate was calculated for burst times of 1, 5 and 30 seconds. The calculated rates of optical transient events from GRBs, assuming B-V = 0.0, are plotted in Figure 10.1.

An estimate of the B-V value of an optical burst from a GRB source requires an assumption of the mechanism for the production of optical light from GRBs. If the optical radiation is gamma-radiation reprocessed on the surface of a companion star, an assumption of the burst temperature of the companion is sufficient to give a value for B-V. Rappaport and Joss' (1985) value for a typical burst temperature,  $T_b = 8500$  degrees K, yields the value for B-V of -0.15; the resulting curve is not significantly different from the B-V = 0.0 curve which is plotted in Figure 10.1.

Finally, since no observer can make a statement at present about the fraction of GRBs which emit optical light, the plots in Figure 10.1 assume that all GRBs produce optical light.

#### 10.2. Rate of Optical Flashes from Comet Impacts onto White Dwarfs

Tremaine and Zyktow (1985; see Chapter 3) have proposed that optical burst events could be created by the impact of a comet onto a white dwarf. The comets, which are bound in a cloud about

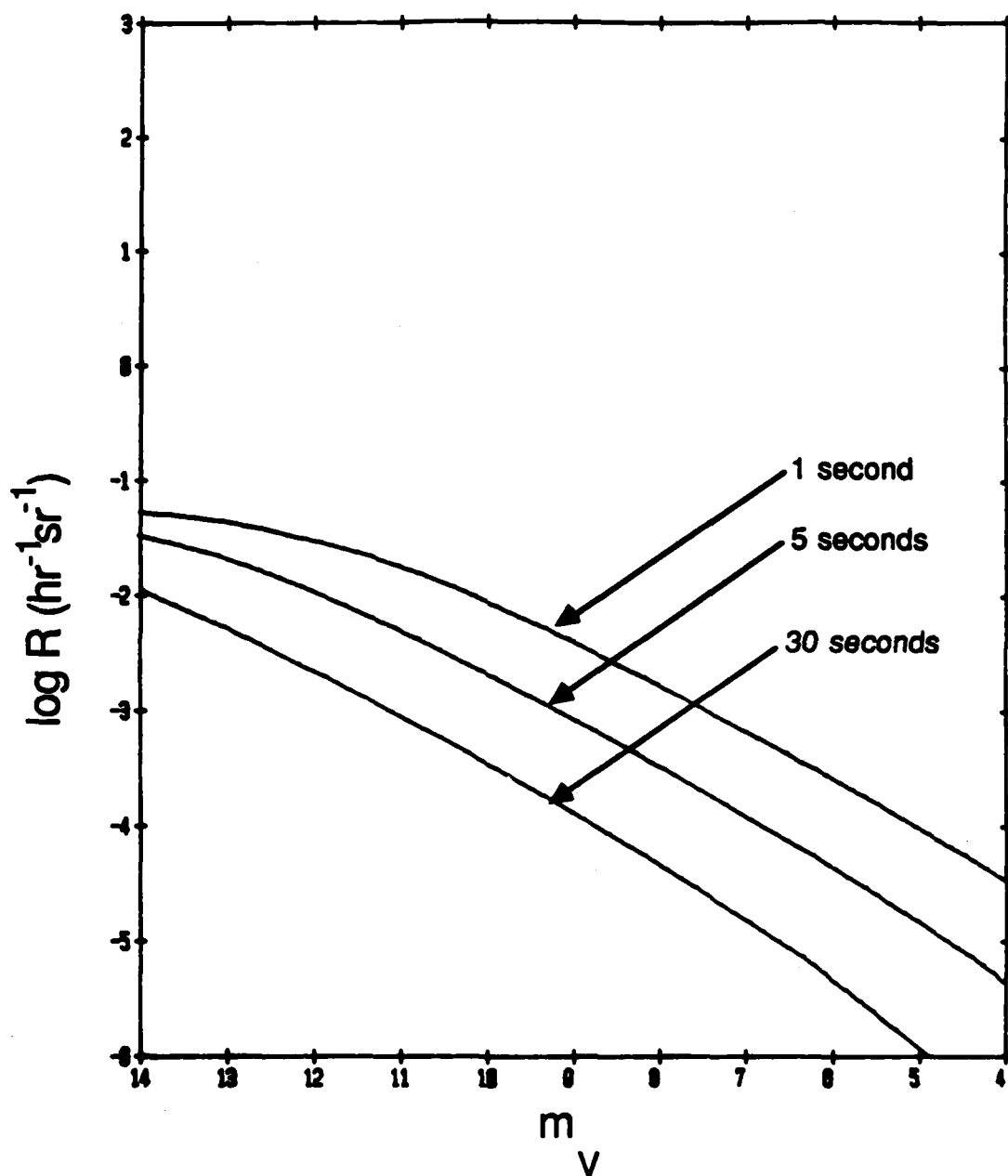


Figure 10.1: The expected rate of optical transient events associated with GRBs, based on a ratio of gamma-ray to optical fluence of 750 and optical burst times of 1, 5 and 30s.

the white dwarf, impact the white dwarf at an average rate of  $1.2 \times 10^{-3} \text{ yr}^{-1}$ . If, as proposed in a scenario by Tremaine and Zytow, the impact of a comet (mass =  $10^{16} \text{ g}$ ) heats the surface of a typical ( $M = 0.5M_{\text{solar}}$ ) white dwarf to  $30000^\circ\text{K}$ , resulting in a burst duration of  $\sim 10\text{s}$ , the absolute magnitude of the burst would be  $M_v = 9.9$  (Lang (1980), pp. 564-5). Given that the space density of white dwarfs is  $0.03\text{--}0.1 \text{ pc}^{-3}$  (say  $0.05 \text{ pc}^{-3}$ ), the rate of optical flashes with  $m_v < 9.9$  is  $2.3 \times 10^{-6} \text{ sr}^{-1}\text{hr}^{-1}$ . Assuming the white dwarfs are isotropically distributed, the  $\log N(>S) - \log S$  relation for white dwarfs will follow an  $S^{-3/2}$  dependence. The rate  $R(m < m_0)$  of optical flashes brighter than magnitude  $m_0$  from white dwarfs is included in the plots in Figures 10.7, 10.8 and 10.9.

The rate of optical flashes expected from white dwarfs increases if one assumes that the missing mass in the Galaxy ( $\sim 0.1 M_{\text{solar}} \text{ pc}^{-3}$ ) consists solely of  $0.5M_{\text{solar}}$  white dwarfs. In this case, the space density of white dwarfs is  $0.2 \text{ pc}^{-3}$ , and the rate of optical flashes with  $m_v < 9.9$  is  $\sim 10^{-5}$ .

### 10.3. Rate of Optical Flashes from Flare Stars

Flare stars are a class of red (primarily M) stars which exhibit frequent brightenings with rise-times of from a few to hundreds of seconds. These flares are brightest (in magnitudes) in the UV (where the star is not very bright), decreasing in brightness with increasing wavelength, until they are virtually undetectable in the red. The frequency of the flares has been empirically determined to be an exponential function of the quiescent absolute magnitude of the star, with fainter flare stars flaring more frequently (Gurzadyan (1980)). Observed flare stars have absolute magnitudes ranging from 8 to 15 and are generally found within 50 pc of the Sun. (A complete review of flare star observations and theory can be found in Gurzadyan (1980)).

Observed flare stars have the following properties, based on information given in Gurzadyan (1980):

- 1) The rate of flares from a given star is a function of its absolute magnitude  $M_v$ :  $\log f_U = 1.78 + 0.148M_v$  flares/hours.
- 2) The probability of a flare star flaring by more than an amount  $\Delta V$  can be roughly modelled as  $\ln P(\Delta V) = -\alpha_p \Delta V$ , where  $1.4 < \alpha_p < 2.2$ .
- 3) The rate of flares of a given  $\Delta m$  in V-band is roughly one-quarter of the rate in U-band.
- 4) Most flare stars are of spectral type M.
- 5) About 40% of all M stars within 6.5 pc of the Sun have been observed to flare; about 3% of all M stars within 20 pc have been observed to flare. This is evidently a selection effect.

Given these observational constraints, an estimate of the rate of flares versus peak flare magnitude can be made with a simple Monte Carlo analysis. In this procedure, the volume of space inside 20 pc is randomly filled with 1000 M stars, according to the density distribution of M stars in Allen (1976). Each star is assigned an absolute magnitude  $M$ , distance  $r$ , apparent magnitude  $m$  (based on  $M, r$ ) and a flare probability (per hour) based on the absolute magnitude  $M$ . In the Monte Carlo simulation, all stars are checked at regular time intervals (small compared to the smallest flare period). It is established whether each star flared in the preceding interval by comparing a random number to the individual flare probability. If so, the change in visual magnitude during the flare is determined from the rough probability distribution quoted above. The magnitude, distance, flare magnitude and time of each flare are recorded: after the Monte Carlo simulation has ended, these data are used to determine the rate of flares (in  $\text{sr}^{-1}\text{hr}^{-1}$ ) above a threshold magnitude  $\mu$ .

Such a Monte Carlo simulation of flare stars was executed, based on the observed flare star characteristics listed above. The value of  $\alpha_p$  was assumed to be 1.8, and the fraction of M stars that flare was assumed to be 0.5. The simulation was executed in shells of volume about the Sun in order to observe the dependence of flare rate on distance from the Sun. The shells used were 0-20 pc, 20-50 pc, 50-100 pc and 100-200 pc, with each shell being observed for 100000 flares. The flare rates from the various shells were summed to give flare star rates for populations of stars within 20, 50, 100 and 200 pc of the Sun. The results of these simulations are included in Figure 10.2. The straight line in Figure 10.2 represents an extrapolation of these curves to an infinite spherical distribution about the Sun. It is interesting to note how quickly the various curves converge to the infinite-distribution ( $S^{-3/2}$ ) rate: for the sensitivity of the ETC ( $m_v \approx 11-12$ ), the majority of flare star events will come from stars within 100 pc of the Sun.

In order to account for instrument sensitivity, the Monte Carlo simulation was modified to calculate the rate of flare events exceeding 400e<sup>-</sup> (a sensitivity of  $m_v \approx 10.8$ ). This curve is displayed in Figure 10.3.

The uncertainty in the flare star event rate reflects the uncertainty in the observed flare star characteristics. The fact that the value of  $\alpha_p$  is seen to lie between 1.4 and 2.2 affects the event rate by a factor of  $\sim e^{0.4} = 1.2$ . An additional element of uncertainty is introduced with the assumption that 50% of all M stars exhibit flares: the fraction is seen to be at least 0.4, yet could be as high as 1.0, so the flare rate calculated by the Monte Carlo simulation could be low by a factor of 2 because of this assumption.

A factor which has not been included in these calculations is the fact that the ETC is sensitive to changes in brightness in of the order of 1-4s. If the risetime of an optical burst is significantly longer than this, the sensitivity to the burst will drop, since only a fraction of the increase in brightness will be observed in a single exposure. If the rise of brightness to peak is roughly linear, the effective magnitude of the burst (as seen by the ETC) is increased by  $-2.5 \log(t_{\text{exp}}/t_{\text{rise}})$ , where  $t_{\text{exp}}$  and  $t_{\text{rise}}$  are the exposure and risetimes, respectively.

This effect is potentially greater for flare stars, which have typical risetimes of 10-60 seconds, than for optical flashes from GRBs, which may have risetimes of the order of seconds. If we take a typical flare star risetime to be 30 seconds, the decrease in detection sensitivity of a one-second exposure is 3.7 magnitudes. The effects of the typically long flare star brightening times is taken into account in Figure 10.4, which assumes a flare star risetime of 30 seconds. (It is important to note that 30 seconds is a rough median risetime and that actual event risetimes vary over almost two orders of magnitude (Moffett, 1974)).

This effect is, in principle, the same for optical bursts from GRB sources; yet, because of the absence of reliable data on GRB-related optical transient risetimes, the magnitude of the effect is difficult to estimate. This effect is taken into account in Figure 10.7, 10.8 and 10.9, assuming an optical burst time of five seconds.

#### 10.4. Terrestrial Sources of Optical Flashes

The primary known sources of terrestrial optical flashes are satellites and meteors. These flashes would be a particular problem for a single-site ETC, which would not be able to use parallax to discern the terrestrial origin of optical flashes from these sources. The streak-rejection algorithm in the Trigger software (section 8.3.2.4) is capable of rejecting fast satellites and most meteors. However, any source of optical transient radiation with an angular speed small enough to pass the streak-rejection test, such as slower satellites or head-on meteors, would be considered real events by a single-site ETC.

This section describes the rough calculation of event rates due to these sources.

##### 10.4.1. Meteors

A meteoroid is a particle or group of particles, ranging in size from 0.001 cm (micrometeoroids) up to tens of kilometers (asteroids). A meteor is produced when such a particle enters the Earth's

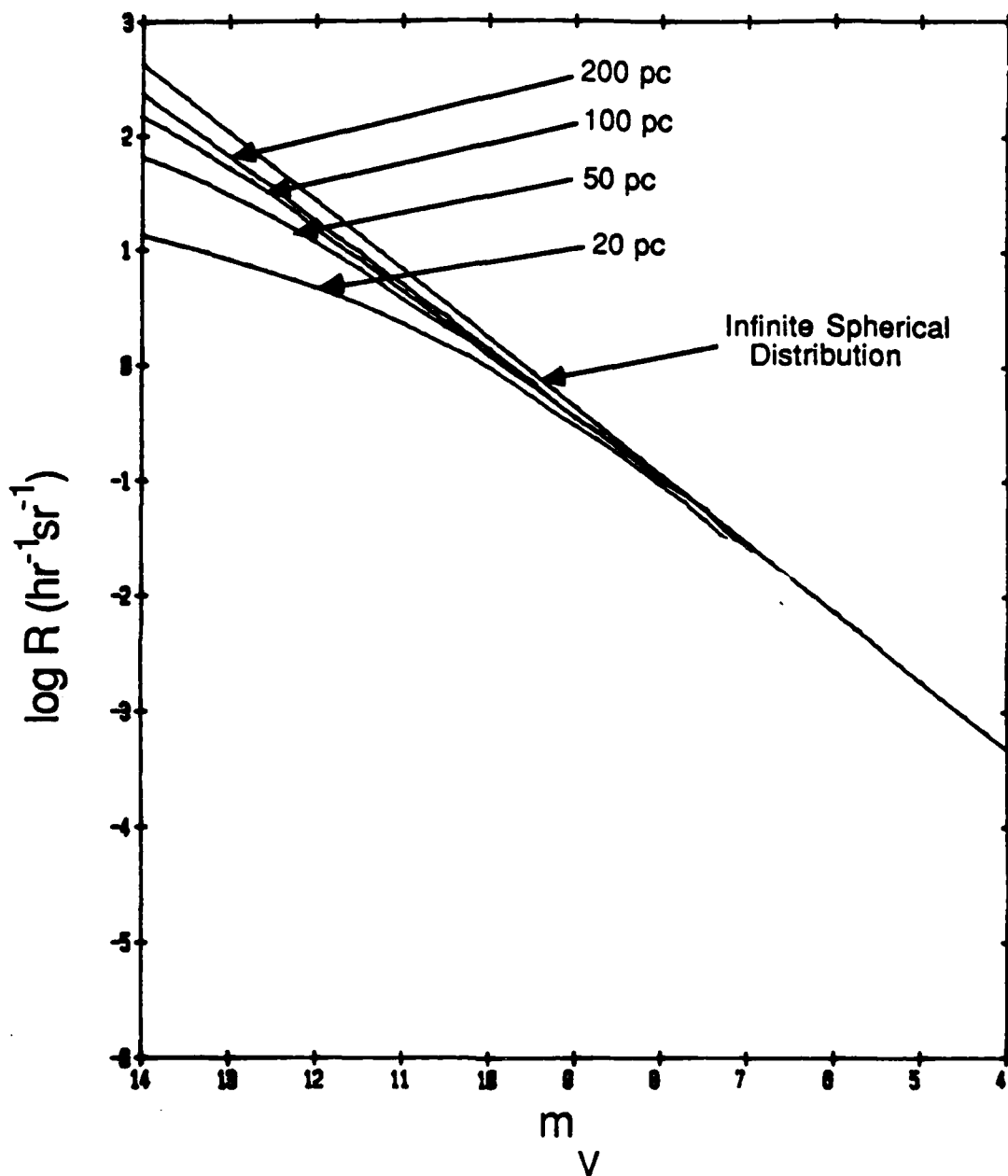


Figure 10.2: The results of the Monte Carlo simulation of flare star event rates discussed in section 10.3. The curves are the flare event rates from populations of flare stars located within 20 pc, 50 pc, 100 pc and 200 pc of the Sun. The straight line is the extrapolation of these curves to an infinite spherical distribution of flare stars about the Sun ( $\log N \sim (-3/2)\log S$ ).

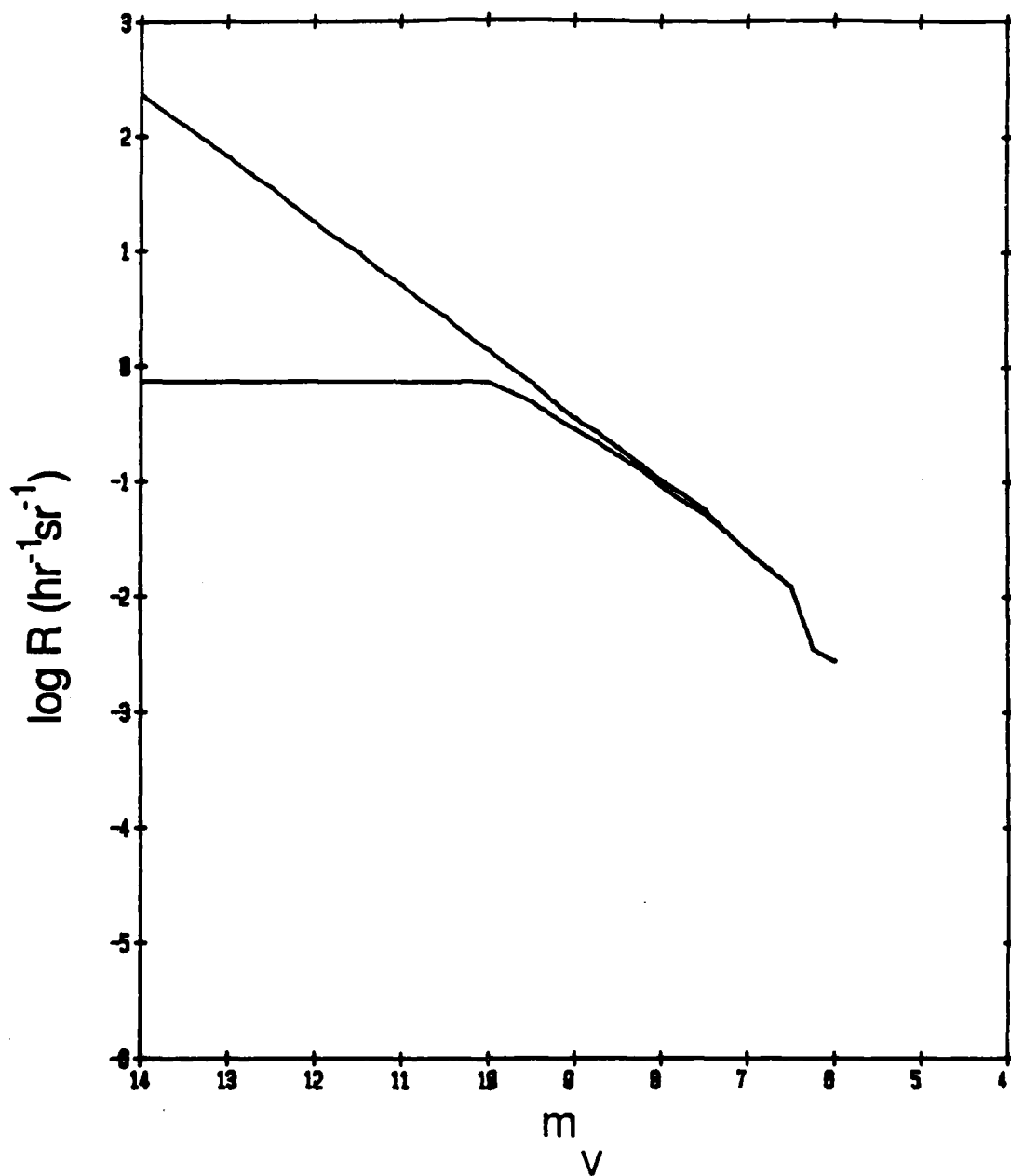


Figure 10.3: The effect of considering a detection threshold on the rate of detection from the 200 pc flare star population of Figure 10.2. The lower curve is of flare stars events by the ETC. The upper curve is the rate of events the convolution of the upper curve with a detection threshold of 400 electrons ( $m = 10.4$ ).



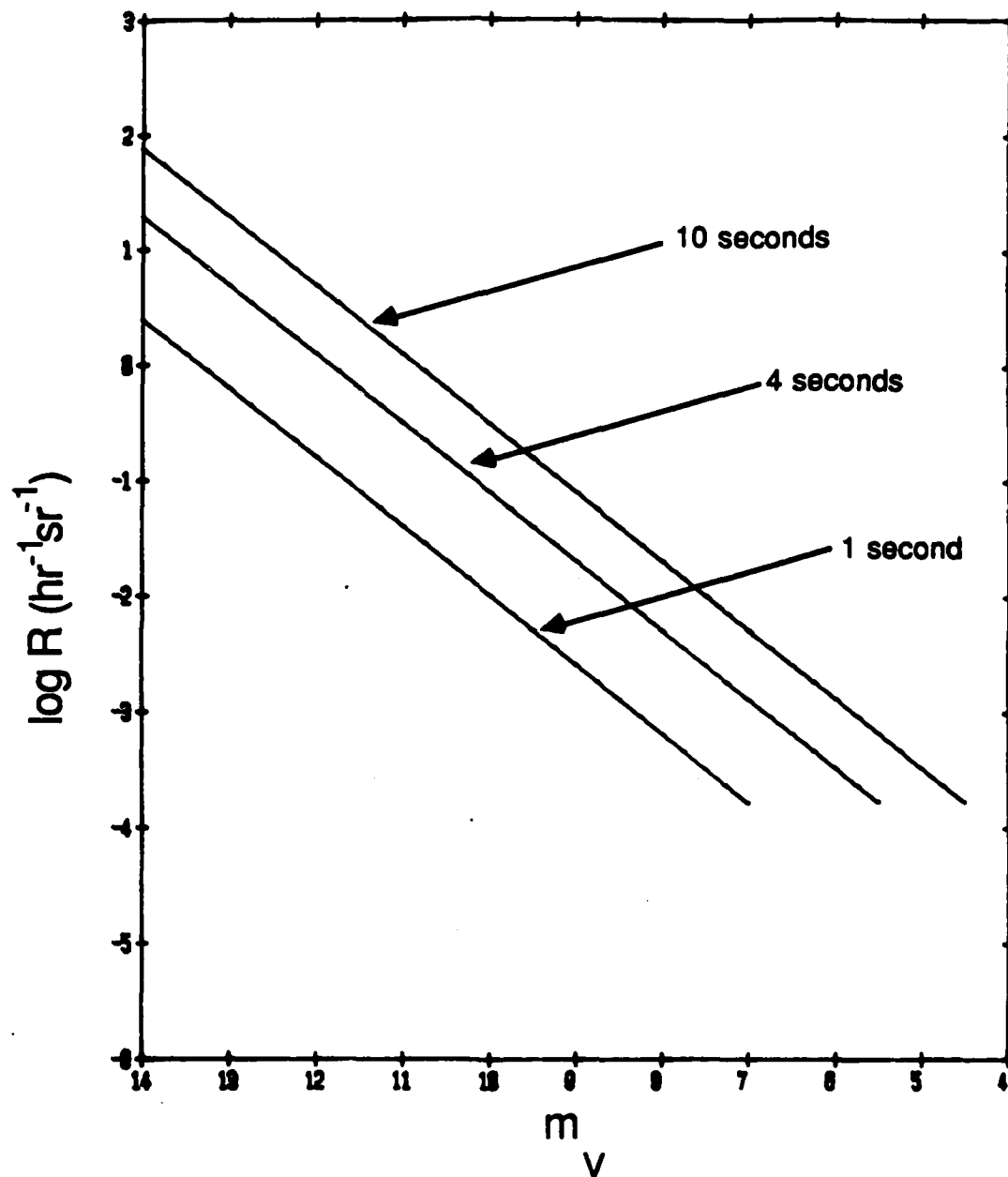


Figure 10.4: The effect of a long flare star risetime on the rate of detected events in the ETC. The lines are the event rates from an infinite distribution of flare stars (Figure 10.2), adjusted for the amount of brightening detected in one exposure time. The flare star risetime is assumed to be 30 seconds: the three curves plotted are detection rates in 1s, 4s and 10s exposures, assuming a linear rise to peak.

atmosphere and is partially or totally vaporized, creating a luminous trail sometimes visible with the naked eye. Upon entry into the Earth's atmosphere, the meteoroid is heated by contact with air molecules and begins to melt and evaporate at a rate dependent on the meteoroid temperature and mass. The rate of emission of meteoroid vapors determines the luminosity of the meteor trail.

A meteor can create a false trigger in the ETC if the angular size of the portion of the trail bright enough to trigger the ETC is smaller than the streak criterion in the Trigger software (section 8.3.2.4). The angular length depends on the angle of incidence of the meteor into the atmosphere, the peak brightness of the meteor, the meteor velocity and the image exposure time. The rate of triggering meteors is a convolution of the probability of a meteor of a given brightness creating a false event in the ETC and the flux of meteors of that brightness entering the atmosphere.

#### 10.4.1.1. Meteor light curve

The "typical" meteor light curve has been modelled by Oepik (1958). (Since meteors come in a variety of types, sizes and brightnesses, no one type can be considered "typical"; however, most of the meteors in the magnitude range of  $-2$  to  $10$  are considered to be created by the steady ablation of matter from a melted meteoroid, the rate of which was roughly modelled by Oepik). From his model, the meteor light curve has the form  $j \propto X(1-X)^2$ , where  $j$  is the brightness of the meteor and  $X = e^{-\Delta h/a}$ , where  $\Delta h$  is the change in altitude of the meteor and  $a$  is the scale height of the atmosphere at the altitude of ablation. From this light curve, Oepik calculates the relative intensity of the meteor to be  $j/j_{\max} = \frac{27}{4} X(1-X)^2$ . Expressed in magnitudes,  $\Delta m = m - m_{\text{peak}} = 2.5 \log(X(1-X)^2) + 0.83$ . Observations of meteor light curves have substantiated this model (Bronshen, 1983).

From the above relation, given a detector sensitivity  $\mu$ , and the peak effective magnitude,  $m_{\text{eff}}$  of the meteor as seen by the detector (taking image exposure time into account), one can calculate the length of the trail (in scale heights) that has a magnitude brighter than  $\mu$ ; i.e., the length,  $\Delta h/a$ , of the trail with  $\Delta m < m_{\text{eff}} - \mu$ .

#### 10.4.1.2. Meteor Geometry

The geometry of the incident meteor is shown in Figure 10.5. A meteor which enters the atmosphere with zenith angle  $Z$  which creates a visible trail over a range of altitudes  $\Delta h$  at a mean altitude  $H$  will create a trail of angular size  $\theta = \tan^{-1}(\Delta h \tan(Z)/H)$ . The probability of a meteor entering the atmosphere with a zenith angle  $Z$  is proportional to  $\cos(Z)\sin(Z)$  (Oepik (1958), p. 67): the probability of the meteor entering the atmosphere with zenith angle less than  $Z$  is  $\sin^2(Z)$ .

Given a detection threshold magnitude,  $\mu$ , some vertical length,  $\Delta h$ , of the trail of a meteor of peak effective magnitude  $m_{\text{eff}}$  will be brighter than  $\mu$ . In this situation, there will be a range of zenith angle  $Z$  which creates a visible trail length  $\theta < \theta_0$ . For a given threshold magnitude  $\mu$ , the rate of meteors with trails brighter than  $\mu$  yet with an angular size  $\theta$  less than a threshold  $\theta_0$  is determined by convolving the rate of meteors of effective magnitude  $m_{\text{eff}}$  with the probability associated with the zenith angle  $Z$ .

#### 10.4.1.3. The Effective Magnitude of a Meteor Trail

The effective peak magnitude of a meteor of actual peak magnitude  $m_{\text{peak}}$  is given by  $m_{\text{eff}} = m_{\text{peak}} - 2.5 \log(t/\tau)$ , where  $t$  is the time the meteor spends in a single pixel and  $\tau$  is the image exposure time. The time spent by a meteor in a single pixel depends on the velocity  $V$  of the meteor: the value of  $t$  is  $V \sin(Z)/H\alpha$ , where  $\alpha$  is the angular size of a pixel. The value of meteor velocity  $V$  is typically  $\sim 40$  km/s; the value of  $H$  ranges between 80 km and 100 km.

##### 10.4.1.3.1. Meteor flux

The flux of meteors in the magnitude range  $-2.4$  to  $+12$  has been measured by Cook, et al. (1981). The result of the observations is consistent with those of Hawkins and Upton (1958) and is

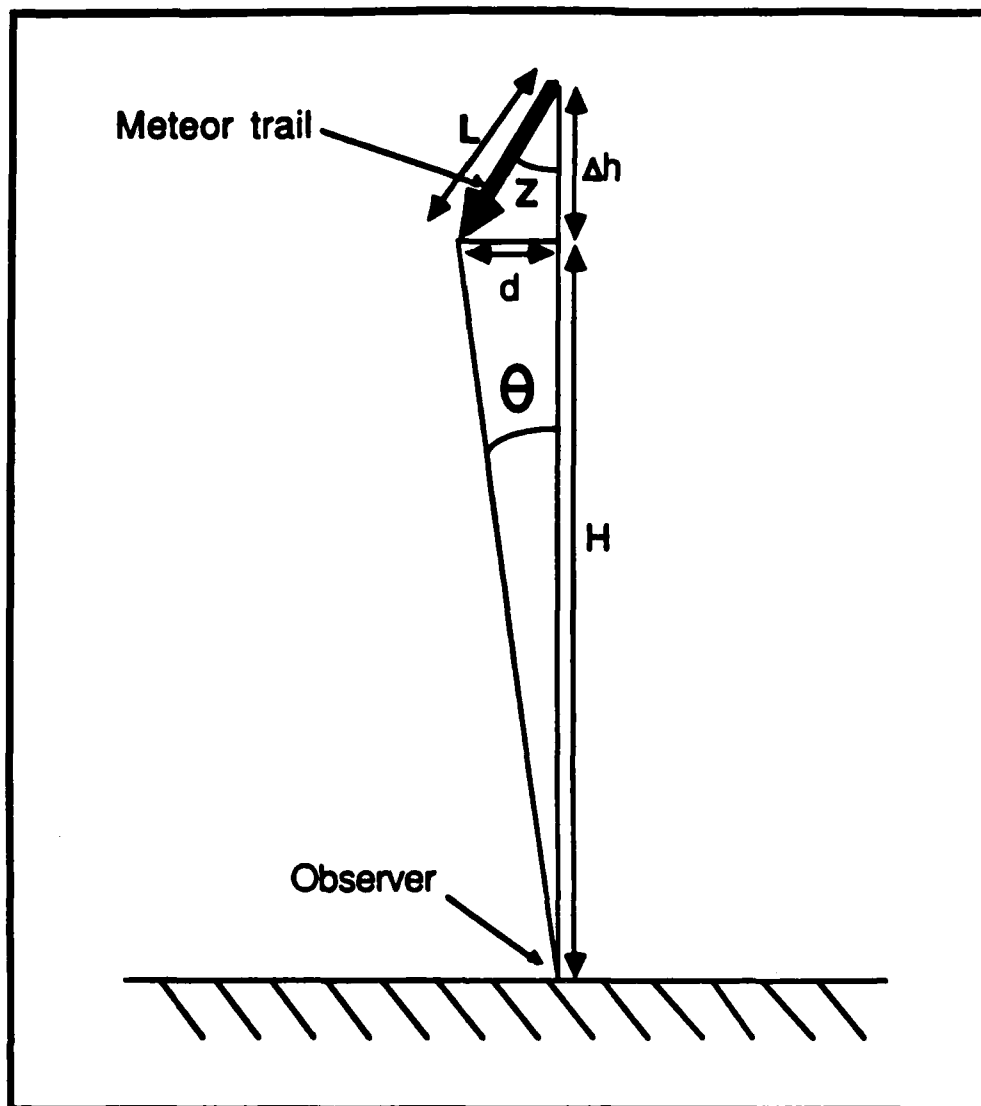


**Figure 10.5:** The geometry of a typical meteor trail. A meteor entering the atmosphere at altitude  $H$  with a zenith angle  $Z$  will subtend an angle  $\Theta = \arctan(L \sin Z / H)$ , where  $L$  is the length of the meteor trail. If the angle is less than the anti-streak criterion for the ETC (presently 13 arc-minutes), the meteor will trigger a single-site ETC as an event. A two-site ETC will be able to reject the meteor by virtue of its parallax over the 1.4 km baseline between the sites.

$$\log f_B (cm^{-1}s^{-1}) = -17.89 + 0.534m_B$$

(This equation is consistent to within a factor of  $\sim 2$  with values found in Allen (1976)). This value can be converted to meteors/frame/second by assuming a typical altitude of 90 km:

$$f_B (frame^{-1}s^{-1}) = 8.35 \times 10^{-6} 10^{0.534m_B}$$

Given the typical colors of a typical meteor ( $B-V = -1.41$  (Allen, 1976)),

$$f_V (frame^{-1}s^{-1}) = 1.47 \times 10^{-6} 10^{0.534m_V}$$

For the ETC, one frame has a solid angle of .086 steradians, so the calibration of  $frame^{-1}s^{-1}$  to  $sr^{-1}hr^{-1}$  is a multiplicative factor of 41900. The flux of triggering meteors in  $sr^{-1}hr^{-1}$  are

$$f_B (sr^{-1}hr^{-1}) = 0.350 \times 10^{0.534m_B}$$

$$f_V (sr^{-1}hr^{-1}) = 0.062 \times 10^{0.534m_V}$$

#### 10.4.1.4. The Net Rate of Head-on Meteors

The total flux of triggering meteors was calculated by considering the threshold magnitude,  $\mu$ , and effective magnitude of a meteor,  $m_{eff}$ , based on the zenith angle  $Z$  and its associated probability. The results for a typical meteor velocity and several exposure times are graphed in Figure 10.6.

It should be noted that a meteor can create a trigger not only if it comes into the atmosphere with a low zenith angle  $Z$ , but also at larger values of  $Z$ , when the section of the meteor trail brighter than the threshold magnitude is small enough to trigger the ETC. This effect is noticeable as an increase of 20-30% in the event rate at fainter threshold magnitudes ( $\mu > 10$ ).

#### 10.4.2. Satellites

The impact of satellites on the ETC could be very large, yet the magnitude of their effect is difficult to calculate. A tumbling satellite can create a false optical flash in the ETC by momentarily reflecting sunlight and appearing to the ETC as an optical glint. The ETC would also consider a moving, non-glinting satellite to be an event if the length of the satellite trail in a single exposure is less than the ETC anti-streak criterion.

The problem of glinting or moving low-Earth-orbit satellites will presumably disappear once the ETC has spread to two sites at Kitt Peak. (The 1.5 km baseline between the two ETC sites on Kitt Peak allows the recognition of terrestrial sources of optical flashes at altitudes of up to 3000 km). A single-site ETC, however, would possibly have to contend with a major fraction of satellite-induced events without the benefit of parallax. Presently, a non-glinting, moving satellite will be detected as an optical flash by a single-site ETC if its angular motion in a single exposure is less than 13 arc-minutes. This means that faster satellites (those in lower orbits) are more likely to be rejected by the anti-streak algorithm.

One method of reducing the event rate due to moving satellites might be to increase the exposure time, so that low-Earth-orbit satellites would always be rejected. Another possibility is the *a posteriori* rejection of satellite events based on three or more collinear glints in a single frame. Nevertheless, the problem of glinting satellites remains a problem until the second ETC site is ready, since, to a single-site ETC, a short glint looks like a point flash of light.

#### 10.4.3. Instrument-related Spurious Events

There is a finite probability of the detection of spurious events due to non-optical effects in the CCD detectors. One source of such false triggers is statistical fluctuations due to shot noise in the CCD: a thorough discussion of this effect is given in Chapter 11. A second source of non-optical false

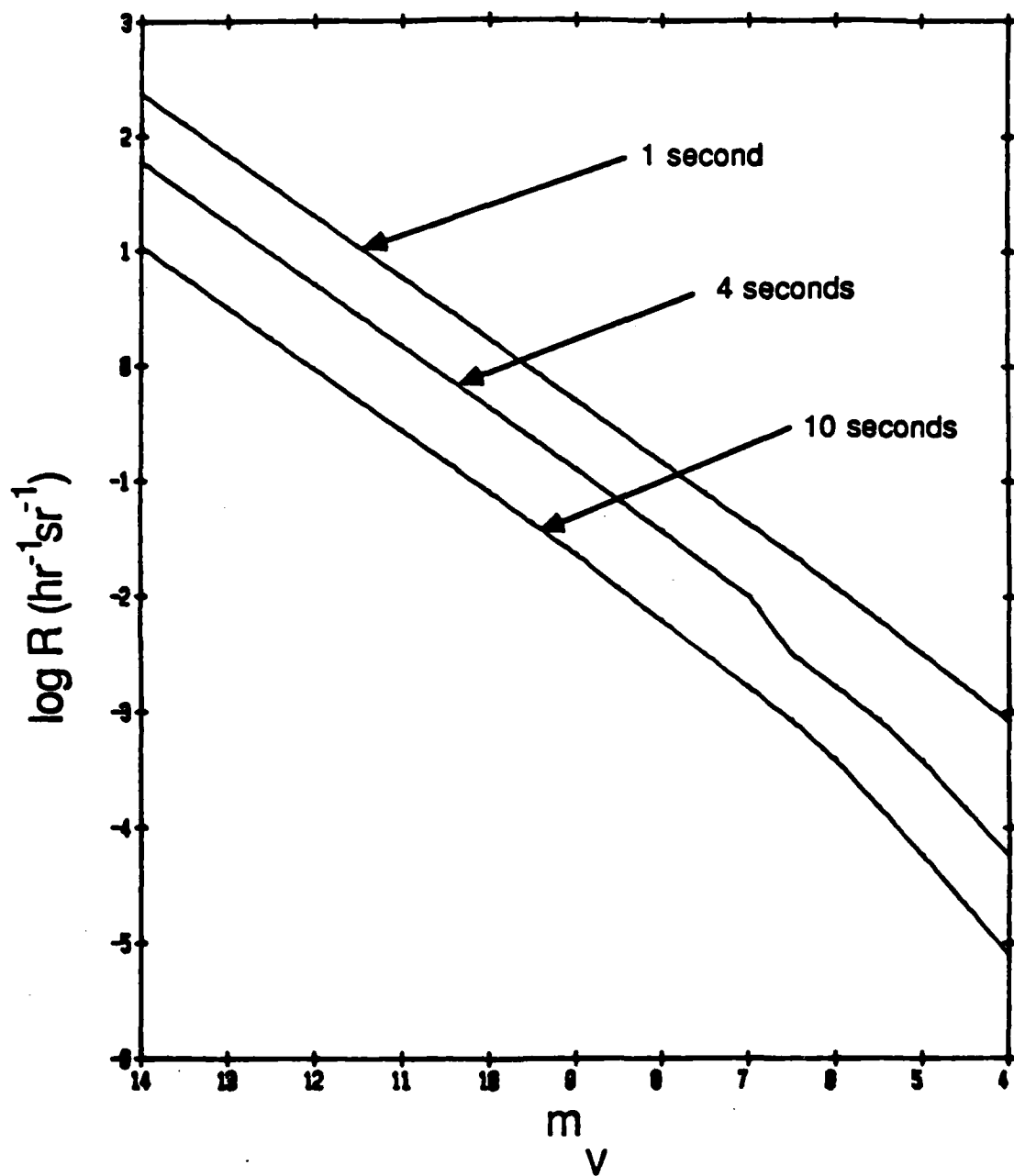


Figure 10.6: The calculated rate of false events due to head-on meteors (see section 10.4.1). The rates assume a meteor velocity of 40 km/sec and exposure times of 1s, 4s and 10s. The criterion for being detected as a head-on meteor by the ETC is an angular extent of less than 13 arc-minutes.

triggers is the interaction of cosmic-rays with the CCDs in the ETC cameras. A cosmic ray passing through a CCD ionizes the silicon it encounters, thereby freeing typically  $\sim 400$  electrons (for a  $3\mu\text{m}$  path length in silicon). A cosmic-ray interaction can mimic an optical flash in a single CCD camera (400 electrons corresponds to a star of  $m = 10.5$ ): properly placed cosmic rays in two CCD cameras can therefore create a false event in the ETC.

The calculation of the rate of false events due to coincident cosmic rays in two cameras is straightforward. The flux of cosmic rays on Kitt Peak is 5-10 per  $\text{cm}^2$  per minute. The rate per  $22.3\mu\text{m}$  pixel per hour is  $1.49 \times 10^{-5}$ . The probability per CCD (of  $10^5$  pixels) of a false trigger is  $2.23 \times 10^{-5}$ /hour. At 0.086 steradians per CCD, the cosmic-ray spurious event rate for the plenary ETC will be  $2.6 \times 10^{-4}$ /hr/sr, independent of sensitivity. This rate is included in Figures 10.7, 10.8 and 10.9.

### 10.5. The Rate of Events Due to All Considerations

The total rate of events due to celestial and terrestrial sources of optical flashes is presented in Figures 10.7, 10.8 and 10.9. The exposure times assumed in these figures are one, four and ten seconds. The duration of optical flashes from GRB sources is assumed to be five seconds in all three figures. Superimposed on each of these graphs is the sensitivity of the plenary ETC to optical flashes in one year of observations. Also included in each figure is a curve representing the sensitivity of the observations made by Schaefer, Vanderspek, Bradt and Ricker (1984), which had been the most sensitive wide-field search for optical flashes before the ETC.

### Caption to Figures 10.7, 10.8 and 10.9

Figures 10.7, 10.8 and 10.9 display the expected rate of optical transients from known terrestrial and celestial sources in one-, four- and ten-second exposures in the plenary ETC, as described in Chapters 4 and 10. Included are the rates of optical transients due to GRBs (as discussed in section 10.1), assuming both one-second and five-second burst durations, flare stars (section 10.2), assuming a thirty-second rise to peak, and comet impacts onto solitary white dwarfs (section 10.3). In addition, the rates of "false" optical transients due to head-on meteors (section 10.4.1) and cosmic rays (section 10.4.2) are included. The three-sigma Poisson sensitivity of the plenary ETC in one year of observations is indicated on each plot (see Chapter 4), as is the sensitivity of the Two-Schmidt survey of Schaefer, Vanderspek, Bradt and Ricker (1984).

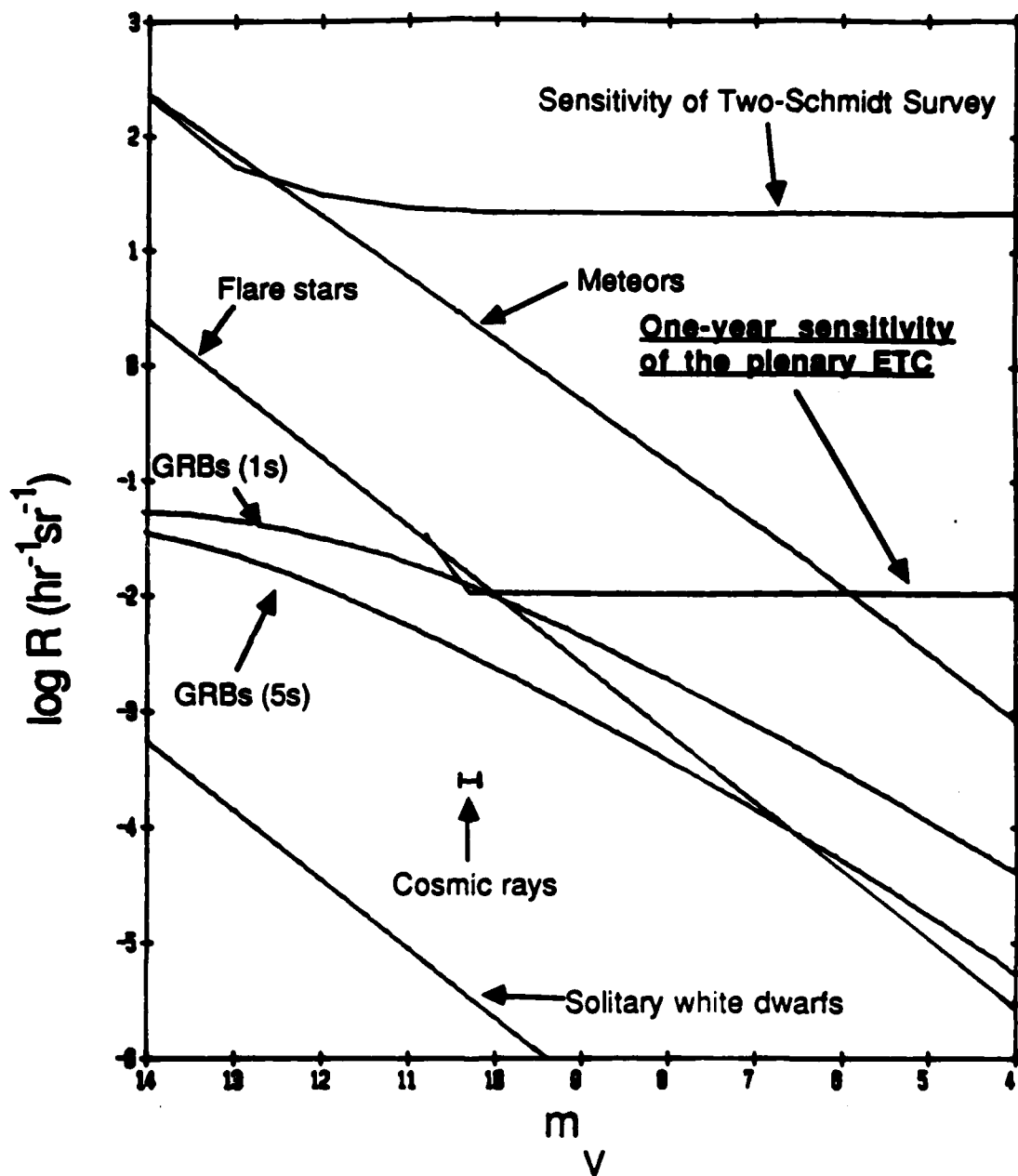


Figure 10.7: The expected event rates in one-second exposures in the plenary ETC.



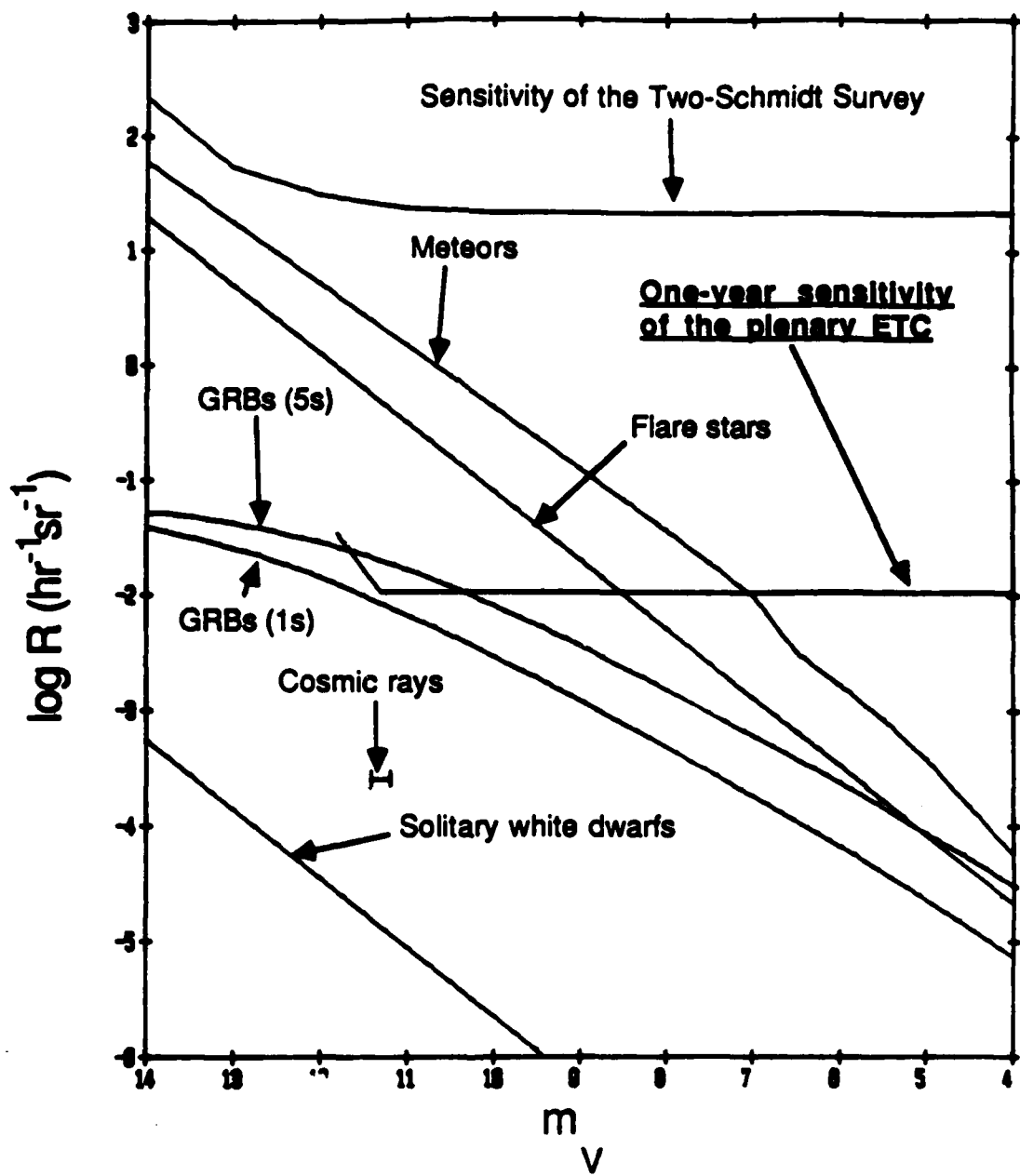


Figure 10.8: The expected event rate in four-second exposures in the plenary ETC.

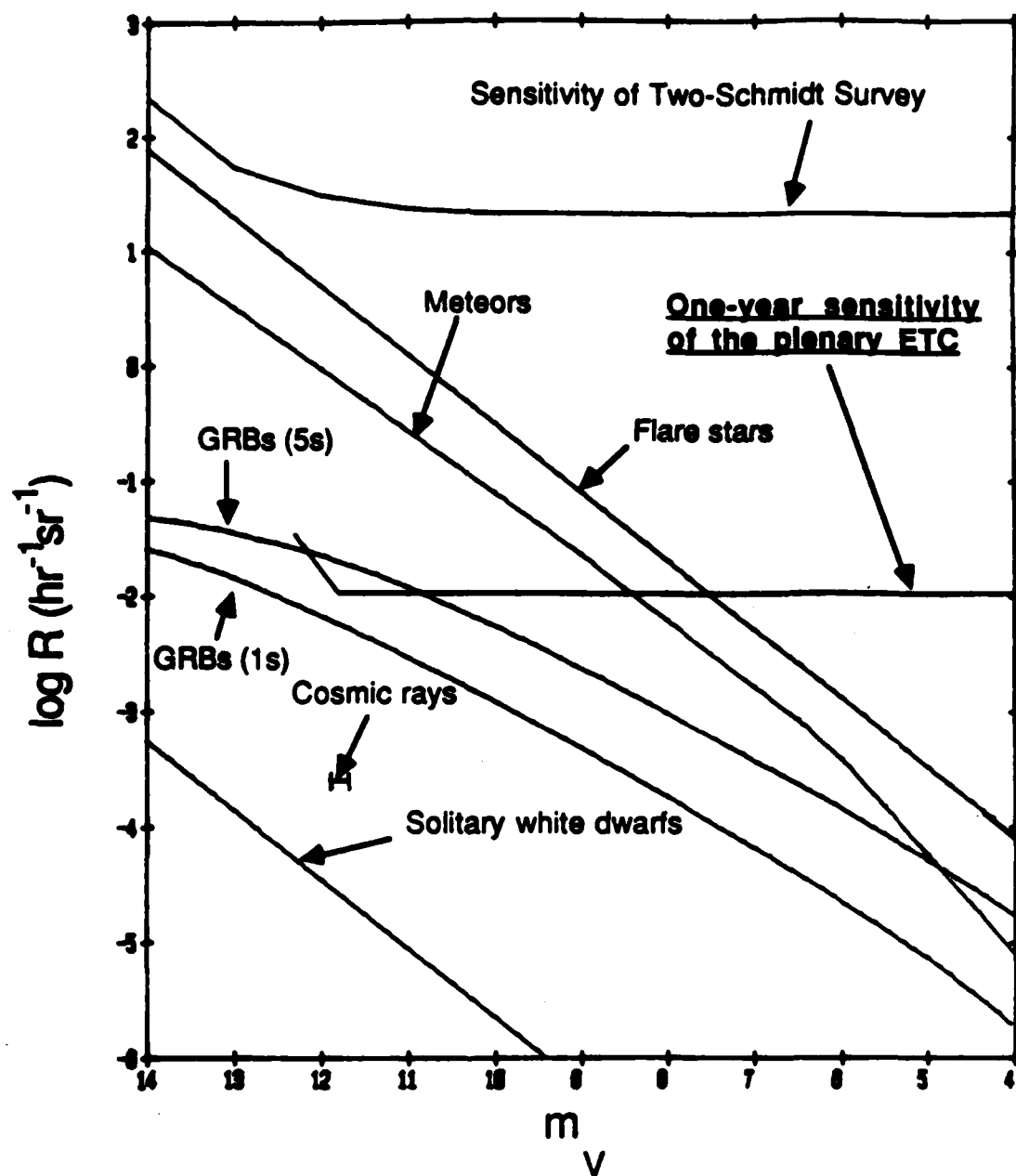


Figure 10.9: Expected event rate in ten-second exposures in the plenary ETC.

## CHAPTER 11

### Results of Observations with the ETC

#### Introduction

The ETC test instrument was set up at Kitt Peak in October and November of 1984. During the following December, January, and early March, the Overseer software was tested and refined. In late March and mid-May, 1985, observations of portions of the night sky were made with the ETC test unit. The goals of the observations with the ETC test unit were 1) to test the concept and operation of the Trigger and Overseer software, 2) to explore the limits of operation of the ETC software package, 3) to test the durability and reliability of the test instrument itself, and, of greatest astronomical interest, 4) to carry out the most sensitive wide-field optical flash search to date. These goals were achieved during the observation period. The following sections describe the tests of the ETC hardware and software; in addition, the observations with the ETC test instrument and the results of the observations are discussed.

#### 11.1. Observations with the ETC Test Unit

The "shakedown" observations with the ETC test unit were made in December, January, March and May, 1985. The quality of the observations software progressed from "very crude" in December to "working and useable" in March of 1985, to "quite satisfactory" in May of 1985. Observations made after 23 March 1985 are particularly useful in the sense that the software was working well enough that events could be detected and all data would be stored. Before 23 March 1985, the quality of the data stored made its astronomical use very difficult.

##### 11.1.1. Description of the ETC Test Unit Hardware

The test observations were made with just two of the four available cameras (cameras B and C of A, B, C and D) due to a malfunction in camera D's support hardware. Camera A, though useable, did not have a coincidence "mate", so that it could not be used to survey an independent part of the sky. Each camera was equipped with a 25 mm lens and a filter covering either the V-, R- or I-band. The filters were necessary because the chromatic aberration of the lenses made wide-band focus impractical (even with the filter, the point-spread-function of the lens was such that a stellar image was smeared over three or four pixels).

The hardware (including Overseer computer, Trigger processors and ICE) in the test unit were as described in chapters 6 through 9. The HSSL transmitter in the ICE was equipped with an EPROM which mapped the 12-bit output of the analog processing board to an 8-bit format according to a half linear, half logarithmic mapping known as the "linlog" mapping (see section 9.1.2.3). The linlog function maps the values 0-50 on the input to 0-150 on the output (linearly) and the values 151-4095 on the input to 151-255 on the output in logarithmic steps, such that each output step above 150 ADU corresponds to 0.0341 magnitudes. (A plot of this mapping can be found in Figure 11.1.) The linlog mapping gives the ETC a full 12 bits of dynamic range: with this mapping, the ETC is sensitive to faint events, which would have peak brightnesses of less than 150 ADU (150 ADU corresponds roughly to an 8<sup>th</sup> magnitude star in a ten-second exposure), while retaining sensitivity to flare events of  $\Delta m > 0.25$  from bright stars ( $m_v < 8$ ). In order to utilize the full range of the linear portion of the mapping, the Overseer software adjusts the sky+bias level in each camera to be between 20 and 50 ADU prior to each observation cycle (see section 11.2.1).

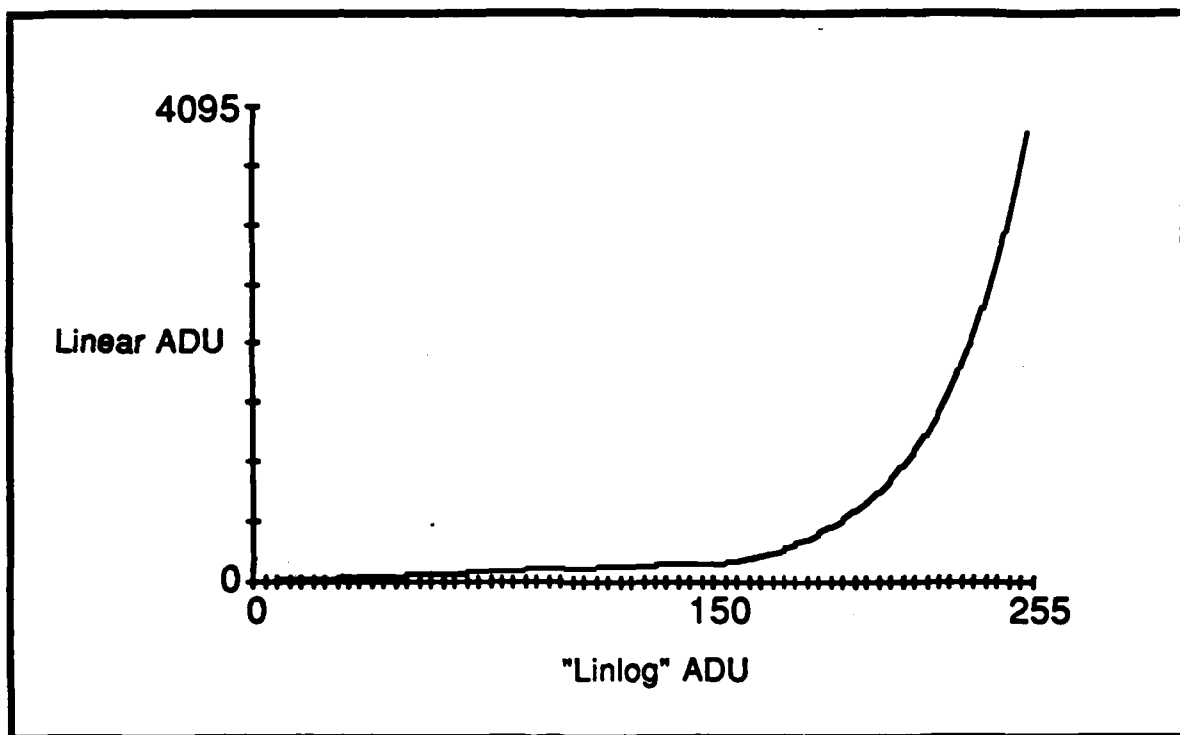


**Figure 11.1:** The mapping of the 12-bit output of the analog processing board to the 8-bit image data used in the ETC. The mapping is stored on a UV-eraseable programmable read-only memory chip (EPROM). The 12-bit input to the EPROM (in units of linear ADUs) is mapped onto its 8-bit output (in linlog units) with the linlog mapping. Input values between 0 and 150 are mapped linearly onto output values 0 to 150. Input values between 151 and 255 are mapped logarithmically onto 151 through 255, so that each output step corresponds to 0.0341 magnitudes.

### 11.1.1.1. ETC Camera Sensitivity and Gain

The sensitivity of the ETC test unit to detected events can be calculated from equation 4.2. However, in order to have a good understanding of the system sensitivity, the gain (in ADU/e<sup>-</sup>) and readout noise (in e<sup>-</sup>) of each CCD camera must be well determined. Therefore, the gain and readout noise of each CCD camera was measured in three different ways: through a light-transfer curve (LTC), from the brightness of stars of known magnitude in the CCD, and from the dark-sky brightness.

The light-transfer curve (LTC) method requires the measurement of the total noise in the CCD at various light levels (the noise is the standard deviation of the values of the difference between two consecutive frames at the same light level). Since the total noise is given by  $\sigma_T^2 = \text{Signal(ADU)}/g + \sigma_{\text{readout}}^2$ , several data points allow for an estimate of the system gain ( $g$ ) and readout noise ( $\sigma_{\text{readout}}$ ).

The second method involves calculating of the relation of the brightness of stellar images (in ADU) to their visual magnitudes. This was done with SAO standard star images on a full CCD image recorded at Kitt Peak for both cameras B and C, and both analyses yielded mappings of the form  $\log(\#ADU) = \text{constant} - m_v \cdot (0.4 \pm 0.02)$ , as was to be expected. Given the transmissivities of the atmosphere and the CCD camera optical system, and the efficiency of the CCD, the system gain can be calculated from this mapping.

The third method requires measuring the brightness of a moonless sky, also on a stored image. From a comparison of the measured dark sky brightness (in ADU/pixel/second) with the actual sky brightness (in photons/pixel/seconds) the gain can be calculated, given the transmissivity of the optical system and the CCD efficiency.

These three methods were used in the calculation of the gain and readout noise of each CCD camera. The results are summarized in Table 11.1. From the analysis, the values of 62 e<sup>-</sup>/ADU and 51 e<sup>-</sup>/ADU were adopted for cameras B and C, respectively. The readout noise was determined from the LTC to be 70 e<sup>-</sup> in camera B and 52 e<sup>-</sup> in camera C.

The values of the various parameters of the ETC optical system implicitly used in the calculation of the sensitivity of the ETC test unit (equation 4.2) are listed in Table 11.2. The values of I-band lens throughput and CCD efficiency are estimates, due to incomplete data in that wavelength band. The values of atmospheric characteristics (transmission and sky brightness) were taken from Allen (1983):

Method	Camera B gain	Camera C gain
LTC	$62 \pm 5 \text{ e}^-/\text{ADU}$ ( $\sigma_{\text{readout}} = 1.15 \text{ ADU}$ )	$46 \pm 7 \text{ e}^-/\text{ADU}$ ( $\sigma_{\text{readout}} = 1.01 \text{ ADU}$ )
Stellar brightnesses	$67 \pm 15 \text{ e}^-/\text{ADU}$	$48 \pm 18 \text{ e}^-/\text{ADU}$
Dark sky brightness	$63 \pm 6 \text{ e}^-/\text{ADU}$	$58 \pm 6 \text{ e}^-/\text{ADU}$

Table 11.1: Results of Gain Calibration of the ETC Cameras

these values are for sea level and differ somewhat from the values at Kitt Peak. The window transmissivity was calculated from the Fresnel equations, which give the reflection losses at each surface of the window. The values for the sensitivity to a detected event in each of the cameras at a signal-to-noise level of 10 are also listed in Table 11.2.

## 11.2. Testing and Operation of the ETC Software

During testing of the ETC test unit, the Overseer software was run in "user" mode, which allows for automatic observations and data storage after human-aided setup. User mode allows the observer to change observational parameters in order to test the performance of the instrument. The following sections describe "user" mode in detail: the methods used in the testing of the limits of the Overseer and Trigger software are described in section 11.2.2.

### 11.2.1. User Mode

The "user" mode of ETC observations was developed as a preliminary to full instrument automation. User mode allows the observer to specify every aspect of the ETC observations, in order to test

Optical Characteristics of the ETC Test Unit			
Focal length	25 mm		
f-number	0.85		
Area of lens	6.8 cm <sup>2</sup>		
Pixel angular size	3.09 arc-minutes		
Camera C gain	51 e <sup>-</sup> /adu		
Camera C readout noise	52 e <sup>-</sup>		
Camera B gain	62 e <sup>-</sup> /adu		
Camera B readout noise	70 e <sup>-</sup>		
	V-band	R-band	I-band
Sky rate (e <sup>-</sup> /pixel/second)	138	602	1046
Filter bandpass	1160 Å	1200 Å	1600 Å
Atmospheric transmission	.82	.92	.95
Filter transmission	.71	.80	.77
Lens transmission	.85	.80	.70
Window transmission	.91	.91	.91
CCD efficiency	.45	.60	.38
Image splitting	.5	.5	.5
One-second event sensitivity	7.5	8.4	8.0
Four-second event sensitivity	9.0	9.7	9.3
Ten-second event sensitivity	9.9	10.5	10.0

Table 11.2: ETC Prototype Optical Characteristics

the quality and speed of the Overseer and Trigger software, whereupon the ETC observes the sky without further interaction by the observer. An example of the observer's interactions with the ETC software's user mode is shown in Figure 11.2: the details of user mode are given below.

Upon entering user mode, the software asks the observer to move the telescope drive (manually or through the slewing motor) to the right ascension appropriate to the observations. Once the right ascension is correct, the software asks the observer to input the exposure time, sift time and the statistical criteria used in the calculation of the thresholds used in the Trigger software (see section 8.3.2). The Overseer computer then measures the sky+bias level of each CCD from images taken by each camera: the bias level is adjusted (if necessary) until the sky+bias level is between 25 and 60.

Once the sky+bias level is correct, the observer has the opportunity to save full images from all cameras onto disk files. The observer is then asked to rotate the dome slit until the cameras view the slit center. The relationship between the dome azimuth and the dome encoder value can then be calibrated. Next, the Overseer computer then calculates the values of threshold offset and brightened delta (see Chapters 7 and 8) from the observer-specified statistical criteria and a measurement of the total noise per pixel in each camera.

At this point, the observer participates in precisely calibrating "pixel address" to celestial coordinates for each CCD camera in turn. The Overseer computer roughly calculates the coordinates of the center of a camera field from its knowledge of the date, time and location of the site, the hour angle of the sidereal drive (through the absolute synchro shaft encoder mounted on the drive) and the declination of the camera (specified in the software). The Overseer computer then calculates the expected locations of 16 SAO standard stars in the field based on these rough coordinates: these locations are circled over an image of the sky taken by that CCD camera and displayed on the color graphics monitor. The observer is requested to tell the Overseer computer how far the circles are from the actual locations of the SAO standard stars. This is an iterative process, which ends when the observer reports that the SAO stars are all circled. The Overseer computer then calculates the precise position of the stellar images on the CCD and calculates the precise astrometric mapping of the CCD location to celestial coordinates (see section 7.1.4.2).

Once all the CCD fields are calibrated, the threshold frames are calculated by the Trigger processors from actual image frames. The Trigger processors are then initialized: at this point, the sequence of observation cycles can begin. The observation cycles run completely automatically, so no observer need be present. An observation cycle consists of twenty minutes of observations, followed by data storage (see section 7.4.2), a check of the sky+bias level, a recalculation of the astrometric mapping and a recalculation of the threshold frames. If the sky+bias level in a CCD has changed significantly, the bias level in the CCD is adjusted automatically. The recalculation of the astrometric parameters is necessary due to a slight ( $\sim 30'$ ) misalignment of the polar axis of the telescope drive; however, the misalignment is small enough that the Overseer computer can recalibrate the mapping without the assistance of an observer. This periodic recalibration is also necessary because of the effects of atmospheric refraction, which vary with hour angle.

The sequence of observation cycles continues indefinitely until 1) sunrise, or 2) the hour angle of the mount exceed six hours. In all, the net efficiency of ETC observations, including startup and recalibration pauses, is 75%: i.e., three-quarters of the time the observation software is running in the Overseer computer, the ETC is taking and analyzing images of the night sky. An individual observation cycle is halted when data has been taken from six prospective candidate events: the data are then stored and the observation cycle is immediately restarted.

### 11.2.2. The Testing of the ETC Software

During testing of the ETC software, the values of threshold offset and brightened delta were varied to determine their effect on the performance of the software. No attempt was made to unduly minimize the rate of "false" (statistical) events: the values of threshold offset and brightened delta were set as low as possible to maximize the chance of detecting a real event. The lower limit on the values of these two variables (which were generally set equal to one another) was the point where the sift

```

ETC 1 data 1 start
Set Out LV 00-31-01 GMT 1968
Null query (B) responds with -1
Trigger B does not respond to a null query
Reset trigger 00
Null query responds with 0
Null query (C) responds with 0
Should I check the COMBINE? a
Null query is 12
Null query is 11
Engaging tracking clutch

ETC Entry Name
Command? a
Engaging tracking clutch

The time is 0:33 UT
Synchro angle converts to ra of 025762
You are now at a right ascension of 025762
Ascendancy? a
PREPARING TO BLEND...
(Synchro reads 11579)

The playing motor will move -30 steps (= 10 cost)
The amount will be in action for 0 seconds
Engaging steering clutch
Engaging tracking clutch
(Synchro reads 11579)
Synchro angle converts to ra of 025891
You are now at a right ascension of 025891
Ascendancy? a
The present exposure time is 500
Enter new exposure time (0 for no change): 0
The present exposure time is 500
The present slit time is 720
Enter new slit time (0 for no change): 0
The present slit time is 720
Should the system attempt automatic astrometry updates? y

Present number of slits used for threshold effect B is 0
Enter new number of slits (0 for no change): 0
Present number of slits used for threshold effect C is 0
Enter new number of slits (0 for no change): 0
Present number of slits used for brightened delta B is 0
Enter new number of slits (0 for no change): 0
Present number of slits used for brightened delta C is 0
Enter new number of slits (0 for no change): 0
The time is 0:34 UT

Adjusting the effects of the cameras so that the
slit level is in the linear range

Reading a slit frame into trigger memory
B complete
C complete
B complete
C complete

slits is 10.11 average is 43.95
The slit level at the center of camera B is 43.25
slits is 1.40 average is 39.37
The slit level at the center of camera C is 39.37
The time is 0:34 UT
(Synchro reads 11567)

This observation will end in 8 hours 4 minutes
The time is 0:34 UT
Save frames? a
The time is 0:34 UT
Sending entire image to GC-MEM.
Enter a character and hit return when the data slit is
properly aligned with the camera
(Synchro reads 11564)
The present slant of the camera is 1348720
The present slant of the dome is 0149500
The time is 0:35 UT
Attempting to determine bias level from two separate exposures
Taking a 1000-contrast second exposure
Reading a slit frame into trigger memory
B complete
C complete

Filling SMD structure for camera C
There are 40 SMD stars in this field
Sending entire image to GC-MEM.
Attempting to autoalign camera B
On a -40, 0y = 13
Completed field alignment
20100.000 0.330 0.004 14673.000 -0.004 0.330
-54732.435 2.970 -0.032 -43995.005 0.032 2.970
Threading 01 out of linear fit
Threading 02 out of linear fit
Threading 03 out of linear fit
Threading 04 out of linear fit
Threading 05 out of linear fit
Threading 06 out of linear fit
Threading 07 out of linear fit
Threading 08 out of linear fit
Threading 09 out of linear fit
Threading 10 out of linear fit
Threading 11 out of linear fit
Threading 12 out of linear fit
20195.437 0.330 0.004 14644.034 -0.003 0.330
-54734.930 2.901 -0.032 -44030.337 0.029 2.901
Threading 01 out of linear fit
Threading 02 out of linear fit
Threading 03 out of linear fit
Threading 04 out of linear fit
Threading 05 out of linear fit
Threading 06 out of linear fit
Threading 07 out of linear fit
Threading 08 out of linear fit
Threading 09 out of linear fit
Threading 10 out of linear fit
Threading 11 out of linear fit
Threading 12 out of linear fit
20097.709 0.330 0.004 14637.404 -0.003 0.330
-54751.001 2.905 -0.032 -44130.910 0.031 2.905
Attempting to autoalign camera C
On a -40, 0y = 13
Completed field alignment
20137.999 0.330 0.001 14702.200 -0.001 0.330
-54747.444 2.970 -0.009 -43640.004 0.009 2.970
Threading 01 out of linear fit
Threading 02 out of linear fit
Threading 03 out of linear fit
Threading 04 out of linear fit
Threading 05 out of linear fit
Threading 06 out of linear fit
Threading 07 out of linear fit
Threading 08 out of linear fit
Threading 09 out of linear fit
Threading 10 out of linear fit
Threading 11 out of linear fit
Threading 12 out of linear fit
20203.343 0.330 0.000 14708.211 -0.002 0.330
-54895.290 2.975 -0.019 -44443.907 0.017 2.909
Threading 01 out of linear fit
Threading 02 out of linear fit
Threading 03 out of linear fit
Threading 04 out of linear fit
Threading 05 out of linear fit
Threading 06 out of linear fit
Threading 07 out of linear fit
Threading 08 out of linear fit
Threading 09 out of linear fit
Threading 10 out of linear fit
Threading 11 out of linear fit
Threading 12 out of linear fit
20133.501 0.330 0.001 14691.670 -0.002 0.330
-54680.170 2.975 -0.012 -44330.930 0.019 2.970
Reading a slit frame into trigger memory
B complete
C complete
C complete
B complete

slits is 10.12 average is 40.90
The slit level at the center of camera B is 40.67
slits is 2.99 average is 42.42
The slit level at the center of camera C is 42.30
Taking a 500-contrast second exposure
Reading a slit frame into trigger memory
B complete
C complete
C complete
B complete

slits is 15.75 average is 45.04
The slit level at the center of camera B is 45.25
slits is 1.50 average is 39.34
The slit level at the center of camera C is 39.27
Slit level of C is 36
Calculating total noise in each camera
slits is 15.75 average is 45.04
The slit level at the center of camera B is 45.25
Calculated total noise to be 72.3 electrons for B
slits is 1.50 average is 39.34
The slit level at the center of camera C is 39.27
Calculated total noise to be 62.6 electrons for C
Determining thresholds for all cameras
Threshold level of B is 9
Threshold level of C is 8
The time is 0:35 UT
(Synchro reads 11545)
Synchro angle converts to ra of 024607
Preparing to align cameras with the slit
Reading a slit frame into trigger memory
B complete
C complete

Filling SMD structure for camera B
There are 39 SMD stars in this field
Sending entire image to GC-MEM.
Sending entire image to GC-MEM.
The time is 0:47 UT
Calculating comparison frame for all cameras
Reading a slit frame into trigger memory
B complete
C complete
B complete
C complete
B complete
C complete
Requesting of B with effect of 9
Requesting of C with effect of 0
Camera B responded
Camera C responded
The time is 0:47 UT
Setting the necessary trigger parameters
The time is 0:47 UT
Beginning observation cycle
(Synchro reads 11426)
Attempting to adjust the dome by 20367 micro-radians
Attempting to adjust the dome by 10722 micro-radians
(Synchro reads 11429)
The time is 0:47 UT
Checking for dome occultation...
Reading a slit frame into trigger memory
B complete
C complete
C complete
B complete
Sending entire image to GC-MEM.
YOU HAVE 5 SECONDS TO MAKE A JUDGMENT
Sending entire image to GC-MEM.
The time is 0:48 UT
Beginning observing sequence
Null query (B) responds with 0
Null query (C) responds with 0
127 127 120 120
Reading a slit frame into trigger memory
B complete
C complete
C complete
B complete
Starting archival standards at observation's start
At 0.00
At C 0.00(0.010) At C(0.010)
At 0.00
At C(0.010) At C(0.010)
At 0.00
At C(0.010) At C(0.010)

```

Figure 11.2: A transcription of the observer-computer interaction during the setup phase of "user" mode, described in section 11.2.1.



algorithm was unable to complete the sifting of a typical frame in the time allotted, because of the large number of pixels passing the first level of sifting (see section 8.3.2.1). The sift time was then increased to allow further decrease in the values of the detection variables until the amount of time left to the Overseer computer for data transfer (data transfer time = exposure time - sift time) was too small and exposure time limits were exceeded when the Overseer computer attempted to collect data from the Trigger processors. It was determined that the present Overseer software requires ~0.6 seconds per flash to acquire data from two Trigger processors. The bulk of actual observations was performed with ten-second integrations, with sift times of four to six seconds. The values of threshold offset and brightened delta were adjusted until the rate of single events from a given camera was between 10 and 20 per exposure. These observation settings assured that >90% of all exposures were "good" (an exposure was considered "good" if the sifting completed with no errors and the Overseer computer had sufficient time to collect all the image data).

### 11.3. Details of Observations with the Test Instrument

The observations with the ETC test instrument were conducted between 24 March and 1 April 1985 and again between 12 May and 28 May, 1985. The observations were made primarily in V-band, with some bright-time observations in R- and I-band. A list of the times and filters of observation can be found in Table 11.3.

Cameras B and C were used in coincidence with a total field overlap of 236 square degrees (after accounting for imaging area lost to CCD defects, pixels disregarded by the Trigger processors, a small degree of misalignment between the cameras and an average of 5% of the imaging area lost to dome

UT date	Filter	Time observed (hours)
24 March 1985	V	2.67
25 March 1985	V	5.17
26 March 1985	V	2.31
27 March 1985	V	3.08
28 March 1985	V	1.18
30 March 1985	R	2.46
31 March 1985	I	3.49
1 April 1985	I	3.36
12 May 1985	R	1.44
13 May 1985	V	3.45
14 May 1985	V	4.75
15 May 1985	V	3.85
18 May 1985	V	3.04
19 May 1985	V	4.26
20 May 1985	V	1.35
21 May 1985	V	1.22
24 May 1985	V	1.77
25 May 1985	V	3.45
26 May 1985	R	3.08
28 May 1985	R	1.34

Table 11.3: Dates and Times Observed with ETC Prototype

occultations). A total of 41.1 hours were observed in V-band, 8.3 hours in R-band and 6.9 hours in I-band. The solid-angle-time product observed, then, was 2.95 steradian-hours in V-band, 0.60 steradian-hours in R-band and 0.50 steradian-hours in I-band.

The choice of fields observed by the ETC test unit was affected in part by the potential for detection of possible sources of optical transients. The declination of the center of each camera was  $+25^{\circ} \pm 2^{\circ}$ ; the right ascensions of the center of the fields observed were within a few minutes  $10^h$ ,  $12^h$ ,  $15^h$  and  $17^h$ . Generally, the fields were chosen to be near the meridian at certain hours of the night, (in order to reduce the effects of occultation by the dome and extinction by the atmosphere) but some effort was made to include potential sources of optical flashes. One of these fields ( $12^h$ ) contained the error circles of three gamma-ray bursters (GRB1200+21 (24 November 1978), GRB1152+20 (1 January 1979) and GRB1140+20 (2 May 1979); Baity, et al., 1984), while another ( $17^h$ ) contained the flare stars V475 Her, Ross 867 and Ross 868 (Gurzadyan, 1980).

Observations were made primarily during dark or grey time (roughly six days on either side of new moon). The sky brightness during bright time was found to be so high that the vignetting of the lens (see section 6.1.1.2) becomes significant. If the sky brightness at the center of the CCD is 200 ADU per pixel (a typical value during bright time), the sky brightness at the edge of the CCD is 140 ADU, due to the 30% vignetting of the lens. Since the Overseer Computer will set the bias level of the CCD to a point where the sky+bias level at the center of the CCD is  $\sim 40$ , a large area near the edge of the CCD will have sky+bias levels less than zero, rendering it useless for observations. Raising the bias level to bring the values of the edge pixels above zero would bring the values of most of the CCD pixels close to the logarithmic section of the linlog mapping, thereby reducing the sensitivity of the CCD as a whole. In addition, the increased sky noise during bright time significantly reduced the overall sensitivity.

#### 11.4. Results of the Observations with the ETC Test Unit

A total of 725 coincident events were reported during the observations with the ETC test unit. These events were categorized by hand, primarily through the analysis of the  $9 \times 9$  pixel image subarrays of the event location from before and during the flash event. The data fell into several categories, based on the event profiles. The event categories are:

- 1) Satellite events: a satellite passing through the field-of-view created the event. A satellite is confirmed by second and third triggers from its trajectory. (see section 11.6 for a further discussion)
- 2) Inconsistent coordinate events: the events in the two cameras were obviously unrelated. This is usually determined by the relative positions of bright objects in the  $9 \times 9$  image subarrays of the event from the detecting cameras.
- 3) Cloud triggers events: the events (always in groups of five or six, because the maximum allowed number of events per observation cycle is six) were due to patchy clouds. These events were recognized a) because of the low number of "good" integrations in that observation cycle and b) from notes made at the time in the observations log.
- 4) Occultation events: the event occurred in a portion of camera which was partially obscured by the dome.
- 5) General brightening events: the event was induced by a sudden increase in the background light level in the CCD, due to such causes as a flashlight in the dome, a passing car with its lights on, or distant lightning.
- 6) Streak events: the image has a streak-like appearance, but no second trigger to

confirm it to be a satellite.

- 7) No trigger events: the data stored show no evidence of an event having occurred. This is currently an unsolved bug in either the Overseer or Trigger software.
- 8) Statistical events: the event was created by statistical variations in the brightness of a corresponding pixels in both detecting cameras.

A breakdown of the frequency of these types of event is given in Table 11.4, based on 16,700 exposures taken during the test observations.

#### 11.4.1. Statistical Events

After the events of types 1-7 had been identified in the ETC data bank, a total of 355 statistical events remained. These events are subclassified into four groups, based on their morphology:

- 1) Class I events occurred when the brightest pixel in a stellar image brightened in both detecting cameras.
- 2) Class II events occurred when the brightest pixel of a stellar image brightened in one detecting camera while an immediate neighbor pixel brightened in the other.
- 3) Class III events occurred when a pixel neighboring the brightest pixel of a stellar image brightened in both cameras.
- 4) Class IV events occurred when background pixels brightened in both cameras, or when a pixel near, but not immediately neighboring a very bright star triggered in both cameras.

Most of these events barely exceeded the event thresholds, and all but a few of these events showed no appreciable light curve in both cameras. Because of the high CCD readout noise (50-70 e<sup>-</sup>/pixel), it is probable that most, if not all of these events were caused by statistical fluctuations in the CCDs. The

Type of event	Number detected	% of total	Number/exposure
Satellite	159	21.9	0.0095
Inconsistent coordinates	34	4.7	0.0020
Cloud trigger	110	15.2	0.0066
Occultation	5	0.7	0.0003
General brightening	13	1.8	0.0008
Streak	17	2.3	0.0010
No trigger	14	1.9	0.0008
Statistical Class I	194	26.8	0.0116
Statistical Class II	46	6.3	0.0028
Statistical Class III	92	12.7	0.0055
Statistical Class IV	43	5.9	0.0026
Total	725	100.0	0.0434

Table 11.4: Breakdown of Events Detected by the ETC Test Unit

rate of these events (355 events in 16,700 exposures, or  $\sim .021$  events per exposure) are shown below to be comparable to the expected rate of correlated events due to statistical fluctuations in the CCD. The calculation of the expected false event rate is based on the fact that the ETC software does not detect sudden brightenings of image pixels, per se, but rather large differences in the value of image pixels from one image to the next.

#### 11.4.1.1. The Difference-Sensitivity of the ETC

When discussing the statistics of an ETC event, one must take into account that the ETC instrument is not level-sensitive, but *difference*-sensitive. The ETC is not an instrument monitoring a sky of static brightness levels with a noiseless CCD, waiting for a part of the sky to increase its brightness by more than a certain amount in a single exposure time; rather, the ETC is monitoring a sky where the brightness levels vary from frame to frame due to shot noise and readout noise, waiting for the *difference* between two frames to exceed a certain amount in a single exposure time. The difference-sensitivity of the ETC has significant implications for the sensitivity and expected statistical trigger rate of the ETC.

The first implication of the ETC's difference-sensitivity is the fact that the event sensitivity is lower than the sensitivity of a camera to the detection of a stellar image by a factor of  $\sim \sqrt{2}$ , as briefly mentioned in chapter 4. This is due to the fact that the readout and shot noises must be taken into account twice in the calculation of the total noise associated with an event, because two frames are involved in the event detection. The equation giving the level of significance,  $q$ , of a detected event is

$$q = \frac{S_{\text{after}} - S_{\text{before}}}{(S_{\text{before}} + S_{\text{after}} + 2\sigma_R^2)^{1/2}},$$

where  $S_{\text{before}}$  and  $S_{\text{after}}$  are the total signal above the bias level (in electrons) in a given pixel in two consecutive images. Substituting  $S_{\text{after}} = S_{\text{before}} + \Delta S$ , where  $\Delta S$  is the amount of brightening in the event, one gets

$$q = \frac{\Delta S}{(2(S_{\text{before}} + \sigma_R^2) + \Delta S)^{1/2}} \quad (11.1)$$

The second and more important implication of the ETC's difference-sensitivity is that the significance of a detected event is not simply that determined by Gaussian statistics: that is, an event that showed a brightening corresponding to a statistical significance of  $N\sigma$ , where  $\sigma$  is the total noise (the denominator of equation 11.1), cannot be assigned a confidence level associated with the Gaussian probability of an  $N\sigma$  event occurring randomly. The problem, again, is the fact that the ETC detects an event when the value of a pixel increases by a certain value from one exposure to the next. This means that an  $N\sigma$  event can be created if, for example, the pre-event pixel value is  $N\sigma/2$  below the mean value and the event pixel is  $N\sigma/2$  above the mean value. The probability of this situation occurring randomly is  $(p_G(N/2))^2$  (where  $p_G(x)$  is the probability of an event of  $>x\sigma$  occurring according to Gaussian statistics), which is significantly greater than  $p_G(N)$  for most values of  $N$ . In assigning a confidence level to an event, one must therefore not use the Gaussian probability function  $p_G(x)$ , but rather the probability function  $p_\Delta(x)$ , which is defined as

$$p_\Delta(x) = \int_{-\infty}^{\infty} \text{prob}(<y) \text{prob}(>(x+y)) dy$$

where  $\text{prob}(<y)$  is the Gaussian probability of an event being less than  $y\sigma$  (including the probability of an event being below average) and  $\text{prob}(>(x+y))$  is the Gaussian probability of an event being greater than  $(x+y)\sigma$ . The function  $p_\Delta(x)$  gives the probability that the difference between a pixel's value in consecutive images will have a significance greater than  $x\sigma$ . The value of  $p_\Delta(x)$  exceeds the value of  $p_G(x)$  significantly for more values of  $x$ , as can be seen in Figure 11.3.

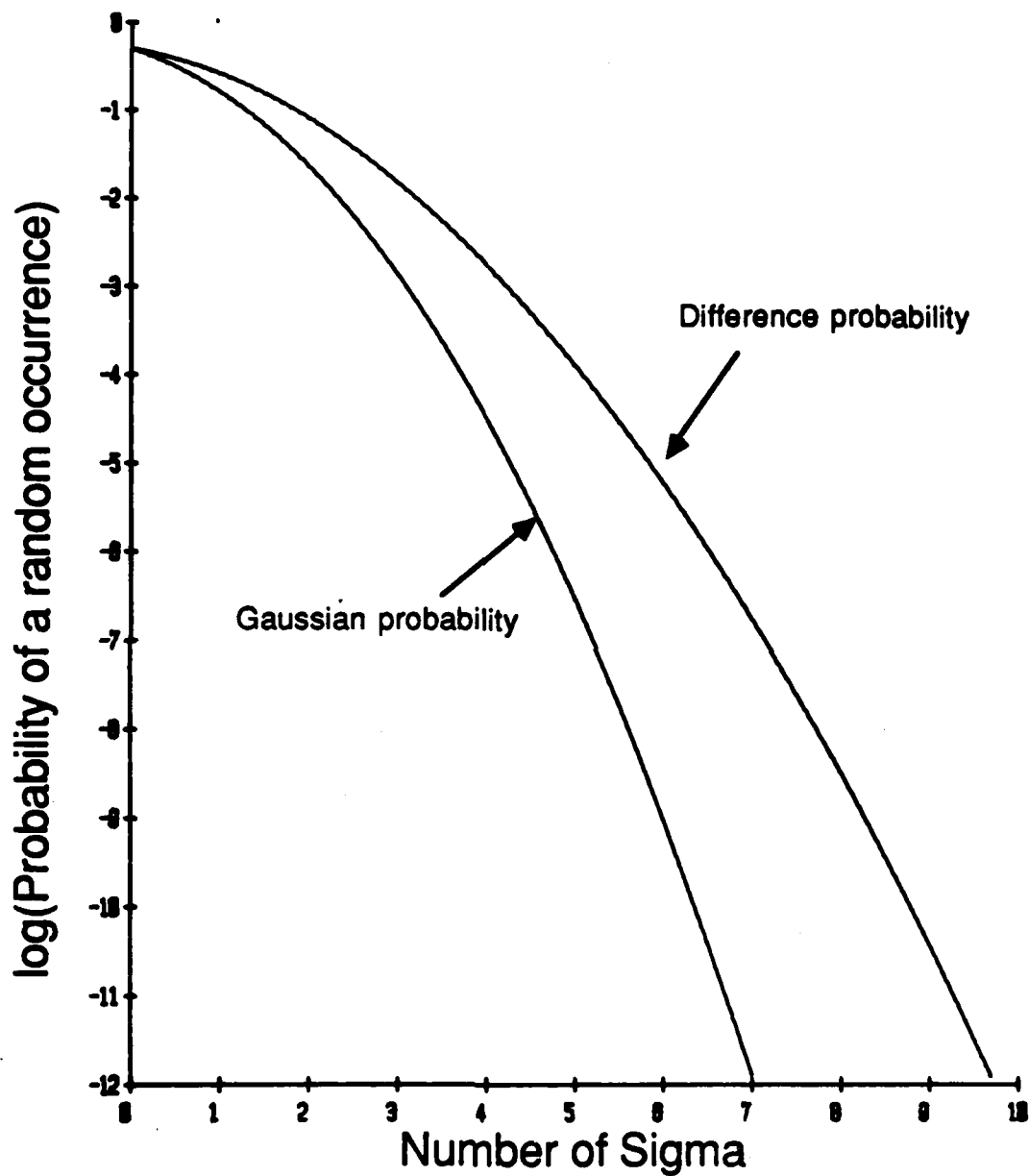


Figure 11.3: The relative probability of a random event in the ETC. The curve marked "Gaussian probability" indicates the probability of a pixel value being  $N$  sigma above its mean value. The curve marked "Difference probability" indicates the probability of the difference in the value of a pixel in two consecutive measurements being greater than  $N$  sigma (see section 11.4.1.1).

#### 11.4.1.2. Calculation of the expected statistical event rate

The expected rate of false ETC events due to Gaussian variations of the values of image pixels can be estimated, given the function  $p_{\Delta}(x)$  and the distribution of the pixel values in a typical ETC image. The distribution of pixel values in a CCD image can be divided into three populations, each with a different rate of statistical brightening. The pixels with values between a few ADU above the median of all pixel values in an image and  $\sim 140$  ADU are parts of stellar images and, because of their larger shot noise, are more likely to create a statistical event than pixels with values near the median value. However, 90% of the image pixels have values within 5 ADU of the median, so the net rate of statistical events from these two populations is balanced somewhat. (Empirically, it was determined that the majority of statistical events occurred near stellar images; cf. Table 11.4). Those pixels with values greater than 150 are in the range of pixel values where each step is logarithmic, and therefore significantly larger than those in the linear range: statistical events with values greater than 150 are therefore very rare.

The expected rate of events was calculated with a computer program which, using a full ETC frame from either camera, calculates the probability of detecting a correlated event in the two cameras, based on the values of the total noise and the detection threshold in each camera. The program reads the values of the image pixels in order, calculating for each the total noise,  $\sigma$ , (based on twice the signal shot noise and readout noise) in both cameras (after converting the pixel value in the one camera to the equivalent value in the other camera by multiplying by the ratio of the camera gains). From the ratio of the detection threshold value to the total noise in a pixel the probability of a random fluctuation in that pixel leading to an event in a single camera is calculated, using the  $p_{\Delta}(x)$  function described above. The probability of a correlated event due to random fluctuations is just the product of the two single-camera probabilities. The probability is calculated for all pixels and summed to give the probability of statistical triggers per exposure.

A direct comparison of the results of this computer analysis with the observed rate of correlated events is complicated for several reasons. First, the observations were made under many different sky conditions (dark time, grey time, bright time) and at various values of detection thresholds in both cameras (typical values were 7 ADU in camera B and 6 or 7 ADU in camera C). Those observations made under bright sky conditions (partial moon) suffer from a higher sky noise and therefore would be expected to have a higher rate of statistical events. Observations made under brightening sky conditions (during sun- or moonrise) are also expected to have a higher event rate because the sky brightness is increasing slowly during observations, thereby increasing the fraction of pixels able to pass Level 1 of sifting (see chapter 8 and below).

In addition, the rate of statistical events from pixels with values near the median value is significantly reduced by the fact that there is a probability of  $\sim 50\%$  that the pre-event pixel value is below its mean value, in which case a typical brightening will not pass Level 1 of sifting.

Nonetheless, in order to show that statistical fluctuations are sufficient to account for the rate of correlated events observed in the prototype ETC, the program described above was run with a dark-time image with both detection thresholds set at 7 ADU (so that a  $\Delta S \geq 8$  ADU will trigger - a typical situation during test observations). The rate of correlated events based on camera B and converting to camera C was .063 per exposure and the rate based on camera C was .048 per exposure, averaging to .05 per exposure. Taking into account that about half of the pixels with values near the median value will not trigger because they are not able to pass Level 1 of sifting (as discussed above) reduces the expected event rate by  $\sim 20\%$ , to 0.045 events per exposure. This is more than sufficient to account for the bulk of the 355 "statistical", "stellar" and "other" events, which occurred at a rate of  $\sim 0.02$  events/exposure.

A final complication of this analysis process is that the Overseer software allowed fluctuations to be considered a correlated event even if the celestial coordinates differed by up to two pixels. This means that a pixel in one camera can trigger not only with its direct counterpart in the other camera, but also with neighbors of the counterpart. The program described above was modified to deliver the probability of a correlated flare with the nine nearest pixels in the other camera: the result was an

increase in the expected event rate by a factor of 2-3. Because the actual software allowed correlated events to occur not from the nearest nine pixels, but rather from an area of  $<2\pi$  pixels, the actual effect is more modest. The expected increase in event rate is  $\sim 75\%$ , raising the expected rate to  $\sim 0.08$  events per exposure.

#### 11.4.2. Satellite Detections by the ETC Test Unit

The high frequency of detection of satellites by the ETC was somewhat surprising. It had been assumed that low-Earth-orbit satellites would be moving too fast to be accepted as ETC events, due to the fact that their long trails on the CCD would be noticed by the Trigger processor streak-rejection algorithm (section 8.3.2.5). Generally, the detected satellite trails were indeed long enough to have tripped the streak rejection algorithm, yet none of the perimeter pixels had brightened sufficiently. This may be attributable to statistical fluctuations in the perimeter pixels. Indeed, the bulk of the satellite trail across the CCD very likely was rejected as a streak; only those few images of the satellite trail where the perimeter pixel was lower than it should have been due to statistical fluctuations escaped rejection. (A typical satellite triggered the ETC an average of six times during its traversal of a field: during this time, roughly 200 exposures were made of the field).

A total of 29 satellite trails were detected by the ETC during prototype observations. The satellites were divided into those with a roughly east-west trajectory and those with trajectories making an angle of roughly  $60^\circ$  with east-west. Judging by the times of detection and angles of the paths of some of the trails, several trails may have been made by the same satellite. Data from two typical satellite detections are shown in Figure 11.4.

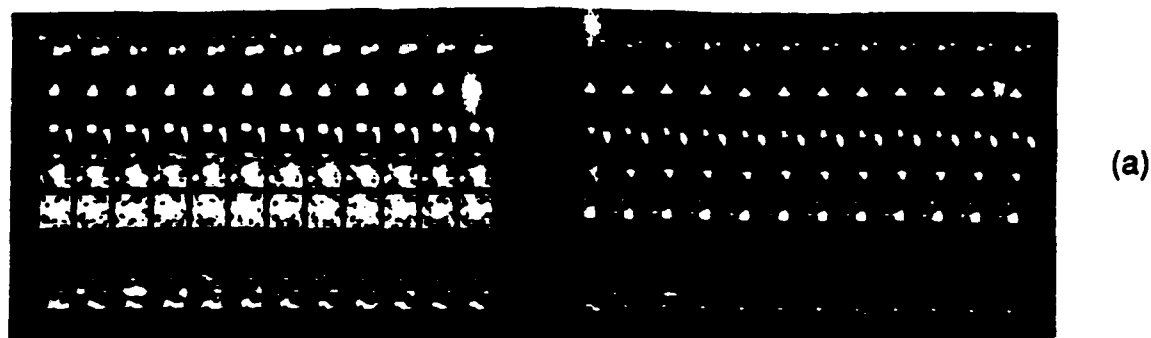
The satellite trails detected were made by satellites of visual magnitudes from 6 to 9. The angular speeds of the satellites at the time of detection were consistent with circular orbital periods of 4 to 12 hours: it should be noted, however, that no estimate of the orbital eccentricity was made from these detections, so that estimates of orbital periods are uncertain.

The rate of expected satellite events ( $\sim 0.01$  per ten-second exposure) will pose a problem for the plenary ETC, since the associated event rate is very large compared to celestial event rates. (The rate is one event per 15 minutes, on the average, but the events are clumped in groups and trigger at a rate of one event per one or two minutes in these groups). One solution is to lower the streak-rejection criterion from 7 to 5 pixels (cf. section 8.3.2.5): this criterion would have rejected a significant number of the satellites detected during the observations with the test instrument. Another possible means of rejecting satellite events is for the Overseer computer to monitor the coordinates of reported events: if any three are shown to be collinear, they would be considered having been due to a satellite crossing the field.

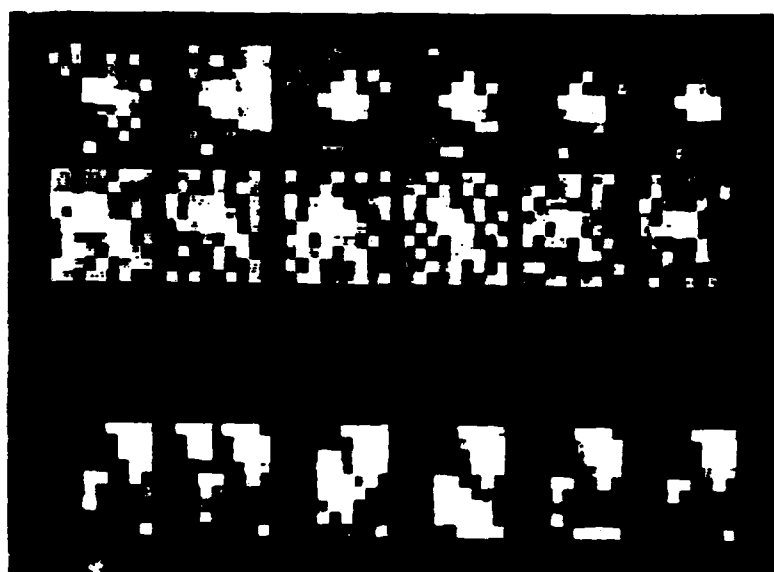
#### 11.5. Interpretation of Results

The observations with the ETC test instrument yielded no optical flashes which could not be explained by local, terrestrial or statistical sources of optical transient events. The total solid-angle-time product observed by the ETC in the visual band is 2.9 steradian-hours. Given the ten-second sensitivity of the ETC test unit to detected events ( $m_v = 9.9$ : a  $10\sigma$  criterion), the test observations were expected to have detected 1.5 flare stars and 0.008 optical transients from GRB sources (see Figure 11.5). The test results define a  $3\sigma$  Poisson upper limit of 2.2 optical flashes per hour per steradian at  $m_v = 10$  (Gehrels, 1985). This result is superimposed on the graph in Figure 11.5.

The results of the observations with the ETC test unit have no significant impact on differentiating between the models of optical transient events described in Chapter 3. However, the observations made with the ETC test unit make up by far the most substantial wide-field survey of the night sky for short-timescale optical transients. The  $3\sigma$  Poisson upper limit of  $<2.2$  flashes per hour per steradian is an order of magnitude lower than the  $3\sigma$  upper limit of  $<22$  flashes per hour per steradian determined by the previous best effort of Schaefer, Vanderspek, Bradt and Ricker (1984). It should be noted that this upper limit result was determined with *one-sixteenth of the plenary ETC in five weeks of observation!* The results achievable by the plenary ETC in one year of observation should be a factor



(a)



(b)

**Figure 11.4:** Two views of ETC data collected during March and May, 1985. Figure 11.4a is a display of all image data collected after the detection of an optical flash event. The data displayed are 9x9 pixel image subarrays about the locations of the flash event and five SAO standard stars in each camera. In Figure 11.4a, the left-hand six rows contain data from camera B and the right-hand six rows contain image data from camera C. Of each set of six rows, the upper five rows contain images of SAO standard stars and the lowest row, set apart from the others, contains data from the flash location. The images are order chronologically from the left. The far left column contains the 'old' images, taken at the beginning of the observation cycle. The next column contains the 'recent' images, taken immediately before the detection of the event. The remaining columns contain data taken at and after the flashevent. All exposure times are ten seconds. Figure 11.4a shows the detection of an east-west-moving satellite; Figure 11.4b, a close-up of another set of flash data, shows the detection of a satellite withan inclination of ~60 degrees. Both satellites are of roughly 6th to 8th magnitude.



of 160 better than the results presented here, and a factor of 1600 better than the efforts of Schaefer, Vanderspek, Bradt and Ricker (1984)!.

The observations with the test unit indicate that the flash background rate (the rate of flashes from non-cosmic sources) is dominated by satellite events. The plenary ETC, with its capability of recognizing a satellite by its trail across a CCD as well as by the use of parallax, will be able to reduce significantly the event rate due to satellites. The detection of these satellites indicates that the events detected by Pedersen, et al. (1985), may have been created by a satellite. The angular speed of a typical satellite (detected by the ETC) is  $\sim 70''/\text{second}$ . The longest dimension of the photometer aperture used by Pedersen was  $\sim 80''$ : therefore, optical events with durations less than 1.2 seconds could be created in Pedersen's photometer by the passage of a typical satellite.

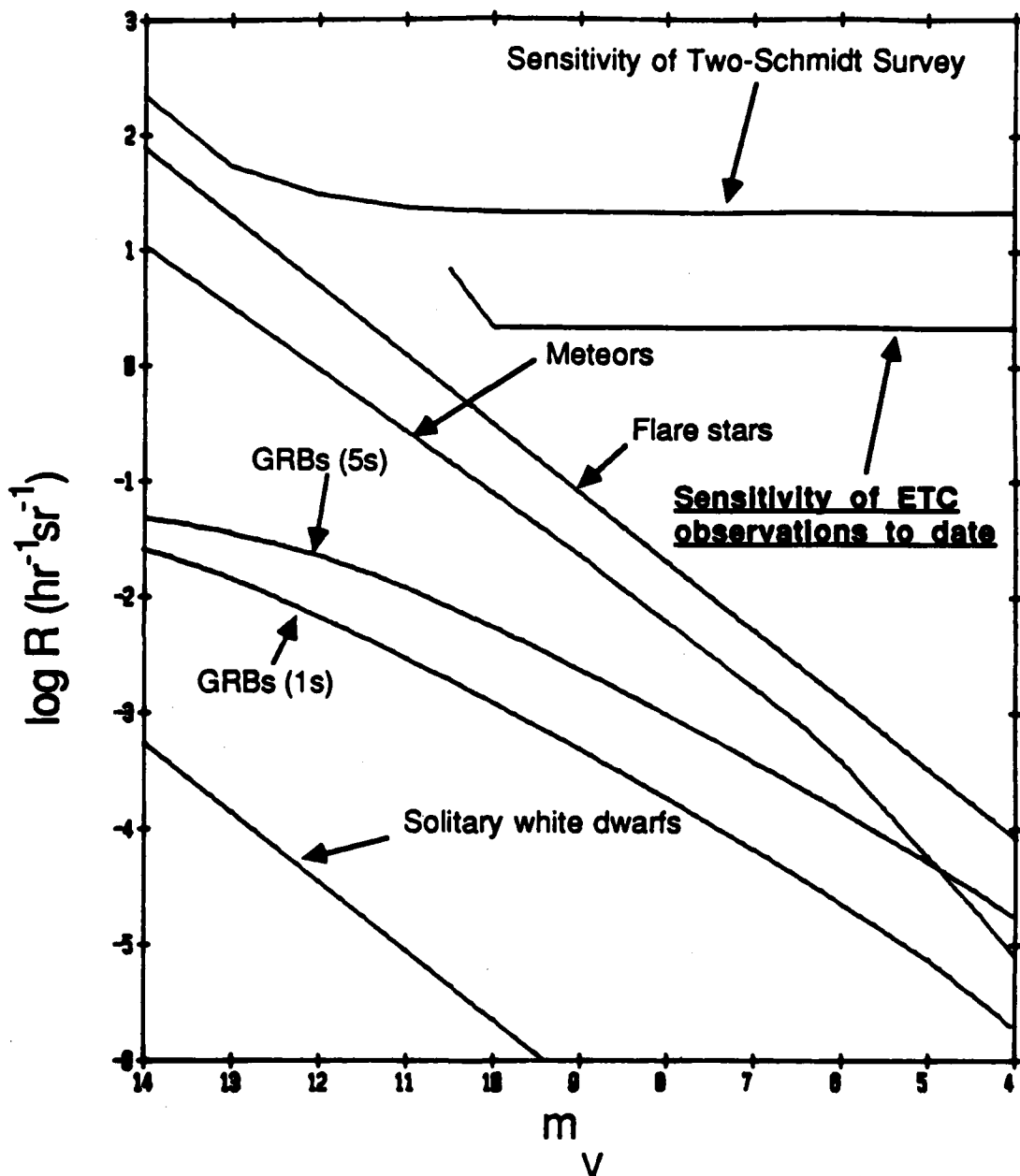


**Figure 11.5:** The expected rates of optical flashes in ten-second exposures in the ETC test unit. The curves represent the expected event rates due to GRBs (section 10.1), flare stars (section 10.2), comet impacts onto white dwarfs (section 10.3), and head-on meteors (section 10.4.1) and the upper limit on the event rate due to cosmic rays. The three-sigma Poisson sensitivity of ETC observations to date are indicated, as well as the sensitivity of the Two-Schmidt survey, conducted by Schaefer, Vanderspek, Bradt and Ricker (1984).

## CHAPTER 12

### Future Work

#### Introduction

Although the four-camera ETC test instrument was able to operate successfully in a semi-automatic mode during the test phase, there are a number of weak links in the ETC instrumentation. These weak links must be corrected before the ETC can be expected to operate for long periods without an observer on site. The general problem with the ETC instrumentation is that several of its components are not reliable: under certain situations, the state of the instrument hardware cannot always be consistently predicted. Plans for the correction of the problems. In addition, the weak spots in the ETC software, which all center around its operational speed, will be mentioned.

#### 12.1. General Plans for the Improvement of the ETC

The observations made with the ETC test instrument revealed several areas for general improvement in the ETC. These improvements include:

- 1) The Overseer computer disk memory will be upgraded by at least 20 Mbytes to allow for more disk data storage, so that the interval between successive data storage onto magnetic tape is longer.
- 2) The Overseer computer core memory will be upgraded to at least 2 Mbytes to increase the speed of the Overseer software.
- 3) A Cipher Floppy Tape unit will be introduced as the medium for mass data storage. The Floppy Tape unit stores data onto standard 1/2" cartridge tapes.
- 4) The Trigger processors will be replaced by Heurikon HK68 single-board microcomputers with built-in DMA. The Heurikon board will include 1 Mbyte of hard memory to allow for substantial data storage in the Trigger processors.
- 5) The HSSL will be replaced by a new, more reliable fiber-optic link.
- 6) The ETC CCD cameras will be replaced by thermoelectrically-cooled CCD cameras designed by Gerard Luppino of MIT. The use of these cameras will eliminate the problem of the bulky coolant hose associated with the closed-cycle refrigerator. In addition, since each camera is cooled individually, a single camera can be warmed and brought to atmospheric pressure without affecting the operation of the other CCD cameras. In addition, the preamplifiers, which had been housed inside the CCD cameras, will be moved outside of the CCD housing, removing both a source of heat and a source of noise from inside the CCD housing.
- 7) The ETC CCD cameras will be outfitted with new, better lenses. These custom-built lenses will allow one- or two-pixel focus over a broad band (3000 Å) of wavelengths, which will significantly improve the signal-to-noise performance of

the ETC.

The following sections will discuss specific problems encountered during the test phase of the ETC instrument.

## 12.2. The ETC Electronics

The majority of the problems with the ETC electronics are related to reliability. Specifically,

- 1) Some parts of the Instrument Control Electronics, which are located in the second floor of the ETC dome, tend to stop working correctly when the ambient temperature drops below  $-0^{\circ}\text{C}$ . The symptoms indicate that the problems are not construction-related (e.g., a cold solder joint on a circuit board), but rather are related to design flaws or the choice of chips used in the boards. The intermittent nature of these problems has hindered their exact localization to date.
- 2) The High Speed Serial Link (HSSL) receivers in the Trigger processors occasionally lose data. This problem is due to improper ground return wiring of the receiver chips in the HSSL receiver. Although the rate of data loss has been reduced (less than .1% of all frames are affected, and the presence of the problem is always apparent), it still should be eliminated completely.
- 3) One of the Digital-to-Analog converter (DAC) boards has a tendency to drop out of operation altogether every few weeks. This problem has not yet been definitively located, but the application of pressure on one or more chips on the board generally solves the problem. This problem is most likely due to the use of a prototype construction technique in fabricating the DAC boards, a method which has occasionally resulted in reliability problems in the past.
- 4) The ICE in general have a problem with the loss of static-sensitive CMOS chips because of electrostatic discharges. Although the loss rate due to static electricity is low, it must be reduced to zero in the plenary ETC.

The solutions to these problems which have been proposed to date are:

- 1) Put the ICE in a warm place. The locations of the sources of the problems of cold-sensitivity to date have not yet been found. Even if they were, the problem could occur in other locations in the ICE. The best solution is to create a warm area in the dome for the ICE.
- 2) The problems with the HSSL receivers is not so severe as to warrant major revisions of its construction. However, the new fiber-optic HSSL should eliminate all the problems associated with the present HSSL.
- 3) Recently, printed-circuit DAC boards were constructed for use at MIT. These boards do not have the problem of loose sockets and should prove to be error-free in use in the ETC.
- 4) Much effort must be yet put into static protection of the ICE. The carpeting in the second floor of the ETC dome must be covered with static-free matting to guard against accidental static discharges to the electronics.

In addition to the above reliability problems, two specific aspects of the ETC electronics should be improved. First, the effective CCD readout noise is higher than specified for the CCDs. This increased noise is due to improper "tuning" of the CCD analog electronics. Future ETC CCD camera systems should be thoroughly "tuned" before they are sent out into the field. The latest generation of CCD electronics has a much better noise performance than the present ETC cameras: system noises of less than 20 e<sup>-</sup> with good charge transfer efficiency are being achieved regularly.

Second, the dome encoding scheme should be improved. Presently, it is a relative encoder, with no absolute zero point. This situation makes it necessary to rotate the dome to a specific position regularly in order to zero the encoder. This problem will be corrected in the Fall of 1985 by encoding the dome absolutely.

### 12.3. The ETC Instrument Mechanical Hardware

The current ETC mechanical hardware also has a number of problems which will hamper progress towards automation. The major problems are:

- 1) The vacuum cavity which is shared by the four ETC cameras and the manifold is not leak-free. The system maintains a good vacuum (with the closed-cycle refrigerator on) for ten days to two weeks at a time, but then can spontaneously return to near atmospheric pressure with little warning. Evidently, the cooling probe acts as a cryopump when cold, adsorbing molecules leaked into the system onto its surface. When the surface of the cooler is saturated, the pressure increases slowly due to a leak in the system, until the ion pump shuts off, resulting in a rapid pressure rise.
- 2) The telescope mount is misbalanced, primarily due to the weight of the coolant hose wrapped around the axis of the manifold. The result is that it is very difficult to slew the telescope mount at hour angles of more than ~3 hours.

Proposed solutions to these problems are:

- 1) A new camera/manifold system will be used in future ETC cameras. The present system relies heavily on rubber O-rings between flat aluminum faces. The improved system will utilize steel knife-edge vacuum interfaces with rubber gaskets, so the vacuum integrity of the system will be much improved.
- 2) The cooling system in future ETC cameras will not require stiff cooling hoses. The new cameras, designed by Gerard Luppino, are cooled by thermoelectric coolers and will not impede the slewing of the mount. Without the coolant hose, which tended to accumulate ice when cold, balancing the telescope will also not be as difficult a problem as it is now.

Another advantage to the new ETC camera/manifold design is that access to the camera interiors will be much simpler than it is now. The method of cooling individual cameras will allow one camera to be taken off line without warming the others.

### 12.4. ETC Software

The main problem with the ETC software is that it is not fast enough to support one- to three-second integration times. There are several bottlenecks in the software which slow it down substantially:

- 1) Whenever a candidate report is received by the Overseer computer, the location of

the event is converted into its celestial coordinates. The conversion of event location to celestial coordinates involves calculating of  $\sim 10$  trigonometric functions, with each function requiring 10 milliseconds. Thus, each candidate report requires  $\sim 0.1$  seconds to be fielded.

- 2) The transfer of event image data between the Trigger processors and the Overseer computer takes  $\sim 0.6$  seconds per flash event per exposure.

The next revision of the ETC software will transfer more of the computational burden from the Overseer computer to the Trigger processors, which should improve overall system speed. Specifically,

- 1) Each Trigger processor will be given the parameters of the astrometric mapping of its associated camera, so that it may calculate the celestial coordinates of each candidate event itself. In this way, the Overseer computer will act as a book-keeper of candidate events, and not as a calculator. In addition, the coordinates will be calculated in the form of three-vectors, which avoids the calculation of slow trigonometric functions.
- 2) Each Trigger processor will store image data in its own memory structure during observations. At the end of an observation cycle, each Trigger processor can then transfer its image data to the Overseer computer without time pressures.

Some general areas for the improvement of the ETC software are:

- 1) The sifting algorithms do not reject signal fluctuations in bright stars. Some method of recognizing the higher shot noise in bright stars must be devised.
- 2) The criteria for coincidence of celestial coordinates must be tighter than in the test observations, in order to reduce the rate of statistical false triggers.
- 3) The calculation of the precise celestial coordinates of the center of each CCD, presently observer-aided in "user" mode (see Chapter 11), must be made automatic. A field-finding algorithm, used by the third Small Astronomical Satellite (SAS-3), will be altered for use in the ETC.

## CHAPTER 13

### Acknowledgements

The number of people who were involved in getting the ETC test instrument working is large. The ETC test instrument is intricate and complex, and without the help of these people, the test unit could easily have incurred delays of a year or more. The people primarily responsible for the successful construction of the ETC test unit are John Vallerger, Gerard Luppino, George Ricker and John Doty.

George Ricker, as my advisor, was responsible for the development of the concept and realization of the ETC. His choice of me to design and construct the test ETC was, for me, an excellent one, as it allowed me to develop as an experimental and observational astrophysicist in addition to working on one of the most exciting astronomical projects of the decade. George's experience in observational astronomy and his training of me have stood me in good stead during the construction of the ETC. George also provided useful suggestions and guidance during the writing and implementation of the Overseer software.

John Doty's contributions to the ETC were in many ways more subtle. The bulk of the CCD electronics, the concept of the Overseer computer and the HSSL were all his brainchild, and the refinement of these aspects of the ETC is being assisted by him. The concept of how the Trigger software should work was also developed by John Doty. His further contributions have been in the form of streamlining the Trigger and Overseer software: the five days he spent at the ETC site at Kitt Peak should be counted as some of the most critical time spent with the ETC by anyone, since he used the time to remove an intricate system problem that would have made efficient execution of the ETC software very difficult.

John Vallerger and Gerry Luppino were indescribably helpful in teaching me how to build an instrument. With their guidance, many mistakes in the construction and testing of the ETC electronics were avoided or caught before they became critical. In addition, their ongoing efforts to improve the CCD electronics proved very useful for the ETC ICE, which was developed in parallel with their efforts.

In addition to the above four, several undergraduates at MIT have made significant contributions to the ETC instrument. Steven Rosenthal was responsible for the development and implementation of the DMA/HSSL transmitter/receiver boards (with Charles Kimball working some on the ICE HSSL transmitter). Steve also wrote and tested the Trigger software as his senior thesis.

Duane Thresher was the primary builder and tester of the ETC's clock driver generation and analog processing boards. His knowledge, patience, good humor and invariable presence at odd hours made the construction of the ETC much more bearable.

Howard Stearns developed and built the ETC frame timer and the Trigger hardware reset. His hardware implementations and Overseer driver code changes have worked almost flawlessly.

George Mitsuoka was significant in contributions to the writing of several drivers, not least noticeably the HSSL driver. Erica Ellingson wrote her senior thesis on the ETC optical system and the effects of cosmic rays on ETC observations.

Kip Dee Kuntz's efforts to observe with an underdeveloped ETC in December, 1984, are noted with admiration and gratitude. His presence at Kitt Peak will be remembered by many.

Among the "cast of thousands" of undergraduates at MIT who worked on the ETC as UROP students in a sometimes more, sometimes less effective way were Anna Franco, Carlos Montero-Luque, Nancy Ellman and Geoff Engelstein.

Several non-MIT persons were deeply involved in the ETC project. Dr. Frank Melsheimer of DFM Engineering, Inc., was the primary designer of the ETC camera/manifold system and the interface with the MFC-100 cooler. Cindy Reiter and Doug Fraser of FTS Systems, Inc., were very helpful in the selection and testing of the MFC-100 cooler for the ETC test unit.

I would also like to thank Sidney Wolff, Buddy Powell, Bob Barnes, Dick Doane, John Settlemyre, John Africano and the TA support staff at KPNO for their patience and help during the construction of the ETC.

I would also like to thank Cheryl Simmons and Dan Calileo of MIT's Center for Space Research for their patience and guidance in the management of the ETC budget.

I thank Claude Canizares and Paul Joss for a careful reading of this thesis and a bloodless thesis defense. Saul Rappaport also provided useful comments and suggested the Monte Carlo approach to the flare star calculations.

Finally, I'd like to thank the countless people who supported the ETC effort, and my family and friends for supporting me as a person during the sometimes very trying moments during the construction and testing of the ETC.



## References

- Allen, C.W. 1976, "Astrophysical Quantities", London, The Athlone Press.
- Apparao, K.M.V and Allen, D. 1982, *Astron. Astrophys.* 107, L5.
- Baity, W.A., Hueter, G.J. and Lingenfelter, R.E. 1984, in "High Energy Transients in Astrophysics", ed. S.E. Woosley (AIP Conf. Proc. No. 115; New York, AIP), 434.
- Bronshten, V.A. 1983, "The Physics of Meteoric Phenomena", Boston, D. Reidel Pub. Co.
- Chevalier, C., Ilovaisky, S.A., Motch, C., Barat, C., Hurley, K., Niel, M., Vedrenne, G., Laros, J.G., Doyle Evans, W., Fenimore, E.E., Klebesadel, R.W., Estulin, I.V., and Zenchenko, V.M. 1981, *Astron. Astrophys.* 100, L1.
- Cline, T.L. 1982, in "Gamma Ray Transients and Related Astrophysical Phenomena", eds. Lingenfelter, R.E., Worrall, D.M., and Hudson, H.S., (AIP Conf. Proc. No. 77; New York, AIP), 17.
- Cline, T.L. 1983, in *Proceedings of Tenth Texas Symposium on Relativistic Astrophysics*.
- Colgate, S.A., and Petschek, A.G. 1981, *Ap. J.* 248, 771.
- Cook, A.F., Week, C., Williams, J.T., and O'Mongain, E. 1980, *Mon. Not. R. Astr. Soc.* 193, 645.
- Fishman, G.J., Duthie, J.G. and Dufour, R.J. 1981, *Astrophys. Space Sci.* 75, 135.
- Fryxell, B.A., and Woosley, S.E. 1982, *Ap. J.* 258, 733.
- Golenetskii, S.V., and Ilyinskii, V.N., Mazets, E.P. 1984, *Nature* 307, 41.
- Gurzadyan, G.A. 1980, "Flare Stars", Pergamon Press.
- Gehrels, N. 1985, preprint.
- Harwit, M. and Salpeter, E.E. 1973, *Ap. J.* 186, L37.
- Hawkins and Upton. 1958, *Ap. J.* 128, 727.
- Helfand, D.J., and Long, K.S. 1979, *Nature* 282, 589.
- Hertzsprung, E. 1927, *Harvard Bull.* No. 845, 3.
- Hills, J.G. 1981, *Astron. J.* 86, 1730.
- Hills, J.G. 1983, *Ap. J.* 267, 322.
- Hjellming, R.M., and Ewald, S.P. 1981, *Ap. J.*, 246, L137.
- Hurley, K. 1982, in "Gamma Ray Transients and Related Astrophysical Phenomena", eds. Lingenfelter, R.E., Worrall, D.M., and Hudson, H.S., (AIP Conf. Proc. No. 77; New York, AIP), 85.
- Hurley, K. 1983, *Adv. Space Res.*, Vol. 3, No. 4, 163.
- Jennings, M.C., and White, R.S. 1980, *Ap. J.*, 238, 110.
- Jennings, M.C. 1982, *Ap. J.* 258, 110.

- Jennings, M.C. 1985, *Ap. J.* 295, 51.
- Joss, P.C., and Rappaport, S. 1984, in "High Energy Transients in Astrophysics", ed. S.E. Woosley (AIP Conf. Proc. No. 115; New York, AIP), 555.
- Katz, J.I. 1982, *Ap. J.* 260, 371.
- Katz, J.I. 1984, in "High Energy Transients in Astrophysics", ed. S.E. Woosley (AIP Conf. Proc. No. 115; New York, AIP), 65.
- Katz, J.I. 1985, *Astrophys. Letters*, 24, 183.
- Klebesadel, R.W., Strong, I.B., and Olson, R.A. 1973, *Ap. J.* 182, L85.
- Klebesadel, R.W., Fenimore, E.E., Laros, J.G. and Terrell, J. 1982 in "Gamma Ray Transients and Related Astrophysical Phenomena", eds. Lingenfelter, R.E., Worrall, D.M., and Hudson, H.S., (AIP Conf. Proc. No. 77; New York, AIP), 1.
- Klemola, A.R. 1983, *Pub. A.S.P.* 95, 241.
- Lamb, D.Q. 1984, in "High Energy Transients in Astrophysics", ed. S.E. Woosley (AIP Conf. Proc. No. 115; New York, AIP), 512.
- Laros, J.G., Evans, W.D., Fenimore, E.E., Klebesadel, R.W., Barat, C., Hurley, K., Niel, M., Vedrenne, G., Estulin, I.V., Zenchenko, V.M., and Mersov, G.A. 1981, *Ap. J.* 245, L63.
- Liang, E.P. 1984a, in "High Energy Transients in Astrophysics", ed. S.E. Woosley (AIP Conf. Proc. No. 115; New York, AIP), 77.
- Liang, E.P. 1984b, in "High Energy Transients in Astrophysics", ed. S.E. Woosley (AIP Conf. Proc. No. 115; New York, AIP), 597.
- Lipunov, V.M., Moskalenko, E.I., and Shakura, N.I. 1982, *Astrophys. Sp. Sci.* 85, 459.
- London, R.A., and Cominsky, L.R. 1983, *Ap. J.* 275, L59.
- Mazets, E.P., Golenetskii, S.V., and Gur'yan, Yu.A. 1979a, *Sov. Astron. Lett.* 5(6), 343.
- Mazets, E.P. 1979b, *Nature* 282, 587.
- Mazets, E.P., Golenetskii, S.V., Ilyinskii, V.N., Panov, V.N., Aptekar, R.L., Guryan, Yu.A., Proskura, M.P., Sokolov, I.A., Sokolova, Z.Ya., Kharitonova, T.V., Dyatchkov, A.V. and Khavenson, N.G. 1981, *Astrophys. Space Sci.* 80, 3.
- Mitrofanov, I.G. 1984, *Astrophys. Space Sci.* 105, 245.
- Moffett, T.J. 1974, *Ap. J. Suppl.* 273, 29, 1.
- Nautical Almanac, 1984, U.S. Naval Observatory.
- Newman, M.J. and Cox, A.N. 1980, *Ap. J.*, 242, 319.
- Oepik, E.J. 1958, "The Physics of Meteor Flight in the Atmosphere", New York, Interscience

## Publishers.

- Pacini, F. and Ruderman, M. 1974, *Nature* 251, 399.
- Pedersen, H., Motch, C., Tarengi, M., Danziger, J., Pizzichini, G., Lewin, W.H.G. 1983, *Ap. J.* 270, L43.
- Pedersen, H., Danziger, J., Hurley, K., Pizzichini, G., Motch, C., Illovaisky, S., Gradmann, N., Brinkmann, W., Kanbach, G., Rieger, E., Reppin, C., Trumper, W., and Lund, N. 1984, *Nature* 312, 46.
- Pizzichini, G. 1982, in "Gamma Ray Transients and Related Astrophysical Phenomena", eds. Lingenfelter, R.E., Worrall, D.M., and Hudson, H.S., (AIP Conf. Proc. No. 77; New York, AIP), 101.
- Pizzichini, G., Gottardi, M., Atteia, J.-L., Barat, C., Hurley, K., Niel, M., Vedrenne, G., Laros, J.G., Evans, W.D., Fenimore, E.E., Klebesadel, R.W., Cline, T.L., Desai, U.D., Kurt, V.G., Kuznetsov, A.V., and Zenchenko, V.M. 1985, preprint, to be published in *Ap. J.*
- Podobed, V.V. 1965, "Fundamental Astrometry", University of Chicago Press.
- Popovic, G.M. 1982, *Bull. Inform. du Centre de Donnees Stellaires (Strasbourg)* No. 22, 96.
- Rappaport, S.A. and Joss, P.C. 1985, preprint, to be published in *Nature*.
- Ricker, G.R.R., Doty, J.P., Lewin, W.H.G., Vallerger, J.V. and Vanderspek, R.K. 1984, in "High Energy Transients in Astrophysics", ed. S.E. Woosley (AIP Conf. Proc. No. 115; New York, AIP), 669.
- Schaefer, B.E., 1981, *Nature* 294, 722.
- Schaefer, B.E., Seitzer, P. and Bradt, H.V., 1983, *Ap. J.* 270, L49.
- Schaefer, B.E. and Ricker, G.R. 1983, *Nature* 302, 43.
- Schaefer, B.E., Bradt, H.V., Barat, C., Hurley, K., Niel, M., Vedrenne, G., Cline, T.L., Desai, U., Teegarden, B.J., Evans, W.D., Fenimore, E.E., Klebesadel, R.W., Laros, J.G., Estulin, I.V., and Kuznetsov, A.V., 1984, *Ap. J.* 286, L1.
- Schaefer, B.E., Vanderspek, R., Bradt, H.V., and Ricker, G.R. 1984, *Ap. J.* 283, 887.
- Schaefer, B.E. and Cline, T.L. 1985, *Ap. J.* 289, 490.
- Shklovskii, I.S. and Mitrofanov, I.G. 1985, *Mon. Not. R. Astr. Soc.* 212, 545.
- Teegarden, B.J. 1982, in "Gamma Ray Transients and Related Astrophysical Phenomena", eds. Lingenfelter, R.E., Worrall, D.M., and Hudson, H.S., (AIP Conf. Proc. No. 77; New York, AIP), 123.
- Teegarden, B.J., von Rosenvinge, T.T., Cline, T.L. and Kaipa, R. 1984, in "High Energy Transients in Astrophysics", ed. S.E. Woosley (AIP Conf. Proc. No. 115; New York, AIP), 687.
- Tremaine, S. and Zytow, A.N. 1985, preprint.
- Van Buren, D. 1981, *Ap. J.* 249, 297.

Ventura, J. 1983, Adv. Space Res., Vol. 3, No. 4, pp. 185.

Wdowiak, T.J. and Clifton, K.S. 1985, Ap. J. 295, 171.

Wood, K.S., Byram, E.T., Chubb, T.A., Friedman, H., Meekins, J.F., Share, G.H., and Yentis, D.J. 1981, Ap. J. 247, 632.

Woosley, S.A. and Wallace, R.K. 1982, Ap. J. 258, 716.

Woosley, S.A. 1984, in "High Energy Transients in Astrophysics", ed. S.E. Woosley (AIP Conf. Proc. No. 115; New York, AIP), 485.